UAB
Universitat Autònoma de Barcelona

Interfacial phenomena in graphene materials, devices and applications

Marta Delgà Fernández

ADVERTIMENT. L'accés als continguts d'aquesta tesi queda condicionat a l'acceptació de les condicions d'ús establertes per la següent llicència Creative Commons: https://creativecommons.org/licenses/?lang=ca

ADVERTENCIA. El acceso a los contenidos de esta tesis queda condicionado a la aceptación de las condiciones de uso establecidas por la siguiente licencia Creative Commons: https://creativecommons.org/licenses/?lang=es

WARNING. The access to the contents of this doctoral thesis it is limited to the acceptance of the use conditions set by the following Creative Commons license: https://creativecommons.org/licenses/?lang=en

Interfacial phenomena in graphene materials, devices and applications

Marta Delgà Fernández

Facultat de Química
Universitat Autònoma de Barcelona

A thesis submitted for the degree of Doctor of Philosophy
PhD program in Materials Science

Supervisors: Dr. Elena del Corro
Prof. Dr. Jose A. Garrido
Tutor: Prof. Dr. Jose A. Garrido
Defense date: July 2024

Barcelona, 2024

I hope that we continue with exploration.

- Margaret H. Hamilton

Acknowledgements

I want to thank everyone who walked alongside me on this PhD journey and helped me make this thesis possible. Firstly, I would like to sincerely thank my PhD supervisors. A Jose Garrido le agradezco haberme permitido realizar esta tesis doctoral en el grupo AEMD del ICN2 y haber podido tener el privilegio de aprender de su liderazgo científico en el campo de los dispositivos de grafeno, su visión y trabajo. También le agradezco haberme permitido completar mi período doctoral con estancias en centros de investigación internacionales que han sido claves en mi crecimiento científico y personal. A Elena del Corro le agradezco su supervisión y enseñanza continua, que me han ayudado a crecer como científica y como persona. Le agradezco haberme animado siempre a avanzar con perseverancia, confianza y haber sido, en definitiva, mucho más que una directora.

Thank you to the former and current members of the AEMD group: Andrea, Damià, Ramon, Nathan, Taygun, Nicola, Anna, Alex, with whom I have learnt and who have been partners in this journey. Especialmente, quiero agradecerle a Antonio Pablo haber sido mi maestro en el arte de crecer grafeno, una de las primeras cosas que aprendí cuando empecé el doctorado. A Pilar, gracias por todas las vivencias dentro y fuera del laboratorio y por ser la responsable de muchas risas estos años, que tanto han ayudado en los momentos más difíciles. A Jose Cruz, gracias por ayudarme siempre que lo he necesitado. Chris, thank you for organizing one of the best plans outside the lab and for sharing all your knowledge about MoS_2 with me. Thank you to the bachelor and master students with whom I have worked. A l'Aina i la Laura, que van arribar al grup quan encara no havien acabat el grau i s'ha acabat quedant i esdevenint persones molt importants. És molt emocionant veure els vostres avenços. A en Miquel i la María, gràcies pels bons moments i per fer que l'ambient al laboratori sigui excel·lent. También quiero darle las gracias a Amador por su ayuda en el análisis de XPS y UPS. Gracias a Patricia por ayudarme desde el principio y a Sara B. que en poco tiempo se convirtió en pieza clave para que todo funcionara y que

con su energía y vitalidad hace los días más alegres. Gracias también a Sara M. y a todo el equipo de administración del ICN2.

Vull agrair a tots els members del GAB, al CNM, en especial l'Anton Guimerà, per l'ajuda en l'anàlisi de mesures d'impedància, que fonamenten bona part dels estudis de la tesi; en Xavi Illa, pel suport en la fabricació dels dispositius; l'Eli Prats i en Sergi Brosel, per compartir coneixements sobre detecció de biomol·lècules i per totes les bones estones.

Thank you to the collaborators with whom I have worked in the framework of this thesis outside and inside the ICN2: a Roque, el mejor compañero de oficina y responsable de hacer posible muchos experimentos de esta tesis; a en Jose Santiso y a la Jessica, responsables dels experiments de XRD; a Guillaume, por las conversaciones y la ayuda con el XPS; a Raúl, Javi Sainz y a Rafa.

In my stays abroad, I met extraordinary people who inspired me and helped me along the way. I want to express my gratitude to Prof. Marcos Pimenta and all the people of his group at the UFMG in Belo Horizonte. I also want to deeply thank Liam Collins, Martí Checa and Neus Domingo for making me feel at home when I was very away from home, during my stay at the ORNL. I am also thankful to Alexis for all the incredible experiences in the USA and for becoming one of the best friends I have now. Finally, I want to really thank Miquel Salmeron and his wife, Greta, for their hospitality and help during my stay at the LBNL, in Berkeley. I feel privileged for having had the opportunity to know all you.

Vull agrair el suport de la Júlia i la Clàudia. La seva amistat ha fet el camí més bonic. Gràcies a la Lía i a la Katherine, qui vaig conèixer a Nijmegen durant l'Erasmus i amb qui he viscut moltes experiències. Gracias a María Tenorio y a Bárbara. No podría haber tenido más suerte en conoceros. Gràcies a la Susanna per animar-me sempre, alegrar-se per totes les coses bones i celebrar-les amb mi. Vull agrair-li també, especialment, a l'Adriana haver-me ajudat amb el disseny i l'edició de la tesi amb una il·lusió emocionant des del primer moment que li vaig proposar. A la Laia, per la seva amistat i alegria sempre.

Aquesta tesi no hagués estat possible sense la meva família: les meves àvies; Loreto, a qui trobo molt a faltar, i Mercè. Tots els meus tiets, tietes, cosins i cosines, l'Aina i la Montse, sempre han estat al meu costat i jo aprenc d'ells cada dia. Gràcies a la tieta Neus, que ha estat sempre un suport importantíssim. Al meu germà Ferran, el millor regal que m'han fet els pares. Al pare i la mare, que m'han ensenyat que la millor recompensa arriba sempre després de treballar

molt, i que el més important és que sigui feliç amb el que faci. A en Marc, el millor company de viatge i amb qui espero viure molta vida. Us estimo molt.

Abstract

Due to its unique mechanical, optical and electrochemical properties, graphene has raised great interest for biosensing and bioelectronic applications. Although current graphene-based technology has demonstrated remarkable potential in the biomedical field, fundamental knowledge about graphene interaction with the media surrounding it is still missed. This PhD thesis is devoted to the study of interfacial phenomena that can govern the performance of graphene devices, from its synthesis to the final application.

Concerning graphene synthesis, we prepare rigid, flat and reusable copper supports for the growth of high-quality, large-scale graphene to be used in electronic devices. The engineered Cu-based substrates are presented as a promising alternative to the currently most used Cu foils for graphene growth.

Graphene based electronic devices in biomedical applications are aimed to work in an aqueous media. In this dissertation, we study how the graphene/substrate and the graphene/electrolyte interfaces govern the electronic performance of such devices. Furthermore, a study of the impact of the wafer-scale fabrication is conducted, highlighting the importance to preserve the graphene surface throughout the process for optimal and reproducible performance of graphene SGFETs.

For biosensing applications, graphene functionalization is key. In this work, we propose a novel approach based on the in-vacuum sublimation of a pyrene-based molecule. This molecule can be deposited on the graphene surface in a controllable, reproducible way. A methodology for the characterization of the resulting functionalized graphene surface, as well as for the quantification of the functionalization is discussed. The functionality of the functionalized graphene SGFETs is tested in different pH conditions and compared with standard, non-functionalized devices. With that, we demonstrate that the proposed functionalization approach is a promising path towards the optimization of graphene-based biosensors for the detection of a variety of biomolecules, including neurotransmitters.

Resum

El grafè és un material de gran interès per a aplicacions biomèdiques, gràcies a l'excel·lent combinació de les seves propietats mecàniques, òptiques i electroquímiques. Actualment, tot i que la tecnologia basada en grafè ha demostrat el seu potencial en el camp de la biomedicina, és necessari aprofundir en el coneixement sobre les interaccions que s'estableixen entre aquest material i el medi que l'envolta. Aquesta tesi doctoral es centra en l'estudi dels fenòmens d'interfície que poden regir el comportament dels dispositius de grafè, des de la seva síntesi fins l'aplicació final.

En relació a la síntesi escalable de grafè per a dispositius electrònics, s'han preparat substrats reutilitzables, rígids i de baixa rugositat basats en coure. Aquests substrats es presenten com una alternativa prometedora a les làmines de coure, que actualment s'utilitzen majoritàriament per la preparació de grafè.

Els dispositius electrònics de grafè, quan s'utilitzen per aplicacions biomèdiques, es troben en medi aquós (electròlit). En aquesta tesi, s'estudien les interaccions grafè/substrat i grafè/electròlit i la seva influència en el comportament electroquímic dels dispositius SGFETs. Així mateix, s'avalua l'impacte del procés de fabricació a escala d'oblia dels SGFETs en el seu rendiment. Especialment, es remarca la importància de preservar la superfície del grafè durant cada pas del procés per tal que el rendiment sigui òptim.

Per a la fabricació de biosensors de grafè, cal funcionalitzar-lo. En aquesta tesi, es proposa un mètode basat en la sublimació en buit d'un derivat del pirè, una molècula que pot ser dipositada a la superfície del grafè de manera controlada i reproduïble. Per a caracteritzar i quantificar la funcionalització, es desenvolupa una metodologia basada en tècniques espectroscòpiques i de microscopia de força atòmica. Els dispositius fabricats de grafè funcionalitzat demostren ser viables en diferents condicions de pH. Per tant, es demostra que el mètode de funcionalització proposat és prometedor i podria aplicar-se per la fabricació de sensors capaços de detectar una àmplia varietat de biomol·lècules, inclosos neurotransmissors.

Thesis Framework

This thesis has been prepared within the PhD program in Materials Science of the Autonomous University of Barcelona (UAB). The work presented was developed with the financial support of: the MCIN/ AEI /10.13039/501100011033 under the project Neuro2Dtech (PID2020- 113663RB-I00) and the Spanish State Research Agency ref.PRE2018-086251; AEI/ESF, EU; the European Union's Horizon 2020 research and innovation programs under grant agreements Nº 785219 (Graphene Flagship Core Project 2) and Nº 881603 (Graphene Flagship Core Project 3). The core experimental part of the dissertation was performed in the Advanced Electronic Materials and Devices (AEMD) laboratory, led by Prof. Jose A. Garrido and Dr. Elena del Corro at the Catalan Institute of Nanoscience and Nanotechnology (ICN2) and at the ICN2's associated research support units with facilities for nanomaterials growth, electron microscopy, photoemission spectroscopy, X-ray diffraction, and nanofabrication. Great part of the device fabrication was carried out at the clean room facility of the Institute of Microelectronics of Barcelona (CNM-IMB, CSIC), thanks to a close collaboration between the AEMD and the Biomedical Applications group (GAB) there. Experiments using Dual-harmonic Kelvin Probe Force Microscopy have been mainly carried out during a research stay at the Functional Atomic Force Microscopy Group of the Center for Nanophase Materials Sciences at Oak Ridge National Laboratory (Tennessee, USA).

Accronyms

2D Bidimensional

AFM Atomic force microscopy

AP 1-aminopyrene

BSE Back-scattered electrons

CB Conduction band

CCD Charge-coupled device

CE Conter electrode

CNP Charge neutrality point

CNTs Carbon nanotubes

CPE Constant phase element

CV Cyclic voltammetry

CVD Chemical vapor deposition

DAQ Data acquisition card

DC Direct current

DH Delta height

DH-KPFM Dual-harmonic Kelvin probe force microscopy

DIW Deionized water

DOS Density of states

DUT Device under test

DSC Differential scanning calorimetry

EBSD Electron backscatter diffraction

EDL Electric double layer

EFM Electrical force modulation

EIS Electrochemical impedance spectroscopy

FET Field effect transistor

FWHM Full-width-at-half-maximum

GC Gouy-Chapman

GCS Gouy-Chapman-Stern

GIWAXS Grazing Incidence Small-angle X-ray scattering

gSGFET graphene solution-gated field effect transistor

ICN2 Catalan Institute of Nanoscience and Nanotechnology

ICP-RIE Inductively coupled plasma - Reactive ion etching

IP Ionization potential

IPE Ideal polarizable electrodes

LPCVD Low pressure chemical vapor deposition

NTEZ Low temperature effusion cell

OHP Outer Helmholtz Plane

ORR Oxygen-reduction reaction

OMBE Organic molecular beam epitaxy

PBA 1-pyrenebutyric acid

PBS Phosphate buffered saline

PCB Printed circuit board

PDMS Polydimethylsiloxane

PF Pole figure

PID Proportional-integral-derivative

PMA Poly(methacrylic) acid

PMMA Poly(methyl methacrylate)

PEIS Potentiostatic electrochemical impedance spectroscopy

QCMB Quartz crystal microbalance

RE Reference electrode

RHEED Reflection high-energy electron diffraction

RMS Root-mean-square

SE Secondary electrons

SEM Scanning electron microscopy

TEM Transmission electron microscopy

TLM Transfer length method

UPS Ultra-violet photoelectron spectroscopy

VB Valence band

XPS X-ray photoelectron spectroscopy

XRD X-ray diffraction

WE Working electrode

ZA Zone axis

Table of Contents

Title Page i

Abstract ix

Resum xi

Thesis Framework xiii

Accronyms xv

List of Figures xxiii

List of Tables xxix

1 Motivation & Objectives 1

1.1 Scope and objectives of this thesis 6

2 Materials & Methods 9

2.1 Electronic properties of graphene 9

2.2 Standard graphene growth on copper foils 11

2.3 Graphene growth on rigid substrates 13

2.4 Graphene-based devices fabrication 15

2.4.1 Graphene transfer 15

2.4.2 Wafer-scale fabrication 17

2.5 Advanced characterization procedures 18

2.5.1 Raman spectroscopy and spectroelectrochemistry 18

2.5.2 Atomic Force Microscopy and Kelvin Prove Force Microscopy 22

2.5.3 Scanning Electron Microscopy and Electron backscatter diffraction 23

2.5.4 X-ray diffraction 25

2.5.5 Electrical characterization of graphene Solution-Gated Field Effect Transistors 28

3 Substrate engineering for graphene growth 31
3.1 General overview of graphene synthesis techniques 31
3.1.1 Chemical Vapor Deposition for graphene growth 33
3.2 Sapphire substrate preparation 37
3.2.1 Copper annealing 41
3.3 Graphene growth 47
3.3.1 Graphene transfer and device fabrication 50
3.4 Substrate reusability 52

4 Physicochemical characterization of the graphene/substrate and graphene/electrolyte interfaces 55
4.1 Graphene electronic devices in aqueous media 55
4.2 Electrochemical double layer at the graphene-electrolyte interface 56
4.2.1 Electrode-electrolyte interface: Electrochemical Double Layer 56
4.2.2 Graphene Quantum Capacitance 58
4.2.3 Electrochemical Impedance spectroscopy 59
4.3 Substrate effect on the electronic properties of graphene 62
4.4 Electrolyte effect on the electronic properties of graphene 78
4.5 Effect of adsorbed charge on graphene electrodes performance . . 83
4.5.1 Monitoring of wafer-scale fabrication residues on graphene electrodes 98

5 Graphene functionalization towards a universal biosensing platform based on graphene/pyrene surfaces 107
5.1 Graphene devices for biosensing applications: g-SFETs 108
5.2 Graphene functionalization strategies 109
5.2.1 Noncovalent functionalization of graphene: pyrene derivatives 110
5.2.2 Graphene functionalization with 1-pyrenebutyric acid . . 111
5.3 PBA sublimation for graphene functionalization 112
5.4 Optimization of the evaporation parameters 120
5.4.1 PBA evaporation temperature 120
5.4.2 Substrate temperature 123
5.5 Graphene/PBA surface characterization 128
5.6 Electrical characterization of graphene/PBA SGFETs 130

6 Conclusions & Outlook 135

Appendix A Chapter 3 complementary data **139**
A.1 600 nm thickness of copper on c-sapphire 139
A.2 Heating and cooling rates of the copper annealing 141

Appendix B Chapter 4 complementary data **145**
B.1 Resources available online 145
B.2 PEIS fitting parameters 145
B.3 Capacitance simulation details and charge density profiles 146
B.4 PEIS data of pyrex/graphene and ITO/graphene electrodes . . . 151
B.5 Measurements on Au/graphene electrodes 152
B.6 Challenges on the integration of the Cu protection strategy to the standard fabrication of wafer-scale graphene electronic devices . . 156

Appendix C Chapter 5 complementary data **159**
C.1 Aminopyrene deposition on graphene 159
C.2 Standard effective gate noise values of gSGFETs 161
C.3 Aptamer incorporation to graphene/PBA surfaces and thrombin detection 162
C.4 Grazing Incidence Small-angle X-ray scattering on graphene/PBA surfaces 164

Appendix D Water intercalation in graphene devices **167**

Appendix E In-liquid Dual-Harmonic KPFM for the study of electronic properties of graphene materials and devices **173**
E.1 DH-KPFM of an in-operando gSGFET 179

Appendix F Experimental techniques: fundamentals and equipment **183**
F.1 Metal deposition 183
F.1.1 Electron-beam evaporation 184
F.2 Raman spectroscopy 185
F.3 AFM and KPFM 187
F.4 X-ray and ultraviolet photoelectron spectroscopy 189
F.5 SEM and EBSD 193
F.6 X-ray diffraction 195
F.7 Electrical characterization of gSGFETs 197

Publications **199**

References **201**

List of Figures

2.1 Graphene lattice and electronic structure 10
2.2 Graphene growth at the CVD1 reactor 12
2.3 Electropolishing of Cu foils 13
2.4 Reactor: CVD2 13
2.5 Rigid substrates preparation for graphene growth 14
2.6 Hoberseal furnace for sapphire surface preparation 15
2.7 Graphene wet transfer 16
2.8 Fabrication of graphene devices 17
2.9 Raman spectroscopy of graphene 19
2.10 Raman ω_{2D}-ω_G correlation map of a graphene sample 20
2.11 Raman spectroelectrochemistry setup 21
2.12 Representation of graphene macroelectrodes 22
2.13 AFM of graphene on pyrex 23
2.14 SEM images of graphene grown on Cu foils 24
2.15 Cu crystallographic structure and orientations defined by Miller indices 25
2.16 EBSD map of a Cu foil 25
2.17 XRD measurement of evaporated Cu on sapphire. 27
2.18 Description of the common features for Pole Figure scans 27
2.19 g-SGFET 28
2.20 Graphene field-effect transistor transfer curve (I_{ds}-V_{gs}) 29
2.21 Graphene SGFET wafer-scale devices 30

3.1 Timeline of graphene growth techniques since its first isolation in 2004 32
3.2 Classification of CVD methods 33
3.3 Schematic illustration of CVD graphene growth mechanism . . . 35
3.4 Graphene on different Cu orientations 36
3.5 Sapphire crystal structure and vicinal structure 37

3.6 Sapphire surface reconstruction 38
3.7 Cu on SiO_2/Si evaporation rate study 39
3.8 Sapphire surface impact on Cu thin film 40
3.9 Impact of H_2 on the Cu roughness 42
3.10 Cu annealing temperature series. 43
3.11 Effect of annealing time on Cu surfaces 44
3.12 XRD analysis of annealed sapphire/Cu. 45
3.13 sapphire/Cu annealing at 1000°C for 120 minutes. 46
3.14 Pole figures of annealed sapphire/Cu 47
3.15 Characterization of graphene grown on sapphire/Cu 49
3.16 Reproducibility of graphene growth 50
3.17 Sapphire substrate after graphene dry transfer 51
3.18 Raman characterization from growth to fabrication 52
3.19 Sapphire surface after graphene wet transfer 53
3.20 Graphene grown on a reused c-sapphire substrate 53

4.1 GCS electrochemical double layer (EDL) model 58
4.2 Capacitance at the graphene-electrolyte interface 59
4.3 Electrode/electrolyte interface frequency response and Randless circuit 61
4.4 PEIS experimental setup and Bode plot illustrating changes in R_s 62
4.5 EIS: Bode plots and equivalent circuit models 63
4.6 PEIS analysis of graphene electrodes 66
4.7 PEIS of bare ITO and Au 68
4.8 Mott-Schottky plot of ITO substrate 68
4.9 Raman maps of the ω_G of pyrex/graphene, ITO/graphene and Au/graphene electrodes 69
4.10 Raman spectroscopy analysis of graphene electrodes 71
4.11 Water intercalation in graphene electrodes 73
4.12 Series and parallel configurations in graphene electrodes 74
4.13 Depletion region between an ITO substrate and the electrolyte . 75
4.14 Numerical simulations on the ITO-intercalated water-graphene-bulk electrolyte interface 77
4.15 Numerical simulations for the calculation of C_{total} 78
4.16 Electrolyte pH and ionic strength effect on electrochemical response of pyrex/graphene electrodes 80
4.17 PMMA stability under different pH conditions in aqueous media 81
4.18 Electrolyte effect on graphene ω_G-V response 83
4.19 PEIS of graphene electrodes after fabrication 85

4.20 PEIS of pyrex/graphene electrodes after fabrication at different pH (V = 0.3 V). 86
4.21 Pyrex/graphene phase modulation with voltage at 10 Hz from PEIS measurements 87
4.22 Raman spectroscopy of fabricated graphene electrodes 88
4.23 XPS characterization of graphene samples 90
4.24 UPS analysis for workfunction calculation 92
4.25 Potential and charge schemes of the graphene/electrolyte interface 94
4.26 Graphene G band frequency vs electrolyte ionic strength. 95
4.27 Raman spectroscopy of wafer-scale graphene electrodes at different electrolyte pH with increasing [KCl 96
4.28 Raman spectroscopy of pyrex/graphene and ITO/graphene electrodes with increasing [KCl 98
4.29 Schematics of sample preparation for the assessment of the impact of fabrication residues on graphene's electronic properties 99
4.30 Impact of the fabrication on graphene assessed by Raman spectroscopy 101
4.31 Schematics of the fabrication of wafer scale graphene devices . . 102
4.32 Cyclic voltammetry and XPS for monitoring Cu etching after graphene devices fabrication. 103
4.33 Characterization of graphene surfaces on devices fabricated with and without Cu protection. 105

5.1 Pyrene and 1-pyrenebutyric acid 111
5.2 Differential Scanning Calorimetry of 1-pyrenebutyric acid 113
5.3 XPS monitoring of graphene functionalization with PBA 114
5.4 XPS monitoring of graphene functionalization with PBA. Peak deconvolution 115
5.5 Laboratory equipment assembled and used for vacuum-based functionalization of graphene 116
5.6 Characterization of annealing of as-transfer graphene samples . . 118
5.7 Raman spectra of graphene and graphene/PBA 119
5.8 Raman characterization of the T_{PBA} series 121
5.9 AFM characterization of the T_{PBA} series 122
5.10 Raman characterization of the T_{subs} series 123
5.11 AFM characterization of the T_{subs} series 124
5.12 T_{subs} 40°C Raman cluster analysis 125
5.13 T_{subs} 60°C Raman cluster analysis 125
5.14 AFM step characterization of graphene/PBA 126

5.15 Electrical characterization in g-SGFET configuration 129
5.16 Raman spectroelectrochemistry for doping quantification 130
5.17 Electrical characterization of pyrex/graphene transistors before and after PBA functionalization 132
5.18 Electrical characterization of SiO_2/Si/graphene transistors before and after PBA functionalization 133

A.1 Temperature series of the annealing of Cu (600nm) on c-sapphire 140
A.2 Time series of the annealing of Cu(600nm) on c-sapphire 141
A.3 Cu annealing heating rates 142
A.4 Cu annealing cooling rates 143

B.1 Numerical simulations of C_{ITO}^{bulk} and C_{ITO}^{conf} 148
B.2 Effect of ε_w on charge density vs V profiles at the ITO/confined water/bulk electrolyte structure 149
B.3 Contribution of the charge density of the confined water region and the bulk electrolyte to the total capacitance for different ε_w 149
B.4 Effect of t_w on charge density vs V profiles at the ITO/confined water/bulk electrolyte structure 150
B.5 Contribution of the charge density of the confined water region and the bulk electrolyte to the total capacitance for different t_w . 150
B.6 PEIS of graphene electrodes after fabrication in PBS, pH 3 and 10 152
B.7 PEIS of Au/graphene electrodes after fabrication in PBS at different pH 153
B.8 Raman spectroscopy of Au/graphene electrodes 153
B.9 XPS analysis of Au/graphene electrodes 154
B.10 UPS analysis of Au/graphene electrodes 155
B.11 Raman spectroscopy of Au/graphene electrodes after fabrication in PBS with increasing [KCl 156
B.12 Issues in the integration of the graphene protection with Cu to the standard fabrication protocol 157
B.13 Electrical characterization of gSGFETs fabricated by standard fabrication and using a protective Cu layer 158

C.1 DSC analysis of aminopyrene 160
C.2 Graphene functionalization with aminopyrene 161
C.3 Electrical characterization of graphene gSFETs (standard) 161
C.4 Aptamer binding to graphene/PBA 163
C.5 Thrombin detection 163
C.6 2D GIWAXS of graphene/PBA 165

D.1 Water intercalation in as-transfer graphene on pyrex 168
D.2 DUT design 169
D.3 Water intercalation in graphene devices observed by Raman spectroscopy 170
D.4 Electrical characterization of gSGFETs before and after immersion in PBS 171

E.1 DH-KPFM setup 175
E.2 In-liquid DH-KPFM on pyrex/graphene 176
E.3 In-liquid DH-KPFM on ITO/graphene 177
E.4 CPD values from DH-KPFM 178
E.5 Transistor design for in-liquid DH-KPFM measurements 180
E.6 DH-KPFM of an *in-operando* graphene transistor 181
E.7 In-liquid DH-KPFM of an *in-operando* graphene transistor 181

F.1 Electron-beam evaporator 185
F.2 Basic principle of Raman spectroscopy 186
F.3 Raman spectrometer 187
F.4 Representation of the KPFM working principle 188
F.5 AFM 189
F.6 X-ray photoelectron spectroscopy 190
F.7 XPS-UPS system 192
F.8 XPS system with a coupled OMBE evaporator 193
F.9 SEM Quanta 650 FEG at ICN2 195
F.10 XRD equipment 196
F.11 gSGFETs characterization setup 197

List of Tables

4.1 |Z| values from PEIS measurements at low and high frequencies . 64
4.2 Band structure extraction from UPS. Energy difference E^F_{VB} between the Fermi level and valence band maximum E_{VB}, secondary electron cut-off $E_{cut-off}$, ionization potential IP and work function Φ, extracted from UPS spectra of the graphene on pyrex and ITO, and of the bare ITO samples. 91
4.3 Workfunction values of graphene on different substrates obtained by UPS 91

5.1 ω_G and I_{2D}/I_G values for the samples corresponding to the T_{subs} study. For T_{subs} = 40°C and 60°C, the two values correspond to the two areas of the samples, with and without PBA aggregates. 126
5.2 Thickness of functionalized graphene. Step analysis of AFM images in Figure 5.14 127

B.1 Fitting boundaries for each parameter of the Distributed model equivalent circuit used to determine the CPE from the PEIS data. R_n and R_{ct} (accounting for the processes at the electrode involving charge transfer), are the two contributions of R_{sh} 145
B.2 Fitting boundaries for each parameter of the Simple model equivalent circuit used to determine the CPE from the PEIS data 146
B.3 Band structure extraction from UPS on Au/graphene. Energy difference E^F_{VB} between the Fermi level and valence band maximum E_{VB}, secondary electron cut-off $E_{cut-off}$, ionization potential IP and work function Φ, extracted from UPS spectra of the graphene on Au, and of the bare Au samples. 155

1

Motivation & Objectives

Materials science has shaped human history by enabling the accomplishment of crucial technological milestones that have led us to the world as we know it today. Since the Neolithic Revolution, 12,000 years ago, until the recent advancements in artificial intelligence in the recent years, the evolution of humanity has been strongly linked to the properties that new materials offer. One of the most recent and important technological milestone reached was the invention of the first transistor in 1947 by researchers at Bell Laboratories [1]. This was possible after key advances in the semiconducting materials field, both gaining theoretical knowledge and succeeding in the isolation of germanium and silicon crystals [2, 3]. Silicon-based transistors have enabled the development of compact computers, playing a pivotal role in stimulating the invention of powerful technologies in many different scientific areas. Recent developments have pushed the down-scale of commercial transistors to dimensions < 2 nm. Keeping this scalability trend is not easily allowed by using silicon-based technology [4]. The irruption of bidimensional (2D) materials, that started with the isolation of graphene 20 years ago [5], has the potential to revolutionize the field of electronics and optoelectronics, which could imply almost limitless number of applications [6]. The Advanced Electronic Materials and Devices (AEMD) group at the Catalan Institute of Nanoscience and Nanotechnology (ICN2) was established in 2016 and, since then, focuses its work on developing a 2D materials-based technology for the pioneer development of the next generation neural interfaces.

The main requirements of neural implants are the efficient recording and stimulating of neural activity and stability. High stability of neural implants in contact with the brain tissue is achieved by ensuring high biocompatibility and flexibility [7]. High biocompatibility, meaning the high capability of a material to be in contact with human tissues without harming them [8], is required to ensure a long-term stability of the devices and to avoid complications after surgical implantation in the nervous system. The biocompatibility of an implant is determined by its position in the organism, the probe geometry and also the mechanical and chemical properties of the materials conforming it, as those will govern the bidirectional tissue-implant interaction [9, 10]. Biocompatibility studies using SiO_2/Si-based implants have revealed a level of tissue damage that limit their implementation in humans [11, 12]. Given the curved surface of the brain and the mechanical matching between tissue and soft materials, the use of flexible materials for neural implants is a promising strategy to enhance biocompatibility [13, 14]. In that direction, silicon nanomembranes on flexible substrates have been tested [15]. However, there has been no success in insulating silicon from the biological fluids to prevent device degradation. Other materials based on organic semiconductors have been proposed to be used as neural implants [16]. However, their electronic properties do not fulfill the requirements to be promisingly applicable in a near future [17]. Additionally, transparent neural implants would enable simultaneous imaging, which is strongly desired to widen the devices functionality [18]. From the electronic properties point of view, it is also important to note that an optimal material to be implemented as a neural interface with sensing capabilities requires semiconducting or conducting properties with high electrical mobility [19].

Graphene properties

Since its discovery, graphene has been foreseen as a revolution in materials science due to its unique combination of mechanical, optical, chemical and electronic properties. Graphene is known as the strongest bidimensional material, with a Young's modulus of 1 TPa and high breaking and intrinsic strength (42 N m^{-1} and 42 N m^{-1} respectively) [20]. Due to its low thickness, graphene is highly transparent in the visible spectra range [21]. As a carbon allotrope, made by sp^2 carbon atoms, it has a high chemical stability. Nevertheless, surface engineering of graphene is also possible thanks to the ability of the delocalized electrons of the sp^2 system with other molecules of interest, as it will be discussed later. As for the electronic properties, they are governed by graphene's unique band structure, explained in more detail in Section 2.1. Graphene possesses high charge

carriers mobility, which makes it highly interesting to be explored for electronic applications.

Graphene-based materials offer a plethora of possibilities in the biomedical field. Since the first years after its experimental isolation, graphene has been widely explored for the development of novel medical diagnostic and therapeutic technologies. For instance, graphene-based materials have been investigated for biomedical imaging [22, 23], drug delivery [24], antibacterial agents, optogenetics [25] and biosensing. But one of the field where graphene-based materials have most potential in biomedicine is in implantable electronic devices for the diagnosis and treatment of neural-related illnesses. For that, graphene-based implants such as retinal and brain implants have raised great interest [26, 27].

Particularly in the field of brain neural implants, graphene-based devices overcome the main issue from current silicon-based technology, mainly thanks to their transparency and flexibility, and therefore, being less invasive and offering high spatial resolution both for recording and stimulation, while enabling simultaneous imaging [22, 28]. Currently, graphene-based brain implants have demonstrated high potential in neural activity recording and stimulation [29, 30, 31, 32].

Graphene synthesis

Synthesis of graphene can be conducted by different methods. In brief, graphene can be obtained by mechanical exfoliation of graphite, by epitaxial growth on SiC or by chemical vapor deposition (CVD) growth on diverse substrates. Mechanical exfoliation of graphite has been reported to produce the highest quality graphene, with high carrier mobilities (up to $1.4{\cdot}10^5$ $cm^2/V{\cdot}s$ at room temperature) [33]. However, CVD growth, based on the decomposition of a carbon precursor and graphitization on a catalytic substrate, has been demonstrated to be the most promising technique for the production of large-area high quality graphene. Using CVD, production areas of tens of inches have been reported, with carrier mobilities of $5.1{\cdot}10^4$ $cm^2/V{\cdot}s$ at room temperature [34]. Hence, CVD is the most used technique for graphene synthesis in the fabrication of electronic devices for biomedical applications, as in other fields.

In general, CVD graphene growth is performed using substrates, mostly metallic catalysts, that are different from the ones that configure the electronic devices in an application. Growth substrates strongly influence graphene quality. Nowadays, most of the substrates used for CVD graphene growth, for instance metallic foils, are not specifically produced for the semiconductor industry; for that reason, their morphology and chemical composition can be very different between

suppliers and different batches [35]. During the last decade, high-quality graphene grown by CVD has been achieved thanks to the progress in understanding the graphene growth mechanism and how to control growth parameters (pressure, precursor, temperature, and growth time) [36]. However, due to the properties of the used metallic substrates, graphene growth conditions are irreproducible from batch to batch and when changing suppliers of the growth substrate. This highly compromises the scalability of the synthesis of high quality graphene, hindering the development of graphene-based technology and, consequently, the commercialization of CVD graphene products [37].

Characterization of graphene surfaces

Graphene's morphology, structure and carrier mobilities are generally characterized in dry conditions using different microscopic (e. g. scanning electron microscopy), spectroscopic (e. g. Raman spectroscopy) and electronic techniques. However, when being part of an electronic device for biomedical applications, graphene is in a liquid environment containing ions and molecules that may interact with its surface and affect its electronic properties and, therefore, its applications [38, 39]. Numerical simulations and experiments have revealed that the electrolyte ionic composition and concentration determine the ionic adsorption and the properties of water in the direct vicinity of the graphene surface [40, 41, 42]. Moreover, it has been proved that the substrate underneath graphene also plays a role in governing the electronic performance of graphene-based devices in liquid. Therefore, it is important to use suitable *in situ* characterization methods capable of studying the interfacial substrate/graphene/electrolyte phenomena to understand graphene's electronic behaviour in liquid environments.

Wafer-scale fabrication of graphene devices

Reproducible, clean, cost-effective and large-scale methods for the fabrication of graphene devices is as crucial as graphene synthesis optimization for pushing the boundaries of graphene technology [43]. The fabrication of graphene electronic devices mostly requires a series of photolithography-based processes performed in cleanroom facilities. Those processes require dedicated technical equipment and specific protocols, which are nowadays generally adapted from the ones used for the production of silicon-based technology. However, differently from the case of silicon and due to the bidimensional nature of graphene, the impact that these fabrication protocols may have on graphene's properties and, therefore, on the performance of the devices, is not fully understood.

As a first step of the fabrication process, graphene needs to be transferred from the growth substrate to the substrate patterned with metal tracks, that will configure the final devices. A great number of transfer processes are reported in literature, and the choice to use one or another depends on the strength of the substrate/graphene interaction, the area of the samples to be transferred and the application [44, 45, 46, 47]. Despite that, graphene transfer is a highly manual process in most of the cases and, moreover, requires graphene to be in contact with polymers [48]. The fact that this process is not yet automatised in a reproducible way, and the introduction of residues from the polymer(s) in contact with graphene that may be not effectively removed, difficult the translation of the process into an industrial scale.

Once graphene is transferred to the target substrate, the subsequent fabrication steps involve the use of a series of photolithography resins and cleaning methods that may have an impact on the morphology and the chemical stability of graphene. This, consequently, compromises the device-to-device homogeneity and the efficiency of the fabrication process, meaning that the yield of operational devices per wafer is suboptimal [49]. High efforts are being devoted to overcome these challenges. In general, a promising approach relies on graphene protection using sacrificial metallic or dielectric layers covering its surface throughout the fabrication process, subsequently being removed as a final step [50].

Graphene functionalization

As previously introduced, graphene's chemical structure makes it a very stable, biocompatible material. At the same time, the high stability of the graphene's delocalized π electrons limits its reactivity, thus the applicability in the biomedical and sensing field is hindered unless undertaking surface modification. Hence, graphene functionalization is widely investigated to modulate chemical and physical properties of graphene, widening the range of the applications of graphene-based electronic devices.

The functionalization of graphene can be conducted by two types of strategies: covalent, and non-covalent [51]. The covalent functionalization is based on the formation of a covalent bond between graphene and the desired molecule. Consequently, the pristine structure of graphene is altered, and so its intrinsic properties. For some applications, this may be desired. Nevertheless, the functionalization of graphene while maintaining its pristine structure unaltered is object of high interest. Non-covalent functionalization of graphene, based on the π-π interactions between graphene and the desired molecule, preserves graphene's

morphology while introducing novel functionalities at the graphene structure [52].

The next generation of neural implants is aimed to combine not only recording and stimulation functionalities, but also controlled drug delivery and chemical sensing functionalities [53]. Hence, incorporating in-situ biosensing of molecules related to neural diseases would provide deeper understanding of how the brain works, thus helping in the development of new diagnostic tools and therapies.

1.1 Scope and objectives of this thesis

Although graphene-based devices have demonstrated potential capabilities as neural interfaces, high efforts are devoted nowadays to overcoming the following main **challenges**:

- **Reproducibility in high quality graphene synthesis:** although much has been advanced in the development of graphene growth techniques, a reproducible, high-quality, large-scale method has not been yet achieved. This is mainly due to not employing substrates specially designed for graphene growth, but relying on commercial suppliers. Advances in substrate engineering for graphene growth would provide growth substrates with very low impurity levels and reproducible morphology for high-quality, scalable graphene growth.

- **Development of advanced characterization methods** to study the substrate-graphene-electrolyte system: graphene-based devices for biomedical applications are aimed to work in an aqueous environment, as neural implants will be placed inside the brain, but also biosensors need to be in contact with the liquid media containing the analyte to detect. Therefore, the study of the electrochemical behavior of graphene in aqueous solutions is crucial. Until now, regardless its importance, little is known about the graphene-water interface and its dependence with factors such as the graphene surface quality, the interaction with the substrate, the electrolyte ionic concentration, pH and the adsorbed residual charge at graphene's surface. Furthermore, when considering graphene biosensors, there is still much unknown regarding graphene chemical surface engineering through functionalization with molecules to enhance specificity to analytes.

- Improving wafer-scale **fabrication** of graphene-based technology: current microfabrication methods fail to accomplish clean and homogeneous devices. While diverse approaches have been proposed to protect graphene's surface

throughout the fabrication process, there is still room for improvement. Surface and interfacial phenomena between the graphene and its supporting substrate influence the potential success of the proposed approaches.

- Improving **graphene functionalization** control, specificity of the functionalization and characterization. Graphene surfaces must be clean for an effective functionalization. As commented before, this involves advances in the methods employed for the devices fabrication. Currently, characterization of functionalized graphene surfaces with different molecules does not provide quantification. That is, although electrochemical techniques allow the determination of the surface coverage, it is difficult to quantify the homogeneity and the number of layers of molecules that are placed at the graphene surface.

Responding to the challenges above, this PhD thesis studies graphene-related interfaces as a step towards the development of the next generation biomedical devices, with the following specific **objectives**:

- The construction of a chemical vapor deposition (CVD) reactor at the AEMD laboratory to initiate the study of graphene growth on rigid copper catalytic substrates, to set the basis in the group for the advancement towards a reproducible, large scale, high quality and cost-effective synthesis method.

- The development of a detailed study about the interfacial phenomena occurring at the substrate-graphene-electrolyte interface and the assessment of how water impacts on graphene's electronic properties and on the techniques to measure them.

- The exploration of an alternative to the standard fabrication of graphene-based devices, which incorporates a copper sacrificial layer to protect the graphene surface and preserve its structure and properties through the process.

- The study of a proposed novel approach for graphene functionalization with 1-pyrenebutyric acid (PBA), a molecule capable to bind with graphene's π system and attach to an aptamer for biosensing purposes.

Therefore, this doctoral thesis is structured in **5 chapters**: **Chapter 2** provides an explanation of the materials and methods used, with descriptions of the information provided by each characterization technique and the data interpretation. **Chapter 3** corresponds to the first chapter of results. After an

introduction containing the state of the art of graphene synthesis techniques and a more detailed explanation of the one used here, CVD, it continues with the explanation of the activities carried out to start the new research line in the group about graphene growth on rigid substrates. This Chapter, thus, is about the construction of the CVD reactor, the optimization of copper-based substrates and the first experiments regarding graphene growth on them. **Chapter 4**, the second chapter including results, starts with an introduction about the electrochemical double layer at the graphene/electrolyte interface and an important technique for its characterization, electrochemical impedance spectroscopy. After presenting the main challenges of the study of the substrate/graphene/electrolyte and the importance of its study for advancing in graphene-based technology, the results and its discussion are presented corresponding to each study. Finally, after highlighting one of the main challenges currently existing in the fabrication of graphene-based devices, an alternative fabrication approach is explored. **Chapter 5** is the last chapter of results. Its introduction explains the use of graphene devices as biosensors, while presenting the current functionalization approaches and the challenges of the technology, nowadays hindering its functionality in the biomedical field. Then, results regarding the study of graphene functionalization with PBA using a method based on the molecule sublimation in vacuum are presented, followed by an extensive characterization of the graphene/PBA surface and an evaluation of the fabricated devices functionality. Finally, **Chapter 6** is dedicated to sum up the conclusions from the experimental studies and discussions developed in each chapter. Experimental studies to further continue with the scientific lines involved in this dissertation are also proposed.

In summary, in this thesis we investigate the fundamental interfacial phenomena in graphene-based materials, devices and applications to provide insights on the importance of this basic research towards overcoming current challenges in graphene synthesis, fabrication and functionalization.

2

Materials & Methods

Each chapter of this dissertation is dedicated to study a different aspect of the graphene technology: the synthesis of the material, the fabrication and electrochemical properties of the devices and the functionalization for new applications. These studies have required the development of a variety of experimental methods and characterization techniques, but also incorporating a detailed understanding of the information provided by them, as well as its interpretation and correlation. In this chapter, we provide information about the materials and methods used throughout this PhD thesis.

2.1 Electronic properties of graphene

Graphene is a one-atom thick layer of carbon (C) distributed in a honeycomb lattice, as represented in Figures 2.1a,b. In graphene, the C atoms have an sp^2 hybridization, with a bond-dissociation energy of 3.6 eV, resulting in a mechanically and chemically stable C-C covalent bond. The distance between C neighbouring atoms is of 1.42 Å.

The extraordinary electronic properties of graphene are consequence of its band structure, determined by the p_z orbitals perpendicular to the graphene plane, which configure a delocalized π-orbital [54]. Graphene's valence and conduction bands meet at the corners of the Brillouin zone, named Dirac points, with a specific Dirac energy (E_D). Figure 2.1c represents the band structure of graphene

with a zoom in the electronic dispersion at the vicinity of the Dirac point. There, the calculation of the energy dispersion relation in graphene is given by [54]:

$$E_{\pm} \approx \hbar \pm v_f |\vec{k} - \vec{K}| \tag{2.1}$$

where $\hbar$ is the reduced Plank constant, $\vec{k}$ is the wave vector, v_f is the Fermi velocity (10^6 m/s) and $|\vec{k} - \vec{K}|$ is the momentum vector of the corner of the Brillouin zone.

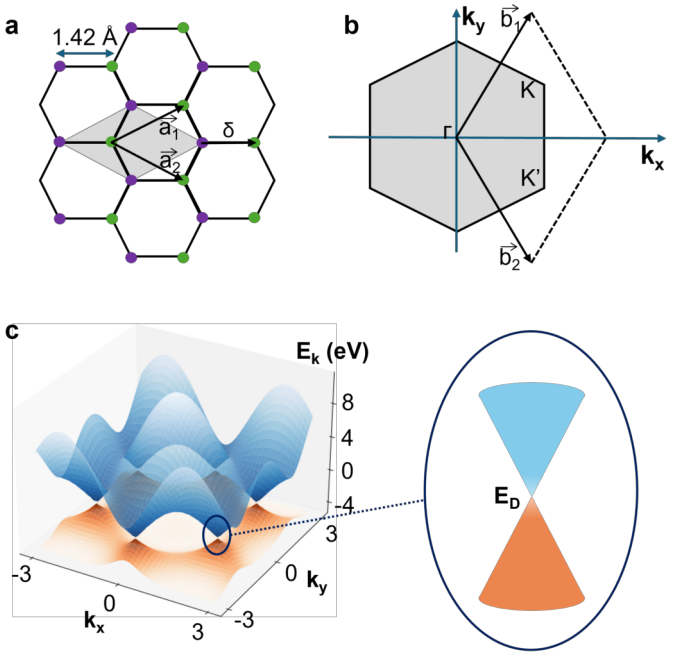


Figure 2.1: Graphene honeycomb lattice and graphene electronic dispersion - **(a)** Graphene lattice structure, with two interpenetrating triangular lattices. a_1 and a_2 are the lattice unit vectors and δ is one of the nearest vectors. **(b)** Brillouin zone of the lattice structure. **(c)** Energy spectrum for $t = 2.7$ eV and $t' = 0.2t$ with a zoom at the energy bands at the vicinity of one Dirac point, being E_D the Dirac energy. The Dirac points are located in the K and K' points in (b). Adapted from [54].

Two important consequences are derived from graphene's band structure: first, the effective mass of the charge carriers is null in the vicinity of the Dirac points. Consequently, they are described as massless Dirac Fermions. The unique behavior of these charge carriers enables the reported high charge carrier mobilities in graphene, with values higher than $1{\cdot}10^6$ $cm^2V^{-1}s^{-1}$ for suspended graphene at low temperatures [55]. The second consequence is the low density of states

(DOS) at the Dirac points, which has consequences for the so-called quantum capacitance. This will be further addressed in Section 4.2.2.

2.2 Standard graphene growth on copper foils

The AEMD group has a protocol for the synthesis of high quality CVD graphene on commercial Cu foils[1]. This graphene is used for the fabrication of wafer scale electronic devices for biomedical applications, e.g. neural implants [30, 32] and biosensors [56]. Figure 2.2a shows a picture of the CVD1 reactor at the AEMD research laboratory. It consists of a quartz tube (length: 1600 mm, diameter: 60 mm) with its central part placed inside a three-zone furnace and connected to a vacuum pump. To perform the desired processes, gases are introduced inside the tube and their gas flows are controlled by mass flow controllers. The process gases are argon (Ar), hydrogen (H_2) and methane (CH_4). Temperature, pressure and gas flows are controlled by a dedicated software. Standard graphene growth process performed in this reactor consists on the following (see scheme in Figure 2.2b): first, the 4×8 cm Cu foil placed at the central part of the tube on a quartz frame is annealed at 1050 °C in an Ar atmosphere (P∼100 mbar) during 90 minutes. Then, for the growth step, the temperature is increased up to 1065°C, and H_2 and CH_4 are introduced at 20 and 0.7 sccm respectively during 20 minutes (P∼25 mbar). After the growth, fast cooling is performed by taking the quartz tube out of the furnace and leaving an Ar flow of 400 sccm for 30 minutes. Samples are removed from the reactor and stored in a desiccator. The quartz tube is periodically annealed at 1200°C during 60 minutes in a Ar/H_2 atmosphere (see Figure 2.2c). This cleaning step is important to avoid the accumulation of residues from growth processes and thus to ensure reproducibility.

[1] Graphene Platform; 99.95%, 0.035 mm

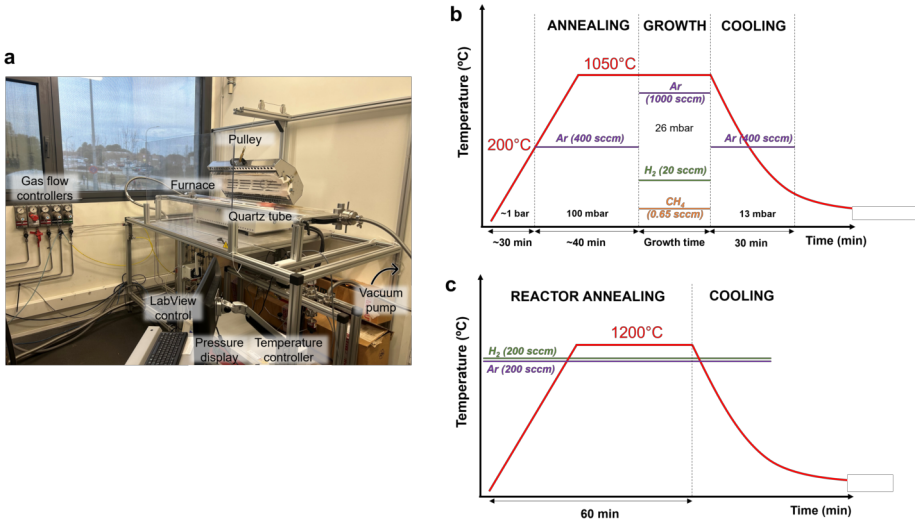


Figure 2.2: Graphene growth at the CVD1 reactor - **(a)** Photograph of CVD1. **(b)** Standard graphene growth process on Cu foils. **(c)** Process for reactor cleaning.

Commercially available Cu foils are electrochemically polished previously to be introduced in the CVD reactor for the graphene synthesis, following a method adapted from [57]. The aim of the electropolishing process is to remove surface contamination and reduce its roughness. A solution containing H_3PO_4, urea, ethanol, isopropanol and H_2O is prepared and introduced in an electrolytic cell (Figure 2.3). Two pieces of Cu foil are cut (14×16 cm) and immersed in the solution attached to Teflon holders. The two foils are connected to two terminals of a DC power supply and a voltage of 7 V is applied during 5 minutes (current density of ∼90 mA/cm^2). One of the foils acts as an anode and it is etched away, while the other acts as a cathode. After 5 min, the Cu foil - anode - is demounted from the holder and rinsed first with distilled H_2O, then with isopropanol and ethanol ensuring that it does not dry in between. Finally, it is blow-dried with nitrogen. The borders of the Cu foil are cut, obtaining a 4 × 8 cm final piece, where graphene will be grown.

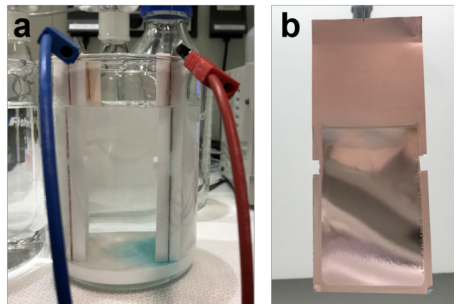


Figure 2.3: Electrochemical polishing of Cu foils before graphene growth - **(a)** Anode and cathode Cu foil pieces inside a beaker filled with the electropolishing solution and connected to the DC power supply. **(b)** Photograph of a copper foil piece after the polishing process. The brighter part corresponds to the area that has been electropolished.

2.3 Graphene growth on rigid substrates

In the framework of this PhD thesis, a CVD reactor was built-up for graphene growth on rigid substrates (Chapter 3). A photograph of the reactor, named CVD2, is shown in Figure 2.4a. Analogously to CVD1, CVD2 consists of a quartz tube connected to a vacuum pump, a furnace and mass flow controllers for Ar, H_2 and CH_4. After installation, processes carried out at CVD2 include the annealing of the Cu-based rigid substrates and the subsequent graphene growth on them. Figure 2.4b summarizes a typical graphene growth process. The optimization of the annealing of the Cu substrates will be discussed in Chapter 3. After each growth, the tube was annealed with the same conditions used for reactor CVD1 (Figure 2.2c).

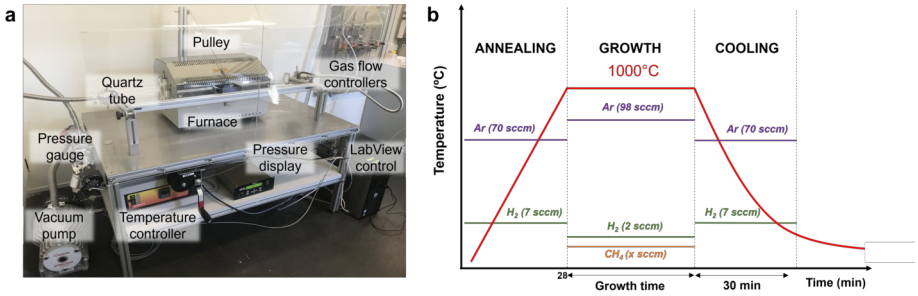


Figure 2.4: Graphene growth at the CVD2 reactor - **(a)** Photograph of CVD2 at the AEMD laboratory, which was built-up as part of this thesis. **(b)** Graphene growth process on Cu rigid substrates.

Copper rigid substrates

The optimization of the Cu rigid substrates preparation for graphene growth is further discussed in Chapter 3. There are basically two experimental steps, schematically represented in Figure 2.5:

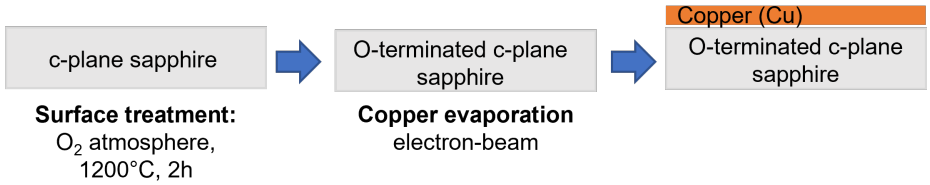


Figure 2.5: Representation of the surface preparation for graphene growth on rigid substrates, including c-plane sapphire annealing in oxygen atmosphere and copper evaporation by electron-beam.

1. **Sapphire annealing:** the use of sapphire as the support substrate will be explained in more detail in Section 4.3. Prior to Cu deposition, sapphire substrates[2] were annealed to obtain the desired surface termination. To accomplished that, the as-received sapphire are cut, the resulting pieces rinsed with deionized (DI) water and put in a clean ceramic crucible. The crucible is then introduced inside a high-temperature furnace (Hobersal, see Figure 2.6) and sapphire is annealed at 1200°C during 2 hours in oxygen atmosphere (50 sccm). Heating and cooling rates are set at 600°C/h and 300°C/h, respectively.

[2]Siegert Wafers; c-plane <0001> oriented, 99.998% purity, 400 μm thickness

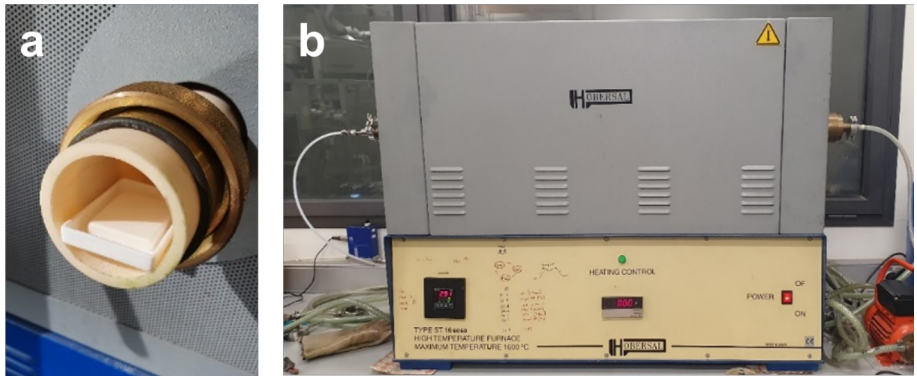


Figure 2.6: Sapphire annealing oven - **(a)** Ceramic crucible containing sapphire substrates. **(b)** Hobersal furnace (st.16 6060) capable to reach temperatures up to 1600°C. A high thermal resistant 99.7% pure alumina tube is fixed inside the furnace, where the crucible containing sapphire substrates is placed. Heating and cooling rates are regulated by a control panel at the bottom part of the furnace. A mass flow controller enables control over gas flow.

2. **Copper evaporation:** deposition of Cu on the sapphire substrates is performed by electron-beam evaporation, which is explained in more detail in Annex F.1.1.

2.4 Graphene-based devices fabrication

2.4.1 Graphene transfer

After grown on the catalytic support, graphene needs to be transferred to the desired target substrate. The unavoidable need of performing a transfer process has led researchers to devote numerous efforts to its optimization. Currently, there exist two main graphene transfer approaches: wet transfer [58] and dry transfer [59]. For graphene grown on Cu foils, we used the wet transfer approach as follows (see schematics in Figure 2.7). First, a PMMA A4[3] layer is spin-coated on the Cu/graphene and cured at room temperature overnight. Then, the graphene grown at the Cu backside is removed by an etching step at an ICP-RIE[4] of 40 W HF, 40 sccm Ar and 40 sccm O_2 at 80 mTorr during 6 minutes. After that, the Cu/graphene/PMMA stack is placed floating on an etchant solution of 0.5 M $FeCl_3$: 2 M HCl (1:2), with the Cu in contact with the solution overnight for a complete Cu etching. The sample is then transferred to a beaker containing deionized water (DIW) and left there with the graphene in contact

[3]MicroChemicals GmbH
[4]PlasmaPro 100 Cobra, Oxford Instruments

with DIW for 2 hours. This DIW cleaning step is repeated one more time and the sample is left to another beaker with new DIW for one hour. After this time, the graphene/PMMA is fished with the target substrate and left on a hotplate at 40°C for 2 hours to ensure complete evaporation of water. Once dried, the substrate/graphene/PMMA is high vacuum-annealed (P$\sim 10^{-7}$ mbar) at 180°C, 1 minute, using a heating ramp rate of 6°C/min. When the sample has cooled down back to room temperature, PMMA is removed by immersing (30 minutes) the sample in a beaker containing acetone, and then immersing it (30 minutes) in another beaker containing isopropanol. Finally, the substrate/graphene is blown dry with nitrogen.

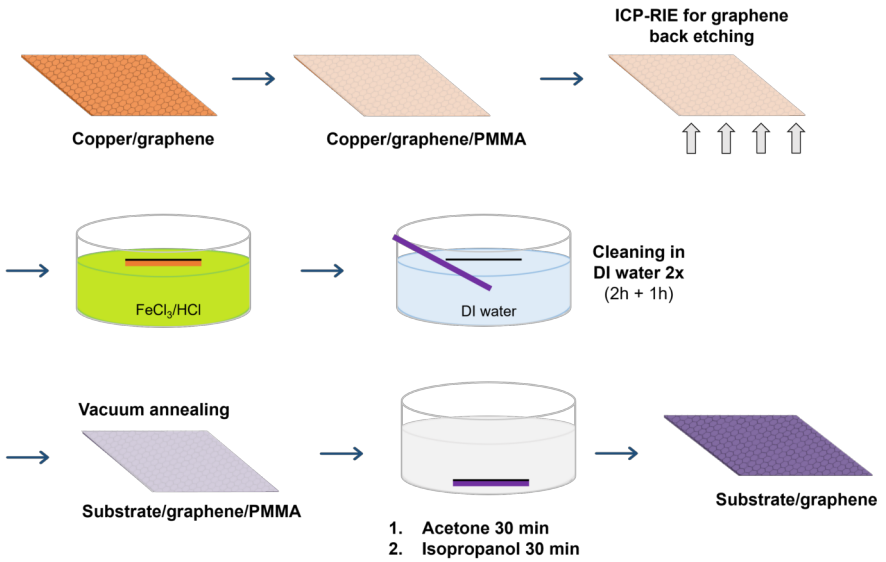


Figure 2.7: Graphene wet transfer - Schematics of the graphene wet transfer process steps used in this thesis.

Despite being widely established as a common transfer process in research and development (R&D) laboratories, the wet transfer presents a major challenge, which is the complete removal of PMMA residues. Numerous works have been published reporting different ways to clean graphene from PMMA [60]. However, most of them can compromise graphene mechanically - in terms of creation of defects - or electronically - in terms of doping -. This will be discussed in more detail in Chapter 4.

In this thesis, depending on the study, graphene is transferred on SiO_2/Si, pyrex (both isolating substrates), indium-tin-oxide (ITO, semiconductor substrate), or gold (Au, conductive substrate).

2.4.2 Wafer-scale fabrication

The wafer-scale fabrication of graphene devices, both electrodes and transistors, is based on a series of photolithography steps, which have been standardized by the group using SiO_2/Si substrates during the last years. In general, graphene is transferred to the target substrate previously patterned with metal tracks and pads, then, graphene is defined according to the device active area and finally passivated to leave only graphene exposed to the media. The individual steps conforming this process are represented in Figure 2.8. In Chapter 4, Section 4.5, an alternative fabrication protocol is explored, based on the use of a Cu sacrificial layer on graphene to preserve its structure throughout the process.

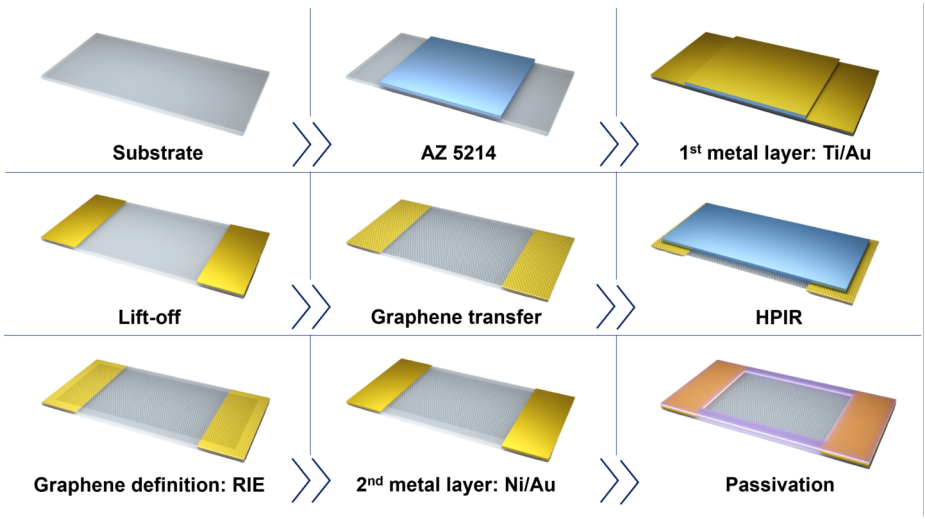


Figure 2.8: Fabrication of graphene devices - Process steps for the wafer-scale fabrication of graphene devices.

A summary of the fabrication steps is described below:

- **Track metalization:** metal tracks are defined by photolithography using AZ 5214[5], which is a negative resist.
- **First metal layer:** titanium/gold (Ti/Au, 10/100 nm) is evaporated by e-beam (see Annex F.1.1) followed by lift-off in acetone.
- **Graphene transfer:** detailed in Section 2.4.1.
- **Graphene definition:** HPIR[6] positive resist is used to define the graphene at the device's active area. Etching of the unprotected graphene is performed

[5]AZ 5214 E, Merck Performance Materials GmbH
[6]HPIR 6512, FujiFilm

by ICP-RIE (40 W HF, 40 sccm Ar and 40 sccm O_2 at 80 mTorr during 1 minute).

- **Second metal layer:** nickel/gold (Ni/Au, 20/200 nm) is evaporated by e-beam and a subsequent lift-off process in acetone.
- **Passivation:** to leave only the graphene active area in direct contact with the media, the metal tracks are passivated with a SU8 resist[7].

Apart from residues coming from the graphene transfer process (PMMA), additional residues remaining from the fabrication processes described above may affect the final performance of the devices. Thus, improving the fabrication protocol is highly relevant towards obtaining cleaner, high quality devices. As mentioned, the development of methods for monitoring surface residues on graphene and a proposed approach to avoid them is described in Chapter 4, Section 4.5.

2.5 Advanced characterization procedures

2.5.1 Raman spectroscopy and spectroelectrochemistry

In this thesis, Raman spectroscopy and spectroelectrochemistry are used for different purposes: in Chapter 3, we assess graphene quality of the as-grown, as-transfer and fabricated samples; in Chapter 4 we study graphene surface doping in a liquid environment and with the application of a potential. Finally, in Chapter 5 we investigate the degree of functionalization of graphene samples and perform doping quantification. A more detailed explanation of the fundamentals of the technique, as well as of the equipment used can be found in the Annex F, Section F.2.

Due to its particular electronic structure, graphene enables what is known as resonant Raman conditions [61] at the vicinity of the K point of the first Brillouin zone. This is because in those regions, the energy difference between the last occupied orbital (π) and the first empty orbital (π^*) is null, enabling the resonant conditions for any excitation energy. As a consequence, Raman spectroscopy on graphene monolayers provides intense and clear features. A typical Raman spectrum of graphene, depicted in Figure 2.9, presents two principal bands: (i) one at $\sim$1580 cm^{-1}, known as G band [62, 63], corresponding to the in-plane vibrational mode (stretching) of graphene sp^2 carbon atoms, a doubly degenerate zone center E_{g2} mode; (ii) one at $\sim$2700 cm^{-1}, related with the second order of

[7] SU8 2005, MicroChemicals GmbH

zone-boundary phonons, known as 2D band [62, 63]. In defective graphene, a third band is observed at ∼1350 cm^{-1}, known as D band [62, 63]. In monolayer graphene, the relation of intensities between the 2D and the G bands (I_{2D}/I_G coefficient) is < 2 [64, 65, 66].

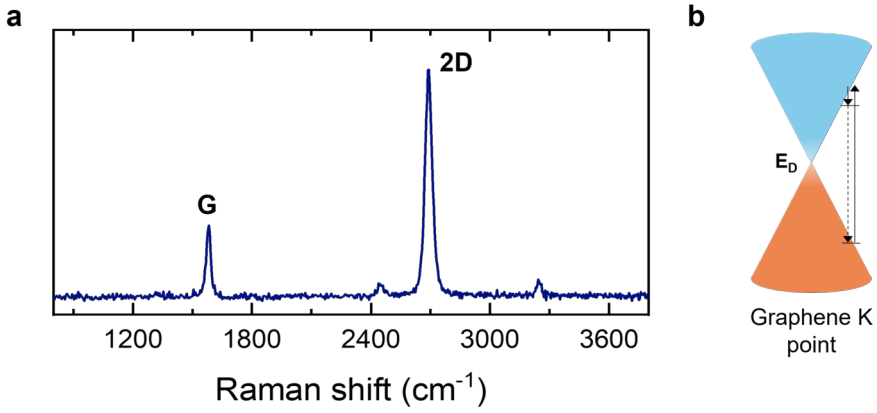


Figure 2.9: Raman spectroscopy of graphene - **(a)** Typical Raman spectrum of graphene. **(b)** Graphene electronic band structure represented at the vicinity of the K point, where Raman resonance, represented by the black arrows, is enabled.

The assessment of the mechanical strain and doping levels in graphene can be performed by correlation analysis of the Raman G and 2D modes [67]. This analysis will be used in Chapter 3 to qualitatively evaluate the reproducibility of the graphene growth using Cu foils and Cu-based rigid supports, in Chapter 4 to analyse the effects of the fabrication process of graphene devices on the graphene strain and doping levels and in Chapter 5, as part of the characterization of graphene/PBA surfaces. Knowing that strain and surface charge variations in graphene induce changes in ω_{2D} and ω_G [68, 69, 70, 71], a graphic representation of ω_{2D} vs ω_G (see Figure 2.10) enables the determination of the strain and doping separate contributions in graphene samples [67]. According to this methodology, based on a vector model, the linear dependence of the ω_{2D} and ω_G ratio under pure uniaxial strain has a slope ($(\Delta\omega_{2D}/\Delta\omega_G)_{strain}$) of ~ 2.2. Under pure hole doping, the slope ($(\Delta\omega_{2D}/\Delta\omega_G)_{doping}$) is of ~ 0.7. The origin of the strain and doping vectors is taken from the ω_{2D} and ω_G values of free-standing graphene (1581.6 cm^{-1} and 2676.9 cm^{-1}, respectively), or, alternatively, from the reference sample used in each study.

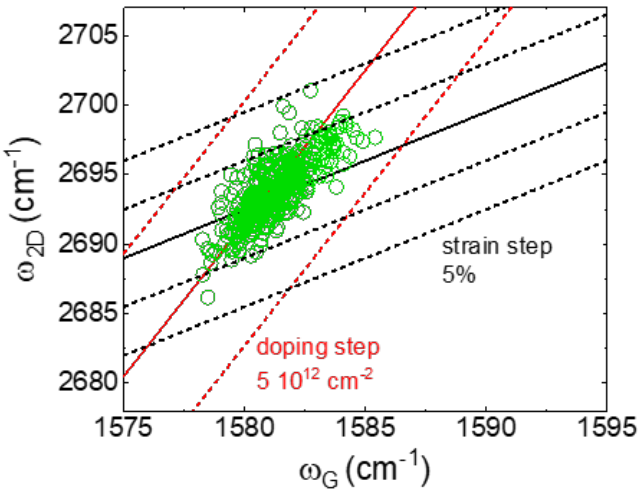


Figure 2.10: Raman ω_{2D}-ω_G correlation map of a graphene sample - The green dots correspond to data obtained from an as-transfer graphene sample on pyrex. Red and black lines indicate doping and strain steps, respectively. The slopes of the lines and the corresponding doping and strain levels are extracted from [67].

The combination of electrochemical techniques with Raman spectroscopy results in what is known as **Raman spectroelectrochemistry**, which is very powerful for monitoring graphene's doping level, as well as for monitoring surface charge modulation in contact with electrolytes. This is thanks to the strong electron-phonon coupling in graphene and the relation between the frequency of the G band (ω_G) with the Fermi level, described by equation 2.2 [71]:

$$\hbar\omega_G - \hbar\omega_G^0 = \lambda(|E_F| + \frac{\hbar\omega_G}{4} ln|\frac{2|E_F| - \hbar\omega_G}{2|E_F| + \hbar\omega_G}) \tag{2.2}$$

where ω_G^0 is the ω_G at the Dirac point and λ is directly proportional to electron-phonon coupling and indirectly proportional to the Fermi velocity υ_F [71]. Hence, by monitoring ω_G with respect to different voltages applied, we can analyse the voltage-dependent electron-hole modulation in graphene. Furthermore, this analysis enables the quantification of the amount of surface charge carriers (electrons or holes) by using [71]:

$$n = \frac{C_g(V_g - V_{Dirac})}{e} \tag{2.3}$$

being C_g the gate capacitance (or alternatively the interfacial capacitance), V_{Dirac} the gate voltage corresponding to the CNP and e the electron charge ($1.6{\cdot}10^{-19}$C). In Chapter 4, this equation will be used in an equivalent form.

To perform Raman spectroelectrochemistry, the graphene sample is placed inside a cell containing an electrolyte (see Figure 2.11). Graphene acts as the working electrode, which is connected to a potentiostat[8] in a 2-electrode configuration, using a Ag/AgCl reference electrode. Raman spectroelectrochemistry measurements are realized by applying a gate voltage between graphene and the reference electrode while simultaneously acquiring a Raman spectra. In this thesis, we have used phosphate-buffered saline (PBS[9]) solutions as electrolyte. The pH was adjusted by the addition of small amounts of HCl 1M or NaOH 1M.

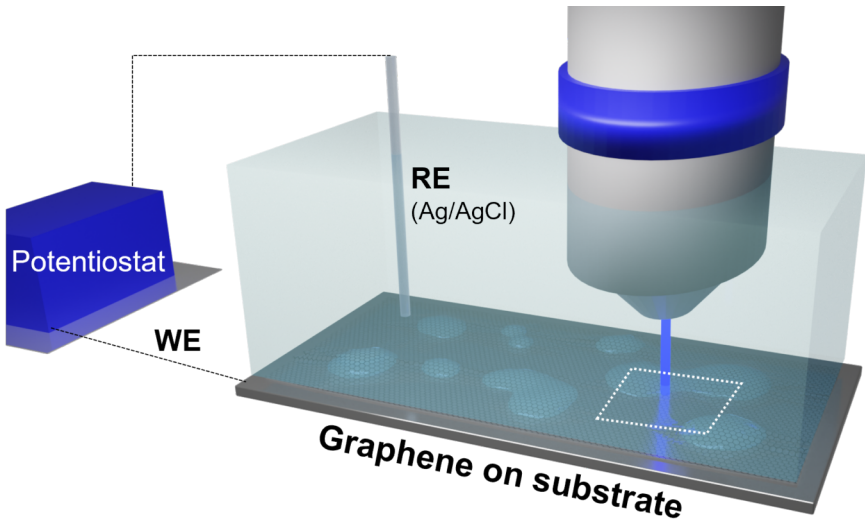


Figure 2.11: Raman spectroelectrochemistry setup - Schematic representation of the Raman spectroelectrochemistry setup: the Raman objective is immersed in the electrochemical cell containing the working electrode (WE, graphene) and the reference electrode (RE, Ag/AgCl) immersed in an electrolyte. The application of different voltages is enabled by the connection to a potentiostat.

For comparative studies using Raman spectroelectrochemistry on graphene electrodes before and after fabrication, we designed macroelectrodes as follows (Figure 2.12). Titanium and gold (Ti/Au) were deposited by electron-beam according to Section F.1.1. 5×5 mm graphene pieces were transferred to the desired substrates. For pyrex/graphene electrodes, Ti/Au (15/150 nm) contacts were evaporated leaving a 2 mm diameter circle in the centre, which was subsequently covered with the 5×5 mm graphene sheet. For the ITO/graphene electrodes, Ti/Au contacts were evaporated leaving a 10 mm diameter circle in the centre, where the graphene sheet was placed without being in direct contact with

[8] Bio-Logic SP-200
[9] Merck Life Science S.L.U.

the Ti/Au. For Au/graphene electrodes, Ti/Au (15/150 nm) were evaporated on SiO_2/Si and the 5×5 mm graphene sheet was placed in the center of the substrate. The passivation was made manually in all cases with PDMS, leaving an exposed graphene area of 0.0314 cm^2.

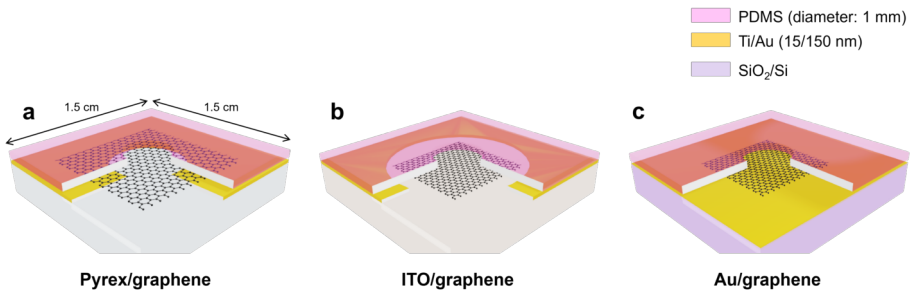


Figure 2.12: Representation of graphene macroelectrodes - (a)(b)(c) Pyrex/graphene electrode, ITO/graphene electrode and Au/graphene electrode, respectively. Ti/Au (10/100 nm) were evaporated previously to graphene transfer, as follows: leaving a 3 mm diameter circle at the center of the pyrex substrates, a 10 mm diameter at the center of the ITO substrates and covering completely the SiO_2/Si substrates.

2.5.2 Atomic Force Microscopy and Kelvin Prove Force Microscopy

Atomic force microscopy (AFM) provides topographic information of surfaces with atomic resolution and offers high versatility as it can be operated in multiple different modes. For a complete study of graphene systems, which is the aim of this dissertation, topographic information is valuable to assess the roughness of the surfaces and its morphology with high resolution. Hence, we used dynamic AFM (also known as tapping mode) to analyse the morphology of the substrates used for graphene growth (Chapter 3). Dynamic AFM was also used to assess the surface of as-transfer and after functionalization graphene devices (Chapter 5). The explanation of the AFM fundamentals is provided in Annex F, as well as information about the equipment used. Figure 2.13 shows an AFM topographic image of graphene on a pyrex substrate.

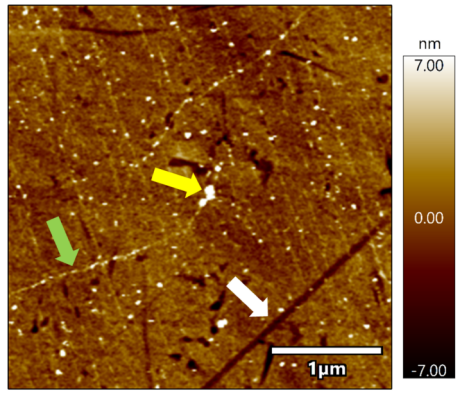


Figure 2.13: AFM of graphene on pyrex - AFM topographic image of a graphene sample transferred to a pyrex substrate. The white arrow indicates a pyrex feature; the green arrow points to a graphene grain boundary; the yellow arrow indicates particles corresponding to residues at the graphene surface, mostly coming from the transfer process.

The surface roughness (standard root mean square roughness, RMS) of the samples is a widely used parameter for surface analysis, thus, we used it in this thesis. It is the average of the height deviations within the measured length and extracted from the mean lines, as indicated by the expression [72]:

$$RMS = \sqrt{\frac{1}{N}\sum_{i=1}^{N} r_i^2} \tag{2.4}$$

where N is the number of points and r_i is the height of each point i minus the average value of the sample height.

Kelvin Prove Force Microscopy (KPFM) is a variation of AFM that enables the analysis of the surface potential distribution of a sample's surface and the measurement of its work function (see Annex F.3 for more details). Additionally, in this thesis we used a particular mode of KPFM that allows operating in liquid environments: Dual Harmonic KPFM (DH-KPFM). A detailed explanation of DH-KPFM is provided in the Annex E.

2.5.3 Scanning Electron Microscopy and Electron backscatter diffraction

Scanning Electron Microscopy (SEM) is a microscopic technique based on the interaction of a focused electron beam on a sample, widely used for morphological and compositional analysis of surfaces. We used SEM mainly for the morphological characterization of copper surfaces and graphene grown either

on Cu foils and on rigid substrates (Chapter 3). Statistics on Cu grain size were obtained performing an analysis with the *ImageJ* software (see details in Annex F.5). Figure 2.14 shows SEM images of different graphene samples on Cu foils: when the graphene layer is not closed, a good contrast facilitates the observation of the grains on the substrate. Analogously, SEM also allows identifying the presence of second nucleation on graphene. On the contrary, when the graphene layer is closed, only a fair contrast enables the observation of graphene grain boundaries.

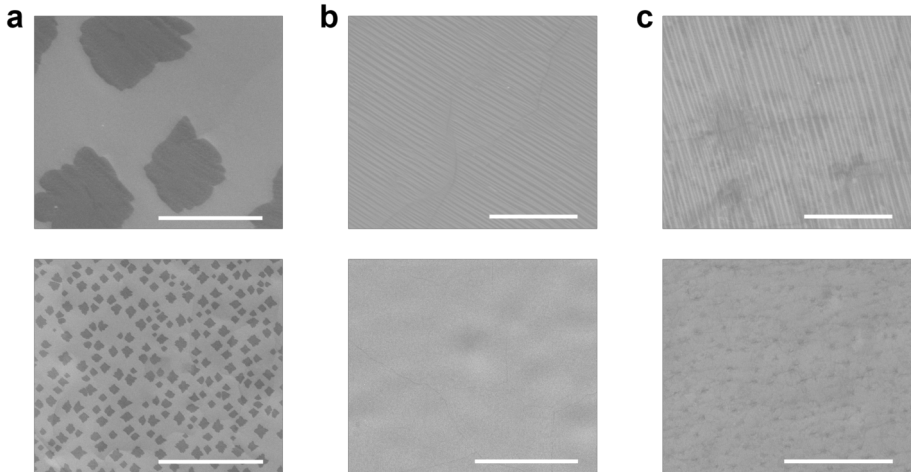


Figure 2.14: SEM images of graphene grown on Cu foils - (a) Open graphene sample. **(b)** Closed graphene monolayer. **(c)** Closed graphene with second nucleation (darker features). Scale bars (top) = 5 μm; (bottom) = 50 μm.

Electron backscatter diffraction (EBSD) is used to obtain crystallographic information of the orientation of the Cu grains on rigid substrates, complementary to X-ray diffraction data (Section 2.5.4). The crystallographic orientation of a solid refers to the spatial arrangement of its atoms, thus we used EBSD to analyse the Cu atoms arrangement when deposited on a solid substrate. Cu has a face-centered crystal structure (fcc), meaning that its unit cell corresponds to a cube with an atom at each vertex and at the center of each face, as shown in Figure 2.15a. If x, y and z axes are considered defining the spatial position of the cube, there are different planes that can be defined with three points, one in each plane. In Figures 2.15b-d, the 001, 101 and 111 planes are illustrated.

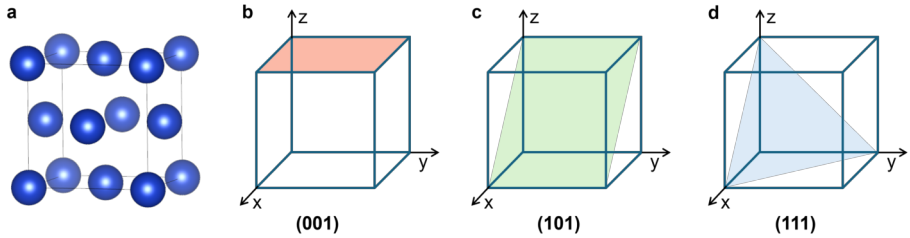


Figure 2.15: Cu crystallographic structure and orientations defined by Miller indices - **(a)** Representation of the face-centered (fcc) Cu unit cell. **(b)(c)(d)** 001, 101 and 111 crystallographic planes of the fcc structure.

Using EBSD, we can obtain information about the Cu crystallographic orientation perpendicular to the surface where it is deposit, that is, the "out-of-plane" orientation, defined by the way the planes (Figure 2.15b-d) are oriented. This information usually is extracted in the form of a colour map, each colour relating to a crystallographic orientation. As an example, Figure 2.16 corresponds to an EBSD measurement of a commercial Cu foil prior to graphene growth, showing its polycrystallinity. As it will be further explained, Cu <111> orientation is the most favourable for high-quality graphene growth, providing an optimal Cu-graphene interface (see Section 3.1.1, Figure 3.4).

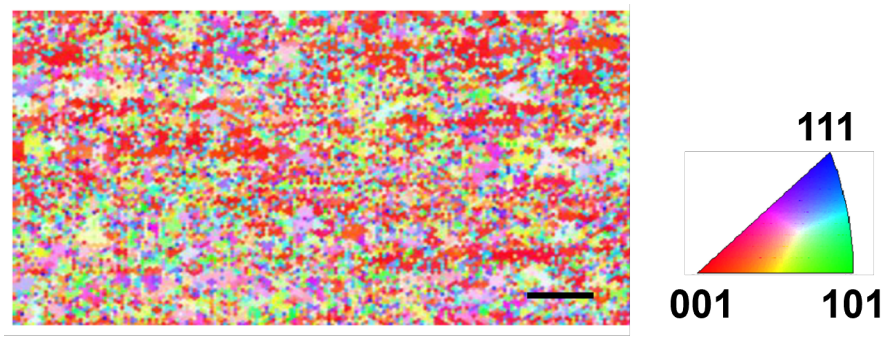


Figure 2.16: EBSD map of a Cu foil - (Left) Polycrystalline Cu foil before graphene growth, with no preferential orientation. Scale bar is 100 μm. (Right) colour legend indicating the orientations correspondence.

2.5.4 X-ray diffraction

X-ray diffraction (XRD) is another technique that allows the analysis of the crystallographic structure of a sample, that can be used complementary to EBSD. The basis for the development of this technique was mainly set by W. H. Bragg

and W. L. Bragg, fundamented on the discovery of X-ray diffraction in crystals by M. von Laue [73]. Nowadays, the versatility and non-destructive character of XRD has made it extensively used in the nanomaterials science field. More information about the fundamentals of the technique, as well as on the equipment used is provided in Annex F.6.

We used XRD to characterize the Cu surfaces (thin films on rigid supports) for graphene growth. More specifically, XRD allowed us identify the evolution of the crystallographic orientation of the Cu grains with the annealing temperature and time (this study is presented in Chapter 3). First, the out-of plane orientation of a sample is analysed in terms of its out-of-plane orientation by performing the so-called 2θ-ω scans, which consist on irradiating the sample with X-rays varying the incident and reflected beams (ω and 2θ, respectively). As stated, more details of the setup are specified in Annex F.6. Figure 2.17 depicts a 2θ-ω scan of Cu evaporated on a sapphire substrate with the peaks labelled with the corresponding orientations.

To obtain information about the distribution in the plane parallel to the substrate (in-plane) of the out-of-plane Cu<111> orientation, we performed another what is called a pole figure scan (PF). This consists on fixing the 2θ angle for the corresponding 200 planes (see Figure 2.18) and rotate the plane of the sample to be able to observe its reflections, which will be exclusively coming from the family with Cu<111> out-of-plane orientation. In general, when performing a PF scan, the planes fixed are chosen depending on the sample. A typical representation of a PF measurement is shown in Figure 2.18b, where the external numbers of the circle indicate the Φ angles and the concentric circles correspond to the χ angles. In our study, as we fixed the Cu 200, the resulting PF is expected to have the following features for an out-of-plane Cu<111> preferentially-oriented sample: (i) 12 possible poles at $\chi = 54.7°$, corresponding to the 4 groups of 3 poles rotated in Φ by 30°, as indicated by the blue arrows in Figure 2.18a, (ii) a secondary pole at the central part of the circle corresponding to a <100> out-of-plane orientation, (iii) the intensity measured between the poles forming a ring may be possibly due to other contributions coming from the substrate or scattering of the different families of in-plane distributions. In general, a highly oriented Cu<111> surface with only one family of distributions in-plane would show three intense poles at the $\chi = 54.7°$ ring, one at each vertex of the triangle formed by the in-plane orientation.

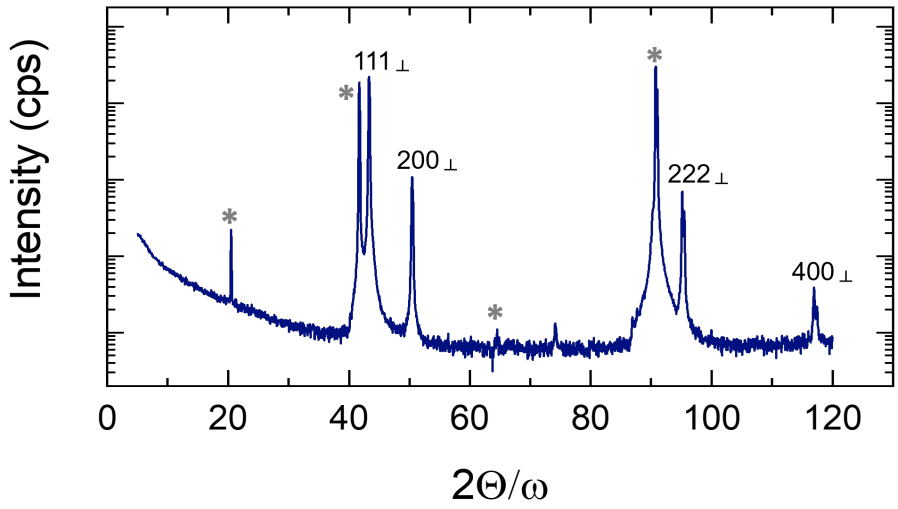


Figure 2.17: XRD measurement of evaporated Cu on sapphire - 2θ-ω scan, where each peak indicates an out-of-plane orientation. The peaks labelled with an $*$ symbol indicate a contribution from the sapphire substrate.

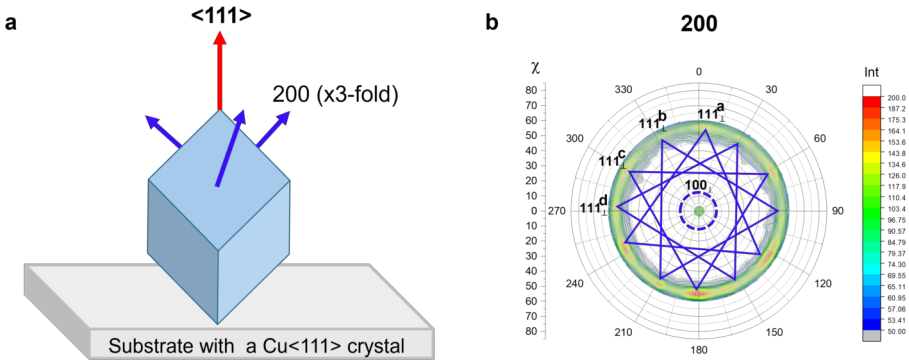


Figure 2.18: Description of the common features for a Pole Figure scan of a Cu<111> oriented surface. - **(a)** Representation of a Cu crystal domain oriented <111> out-of plane (red arrow) and its corresponding 200 directions corresponding to its distribution in-plane. **(b)** Representative PF scan for the 200 in-plane orientation of the Cu<111> out-of-plane. The main features of the figure are the vertexes of the blue triangles represented, which indicate the locations of the poles that would appear from the 200 distribution of the <111> out-of-plane orientation.

2.5.5 Electrical characterization of graphene Solution-Gated Field Effect Transistors

A Field Effect Transistor (FET) is an electronic device capable of modulating the current flow through a semiconductor channel. It consists of three elements, named terminals: the source (S), the drain (D) and the gate (G). The source and the drain are connected by the semiconductor channel and the gate is where the voltage (bias) is applied to. When a voltage is applied to the gate (V_g), the conductivity of the channel is altered. The so-called graphene Solution-Gated Field Effect Transistors (g-SGFETs) use graphene as the channel material, which is directly exposed to a liquid solution and is capable to transduce physical property of interest of the electrolyte into an electrical signal. Figure 2.19a depicts the schematic structure of a g-SGFET using Ag/AgCl as a reference electrode, which applies the gate voltage in this case. As represented, graphene in g-SGFETs is in direct contact with an electrolyte containing different ions and molecules, including analytes of interest in case of the device being used as a biosensor, while the drain and source terminals are typically not in contact with the electrolyte. In the case of their use as neural sensors, neural activity, governed by action potentials, modifies local electric fields and thus can be monitored by measuring changes in graphene's drain-source intensity response to the gate-source voltage, defined as the I_{ds}-V_{gs} (or I-V) transfer curves (Figure 2.19b) [74, 29]. Thanks to that, g-SGFETs are powerful devices for brain activity recording [30, 32] and for sensing of biomolecules [75, 76, 77, 78, 79].

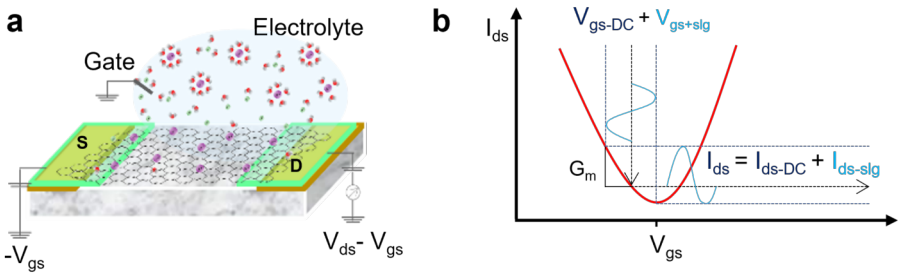


Figure 2.19: g-SGFET - **(a)** Schematic representation of a g-SGFET with the graphene channel, the passivated metal contacts - source and drain - the electrolyte and the gate electrode (Ag/AgCl). **(b)** Typical transfer I-V curve of a g-SGFET, obtained varying the V_{gs} with a fixed V_{ds}. The resulting V-shaped curve is consequence of the ambipolar electronic nature of graphene. Adapted from [80].

The analysis of g-SGFETs I_{ds}-V_{gs} transfer curves can provide useful information. There exist a direct relation between the drain-source current I_{ds} and the mobility of graphene (μ), given by:

$$I_{ds} \propto \mu \cdot C_{int} \tag{2.5}$$

where C_{int} is the interfacial capacitance. Taking this into account, when a gate voltage is applied, the graphene Fermi level E_F is shifted, which results in the modulation of free carriers in graphene. This modulation is reflected in the I_{ds}-V_{gs} transfer curve, with a minimum corresponding to the minimum number of free carriers in graphene, hence the minimum of conductivity, reached at the point where the valence and conduction bands meet: the Dirac point. The gate voltage at which this minimum of conductivity is reached is known as the charge neutrality point, CNP. In a transistor configuration, the current in the graphene channel at $V_{gs}<V_{CNP}$ is dominated by holes, while the current at $V_{gs}>V_{CNP}$ is dominated by electrons, as represented in Figure 2.20. When using a Ag/AgCl reference electrode, a graphene CNP of ~0.15V is expected due to the difference between the Ag/AgCl electrochemical potential level (E_{VAC} = 4.7 eV) and the work function of pristine graphene, 4.6 eV [81, 82, 83].

It is important to note that, when measuring in electrode configuration, the voltage applied with respect to the reference electrode, V vs Ag/AgCl, is the contrary of what is understood of V_{gs}. Hence, the current in the graphene active area at V vs Ag/AgCl < V_{CNP} is dominated by electrons, while the current at V vs Ag/AgCl > V_{CNP} is dominated by electrons. In this thesis V vs Ag/AgCl or V_{gs} are used depending on the measurement configuration, and results are interpreted accordingly.

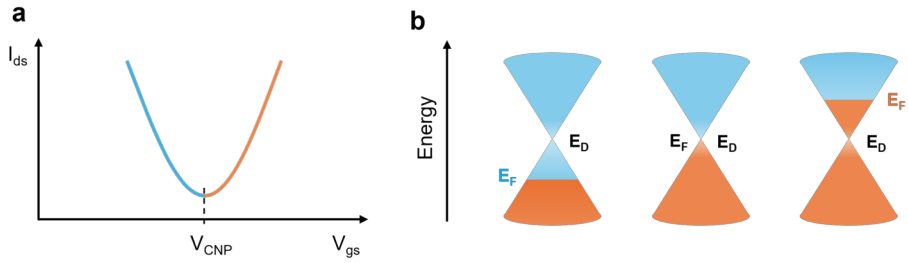


Figure 2.20: Graphene field-effect transistor transfer curve (I_{ds}-V_{gs}) - (a) Graphene I_{ds}-V_{gs} curve. The electronic transport is governed by holes or electrons when the voltage applied is above or below the CNP. **(b)** Graphene valence and conduction bands and its variation with the application of different voltage, which changes the Fermi energy (E_F).

Another important parameter that can be extracted from the transfer curves is the transconductance, g_m:

$$g_m = \left.\frac{\partial I_{ds}}{\partial V_{gs}}\right|_{V_{ds}} \tag{2.6}$$

as described by the equation above, g_m monitors the ratio of small variations of I_{ds} resulting from local changes in V_{gs} at a fixed V_{ds}. Given that the transconductance provides information about the device sensitivity to V_{gs}, the higher it is, the higher the device's ability to detect smaller signals and thus the device has more sensitivity [84, 75].

Random current fluctuations are intrinsic to any semiconductor (internal noise) [85]. In general terms, it is agreed that the sources of noise in graphene SGFETs may include charge traps at the substrate interface, as well as what is called charge noise [86]. Dividing the intrinsic device current noise (I_{rms}) of the g-SGFET by the g_m, we obtain the effective gate noise (V_{gs}^{rms}), a figure of merit that can be used to assess the signal-to-noise ratio (SNR).

In this PhD thesis, g-SGFETs are characterized in Chapter 4 and 5 (see Sections 4.5, 5.6 and C.3). Our focus was the assessment of the graphene doping (in relation with CNP), the device sensitivity (g_m) and the noise level (V_{gs}^{rms}).

g-SGFET arrays

Figure 2.21 shows a fabricated 4-inch wafer including 7 chips of 48 g-SGFETs (channel length is 50 μm). In this thesis, these devices are used for electrical characterization, using SiO_2/Si and pyrex substrates. The experimental details of the measurements are explained in Annex F.7.

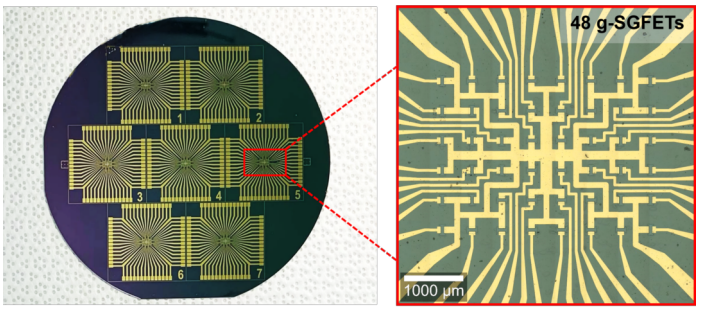


Figure 2.21: Graphene SGFET wafer-scale devices - Photograph of a 4-inch SiO_2/Si wafer with fabricated g-SGFETs and zoom in the central part of one chip showing the 48 g-SGFETs.

3

Substrate engineering for graphene growth

3.1 General overview of graphene synthesis techniques

In real applications, graphene properties are governed by the used synthesis method. Hence, the selection of one or another depends on graphene's given final application. Graphene synthesis techniques can be classified in top-down or bottom-up approaches. Initially, in graphene's first experimental isolation by Novoselov *et al.* [5], it was obtained by mechanical exfoliation from its bulk material, graphite – a top-down approach -. Nowadays, mechanical exfoliation still provides the highest quality of graphene samples. Therefore, this method enabled the study of the outstanding properties of graphene – mechanical, optical, and electronical -, which was pivotal to raise the interest of the community in a great number of application fields [54, 87]. However, the difficulty to obtain large area, reproducible and scalable monolayer graphene by mechanical exfoliation raised the need of finding alternative synthesis approaches. Up to now, substantial progress has been achieved and the use of techniques ensuring large areas of high quality graphene for electronic applications is broadly adopted.



Figure 3.1:
Timeline of graphene growth techniques since its first isolation in 2004. Adapted from [88].

Bottom-up synthesis methods are promising for obtaining large scale monolayer graphene samples, which is highly challenging in the case of top-down preparation techniques. Among all of them, epitaxial growth on silicon carbide (SiC) and chemical vapor deposition (CVD) are possibly the most relevant.

Investigations on epitaxial graphene on SiC have been based on the early studies by van Bommel *et al* [89] demonstrating the formation of graphitic layers upon heating 6H-SiC(0001) and (0001-) surfaces. From 2006 on, many publications have revealed the mechanisms and characteristics of graphene on SiC [90, 91, 92, 93]. Remarkably, they strongly depend on the face -Si or C- where the graphene is grown [90]. For instance, the first carbon layer grown on the top of the Si face is bonded to the Si atoms, therefore it is called the buffer C layer and graphene grows on it [94, 95]. Differently, a buffer C layer is not formed if the C face is used, yet graphene grows in a way which hinders the control of the number of layers formed [90, 96]. Although being promising [97], nowadays epitaxial graphene growth on SiC does not fulfill one important requirement needed to develop graphene technology for biomedical applications, which is it being cost-effective [98]. Furthermore, using epitaxial growth on SiC would unavoidably necessitate a transfer process for the incorporation of the material to the group's current technology. This represents an additional inconvenient due to the lack of reported knowledge on that matter.

Chemical Vapor Deposition (CVD) is currently the predominant technique for large scale graphene growth for applications in electronics. It has emerged as the most promising approach to provide cost-effective, large area, high quality monolayer graphene [99]. The use of a metallic catalytic substrate for CVD graphene synthesis is currently widespread, while direct growth on dielectric substrates, despite raising interest, remains challenging [98]. The first works on CVD for graphene synthesis were reported on 2006-2009 and employed nickel (Ni), iridium (Ir) and copper (Cu) substrates [100, 101, 102]. These were followed by numerous publications that explored CVD graphene growth on different catalysts

such as platinum (Pt), germanium (Ge) and palladium (Pa) [103, 104, 105] and on metal alloys (for instance, Cu-Ni or Cu-Pt [106, 107]). Thanks to the low carbon solubility on Cu, the use of this metal as the catalytic substrate enables higher controllable monolayer growth [108] (see Section 3.1.1 for a detailed explanation on the graphene CVD growth mechanism). Moreover, Cu supports enable a non-difficult, cost-effective, scalable integration into device manufacturing processes. For all of that, nowadays CVD graphene is prevalently grown on Cu foils.

3.1.1 Chemical Vapor Deposition for graphene growth

In general terms, CVD consists on the deposition of a thin solid film on a substrate by enabling a chemical reaction that decomposes a specific precursor in its vapor phase. For the case of graphene synthesis, diverse variants of CVD have been reported depending on the processing parameters, as summarized in Figure 3.2.

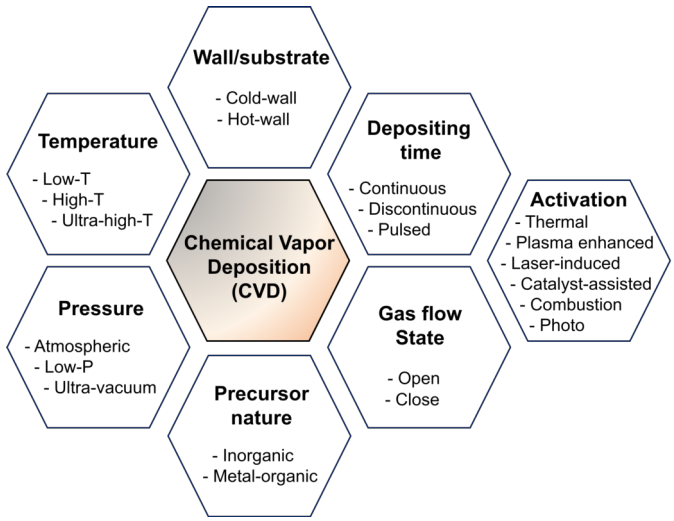


Figure 3.2: Classification of CVD methods - Different types of CVD processes depending on growth parameters. Source: [109]

The following items and parameters are important to be mentioned:

- **Substrate:** the substrate material influences the formation of graphene, for instance depending on carbon solubility, thus allowing the control of the carbon supply and therefore the crystal structure of graphene. Copper has a low carbon solubility [110], which favours the bidimensional growth and enables control over monolayer graphene growth. Differently, nickel presents higher carbon solubility, favouring multilayer graphene formation [111].

- **Carbon precursor:** even though the most used C precursor for graphene growth is in a vapor form, methane (CH_4), there have been other reported precursors suitable for CVD in a liquid form (i. e. hexane) [112] and even solids (i. e. polymethyl methacrylate, PMMA) [113]. CH_4 or other vapour precursors are preferred, instead of the liquid or solid ones, for stability reasons.

- **Pressure:** graphene synthesis has been demonstrated in high vacuum, atmospheric and low pressure [114, 115, 116, 117]. This parameter influences Cu sublimation at the growth stage, and, in consequence, its surface morphology. Growth pressure also influences graphene homogeneity by favouring or not a smooth monolayer formation and the shape of the graphene crystals. More than controlling the total pressure of the growth process, it is key to regulate the partial pressure of the C precursor and other growth gases, namely H_2, to tune graphene's grain sizes [118].

- **Temperature:** graphene nucleation density and growth dynamics are also influenced by temperature, and the optimal one for the obtention of a high-quality graphene varies depending on the catalytic substrate and the above-mentioned parameters, as it has been reported [66]. For Cu substrates, growth temperatures of 600°C-800°C are considered low [57], while typical growth temperatures range between 900 and ∼1000°C [119].

We used low pressure CVD (LPCVD) on copper for the studies performed in this dissertation. Figure 3.3 represents the mechanism of graphene thin film formation on a Cu substrate: carbon is supplied by the precursor, methane (CH_4), which is decomposed as a result of a dehydrogenation process in the reaction chamber (quartz tube) under optimal temperature and pressure conditions. CH_4 is introduced together with hydrogen (H_2) and argon (Ar) as a carrier gas. Inside the chamber, most of the carbon is adsorbed on the Cu surface with minimal penetration into the bulk, thanks to the low C solubility of Cu. The role of H_2 is to catalyse the CH_4 dehydrogenation at the Cu surface. This process results in the formation of active C species whose concentration is expressed as C_{Cu} in Figure 3.3); like C^*, CH^*, CH_2^* and CH_3^*, being CH^* the most favorable one and therefore breaking its C-H bond results in the rate-limiting step. C adsorption on the Cu surface competes with a previous dissociative chemisorption of H_2.

In this PhD thesis, we employ both Cu foils and Cu thin films: on one hand, Cu foils are used for the preparation of the standard CVD graphene following the established protocol of the AEMD group (Section 2.2). On the other hand, we work on the preparation of Cu thin films on rigid supports as a part of the experimental studies, which are explained in Section 2.3. At the Cu surface, the C

species migrate towards graphene nucleation and subsequent growth is started. As depicted in Figure 3.3, sp^2 C-C dimer formation is recurrent during the process, owing to their stability on Cu, higher in comparison with the monomer. After nucleation, graphene grains start to grow as a result of carbon incorporation at the edges of the nuclei. At a certain point, a bidimensional graphene layer is formed on the Cu surface and entirely covers it.

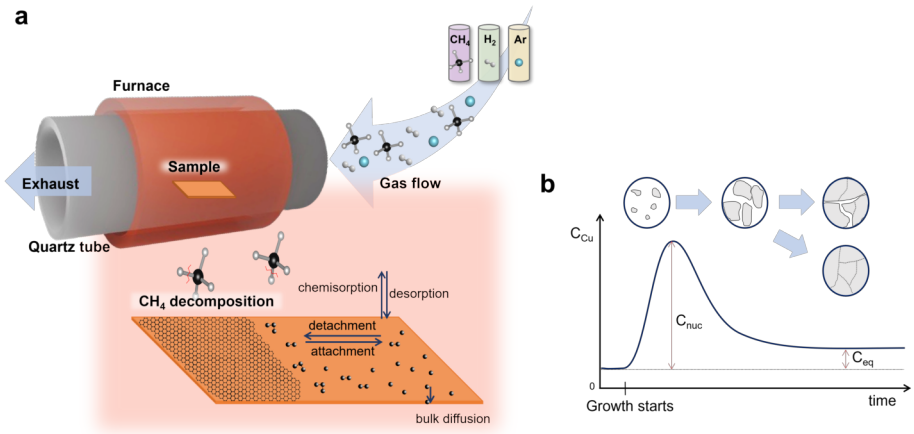


Figure 3.3: CVD graphene growth mechanism - **(a)** Schematic illustration of the growth of graphene in a CVD reactor. The precursor and process gases (CH_4, H_2 and Ar are introduced inside the quartz tube, where the growth substrate (Cu foil) is, in controlled pressure and temperature conditions. During the growth time, different processes take place at the Cu foil: chemisorption-desorption, attachment-detachment and bulk diffusion. **(b)** Graphene grains nucleation and growth evolution with time. First, graphene nucleation sites are formed until reaching a saturation level, C_{nuc}. Then, graphene crystals start growing thanks to the attachment of other C atoms. The growth of the graphene grains can be stopped either by the depletion of absorbed C atoms or due to the C atoms merging together. At the end of the process, an equilibrium between graphene, surface carbon and CH_4/H_2 is reached. The concentration of carbon species on the surface at the equilibrium level is represented by C_{eq}. Adapted from [120].

Graphene quality strongly depends on the substrate used for growth. The widely employed commercial Cu foils present a number of important drawbacks. First, the main use of commercial Cu foils is not intended for semiconductor technology, which makes it extremely challenging to maintain reproducibility and low impurity control from batch to batch [35]. Thus, each new Cu batch requires a re-adjustment of graphene growth parameters. Second, the roughness of commercial Cu foils is too high to ensure low density of defects on the resulting graphene surface. As defects represent potential nucleation clusters, minimizing their presence on Cu enhances the probability of achieving high quality graphene surfaces. Furthermore, it has been demonstrated that the surface roughness of

the as-grown graphene strongly influences the roughness of the graphene after transfer [121, 122, 123, 124]. In this line, when comparing graphene roughness of transferred samples, flatter graphene is achieved when using flatter substrates [125]. Last, reusability of Cu foils is not easy. Instead, the growth of graphene on Cu thin films specifically prepared to that use presents a promising pathway for seamless integration into device fabrication in a high-scalable, cost-effective way. This approach allows complete control on the impurities and morphology of the catalytic substrate, which can be engineered to present significant lower roughness than Cu foils, smooth Cu grain boundaries and a continuous Cu <111> orientation, optimal for graphene growth.

The first reported attempts of graphene synthesis on Cu thin films used evaporated Cu on SiO_2/Si [126, 127, 128, 129, 130]. These early works proved that graphene on Cu films can be grown over a wide temperature range (875°C - 1000°C); further, the growth temperature was found to be related with the Cu film thickness [130]. Nevertheless, Cu films on SiO_2/Si do not present large grains with preferential <111> orientation and, thus, compromise the quality of graphene and its electronic properties [131]. The formation of C-C bonds is stabilized over a <111> oriented Cu surface, as represented in Figure 3.4, due to the hexagonal lattice of Cu <111>, matching graphene's crystallographic geometry [132]. Large copper <111> grains can be obtained after a thermal annealing of the evaporated Cu film. The optimal conditions of this annealing depend on the substrate underneath and the Cu thickness.

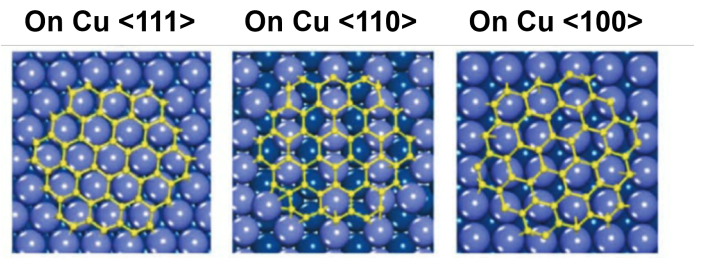


Figure 3.4: Representation of the lattice mismatch between graphene, e.g. C_{54}, (yellow) on different Cu orientations (blue). Graphene on Cu <111> is rotated 0°. Adapted from [133].

Alternatively to SiO_2/Si, various attempts on growing graphene on Cu thin films prepared on sapphire have reported promising results [134, 135, 136]. In this chapter, we discuss the preparation of smooth, <111> oriented copper thin films on sapphire to be used for high-quality, large-scale graphene growth. Moreover, we explore the reusability of the substrate towards a cost-effective technology.

3.2 Sapphire substrate preparation

It is known that the underlying substrate strongly affects the crystal orientation of Cu grains on it. In the following, we study the sapphire surface reconstruction and how it influences the quality of copper thin films. Sapphire is the name given to the α phase of aluminum oxide (α-Al_2O_3) single crystals. Previous research developed in the group demonstrated precise control over the sapphire surface topography and chemical composition by annealing in controlled temperature and atmosphere, in agreement with literature [137, 138, 139, 140]. The sapphire crystal structure is depicted in Figure 3.5a: it consists on an hexagonal crystal with unit cell lattice constants of a = 4.76 Å and c = 12.99 Å. Specifically, c-plane sapphire (c-sapphire [Al_2O_3(0001)]) is used in this thesis. Figure 3.5c illustrates the characteristic stepped surface of sapphire (terraces), which can be obtained after a controlled annealing [141].

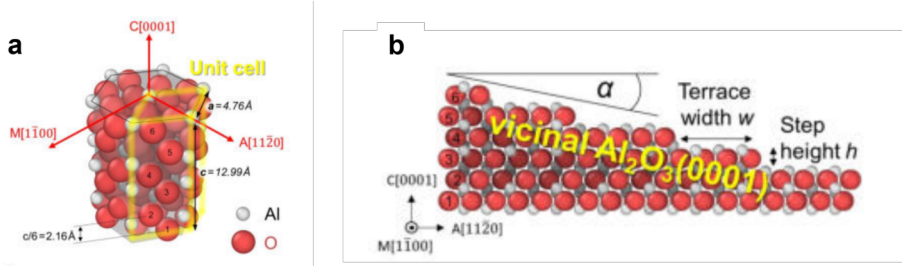


Figure 3.5: Sapphire crystal structure and vicinal structure - (a) Corundum crystal structure of the α-Al_2O_3. The conventional unit cell is highlighted in yellow and the crystallographic axes are marked in red. **(b)** Side-view of the stepped α-Al_2O_3 surface. The step height h is typically a multiple of the Al-O-Al distance c/6. The terraces width is a parameter that depends on the manufactured miscut angle α. From [142].

According to literature, the terraces step height h are in direct relation with the annealing conditions [141, 143]. However, the terrace width w for a specific h depends on what is known as the nominal miscut angle α towards the crystalline plane (c-) [144] and on the surface chemical structure [145]. c-sapphire surface reconstruction was studied after two different annealing treatments: at 1200°C during 2 hours in oxygen atmosphere (see Section 2.3) and the same one followed by an annealing treatment at 1200°C, 2h in H_2/Ar (5% H_2). Figures 3.6a-d show the terrace formation characterized by AFM in all the annealed samples, and the dependence on the miscut angle: wider terraces were formed on sapphire substrates with lower miscut angle, as expected from [145]:

$$tan(\alpha) = \frac{h}{w} \tag{3.1}$$

The chemical structure of the sapphire surface can be either O-rich or Al-rich. Reflection high-energy electron diffraction (RHEED) is a useful technique for crystallographic analysis and here it is used to characterize the sapphire surface. RHEED measurements showed the characteristic diffraction patterns along the [1 $\bar{1}$ 0 0] zone axis (ZA) of Al_2O_3. The as-received sapphire surface presents a RMS of 0.69 nm and a diffraction pattern with a (1×1) surface reconstruction (Figure 3.6a,e, respectively), in agreement with literature [146]. After performing an annealing step to substrates with 0.2 and 0.05 miscut angle at 1200°C during 2 hours in oxygen atmosphere, the RHEED analysis along the [1 $\bar{1}$ 0 0] ZA (Figures 3.6f,g) reveals that the (1×1) structure is maintained, but with a higher degree of crystallinity at the lowest miscut angle, 0.05°, as the Kikuchi lines appear more defined. An annealing treatment at 1200°C, 2h in H_2/Ar (5% H_2) following the first O_2-annealing results, as mentioned, in another terrace-like yet Al-rich surface (Figures 3.6d,h). For this last case, it is important to note that the RHEED characterization performed does not enable a clear visualization of the characteristic $(\sqrt{31} \times \sqrt{31})\pm$R9° reconstruction (the corresponding features are fairy observed in the area marked with a white square). However, the Al-termination is assumed at the c-sapphire after the annealing treatment in H_2/Ar, according to a more detailed RHEED characterization performed previously in the group [142].

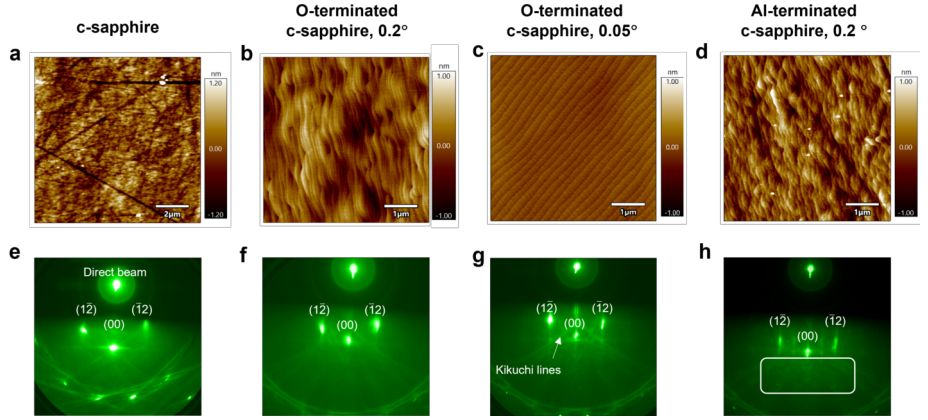


Figure 3.6: Sapphire surface reconstruction - Characterization of untreated c-sapphire, O-terminated c-sapphire with α 0.2° and 0.05°, and Al-terminated c-sapphire with α 0.2° by **(a)(b)(c)(d)** AFM and **(e)(f)(g)(h)** RHEED.

The surface morphology and orientation of Cu films deposited on untreated c-sapphire and treated c-sapphire with miscut angles of 0.2° and 0.05° were analysed after annealing (1000°C, O_2 50 sccm, 60 min[1]), and were compared with Cu deposited on SiO_2/Si. The Cu evaporation rate was determined after the analysis of a series of samples evaporated at 3 different deposition rates (2 Å/s, 4 Å/s and 6-8 Å/s). Samples were analyzed by AFM right after evaporation and after an annealing process (800°C in Ar:H_2 (10:1) at 50 mbar during 6 minutes). The mean square roughness (RMS) obtained by AFM (see Section 2.5.2) can be used to optimize the Cu deposition rate for our specific application. Already after evaporation (Figure 3.7a), we observed that smoother Cu surfaces (lower roughness RMS) were obtained increasing the deposition rate. Moreover, this correlation is maintained after annealing (Figure 3.7b). We tentatively explain this by hypothesizing that the substrate temperature may increase when higher evaporation rates are used, which can increase the mobility of the Cu atoms reaching the surface, resulting in a smoother surface. Reported studies have demonstrated that maintaining the substrate at a controlled temperature is required to achieve smoother Cu surfaces with reduced grain boundaries [147]. Unfortunately, due to equipment restrictions, it was not possible to carry out such study in this thesis.

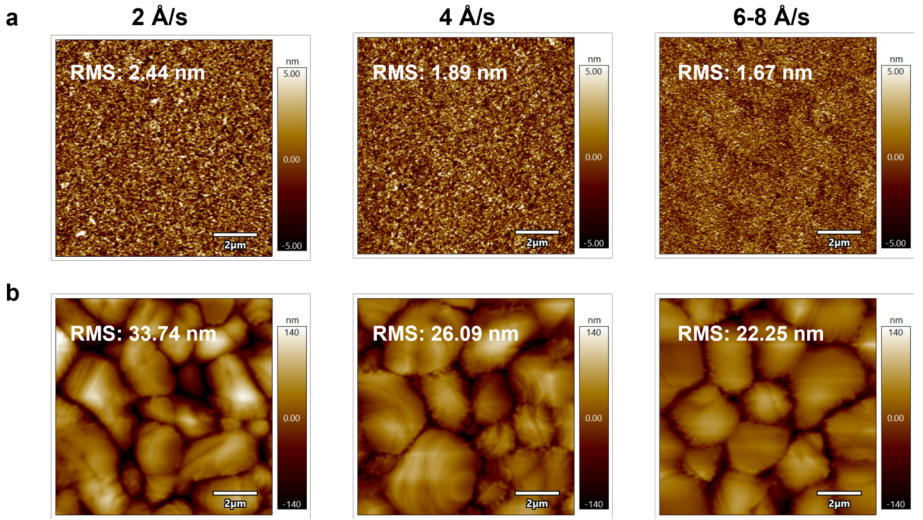


Figure 3.7: Cu deposition evaporation rate study - (a)(b) AFM images and roughness RMS values of Cu on Si_2/Si at different evaporation rates, before and after annealing, respectively. The RMS values in (b) were calculated excluding the Cu grain boundaries. This study was carried out using SiO_2/Si as a support.

[1]Cu annealing conditions are discussed in Section 3.2.1

Figures 3.8a-c, depict the SEM images of the analysed c-sapphire samples after Cu deposition and annealing[2]. A smooth surface with no grooves between large Cu grains could only be achieved using O-terminated c-sapphire with a miscut angle of 0.05°. In the case of the untreated c-sapphire, we obtained significant smaller and less homogeneous Cu grains in comparison with the O-terminated surfaces. The EBSD analysis (Figures 3.8e-g) revealed that the 0.05° miscut angle highly favours the desired Cu <111> orientation. Differently, the Cu on untreated c-sapphire showed a higher degree of polycristallinity with <001> (∼24%), <101> (∼12%) and <111> (∼64%) orientations detected. O-terminated c-plane sapphire with a miscut angle of 0.2° presented a preferential <111> orientation (∼64%) with a smaller percentage of <101> (∼36%). These results confirmed that using sapphire with low miscut angle was of paramount importance in the preparation of the copper thin films.

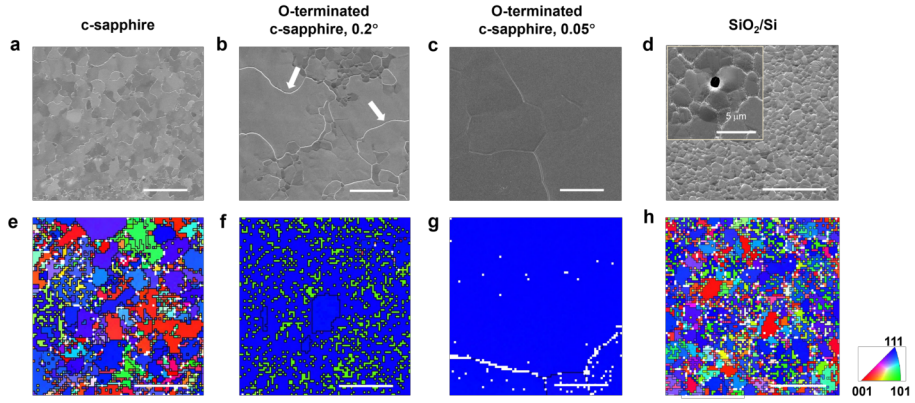


Figure 3.8: Sapphire surface impact on Cu thin film - (a-d) SEM images of Cu evaporated on c-sapphire, O-terminated c-sapphire with a miscut angle of 0.2, O-terminated c-sapphire with a miscut angle of 0.05 and SiO_2/Si, respectively. Scale bar in all images is 50 μm. **(e-h)** EBSD images of the same samples in a-d. Scale bar in all images is 10 μm.

In Figures 3.8d,h we show the analogous SEM and EBSD analysis of Cu deposited and annealed on SiO_2/Si. Cu on SiO_2/Si presented grains of < 5 μm in average without a predominant orientation, with <001> (∼18%), <101> (∼26%) and <111> (∼56%).

Another important aspect to take into account is the dewetting of copper, a phenomenon that is favoured when metals are heated close to its melting point

[2]Cu annealing conditions are discussed in Section 3.2.1

[148], which is our case for Cu. In the areas where Cu has been dewetted from the substrate, graphene can't grow. The inset at the SiO_2/Si/Cu SEM image in Figure 3.8d depicts Cu dewetting observed at the SiO_2/Si/Cu surface. It is important to mention that dewetting was predominantly observed when using SiO_2/Si substrates, rather than when Cu was evaporated on sapphire, in good agreement with literature [135].

In summary, O-terminated c-plane sapphire with miscut angle α of 0.05° allowed the preparation of smooth, <111> oriented Cu surface. These results are consistent with literature, which argues that an enhanced substrate-graphene interaction is achieved in sapphire/Cu substrates [149]. Taking this into account, the following studies were conducted using Cu thin films on O-terminated c-plane sapphire with α 0.05°.

3.2.1 Copper annealing

The main objective of performing an annealing of the substrate/Cu is to prepare the surface for the growth of graphene. To this end, the goal is to obtain a smooth, <111> oriented Cu surface with large grains. Three main parameters have been optimized to achieve that: the content of **H_2**, **temperature** and **time**.

Content of H_2 flow

Hydrogen is a well known reducing agent and there exists evidence in literature of its impact in copper surface modification, mostly on Cu foils [150]. However, there is still not consensus regarding the convenience of using H_2 in the Cu annealing step of the graphene growth [132, 151, 152, 153, 154, 155].

To evaluate the impact of H_2 during the heating and the cooling steps in our reactor, we performed two treatments: the same temperature and time conditions were maintained in both, yet the time of H_2 exposure varied (H_2 7 sccm, Ar 70 sccm, 800°C, P∼50 mbar). AFM roughness analysis revealed smoother Cu grain boundaries in samples annealed maintaining an H_2 flow during the heating and cooling steps (see Figure 3.9).

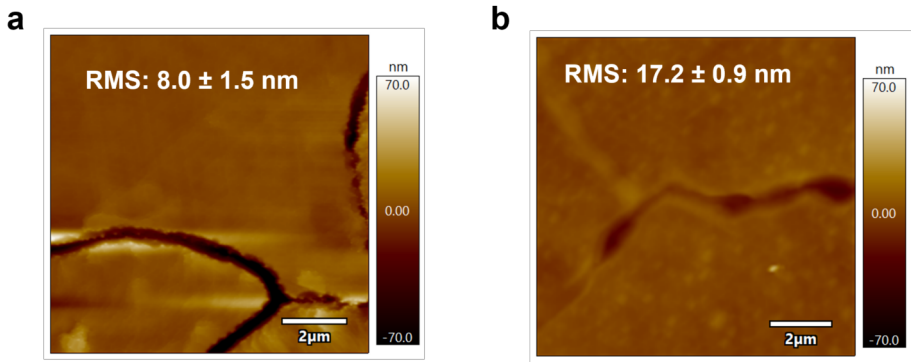


Figure 3.9: Impact of H_2 on the Cu roughness - AFM images of sapphire/Cu surfaces after annealing (800°C, 6 min, P∼50 mbar) in the presence of H_2 **(a)** during the whole process and **(b)** only during 6 minutes while at 800°C. The roughness RMS values were measured excluding the Cu grain boundary regions.

Annealing temperature and time

A series of sapphire/Cu samples were annealed varying temperature and time conditions: from 800°C to 1000°C and from 6 to 60 minutes. Gas flows were always kept at 70:7 sccm (Ar:H_2). Analysis of the annealed samples was conducted by SEM (grain size), AFM (roughness, RMS) and XRD (grain orientation). Figure 3.10 depicts the results for the temperature series, showing that Cu grains became larger as temperature increases, going from ∼12 μm^2 (800°C) to ∼$8{\cdot}10^3$ μm^2 (1000°C). Knowing that Cu melting point is ∼1085°C [156], we did not perform any annealing at > 1000°C, as this would increase the probability of dewetting and thus decrease the quality of the resulting Cu surface. Regarding surface roughness, the RMS parameter calculated from AFM images (excluding the grain boundaries) increases with temperature (Figure 3.10b shows an image corresponding to the sample annealed at 1000°C) until decreasing again for the sample at 1000°C, which is the one with larger grains (see Figure 3.10c). Although temperature has an effect of smoothing the Cu boundaries, it does not prevent them; Cu boundaries may have a detrimental impact on graphene growth. As previously, mentioned, to eliminate grain boundaries on evaporated Cu on sapphire, literature indicates that the substrate must be maintained at a certain, controlled temperature during evaporation [147]. Unfortunately, this was impossible to be performed in the framework of this thesis, due to equipment limitations. Given that, the chosen annealing temperature for Cu on sapphire was 1000°C.

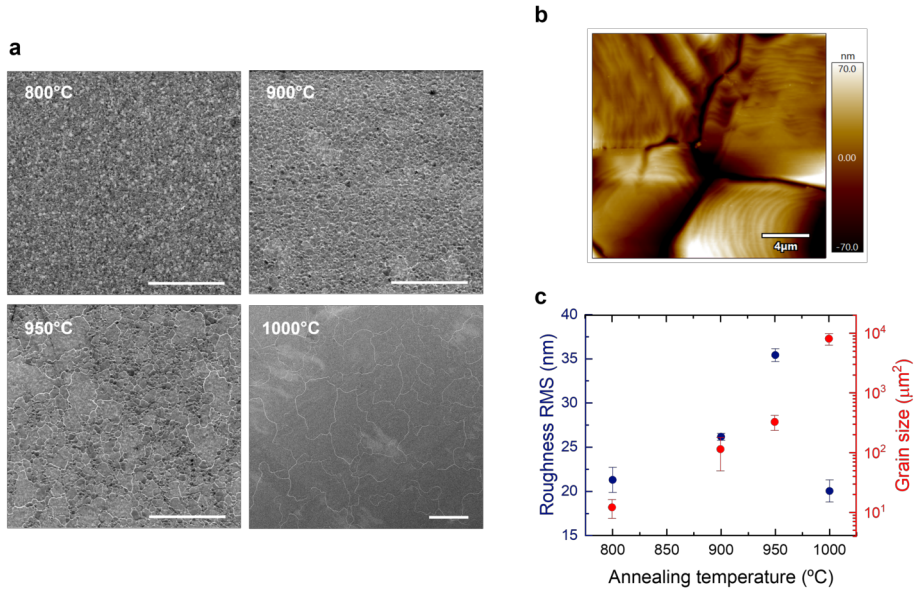


Figure 3.10: Effect of annealing temperature on Cu surfaces - (a) SEM images corresponding to each sample of the temperature series, with an annealing time of 60 minutes. Scale bar in all images is 100 μm. **(b)** AFM image of the sample annealed at 1000°C. **(c)** Obtained roughness RMS and grain size for each sample. The grain size was measured using the ImageJ software, as explained in the Annex F.5. Results are averaged from 5 different images.

Figure 3.11 shows the results corresponding to the annealing time series, revealing that Cu grains became larger with increasing annealing time, going from $\sim$20 μm^2 (6 minutes) to $\sim 8{\cdot}10^3$ μm^2 (60 minutes). Results obtained at annealing times $>$ 60 min were unfavourable, as commented below. Large grain sizes reduces the number of grain boundaries per sample, which is an important fact for subsequent graphene growth. This is expected to lower the possibility of obtaining defective graphene [157, 158]. Surface roughness excluding the grain boundaries decreased with increasing annealing time, as smoother Cu surfaces were obtained. Thus, the sapphire/Cu annealing process was optimized at 1000°C, 60 min in Ar:H_2 (70:7 sccm) at 40-50 mbar.

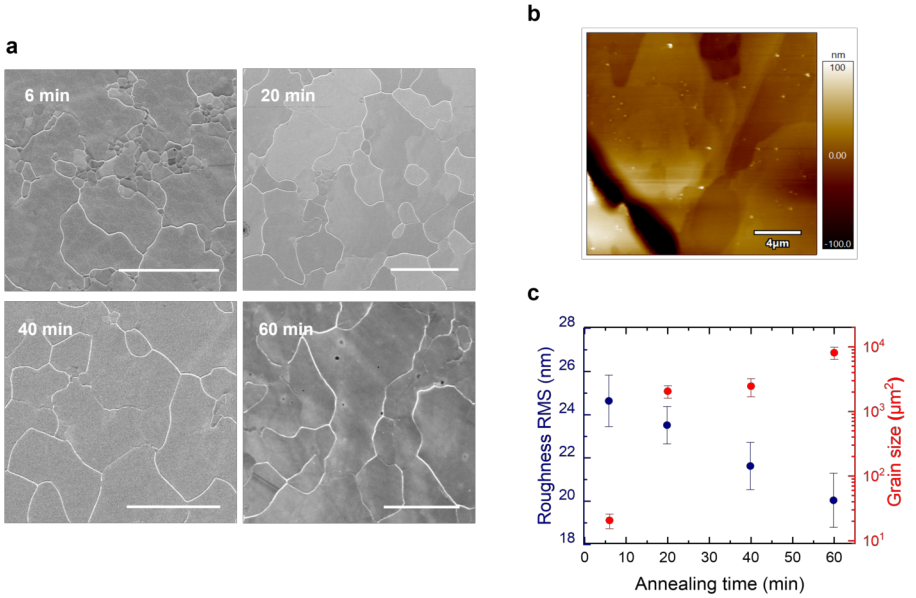


Figure 3.11: Effect of annealing time on Cu surfaces - **(a)** SEM images corresponding to each sample of the time series, with an annealing temperature of 1000°C. Scale bar in all images: 100 μm. **(b)** AFM image of the sample annealed during 60 minutes at 1000°C. **(c)** Obtained roughness RMS and grain size for each sample. Results are averaged from 5 different images.

The Cu orientation of the sapphire/Cu samples was evaluated using XRD. In Figures 3.12a,b, we present $2\Theta - \omega$ scan measurements for the samples of the annealing temperature and time series, which provide information about the out-of-plane crystallographic orientation (see Section 2.5.4). As observed in the $2\Theta - \omega$ scans, the stronger peaks corresponding to Cu<111> and Cu<200> were registered in all sapphire/Cu surfaces, together with the secondary Cu<222> and Cu<400> peaks. To quantify the proportion of Cu<111> orientation in each sample, and visualize possible correlations with the annealing temperature, in Figures 3.12c,d, we show the extracted <111> maximum intensity value divided by the maximum of <200> ($I_{<111>}/I_{<200>}$). The sample annealed at 1000°C exhibits the highest preference for Cu<111> orientation, being its $I_{<111>}/I_{<200>}$ one order of magnitude higher than the lowest $I_{<111>}/I_{<200>}$ measured, corresponding to the sample annealed at 900°C. Interestingly, the $I_{<111>}/I_{<200>}$ for the sample annealed at 800°C is significantly higher, closer to the one at 1000°C than to the ones at 900°C and 950°C. Looking at the time series results, we observe that the sample showing the highest preference for Cu<111> is the one annealed for shortest time, 6 min. Increasing the annealing time beyond 60 minutes was tested with the aim to keep increasing Cu<111> over Cu<200>. The $I_{<111>}/I_{<200>}$ for

annealing time of 120 minutes increases with respect to the 60 minutes sample. However, this also resulted in dewetting of the Cu film (see Figure 3.13b), which is strongly undesired for graphene growth.

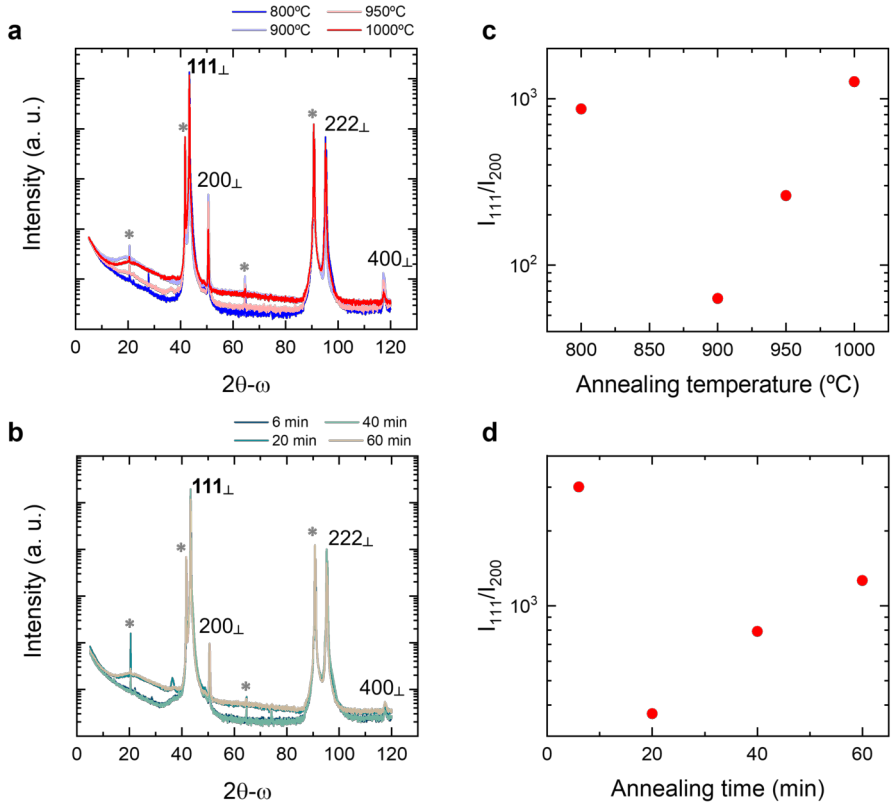


Figure 3.12: Effect of temperature and time of annealing on the orientation of the deposited Cu - (a)(b) $2\Theta - \omega$ spectra of sapphire/Cu samples prepared for the annealing temperature and time series, respectively. Samples corresponding to the temperature series were annealed during 60 minutes and the ones of the time series were annealed at 1000°C. The peaks in a and b marked with * correspond to the sapphire substrate. **(c)(d)** I_{111}/I_{200} corresponding to spectra in (a) and (b), respectively.

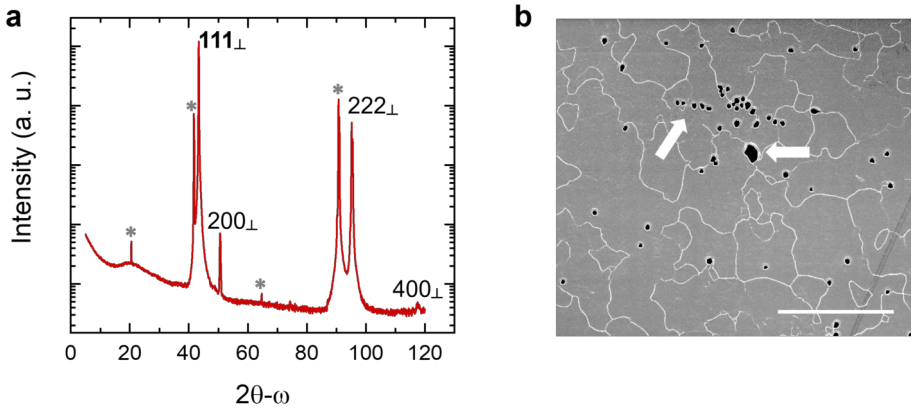


Figure 3.13: Annealing of sapphire/Cu at 1000°C for 120 minutes - (a) $2\Theta - \omega$ spectra shows preferential Cu<111> orientation. The peaks marked with an * are of the sapphire substrate. **(b)** SEM image with white arrows indicating Cu dewetting. Scale bar is 200 μm.

To complete the Cu crystallographic orientation analysis of the annealing temperature and time series, we performed X-ray PF scans. The use of this technique, which is explained more in detail in Section 2.5.4, enables the characterization of the crystallographic in-plane distributions of the out-of-plane preferential Cu <111> orientation. Therefore, by combining information from $2\Theta - \omega$ scans and PF scans, it is possible to determine the epitaxial character of the analysed surfaces [159], thus, providing information about the crystallographic lattice structure alignment between Cu and c-sapphire [160]. If the Cu thin film grows epitaxially on the c-sapphire substrate, the possibility of obtaining a smooth, defect-free surface increases. Hence, for graphene growth on Cu surfaces, not only a highly-oriented Cu<111> is preferred, but also a preferential family of in-plane distributions, since this would imply reduction of Cu grain boundaries and, thus, a smoother, more stable surface [159, 161, 134, 149]. Reported studies about deposition of Cu films on c-sapphire (α-Al_2O_3 [0001]) indicate that epitaxiality is highly dependant on the Cu evaporation and annealing conditions [162]. The PF scans of the Cu samples of the annealing temperature and time series are shown in Figure 3.14. The typical 3 intensity peaks forming an inverse triangle that appear when a sample is preferentially <111> oriented were observed only at the sample annealed at 1000°C during 60 minutes. This signifies that both high temperature and sufficiently long time are needed to achieve a preferred in-plane Cu <111> orientation. In terms of epitaxiality of the Cu on the c-sapphire, it is only achieved at the sample annealed at 1000°C for 60 minutes, as it shows a

highly-preferred Cu<111> out-of-plane orientation with one preferential in-plane distribution.

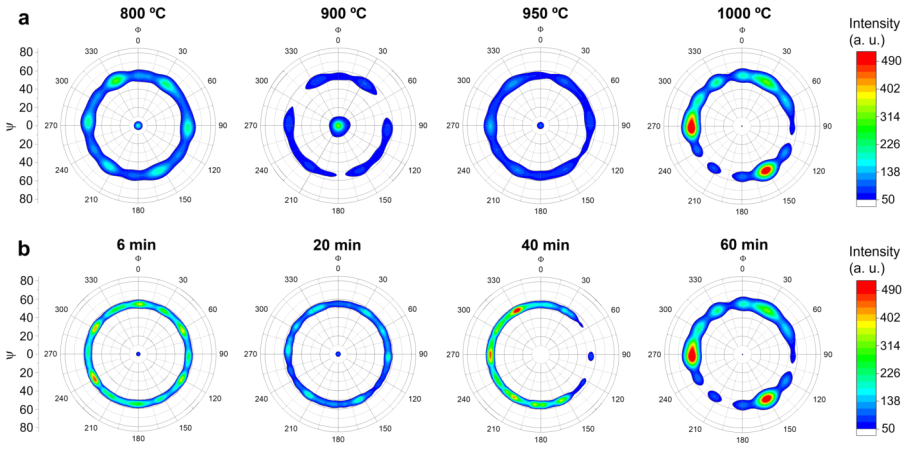


Figure 3.14: Pole figures of annealed sapphire/Cu - (a)(b) Pole figures of the temperature and time series of the sapphire/Cu.

To sum up, we optimized the preparation of a Cu <111> surface on c-plane sapphire. We confirmed that the use of c-plane sapphire with a miscut angle of $\leq 0.5°$ is key to achieve the desired Cu orientation. Detailed surface analysis of sapphire/Cu using different techniques such as SEM, AFM, EBSD and XRD revealed that it is possible to achieve a reproducible, well-oriented surface by performing e-beam evaporation of Cu at high rate (6-8 Å/s), followed by an annealing step in vacuum at 1000°C during 60 minutes.

3.3 Graphene growth

Based on the knowledge previously gained in the group regarding CVD graphene grown on Cu foils, we were able to adapt the conditions to grow graphene on our sapphire/copper substrates. For the growth step, we used 0.5 sccm CH_4 flow in Ar:H_2 (98:2 sccm) at 1000°C and 60-70 mbar. SEM analysis confirmes that a graphene monolayer was closed in 1.5 minutes using these conditions (see Figure 3.15a). Raman spectroscopy analysis (Figures 3.15b-d) shows that the I_{2D}/I_G ratio is 2.6 ± 0.4, in good agreement with the reported values corresponding to closed graphene monolayer [62]. Furthermore, the lack of I_D indicates a very low density of defects at the graphene surface. Raman analysis also suggests that Cu grain boundaries act as nucleation sites for graphene growth, revealing a more intense G band in the grain boundary regions than outside them (see Figure 3.15d).

To specifically determine the graphene grain size of our samples, we carried out different growth attempts to obtain an open graphene sample. However, the short time needed for the graphene layer to close made it impossible at this point. In that direction, further work would include the growth of a monolayer graphene and subsequent oxidation of Cu through the graphene grain boundaries by heating the sample or oxidizing it in a controlled atmosphere [163, 164]. We tentatively consider that the graphene grains obtained by our process are ≥ 50 μm, as SEM analysis suggests that graphene grain boundaries mainly follow the copper grain boundaries, which act as nucleation sites for graphene growth. In some areas of the samples, the visualization of graphene grain boundaries is possible, and the calculated grain size was ≥ 50 μm in all cases. As said before, further experiments and analysis may contribute to a more detailed quantification. To further increase the graphene grain size beyond ~ 50 μm, changing growth parameters could help. However, having confirmed that Cu boundaries act as preferential nucleation sites for graphene, we suggest that any attempt to increase graphene grain size should be intended after reducing the presence of Cu grain boundaries. This, as mentioned before, would be possible if Cu is deposited on sapphire while this is maintained at a certain temperature [147].

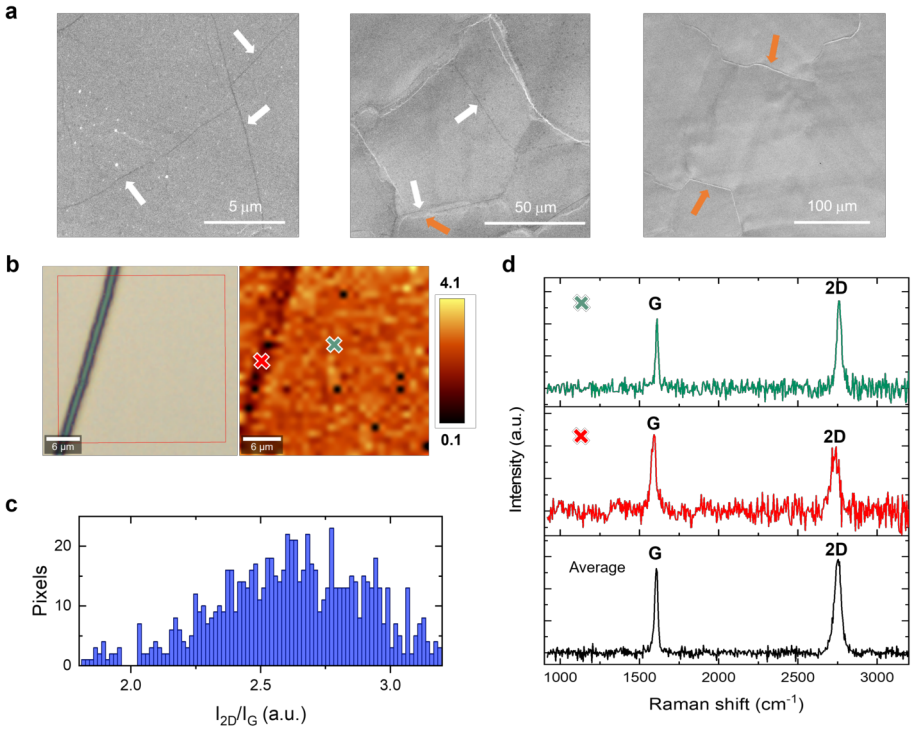


Figure 3.15: Characterization of graphene grown on sapphire/Cu - (a) SEM images of different regions of a graphene sample grown on sapphire/Cu. White arrows indicate graphene grain boundaries, while orange arrows indicate Cu grain boundaries. **(b)** Optical image of the graphene area where the Raman map was performed (left) and corresponding I_{2D}/I_G Raman map (right). **(c)** Histogram of the I_{2D}/I_G from the Raman map at (b). **(d)** Average Raman spectrum (black) of the Raman map, representative spectrum of the graphene at the Cu boundary (red) and graphene at the flat Cu grain region (green). Raman map size: 30×30 μm.

To evaluate the reproducibility of different graphene growths, we performed Raman ω_{2D}-ω_G correlation maps (see Section 2.5.1) of multiple samples and compared them with the standard graphene from CVD1 on Cu foils. In Figure 3.16, Raman ω_{2D}-ω_G correlation maps reveal a high reproducibility achieved for the samples from the rigid sapphire/Cu substrates, as no significant differences were observed in strain (ϵ) or in doping. For the samples grown on Cu foils, we measured certain non-homogeneity between samples, in comparison with the high homogeneity observed for graphene on Cu films, and non-homogeneity within same samples, evidenced by the outlier points at the bottom part of the plot (Figure 3.16b). Regarding the strain gradient, the data clouds were more dispersed for graphene grown on Cu foils ($\Delta\varepsilon = 2.4\%$) than on Cu films ($\Delta\varepsilon = 1.6\%$). The strain differences may be attributed to the different Cu orientations

that may exist more prominently at the Cu foil surface. Variations in the doping of the samples were similar comparing graphene grown on Cu films and on Cu foils. These results demonstrate a promising high reproducibility level of graphene growth on the engineered rigid supports.

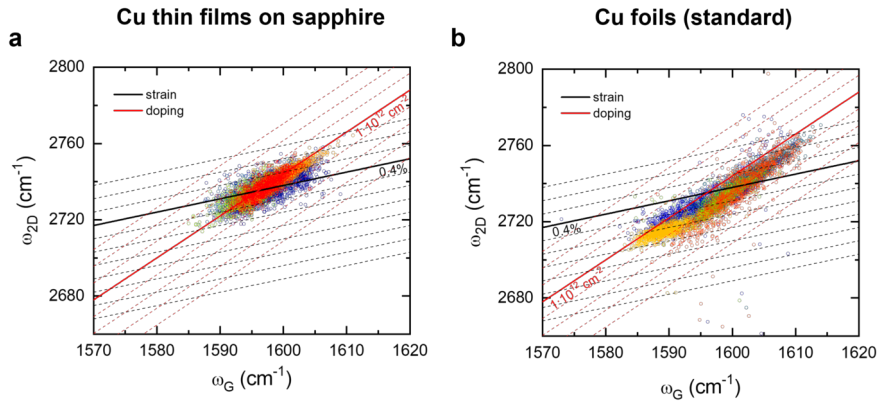


Figure 3.16: Reproducibility of graphene growth - Raman ω_{2D}-ω_G correlation maps of graphene samples grown on **(a)** c-sapphire/Cu rigid supports in the CVD2 and **(b)** commercial Cu foils in the CVD1. n = 6 samples. Raman maps size: 30×30 μm, acquired at the central part of the samples.

3.3.1 Graphene transfer and device fabrication

We evaluated the transfer and wafer scale fabrication process using our graphene grown on sapphire/copper. The dry transfer method has been presented as an interesting alternative to the wet transfer, this last one based on the chemical etching of the metallic growth support. The dry transfer offers a better industrial scalability and reduced doping effects related with the metal etchant [123, 165]. However, dry transfer is very challenging and not fully optimized. Although we explored the dry transfer of the graphene grown on the Cu-based rigid supports, we decided to use wet transfer after observing that the Cu was peeled-off together with graphene. In view of that, we carried out the transfer process described in Section 2.4.1 on pyrex substrates, with a slight modification: after PMMA spin-coating and curing, the sapphire/Cu/graphene samples are immersed in the $FeCl_3$/HCl solution during 2 hours. Once Cu is etched and the graphene layer is separated from the rigid support to remain floating on the solution's surface. The subsequent steps are the same than as for the standard protocol. AFM showed that the sapphire surface contains residues after graphene transfer (Figure 3.17a). XPS analysis revealed that no Cu was detected on the sapphire after the graphene was peeled-off, as no signal was measured at the Cu 2p XPS

spectrum (Figure 3.17b), and that the contamination observed by AFM was mainly due to Fe compounds (Figure 3.17c).

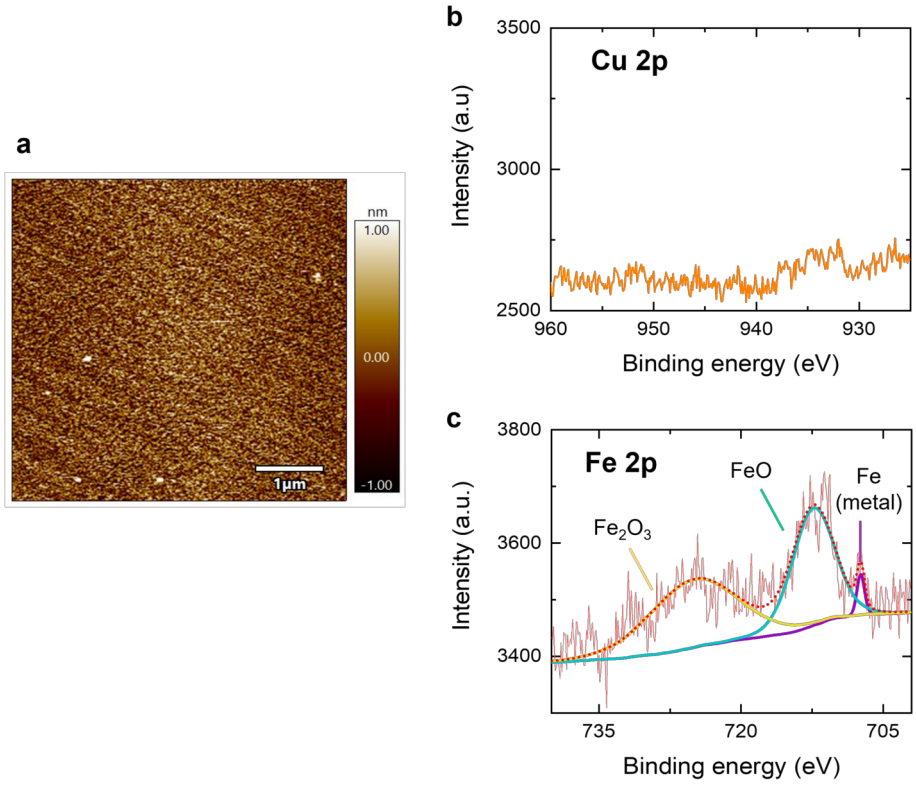


Figure 3.17: Sapphire substrate after graphene dry transfer - **(a)** AFM image of the sapphire surface after peeling of the Cu/graphene. **(b)** XPS Fe 2p core level spectrum showing Fe traces left at the sapphire surface. **(c)** XPS Cu 2p core level spectrum showing no Cu was left on sapphire after graphene transfer.

With the aim to compare the quality of the devices prepared with graphene grown on the sapphire/Cu with that of devices prepared using graphene grown on Cu foils, we carried out the transfer process on SiO_2/Si, (Figure 3.18a). We completed the standard fabrication procedure (see Section 2.4) obtaining a finalized device (Figure 3.18a). Raman spectroscopy characterization at each stage (Figure 3.18b) indicates the appearance of the graphene D band after transfer, which was not present in the as-grown case, and increased after fabrication, with an I_D/I_{2D} ratio < 0.5. In Figure 3.18c, the ω_{2D}-ω_G correlation map shows that the main effect of the fabrication process is a variation in the strain level of 0.65%, which is consistent with the reported range [166] and may be attributed to the different substrate-graphene coupling [167]. Regarding doping variations, the transfer and subsequent fabrication processes induced inhomogeneity, as we

observed increasing dispersion outside of the reference doping line (red line in Figure 3.18c). The doping level after fabrication increased to $2{\cdot}10^{12}$ cm^{-2}.

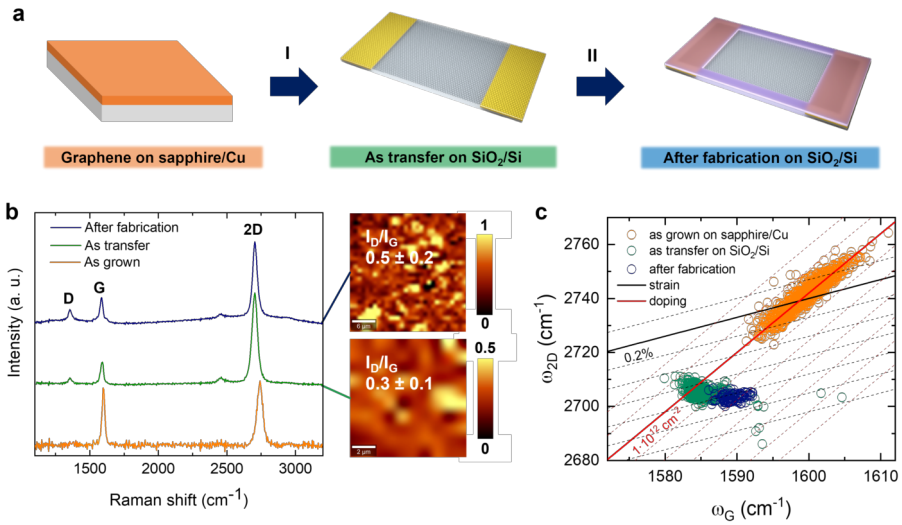


Figure 3.18: (a) Schematic representation of the process from the graphene growth to the fabricated device. The transfer performed in step I is detailed in Section 2.4.1. The fabrication performed in step II is described in Section 2.4. **(b)** Average Raman spectra of the three samples prepared with the I_{2D}/I_G maps obtained for the as transfer and after fabrication ones. **(c)** ω_{2D}-ω_G correlation map of the three samples analysed. Strain and doping levels are included according to [67]. Maps were of 30×30 μm for as grown graphene and of 10×10 μm for both as transfer and after fabrication.

3.4 Substrate reusability

Reusing the substrates for multiple graphene growth processes would represent a huge advantage in terms of achieving a cost-effective methodology. Substrate reusability can be considered in two directions: first, Cu could be reused if a dry transfer approach was available; second, sapphire reusability may be studied after Cu etching. As we worked with the wet transfer, here we present results regarding sapphire reusability.

After transferring the graphene, we treated the sapphire with HCl 5M to remove any remaining Fe residues from the Cu etchant solution. Results from the AFM and XPS analysis are shown in Figure 3.19. AFM measurements revealed that the c-sapphire terraces were maintained after Cu etching. However, we couldn't achieve the complete removal of small particles, that we attribute to Fe impurities. XPS confirmed that Fe residues were insignificant already after 3

hours of cleaning in HCl. Figure 3.19b and the Fe 2p corresponds to background signal.

To test subsequent graphene growth on the same c-sapphire substrate after Cu etching, we further proceeded with e-beam Cu deposition, annealing (Ar:H_2 (70:7 sccm), 1000°, 60 minutes, P∼50 mbar) and graphene growth (0.5 sccm CH_4 flow in Ar:H_2 (98:2 sccm), 1000°C and P∼60-70 mbar). SEM images of the sample after graphene growth (Figure 3.20), reveal large Cu grains and a smooth graphene surface. However, the SEM images also revealed the appearance of dewetting (white arrows in the right image). The presence of graphene was confirmed by Raman spectroscopy, as depicted in the left image.

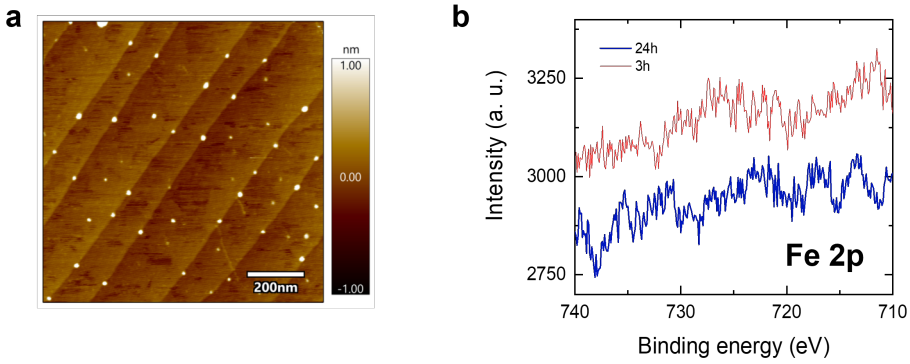


Figure 3.19: Sapphire surface after graphene wet transfer - **(a)** AFM image of the sapphire surface after graphene wet transfer and cleaning in HCl 5 M, 24 hours. **(b)** XPS Fe 2p core level spectra of the sapphire substrate after graphene transfer and cleaning in HCl 5 M for 3 and 24 hours.

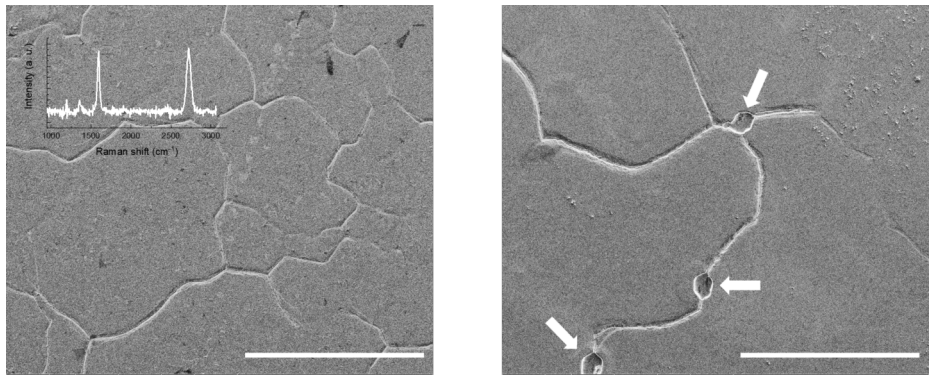


Figure 3.20: Graphene grown on a reused c-sapphire substrate - SEM images of a graphene sample grown on a reused c-sapphire sample, after a new Cu evaporation. Scale bar is 50 μm in both images. Raman average spectrum of an area of 400 μm^2.

These preliminary results demonstrated the feasibility of sapphire reusability for graphene growth. However, further work is necessary to evaluate the scope of it: a series of experiments involving more repetitions of Cu deposition, annealing, graphene growth and transfer on the same c-sapphire substrates, including AFM and SEM analysis to monitor the surface changes would allow the assessment of the impact on the sapphire surface, as well as on the graphene quality achieved after each serie.

4

Physicochemical characterization of the graphene/substrate and graphene/electrolyte interfaces

4.1 Graphene electronic devices in aqueous media

Being a bidimensional material, graphene is extremely affected by its surrounding media. Hence, the interfacial phenomena at the graphene interface dictate the operational performance of electronic devices working in aqueous conditions. Traditionally, the graphene-electrolyte interface has been studied both using experimental and theoretical approaches. Despite of the numerous published works on this crucial topic [38, 39, 40, 41, 42], fundamental questions yet remain to be answered. The reason why we still have little understanding of the interface between substrate-graphene-electrolyte is the complexity of the experimental approach to study it. First, highly reproducible, non-defective graphene sheets

are required. As commented in the previous chapter, this is a challenge on its own. Moreover, graphene in finalized devices contains impurities in form of adsorbed surface charges resulting from the transfer and lithography processes that alter its interface with the liquid and, consequently, have a negative impact in device performance. Despite the fact that a variety of surface cleaning approaches have been proposed up to date [168, 169, 60, 170, 171], this is still an unsolved matter.

Besides these residual charges, other factors may affect the electrochemical double layer (EDL) at the graphene-aqueous electrolyte interface: the ionic concentration [40, 41, 42], the pH or the nature of the substrate where graphene is supported [172, 173]. In addition, not only the bulk water from the electrolyte at the upper face of graphene has to be considered, but also the intercalated water between graphene and the substrate underneath it due to its influence on the electrical coupling with the substrate [174, 175]. This intercalated water comes from the wet transfer process, it is hard to completely remove and persists throughout the fabrication of the devices. Importantly, water intercalation is also a dynamic process that occurs while the graphene-based devices are working in an aqueous - biological- environment [176]. Having this in mind, even performing a water-free transfer process does not ensure avoiding substrate-graphene water intercalation, which makes it an important parameter to be taken into account.

In this chapter of the thesis, the impact of the above-mentioned factors in graphene interfacial phenomena is evaluated after providing a theoretical introduction of the graphene-electrolyte interface and the principal electrochemical technique to characterize it, followed by a discussion of the measurements performed towards the understanding of the whole substrate-graphene-electrolyte system.

4.2 Electrochemical double layer at the graphene-electrolyte interface

4.2.1 Electrode-electrolyte interface: Electrochemical Double Layer

Electrochemical measurements are the basis of electrode-electrolyte interface studies. When graphene is in contact with an aqueous electrolyte, a local potential difference appears at the interface between its surface and the electrolyte solution. The structure of this potential difference follows a distribution of charge that configures what is known as the electrochemical double layer, EDL. During electrochemical measurements, a voltage is applied to the electrode -graphene- and

the EDL structure changes, which can be monitored by measuring the interfacial impedance. Modelling of the EDL has evolved since the first approaches based on the ideal polarizable electrodes (IPE) concept [177] to the Gouy-Chapman-Stern model. In 1853, Helmholtz proposed the first description of the EDL [178]. Its model was based on a thermodynamic analysis of the electrochemical interface in a situation of no electrochemical reactions inducing charge transfer processes. The Helmholtz layer consists on a linear potential gradient between the two plates of the capacitor, the electrode and the electrolyte. This gives the Helmholtz double layer capacitance, expressed by:

$$C_H = \frac{\varepsilon_0 \varepsilon_H A}{d_H} \tag{4.1}$$

where ε_0 and ε_H are the permittivity values of vacuum and of the electrolyte, respectively, A is the electrode surface area and d_H is the distance between the charges in the electrolyte and the charges in the electrode, often considered, in an approximation, as the Debye length [179].

The Helmholtz model does not take into consideration the application of a potential to the electrode, as it describes capacitance independent from voltage, neither the derived thermal motion of the ions and the interaction between the dipole moments of the solvent molecules and the electrode. Gouy and Chapman developed a model including these factors, but treating the ions as points of charge that can arbitrarily approach the electrode surface [179]. Consequently, the Gouy-Chapman (GC) model does not differentiate between high and low electrolyte concentrations, which is not corresponding to reality. In 1924, Stern proposed a combination of the Helmholtz and the GC models, reaching a more accurate description of the EDL. Stern introduced a plane, called the outer Helmholtz Plane (OHP), which includes the ions closest to the electrode surface and result in the so-called Helmholtz capacitance, C_H. The bulk electrolyte, out of the OHP, follow the GC theory and conforms what is known as the diffusive layer [179, 180]. In summary, the Gouy-Chapman-Stern (GCS) model describes the total capacitance of the EDL, C_{EDL} as:

$$\frac{1}{C_{EDL}} = \frac{1}{C_H} + \frac{1}{C_{GC}} \tag{4.2}$$

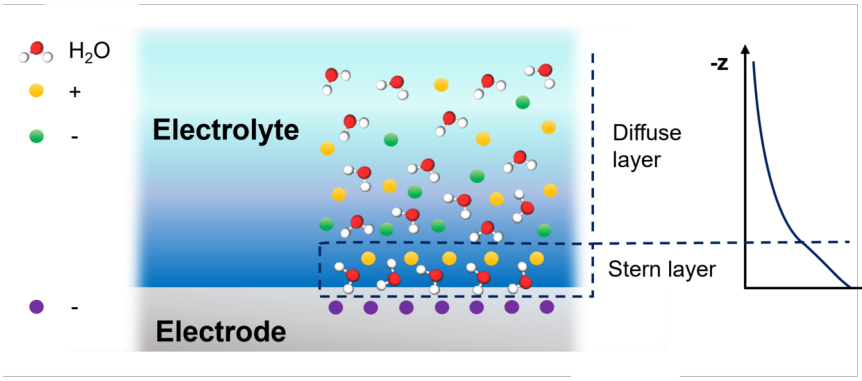


Figure 4.1: Model of the electrochemical double layer (EDL) - Illustration of the ionic distribution in the Gouy-Chapman-Stern model of the EDL and electrostatic potential distribution across the interface.

4.2.2 Graphene Quantum Capacitance

When considering graphene electrodes, equation 4.2 does not describe the experimentally measured capacitance. The reason of that is the additional contribution of the quantum capacitance, C_Q. The existence of the C_Q in graphene is consequence of the electronic structure of this material. Close to the Fermi level, graphene has a low density of states (DOS), which is contrast to the case of a pure metal [181], and with a symmetric distribution with respect to the Fermi level. Consequently, the charge density Q in graphene, which is the difference between the electron and hole densities in the electrodes, can be expressed as [181]:

$$Q = q\int_0^\infty g(E)[f(E+\frac{V_G}{2}+qV) - f(E+\frac{V_G}{2}-qV_a)]dE \tag{4.3}$$

where q is the magnitude of the electronic charge, E is the energy, g(E) corresponds to the DOS, f(E) is the function of the Fermi-Dirac distribution, V_G is the band gap energy, V is the local electrostatic potential, and E_F is the Fermi energy taken to be midgap when V is 0. When applying a voltage to graphene, the energetic distribution of the DOS enable the creation of holes or electrons according to the voltage applied. Taking this definition of Q and the definition of graphene's DOS, the C_Q of graphene is described by the combination of the following equations [182, 183]:

$$C_Q = \frac{2q^2}{\hbar\nu_F\sqrt{\pi}}(|n_G| + |n^*|)^{1/2} \tag{4.4}$$

$$n_G = (\frac{qV_{ch}}{\hbar\nu_F\sqrt{\pi}})^2 \tag{4.5}$$

being $\hbar$ the reduced Planck constant, ν_F the Fermi velocity, n_G the voltage-induced carrier concentration, n^* the effective charge impurity concentration and V_{ch} the electric potential at the graphene electrode.

Thus, C_Q is an additional capacitance appearing in graphene and connected in series to the total capacitance of the EDL. As a consequence, the total capacitance, C_{total} [1], of a graphene-based electrode is considered as [182, 183, 179]:

$$\frac{1}{C_{total}} = \frac{1}{C_{EDL}} + \frac{1}{C_Q} \tag{4.6}$$

The typical value of the graphene's C_Q is on the order of 1-10 $\mu F/cm^{-2}$ [184, 179], depending on the applied voltage range. Figure 4.2 is a graphical illustration of the series combination of the C_{EDL} and the C_Q of graphene.

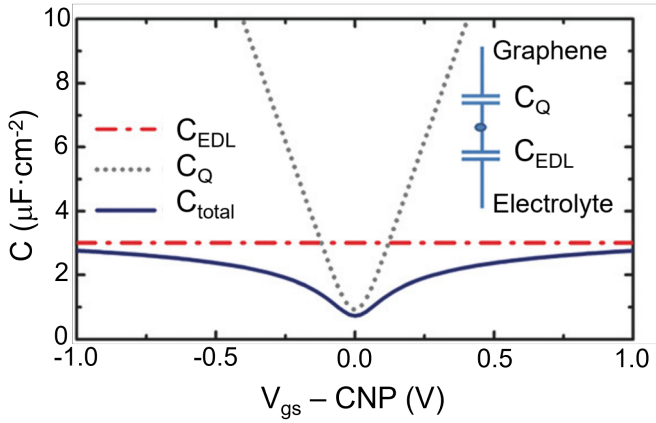


Figure 4.2: Capacitance at the graphene-electrolyte interface - Simulation of the graphene-electrolyte capacitance distribution at different V_{gs}. C_{total} is the combination in series of the double layer capacitance, C_{EDL}, and the graphene quantum capacitance, C_Q. Adapted from [185].

4.2.3 Electrochemical Impedance spectroscopy

Electrochemical Impedance spectroscopy (EIS) is a powerful technique for the characterization of the graphene-electrolyte interface. By applying an alternating current voltage (V_{AC}) to an electrode at different frequencies, it measures the resulting current response. When applying a V_{AC}, the sinusoidal nature of that voltage ($V(t)$) is expressed by:

$$V(t) = V_0 sin(\omega t) \tag{4.7}$$

[1] In literature, C_{total} can be also found as C_{int}

where $V(t)$ is the potential at a certain time, t, V_0 is the amplitude of the signal, and ω is the radial frequency

$$\omega = 2\pi f \tag{4.8}$$

while the current response presents a shift in phase, being expressed by:

$$I(t) = I_0 sin(\omega t + \phi) \tag{4.9}$$

Taking that into account, the voltage-current relationship when a V_{AC} is applied is expressed as impedance, Z, which is composed by a real and an imaginary part, Z_{Re} and Z_{Im}, respectively, and can be represented by the following expression:

$$Z(\omega) = Z_{Re} - iZ_{Im} \tag{4.10}$$

There are different ways to represent the Z response to the frequency of an electrode in an electrolyte, allowing the visualization of both the real and imaginary components (modulus and phase). To interpret the data obtained by EIS, we used the Bode plots form of representation (see Figure 4.3a), which represent Z and phase as a function of frequency, enabling the visualization of the electrochemical response of the electrode at the whole frequency range measured. Thus, different regimes can be identified according to the different contributions from the processes happening at the interface. In the Faradaic regime (very low frequencies), reactions at the electrode surface involving charge transfer affect the EIS response. In the capacitive regime, the EIS response is dominated by the capacitive contribution of the electrode. Finally, in the solution regime (very high frequencies), the resistive components of the system, which include the solution resistance, govern the EIS response.

Generally, EIS data analysis is performed taking an equivalent electrical circuit as a reference. A typical equivalent circuit representing the electrode-electrolyte system is composed by a resistance (related with the electrode contact and the electrolyte solution) and a capacitance (related with the charging of the double layer) connected in series. To account for all the possible processes happening at the interface and for deviations from the ideality of a pure capacitor, one of the most common circuits used for EIS data fitting is the Randless model [180], which is represented in Figure 4.3b. In a Randless model, R_s, is the resistive element that includes the the resistance of the solution and the contact resistance, and the CPE is the constant phase element, which substitutes the C_{dl} to consider non-idealities in the electrode such as surface roughness or distributed time constants for charge-transfer reactions, and thus improve the accuracy of the

model [186, 187]. The CPE impedance is expressed as:

$$Z_{CPE} = \frac{1}{\omega^{\alpha} Q} e^{-i\alpha\pi/2} \tag{4.11}$$

where ω is the angular frequency, i is the imaginary unit and α ($0 < \alpha < 1$) is the ideality coefficient, giving a pure capacitor behavior when $\alpha = 1$ (and then Q is equal to the capacitance), and a pure resistor when $\alpha = 0$ (and then Q is $1/R$) [188]. In systems where processes involving charge-transfer are present (i. e. reduction-oxidation reactions or adsorption-desorption processes), the R_{ct} element of the Randless circuit accounts for the charge transfer resistance. Finally, to describe diffusion processes, the circuit includes what is known as the Warbug impedance, W [180].

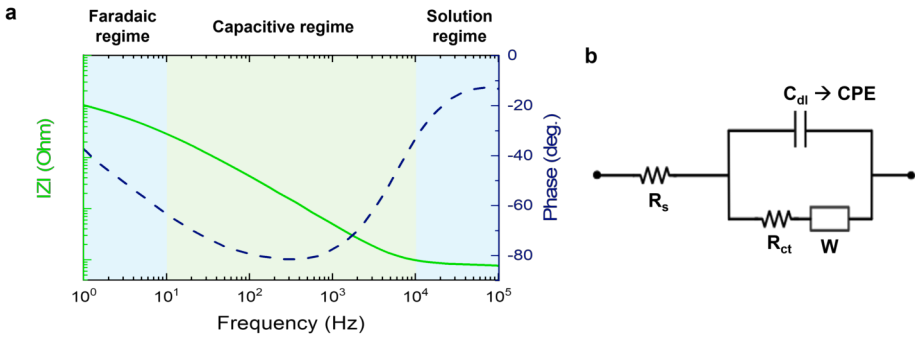


Figure 4.3: Bode representation of the frequency response of the electrode/electrolyte interface and Randless equivalent circuit - **(a)** Bode plot of a typical surface responding according to a Randless circuit, represented in **(b)**.

In this dissertation, we use potentiostatic electrochemical impedance spectroscopy, PEIS, which is the EIS technique performed fixing the voltage, to assess variations in the measured capacitance of graphene aqueous systems on substrates of diverse conductivity nature. For that, we work with a three-electrode configuration, illustrated in Figure 4.4a.

To interpret the PEIS data, we use different equivalent circuits to model each system studied, which will be explained further in the results discussion. When analysing the data to evaluate differences in the electrochemical behavior of the different graphene electrodes (detailed in the following section), we generally focus on these features of the Bode plot:

- Capacitive (CPE) regime: this is defined by the frequency range where the phase magnitude is approximately between 90° and 45°.

- Low-frequency limit: At low frequencies, the graphene electrodes can be charged and thus show a behavior dominated by the capacitance (CPE). The impedance at low frequencies is higher and decreases when the frequency is increased. Phase values approaching to -90° are indicative of a more capacitive nature of the electrode. At very low frequencies ($<10^1$ Hz), the electrochemical response belongs to the so-called Faradaic regime, where lower phase values (closer to 0) are indicative of reactions involving charge transfer at the electrode surface [180].

- High-frequency limit: at very high frequencies, the contribution to the total impedance from the CPE decreases as the electrochemical response is more dominated by the resistive components of the system, including R_s [180]. There, changes in the ionic strength of the electrolyte, for instance, may result in variations of the |Z|, as illustrated in Figure 4.4. Phase values close to 0° represent a more resistive behavior.

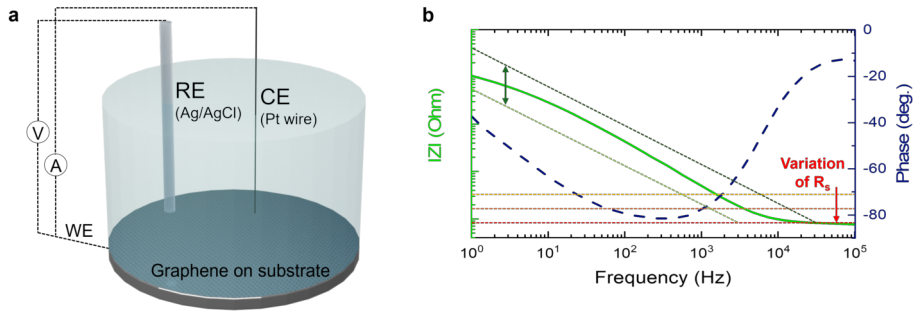


Figure 4.4: PEIS experimental setup and Bode plot illustrating changes in R_s - (a) Schematic illustration of the setup for the measurement of the electrochemical response of the graphene electrodes, representing a graphene electrode in contact with an electrolyte, where the reference electrode (RE) and the counter electrode (CE) are immersed. We used the same Bio-Logic SP-200 potentiostat as for the Raman spectroelectrochemistry measurements (see Section 2.5.1). **(b)** Representative Bode plot of a graphene electrode indicating the effect on the |Z| at high frequencies of variations in R_s produced by an increment of the ionic strength of the solution.

4.3 Substrate effect on the electronic properties of graphene

In order to study the influence of the substrate nature on the characteristics of graphene electrodes, we chose pyrex, ITO and Au substrates, as representative of a non-conductive transparent oxide, a semiconductive transparent oxide and

a metal, respectively. The graphene used in the study was grown in the CVD1 reactor following the method explained in Section 2.2. Once grown, graphene pieces of 5×5 mm were transferred to the three mentioned different substrates and the samples were prepared as explained in Section 2.5.1 (see Figure 2.12). PEIS was performed using an experimental setup based on a three-electrode configuration, according to what is explained above.

Figure 4.5 shows the PEIS Bode plot measured in PBS ([KCl] = 150 mM) pH 7 for the pyrex/graphene, ITO/graphene and Au/graphene electrodes, together with the proposed equivalent circuit models for each electrode configuration, detailed further below. We note the following observations from the Bode plots. The capacitive regime is extended from 40 Hz to $\sim 2 \cdot 10^3$ in the ITO/graphene system, while for pyrex/graphene and Au/graphene electrodes the capacitive response is extended to higher frequencies. For the same ionic strength (i. e. same R_s), the ITO/graphene capacitance is higher than the pyrex/graphene and Au/graphene (see Table 4.1).

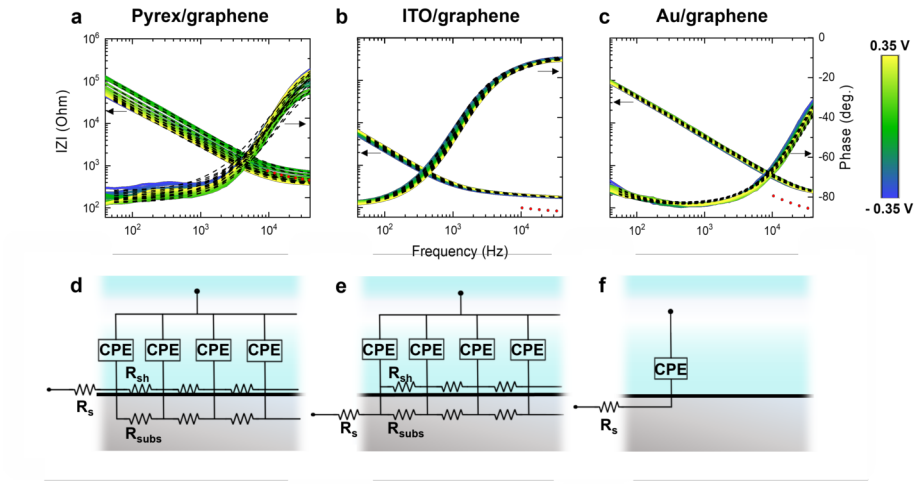


Figure 4.5: Electrochemical Impedance spectroscopy of graphene electrodes - (a-c) PEIS Bode plots of the different configurations of graphene electrodes, pyrex/graphene, ITO/graphene and Au/graphene. Different colours of the lines correspond to the data obtained at different voltages. The red dots at high frequencies correspond to results of measurements performed at higher electrolyte ionic concentration ([KCl] = 400 mM) to illustrate the effect of the ionic strength on the |Z|. **(d-f)** Corresponding equivalent circuit models. The dashed black lines represent the fitting results.

Table 4.1: |Z| values from PEIS measurements at low and high frequencies

	|Z| (Ohm)		
	Pyrex/graphene	ITO/graphene	Au/graphene
40 Hz	$\sim 10^5$	$\sim 5 \cdot 10^4$	$\sim 10^5$
10^4 Hz	$5 \cdot 10^2$-$9 \cdot 10^2$	$\sim 10^1$	$\sim 10^2$

In the resistive regime (frequencies $> 10^4$ Hz), ITO/graphene and Au/graphene are only barely sensitive to the DC voltage. This is not the case of the pyrex/graphene system, which shows significant voltage dependence of the impedance at all frequencies. When graphene is supported on conductive substrates, its associated sheet resistance, R_{sh}, is lower than the resistive component associated to the substrate, R_{subs}, thus the R_s dominates the impedance. On the contrary, the R_s effect on the impedance in graphene on non-conductive substrates is lower. The |Z| at high frequencies of measurements performed increasing the ionic strength of the electrolyte are plotted in Figure 4.5 (red dots) for each system. As observed, the effect of the ionic strength on the |Z| is more noticeable for ITO/graphene and Au/graphene, than for pyrex/graphene electrodes. Finally, a DC voltage-dependency of the impedance is expected for graphene [38]. This dependence is not observed in the ITO/graphene and Au/graphene systems, and it is further studied in this section.

In the following, the equivalent circuit models describing each studied system are explained (see Figures 4.5d-f). R_s contributes to the resistance-dominated region of the system and CPE is the constant phase element representing the double layer capacitance, whose origin is explained in the previous section, R_{sh} represents the distributed sheet resistance of the graphene layer and R_{subs} refers to the resistive component of the substrate. R_{subs} tends to ∞ for the case of pyrex and is considered null for the case of ITO and Au. R_{sh} is the distributed graphene sheet resistance. In the circuit model representing the Au/graphene electrode, an approximation to a CPE connected in series with R_s represents the system. An *in-house* code (see Annex B) has been used to perform the PEIS fitting of the experimental data. This code takes the defined equivalent circuit equation and returns fitted values for each parameter. The fitting parameters can be found in Annex B. Due to the limited conductivity of graphene, the frequency response of graphene devices is governed by a distributed configuration of the R and CPE elements in the graphene-electrolyte interface. This model has been described by Drieschner *et al.* [189], and the total impedance of the electrode

following it is calculated by:

$$Z(\omega) = \frac{-R_n J_0(bL,\omega)}{2\pi L b J_1(bL,\omega)} \tag{4.12}$$

where L is the electrode radius, J_0 and J_1 are the hyperbolic Bessel functions of the first kind and of the zeroth and first order respectively, and b is expressed as:

$$b^2 = -\frac{R_n}{2\pi r \frac{1}{CPE(j\omega)^\alpha}} \tag{4.13}$$

A detailed analysis of the PEIS measurements is presented in Figure 4.6. First, we show the DC voltage dependence of the impedance module (|Z|) measured at high frequency, $\sim 10^5$ Hz (Figures 4.6a-c), where the |Z| response is mostly dominated by the resistive components of the circuit. The pyrex/graphene electrode exhibits the expected graphene dependency, an inverted V-shaped curve [182]. This results from graphene's zero bandgap electronic structure, enabling ambipolar (hole and electron) conductivity, that can be modulated by the application of a voltage [84, 190] and reaches a minimum at the Dirac point, when the valence and the conduction band meet [185]. In relation with the sheet resistance, at more negative voltages (V < CNP), the R_{sh} decreases as the applied voltage increases due to the increasing carrier density (holes conductivity in electrode configuration). At more positive voltages (V > CNP), the R_{sh} also decreases as the applied voltage increases due to the increasing electron conductivity. For the case of conductive substrates, ITO and Au, the contribution of R_{sh} is negligible, such that the impedance at high frequencies is dominated by the R_s. In Figures 4.6d-f, we show the |Z|-V modulation at 54 Hz, where all electrodes have a capacitive behavior. Similarly to what is observed at high frequencies, only the pyrex/graphene electrode shows an inverse V-shape dependency of |Z|. As observed in Figures 4.5d-f, phase values at 54 Hz do not completely reach -90° in any studied case, which would correspond to a pure capacitor characteristic. This justifies the use of the constant phase element (CPE) for the analysis of this PEIS data and correspond to deviations from ideality, as explained in section 4.2.3. Figures 4.6g-i show the α values associated to the CPE element for each electrode. As previously explained, this parameter is related with the degree of capacitive (resistive) behaviour of the electrode, being it more capacitive (resistive) when α tends to 1 (0) [188]. In our case, the fitted α parameter is close to 1 (~ 0.9) in all electrodes, and with a very low voltage dependency.

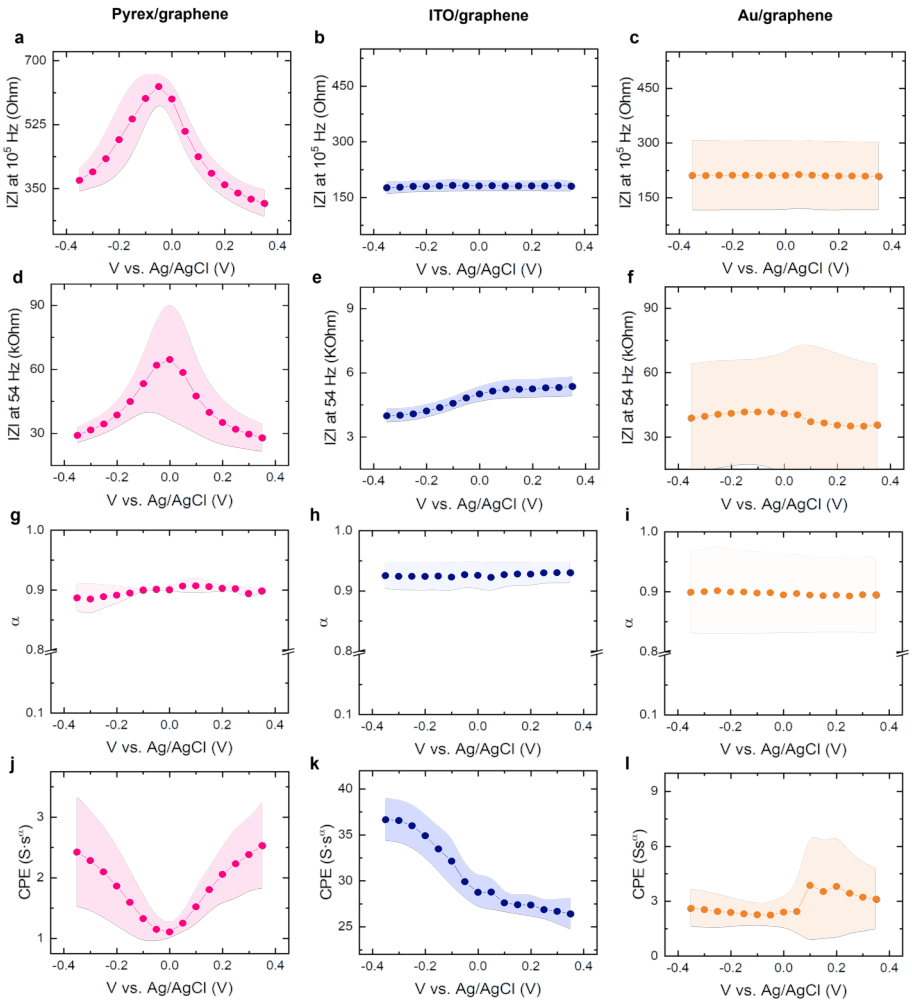


Figure 4.6: Electrochemical Impedance spectroscopy analysis of graphene electrodes -(a-c) Impedance module (|Z|) for each applied V at 10^5 Hz. **(d-f)** |Z| for each applied V at 54 Hz. **(g-i)** α response to V. **(j-l)** CPE modulation with V for the three systems studied. Values are extracted from the fitting using the distributed model for pyrex/graphene and ITO/graphene electrodes and the simple model for the Au/graphene electrodes, as explained in the text. n = 3 electrodes.

Finally, Figures 4.6j-l show the voltage response of the CPE parameters for the three electrode systems. The pyrex/graphene electrodes exhibit the expected symmetrical V-shape response of graphene, with values of ∼1.5 Ss^{α}, in good agreement to the ones reported in literature [184, 191] and corresponding to the series combination of graphene's quantum capacitance (C_Q) and the electrical double layer capacitance (C_{EDL}). The minimum of the curve, the CNP, corresponds to graphene's minimum conductivity [192], as previously explained.

For the ITO/graphene case, we observe clear qualitative and quantitative differences with the pyrex/graphene in the CPE-V curve: on the one hand, the absolute CPE values are higher, reaching ∼35 Ss^{α}. A non-symmetrical behavior of the CPE-V curve is also observed in the Au/graphene electrodes, which present a stepped trend, with slight higher values, around 3 Ss^{α}, than the ones of typical graphene C_Q, in agreement with reported literature [193].

To provide more understanding of the PEIS analysis, we performed the equivalent PEIS measurements for the bare ITO and Au substrates, without graphene on top of them. These measurements are shown in Figure 4.7. The CPE values for the bare ITO and Au substrates, ∼140 Ss^{α} and ∼40 Ss^{α} around 0.0 V respectively (see Figure 4.7c), are in good agreement with the literature [194]. Interestingly, the magnitude of the CPE values measured for ITO/graphene and Au/graphene electrodes (see Figures 4.6k,l) is lower than the ones measured for the bare ITO and Au electrodes, but higher than the ones associated with the graphene C_Q. The phase values for bare ITO and Au (see Figure 4.7d) are ≥ 0.95, that, as commented above, confirm a capacitive behavior of both electrodes. From now on, we will focus on the ITO/graphene system. The ITO substrate used in this thesis is an n-type semiconductor, with a carrier density of $1.12{\cdot}10^{18}\text{cm}^{-3}$, as extracted from the Mott-Schottky plot analysis[2] in Figure 4.8a, and its linearly-decreasing CPE behavior with increasing voltage can explain the lack of symmetric behavior of the ITO/graphene electrode (see Figure 4.6k).

[2]The Mott-Schottky theory is useful for the determination of the doping level of a semiconductor, using the Mott-Schottky equation for n-type semiconductors:

$$\frac{1}{C^2} = \left(\frac{2}{e\varepsilon\varepsilon_0 A^2 N_D}\right)\left(E - E_{FB} - \frac{K}{e}\right) \tag{4.14}$$

where e is the electron charge, ε is the semiconductor dielectric constant, ε_0 is the permittivity of vacuum, K is the Boltzmann constant, T is the temperature, C_{sc} is the space charge layer capacitance, A is the electrode area, N_D is the concentration of dopands, E the bias voltage and E_{FB} the flat band potential [195] which is detailed in the description of the Figure 4.8.

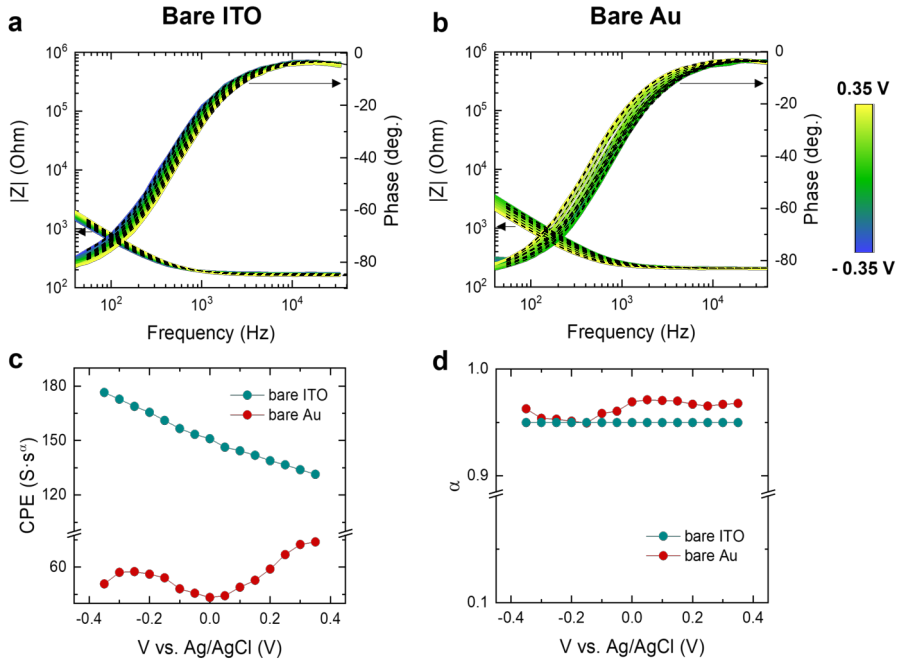


Figure 4.7: Potentiostatic Electrochemical Impedance spectroscopy of bare ITO and Au - (a)(b) PEIS Bode plots of the bare ITO and Au substrates (dashed lines are the fitting performed with the simple model circuit). CPE **(c)** and α **(d)** modulation with V for each substrate.

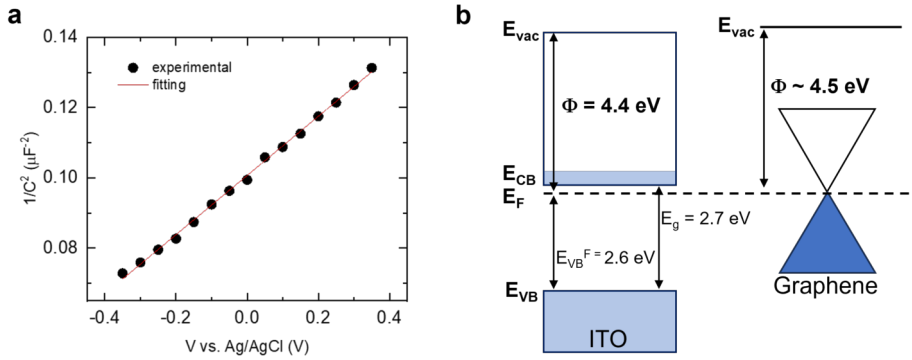


Figure 4.8: Mott-Schottky plot of ITO substrate for doping level calculation and band structure alignment with graphene - (a) Mott-Schottky plot for bare ITO. Doping level is calculated using the slope of the plot ($8.42{\cdot}10^{-2}$ $\mu F^2/V$) and considering the Mott-Schottky equation (4.14) for n-type semiconductors. **(b)** Band diagram model of ITO and graphene derived from photoemission (UPS) studies, explained in detail in Section 4.5.

The differences of measured CPE between the pyrex/graphene, the ITO/graphene and the Au/graphene electrodes give rise to questioning if the the

effective charge modulation in graphene can be limited by the ITO or Au band structures. To shed light on that, we performed Raman spectroelectrochemistry, as it provides a direct measurement of the graphene surface charge density [71]. Raman maps of the graphene electrodes immersed in PBS (pH 7) were acquired while applying different voltages (-0.35 to 0.35 V) vs Ag/AgCl, using the experimental setup explained in Section 2.5.1. Figure 4.9 show two exemplary Raman maps of the frequency of the graphene G band, ω_G, for the three electrodes studied at V = 0.0 V and 0.3 V. Measuring Raman maps instead of single spectra minimize graphene inhomogenities affecting the interpretation of the data, offering statistical information. Thus, the results presented are obtained from the analysis of measurements at each pixel of the map areas (see Figure 4.9). At a first glance, the ω_G shifts with voltage changes in the three systems. These differences, attested in the histograms in Figures 4.9c,f,i, are discussed below.

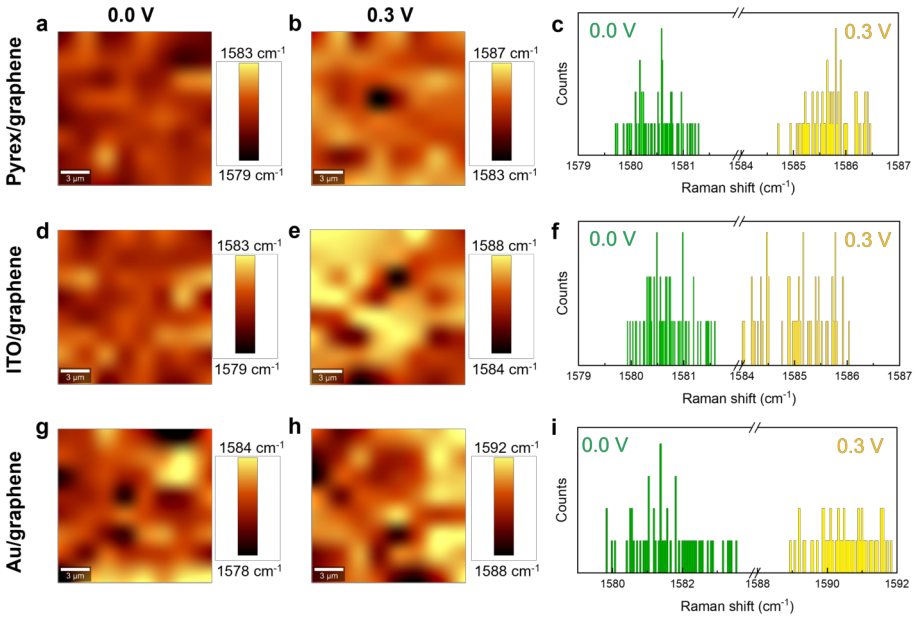


Figure 4.9: Raman spectroscopy measurements of graphene electrodes - **(a)(b)(d)(e)(g)(h)** Raman maps (256 μm^2) of the ω_G of pyrex/graphene, ITO/graphene and Au/graphene electrodes at 0.0 V and 0.3 V. Scale bar = 3 μm. **(c)(f)(i)** Corresponding histograms of the ω_G at the indicated voltages.

As previously mentioned (Section 2.5.1), thanks to the strong electron-phonon coupling in graphene, the energy of graphene G phonon relates with its Fermi energy (E_F) according to equation 2.2, reproduced here,

$$\hbar\omega_G - \hbar\omega_G^0 = \lambda(|E_F| + \frac{\hbar\omega_G}{4} ln|\frac{2|E_F| - \hbar\omega_G}{2|E_F| + \hbar\omega_G})$$

Moreover, according to the following expression, graphene's E_F relates with the carrier density, n [196]:

$$E_F = sgn(n)\hbar\nu_F\sqrt{\pi|n|} \tag{4.15}$$

To properly describe the doping-dependence of the graphene G-band, it is important to analyse the phonon self-energy [197, 198], whose real part is the ω_G and the imaginary part is the full-width-half-maximum (FWHM), Γ_G [196]. Γ_G variations are related with the G-phonon decay into an electron-hole pair (see inset at Figure 4.10d), and follow the expression [196]:

$$\Delta\Gamma_G = \frac{\lambda_\Gamma}{4}\omega_G^0[f(-\frac{\hbar\omega_G^0}{2} - E_F) - f(\frac{\hbar\omega_G^0}{2} - E_F)] \tag{4.16}$$

being ω_G^0 the phonon frequency at E_F=0, $f(E) = [1 + exp(E/\kappa_B T)]^{-1}$ the Fermi-Dirac distribution at a temperature T, the λ_Γ the coefficient of the electron-phonon coupling strength at the gamma point, and Γ_0 the part of the G band FWHM that contains all sources of broadening not related with the carrier density [196]. When representing graphene $\Delta\Gamma_G$ as function of the applied voltage (or the E_F) the $\Delta\Gamma_G$ has an inverted V-shape, which drops at $|E_F| > \hbar\omega_G^0/2$ responding to the exclusion Pauli principle [199, 196]. On the other hand, the ω_G behavior with E_F considers a contribution of G-phonon interactions with virtual electron-hole pairs (see inset at Figure 4.10e) and follows a V-shape trend, which can be approximated to [196]:

$$\hbar\Delta\omega_G \approx \lambda_\Gamma|E_F + \frac{\lambda_\Gamma\hbar\omega_G^0}{4} ln[\frac{|E_F - \hbar\omega_G^0/2}{|E_F + \hbar\omega_G^0/2}] \tag{4.17}$$

Additionally, it is possible to correlate the applied voltage with the E_F by [196]:

$$V - V_0 = \frac{E_F}{e} + sgn(E_F)\frac{eE_F^2}{\pi(\hbar\nu_F)^2 C_g} \tag{4.18}$$

The $\Delta\Gamma_G$ and $\Delta\omega_G$[3] as a function of V, respectively, are presented in Figures 4.10d,e. A theoretical fitting is included (black dashed lines), which is performed according to [196], using equations 4.16 and 4.17 with $\lambda_\Gamma = 0.02$ and C_g [4] = 2.7 μF/cm^2 (pyrex/graphene) and 2.3 μF/cm^2 (ITO/graphene and Au/graphene) to

[3]For clarity, here we plot $\Delta\Gamma_G$ ($\Delta\omega_G$) calculated as the difference between the Γ_G (ω_G) values measured at each V and the minimum of these values for the V sweep.

[4]As extracted from equation 4.18, C_g can be obtained from the slope of the $\Delta\omega_G$-V curves.

fit $\Delta\Gamma_G$ and ω_G data. In these Raman spectroelectrochemistry measurements, the voltage can be approximated as applied at very low frequencies. Hence, we can consider the C_g values as frequency-independent. Those values can be compared, in a first approximation, to the CPE values measured by PEIS for the pyrex/graphene electrode, which are in the range of the reported graphene C_Q [184, 191].

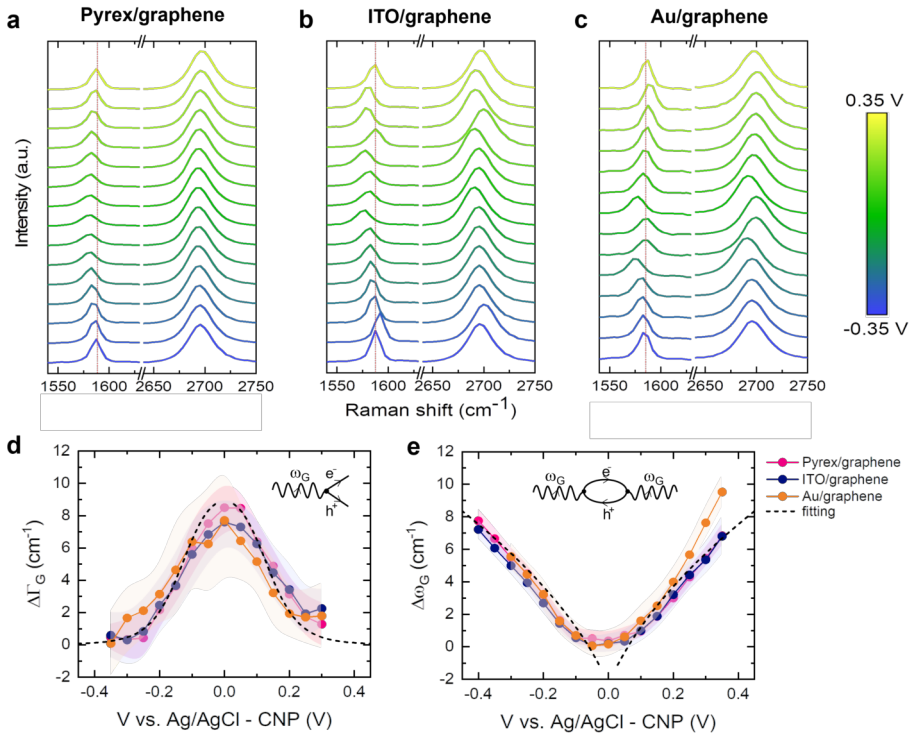


Figure 4.10: Raman spectroscopy analysis of graphene electrodes - (a-c) Average spectra in the G and 2D band regions of graphene supported on the three different substrates of study. Raman maps surface: 256 μm^2. **(d)(e)** $\Delta\Gamma_G$ and $\Delta\omega_G$ modulation with V and the corresponding fitting following the model explained in the text.

$\Delta\Gamma_G$ is analysed first. When graphene is on a substrate, the electron-phonon coupling can be affected by charge density variations resulting, among others, from the substrate self-doping effect. As no significant differences are observed in $\Delta\Gamma_G$ modulation with V (Figure 4.10d), the electron-phonon coupling in graphene on pyrex, ITO and Au can be considered invariable. This fact allows the evaluation of the charge modulation with V by using the method described above, correlating $\Delta\omega_G$ with V (Figure 4.10e). Interestingly, an identical voltage dependence for graphene on pyrex, ITO and Au is observed. Thus, the Raman

spectroelectrochemistry results indicate that the same charge modulation can be effectively induced in graphene by the application of an external potential regardless of the substrate conductivity nature. Moreover, the slopes of the $\Delta\omega_G$-V curves do not present any significant difference, which confirms that the same charge modulation of graphene can be achieved in the three electrodes.

Considering the outcome of the Raman study and comparing it with the PEIS results, which reveal a different impedance for the different electrodes (i.e. one order of magnitude CPE and no V-shape dependence with applied voltage for the ITO/graphene electrode), we dedicate the following discussion to provide an explanation to these observations. We focused this part on the study of pyrex/graphene and ITO/graphene electrodes, provided that both pyrex and ITO are transparent oxides with very different conductivity.

When performing PEIS measurements, the total capacitance of the system of study is measured. The fact that ITO/graphene electrodes show higher magnitude of capacitance than pyrex/graphene ones indicates an additional contribution of the ITO substrate to the total capacitance, beyond that of graphene. Given that ITO is a conductive substrate and pyrex is non-conductive, it is reasonable to think that this additional capacitive contribution may come from the ITO. Considering the PEIS results, this contribution requires the existence of an electrical contact between the substrate (ITO) and the bulk electrolyte. To answer the question, we will discuss the water intercalation phenomenon, briefly introduced at the beginning of this chapter and further explained here.

When graphene devices are immersed in an aqueous electrolyte, for instance during the fabrication of the devices, from the transfer process [200] or during their normal use in applications in which contact with aqueous solution is required (biosensing or bioelectronic applications), water can intercalate through the grain boundaries and thus be present between the graphene and the substrate underneath [201]. As water intercalates through the graphene grain boundaries [176, 202], its dynamics and amount depend on the graphene quality. Consequently, its impact on the measurement of the electronic properties of those devices is undetermined.

Figure 4.11 shows experimental proof of water intercalation in our devices. Specifically, Figure 4.11a depicts Raman spectra of graphene, extracted from Raman maps, before and after immersion in water for 2 hours; Figure 4.11b displays a histogram of the ω_{2D}, corresponding to the Raman maps in Figure 4.11a. Shifts of the ω_{2D} have been previously attributed to graphene-substrate decoupling due to water intercalation [203, 204]. After 2 hours immersion in water, the ω_{2D} presents a down-shift of $\sim$3.5 cm^{-1}, which we attribute to

water intercalation. Furthermore, the increased dispersion observed in ω_{2D} after immersion in water evidences a non-uniform water intercalation between graphene and the substrate, that has been explained by a non-uniform penetration of water through graphene's grain boundaries [200]. Figure 4.11c shows the evolution of ω_{2D} during the time the graphene electrode is immersed in water, revealing that the ω_{2D} down-shifts progressively during the first 90 minutes. Finally, Figure 4.11d shows contact potential difference (CPD) maps acquired using KPFM (see Section F.3 for more information about the experimental details), before and after immersion in water. The CPD map after immersion unveils the presence of regions with different CPD, which we attribute to water islands remaining between graphene and the substrate, in agreement with the inhomogeneous presence of intercalated water reported in literature [174, 205].

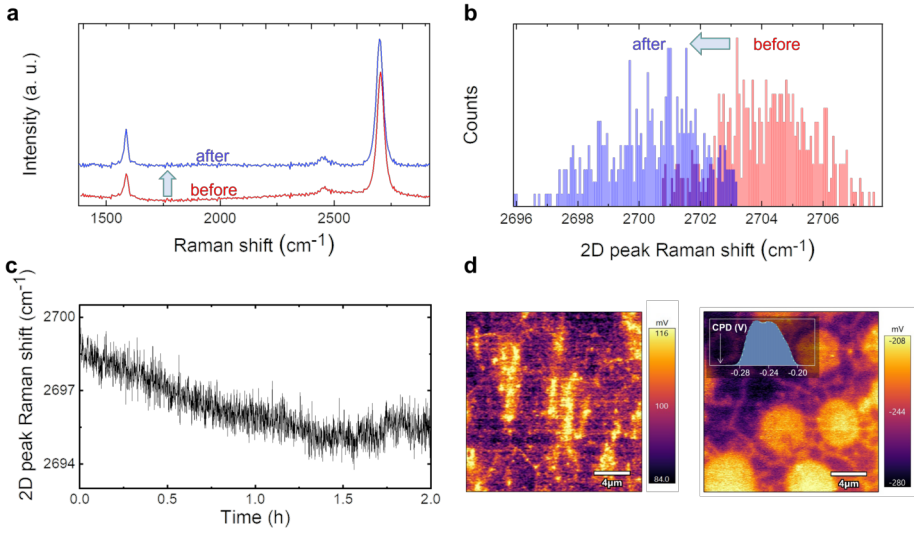


Figure 4.11: Experimental visualization of water intercalation in graphene electrodes - (a)(b) Raman spectroscopy of a graphene electrode (pyrex substrate) and histogram of the ω_{2D} before (red) and after (blue) immersion in water (2 hours). **(c)** Evolution of ω_{2D} with time during electrode immersion in water. Raman maps dimensions: 400 μm^2. **(d)** CPD map obtained by KPFM on a 120×30 μm graphene transistor (SiO_2/Si substrate) before (left) and after (right) immersion in water (2 hours). The histogram in the inset of the right image shows the potential distribution of the CPD measurement.

Once confirmed the presence of the water intercalation in our graphene devices, we now discuss about its impact on capacitance[5] measured for pyrex/graphene and ITO/graphene electrodes. This part of the thesis includes numerical simulations performed in collaboration with the Pervasive Electronics Advanced Research

[5]For clarity, we refer to capacitance in this part of the dissertation, instead to CPE.

Laboratory (PEARL) of the University of Granada (UGr)[6]. Considering the experimental observations, the reality of the graphene electrodes when in liquid is the coexistence of different areas: one where graphene is in direct contact with the substrate (without water intercalation) and another one where graphene is in contact with intercalated water. The electrical circuits that describe the resulting capacitance of these different areas are represented in Figure 4.12.

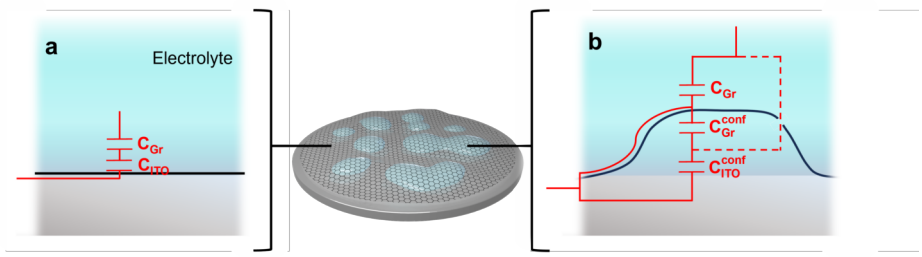


Figure 4.12: Different coexisting interfaces formed on a graphene electrode in contact with an aqueous electrolyte - (a)(b) Schematic illustrations representing the areas without and with water intercalation, respectively, of the graphene electrode illustrated in the centre, including the representative electronic circuits defining the capacitance distribution of each system. C_{Gr} is the graphene capacitance, C_{ITO} is the ITO capacitance, C_{Gr}^{conf} is the graphene contribution to the capacitance considering the regions with water intercalation. C_{ITO}^{conf} is the ITO capacitance considering the regions with water intercalation. C_{Gr}^{conf} is short-circuited with C_{ITO}^{conf} and thus not contributing to $C_{intercalation}$. The water present between graphene and the substrate in the areas with water intercalation is referred in the text as confined water, and it has reduced dielectric properties in comparison with bulk water [206, 207].

As derived from the representations in Figure 4.12, the contributions of C_{Gr} and C_{ITO} are in series for the case without water intercalation, being the total capacitance of the circuit defined by the expression:

$$\frac{1}{C_{no-intercalation}} = \frac{1}{C_{Gr}} + \frac{1}{C^{*}_{ITO}} \tag{4.19}$$

where the C_{Gr} is considered as the experimental capacitance obtained from the PEIS of pyrex/graphene, as the substrate contribution to the total capacitance in this case is negligible, given the non-conductive nature of pyrex. The ITO capacitance C^{*}_{ITO}, however, cannot be experimentally obtained from the PEIS measurements of bare ITO electrodes. In the case of bare ITO electrodes, the measured capacitance, that is named C_{ITO}^{bulk}, corresponds to a situation in which the ITO electrode is directly in contact with the bulk electrolyte. C^{*}_{ITO} can be described by two-parallel plate elements, in correspondence with the beginning of

[6]The PEARL group, lead by Prof. Andrés Godoy, is part of the Department of Electronics and Computer Technology of the UGr.

the depletion region of the ITO and its surface, being the distance between them the size of the depletion region (see Figure 4.13). On the other hand, C_{ITO}^{bulk} is spatially defined by the electrolyte and the substrate. The electrolyte corresponds to the first plate and it is ultimately determined by the closest layer of ions to the substrate, which corresponds to the second plate and is associated to the depletion region in the ITO. Taking the C_{ITO}^{*} and C_{ITO}^{bulk} descriptions into account, it can be assumed that $C_{ITO}^{*} > C_{ITO}^{bulk}$. Furthermore, considering that $C_{Gr} \ll C_{ITO}^{bulk}$, as extracted from the PEIS measurements, and that $C_{ITO}^{*} > C_{ITO}^{bulk}$, then we can conclude that $C_{Gr} \ll C_{ITO}^{*}$. Consequently, we arrive to the assumption that $C_{no-intercalation}$ is governed by C_{Gr}:

$$C_{no-intercalation} \cong C_{Gr} \tag{4.20}$$

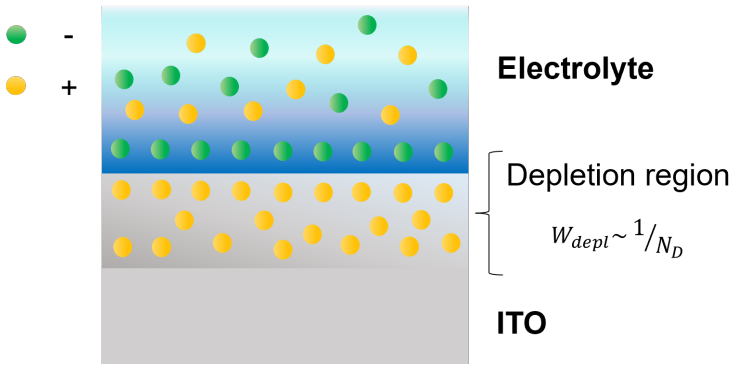


Figure 4.13: Depletion region between an ITO substrate and the electrolyte - Schematic illustration representing the charge distribution between ITO (n-type semiconductor) and an electrolyte. Despite the charge distribution at the electrolyte depends on the electron density, it can be approximated as a metal in this case. W_{depl} is the width of the depletion region formed between the two parallel plates: the ITO and the electrolyte, and it is inversely proportional to the square root of the doping density.

For the case of the electrode areas with water intercalation, the presence of water enables an electrical connection between the substrate and the bulk electrolyte and thus there is a parallel distribution of the graphene an ITO contributions to the total capacitance, $C_{intercalation}$ (see Figure 4.12b). Considering that $C_{Gr} \ll C_{ITO}^{conf}$, we can conclude that $C_{intercalation}$ is governed by the interfacial capacitance of ITO in contact with the confined water, C_{ITO}^{conf}:

$$C_{intercalation} = C_{ITO}^{conf} \tag{4.21}$$

Hence, to know the contribution of $C_{intercalation}$ to the total capacitance of the graphene electrode, it is necessary to know the magnitude of C_{ITO}^{conf}. As we do not have direct experimental access to C_{ITO}^{conf}, we collaborated with the PEARL group to perform numerical simulations to support this analysis. All the numerical simulations here were realized using an *in-house* code [208, 209], being the main parameters the permittivity (ε_w) and the thickness (t_w) of the confined water layer, as these parameters are known to vary with respect to the ones for bulk water [207]. First, the C_{ITO}^{bulk} was simulated to prove that the model used is consistent with the experimental PEIS data of Figure 4.7 for the bare ITO electrode. Then, the simulation of C_{ITO}^{conf} was performed following the approach detailed in Annex B, considering a layer of confined water above the ITO surface with reduced ε_w and certain t_w. To assess the model's sensitivity to these parameters, in Figure 4.14 we depict the calculated C_{ITO}^{conf} varying them in a range that accounts for the reduced dielectric properties of the confined water [207]. To visualize the impact of ε_w on C_{ITO}^{conf} (Figure 4.14b), we considered one layer of water (t_w = 3.4 Å) and varied ε_w from $5\varepsilon_0$ to $25\varepsilon_0$. C_{ITO}^{conf} increases with ε_w. The minimum that appears around 0.2 V is attributed to the minimum of charge density reached by the bulk electrolyte and the confined water, explained by its charge density profiles (see Annex B). This minimum becomes less evident with lower values of ε_w. Furthermore, a maximum at $\sim$ 0.3 V is observed for lower ε_w values, which we attribute to a change in the contribution to the total capacitance of the regions corresponding to the confined water and the bulk electrolyte. At $\sim$0.3 V, the accumulated charge in the confined water region reaches a value capable to partially screen the substrate effect, which consequently reduces the charge modulation in the bulk electrolyte (see Annex B for more details). Regarding the impact of the number of layers of confined water (t_w variations) on C_{ITO}^{conf} (Figure 4.14c), we observe that C_{ITO}^{conf} decreases with increasing t_w for a fixed ε_w of $15.6\varepsilon_0$. Hence, a thicker confined water region leads to a reduction in the coupling between the bulk electrolyte and the ITO. Consequently, a higher impact of the confined water region is manifested for higher t_w values, as revealed by the maximum at $\sim$0.3 V for those curves.

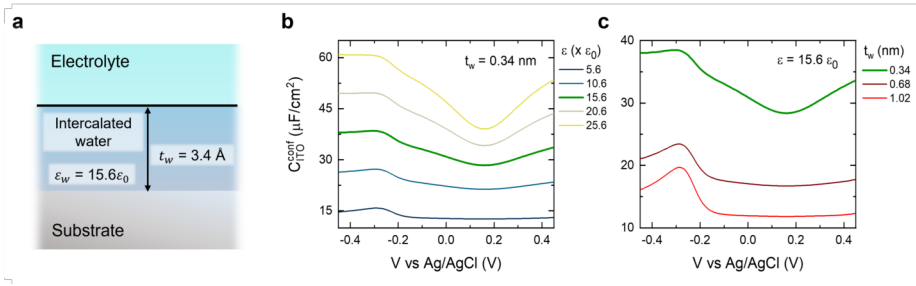


Figure 4.14: Numerical simulations on the ITO-intercalated water-graphene-bulk electrolyte interface - **(a)** Schematic illustration of the substrate (ITO)-graphene-electrolyte interface at the regions with intercalated water. **(b)(c)** Effect of the confined water permittivity and thickness, respectively, on the ITO capacitance, C_{ITO}^{conf}.

After having evaluated the impact of the key parameters of the confined water region, ε_w and t_w, on C_{ITO}^{conf}, we now calculate the total capacitance of the ITO/graphene electrode, C_{total}. As previously explained and confirmed experimentally, water intercalation in graphene electrodes occurs non-uniformly, in the form of cluster or islands [205]. Taking this into account, we can define C_{total} as a weighted sum involving the regions without and with water intercalation, as indicated in equation 4.22:

$$C_{total} = \theta C_{no-intercalation} + (1-\theta) C_{intercalation} \tag{4.22}$$

where θ and 1-θ are the surface coverage of each region, respectively. Figure 4.15a shows that the numerical simulations were able to reproduce the PEIS experimental data for the ITO/graphene electrode (previously presented in Figure 4.6k and reproduced again here) considering $\varepsilon_w = 15.6\varepsilon_0$, $t_w = 3.4$ Å and $\theta = 0.23$[7], meaning that about an 80% of the electrode area presents water intercalation. As stated before, the degree of water intercalation in graphene devices may vary depending on the graphene quality, i. e. the amount of grain boundaries and the defect density, and the substrate hydrophobicity. To provide an indication of how the amount of water intercalation varies the magnitude of the measured capacitance, in Figure 4.15b we depict C_{total} simulated for a range of θ, from 0 (highest amount of water intercalation) to 0.95 (low amount of water intercalation). These results confirm that increasing water intercalation enhances the graphene-substrate decoupling and enables the electrical connection of the substrate with the bulk electrolyte, which results in a measured C_{total} with higher contribution from the capacitance of the ITO substrate. This effect

[7]The numerical model developed enables the simultaneous variation of ε_w, t_w and θ.

would not be observed for the case of graphene electrodes using non-conductive substrates, as pyrex.

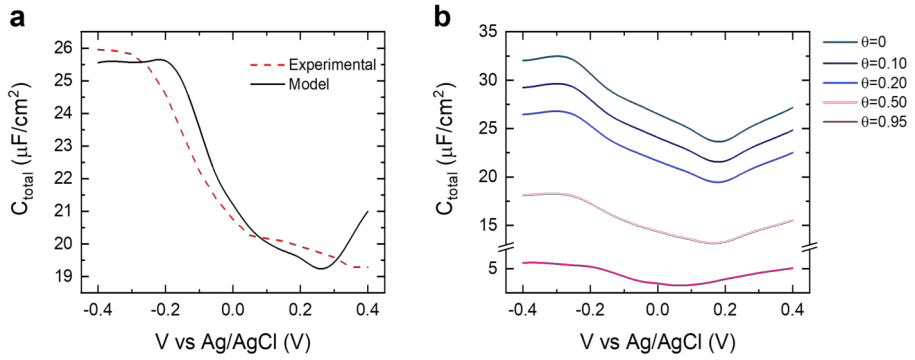


Figure 4.15: Numerical simulations for the calculation of C_{total} - (a) Comparison of the experimental PEIS data, CPE of the ITO/graphene electrode and simulated C_{total} using the ε_w, t_w and θ parameters indicated in the text. **(b)** Simulated C_{total} for different θ values.

An equivalent study could be applied to explain the electrochemical response of Au/graphene electrodes. In this case, the different substrate hydrophobicity, substrate-graphene adhesion, as well as the Au conductivity and its band alignment with graphene should be taken into account. From this point, discussion will be focused on pyrex/graphene and ITO/graphene electrodes. The experiments performed on Au/graphene electrodes, not considered for the discussion, are provided in Annex B.

4.4 Electrolyte effect on the electronic properties of graphene

Results presented until now have revealed the impact of water intercalation on the electrical response of graphene-based devices. As stated at the introduction of this chapter, when graphene devices are in an aqueous electrolyte, not only the substrate nature affects its electrical performance, but other parameters such as the electrolyte ionic strength and pH are important. Here, we assess the effect of those parameters, ionic strength and pH, on the characteristics of as-transfer graphene electrodes. It is known that, depending on the composition of the electrolyte in contact with graphene, there may be variations in the electrostatic charge screening at the surface, the reactions happening at the graphene surface and the doping level [210], which can be associated with the

amount of surface charge on graphene, σ_{ads}. In literature, there is a controversy regarding graphene's sensitivity to pH. In this regard, two hypothesis have been considered. The first one assumes graphene sensitivity to pH due to charging of the C_{EDL} as a consequence of ion adsorption at the graphene surface [211]. The second one establishes that clean graphene surfaces cannot sense pH due to their lack of chemically-charged groups exposed to the electrolyte [212]. Hence, graphene's pH sensitivity is considered to be due to its interfaces with the substrate and the charged species on its surface [213]. To resolve this, it is of importance to distinguish *clean* graphene from *contaminated* graphene. The differences between them, as well as its impact on graphene technology and the consequence challenges associated are further discussed in the following section. Having said that, here we use as-transfer pyrex/graphene electrodes (as in Section 4.3), considering them *clean* graphene.

The influence of ionic strength on EDL can be studied by different methods. Our aim here is to identify possible variations in graphene's capacitance and charge modulation with voltage. For that, the pyrex/graphene electrodes were put in contact with PBS of different pH (3, 7 and 10) and two different ionic strengths, adjusted by [KCl]: 150 and 400 mM. PEIS and Raman spectroelectrochemistry were performed following the same experimental procedures described in Section 4.3.

Figure 4.16a shows the Bode plots of the pyrex/graphene electrodes at different electrolyte pH and ionic strengths, measured with the application of voltage.

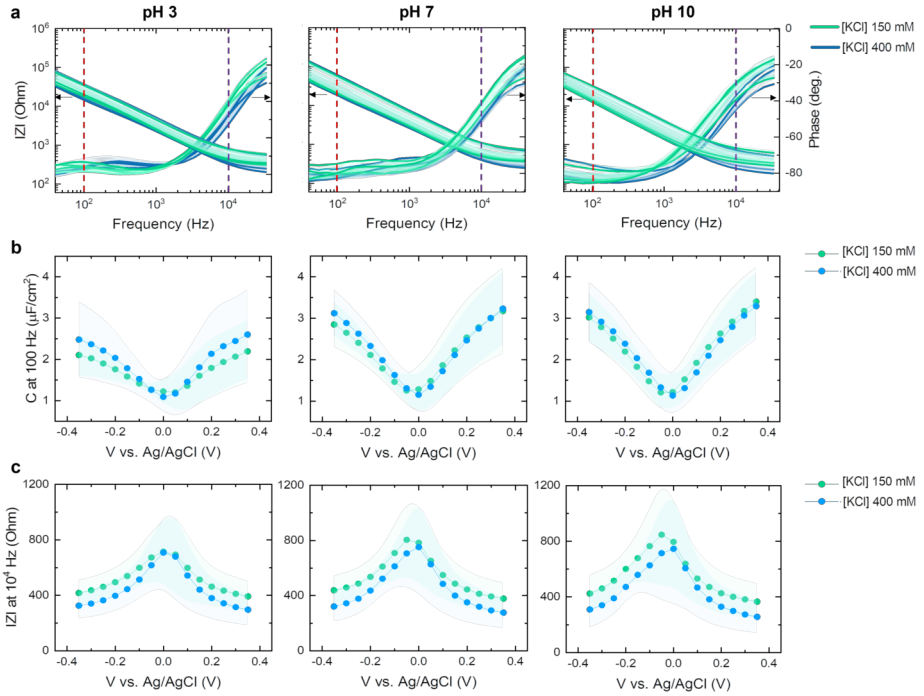


Figure 4.16: Electrolyte pH and ionic strength effect on electrochemical response of pyrex/graphene electrodes - **(a)** Bode plots of a pyrex/graphene electrode measured in PBS pH 3, 7 and 10, [KCl] 150 mM and 400 mM. Different lines of a same colour correspond to different applied voltages (from -0.35 V to 0.35 V, in steps of 0.1 V). In each plot, the more intense lines are the measurements at -0.35 V, 0.0 V and 0.35 V. **(b)(c)** Capacitance extracted from Bode plots at 100 Hz (red dashed lines in (a)) and |Z| extracted at 10^4 Hz (purple dashed lines in (a)) for pyrex/graphene electrodes. n = 3 electrodes.

A noticeable observation is the different phase modulation at low frequencies depending on the pH. At pH 3, there is a small phase change, which appears at different frequency depending on the electrolyte ionic strength (at ∼100 Hz for [KCl] = 150 mM and at ∼300 Hz for [KCl] = 400 mM). At pH 7, this phase change is not observed. At pH 10, the phase starts decreasing at ∼100 Hz at some voltages. This is attributed to electrochemical reactions at the electrode surface involving oxygen-reduction (ORR), as reported in literature [214]. These changes in phase at different pH have been previously attributed in literature to an additional RC element at the system [215]. In the case of the pyrex/graphene electrodes studied here, this could be originated by residues at the graphene surface remaining from the transfer process (see Section 2.4.1), thus, PMMA.

The dashed red lines in the Bode plots of Figure 4.16a indicate the frequency (100 Hz) at which the capacitance, C, is obtained using equation 4.11[8], and plotted as a function of the voltage in Figure 4.16b. The selection of this frequency allow us to minimize the contribution of the additional RC element at pH 3 and avoid the ORR reactions at pH 10. However, in Figure 4.16b we observe that the capacitance modulation is lower at pH 3 than at pH 7 and 10. Interestingly, the CNP of the curves at each pH and ionic strength are centered at 0.0 V. To explain these observations, assuming that clean graphene is not sensitive to pH, we consider at the PMMA chemical response to pH, illustrated in Figure 4.17.

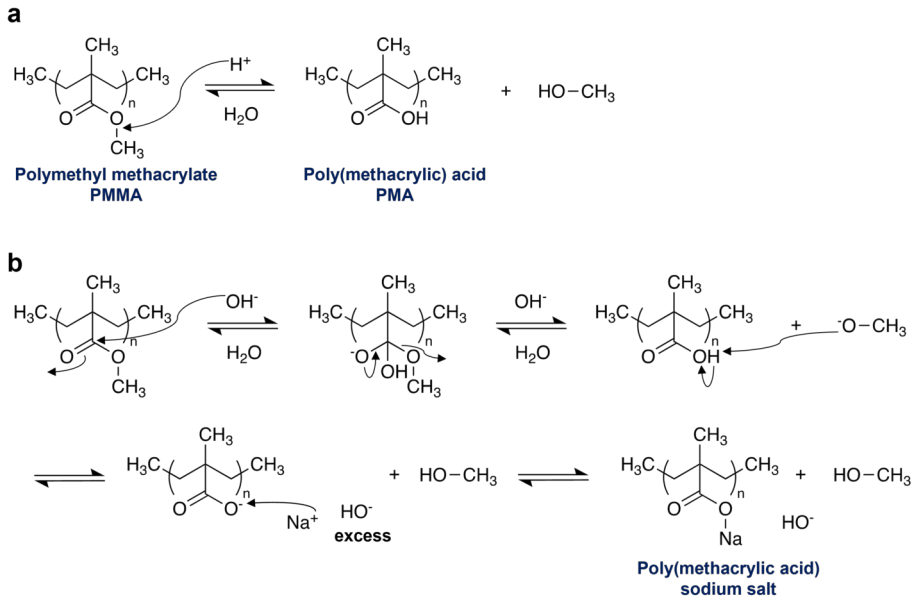


Figure 4.17: PMMA stability under different pH conditions in aqueous media - (a)(b) PMMA in acidic and basic media, respectively. In acidic media, the PMMA ester group gets protonated, resulting in the carboxylic acid group. As a byproduct, methanol (HO-CH_3) is formed. Basic conditions enable a nucleophilic attack by OH^- to the carbonyl carbon of the ester group in PMMA. As a result, a tetrahedral intermediate is formed with the hydroxide attached to the carbonyl carbon. After the intermediate is broken, resulting in the formation of PMA, the methoxy group (CH_3-O^-) intervenes deprotonating PMA. An excess of NaOH allows the formation of the PMA sodium salt. Adapted from [216].

In acidic media, protons interact with the methyl of the ester group of the PMMA to form the poly(methacrylic) acid, PMA [216]. This reaction is reversible, and it is also influenced by the ionic strength of the electrolyte. For instance, in an

[8]Note that, differently from Section 4.3, the PEIS data is not fitted to an equivalent circuit here, as the effect of the electrolyte pH and ionic strength on pyrex/graphene electrodes can be analysed, in a first view, without the need of performing a fitting.

excess of NaOH (basic conditions), the PMMA can result in the poly(metacrylic acid) sodium salt [216]. Considering the complex, pH dependant, chemistry of PMMA, we tentatively explain the lowest C modulation at pH 3 by the effect of PMMA (PMA) residues, as these can affect graphene charge mobility. Moreover, as previously mentioned, the amount of residues in the as-transfer graphene/pyrex electrodes is considered to be very low.

Figure 4.16c presents the modulation of |Z| with V at a high frequency, 10^4 Hz. According to what has been discussed in the previous section, the value of |Z| at high frequency is barely altered with the ionic strength in the case of graphene electrodes on a non-conductive substrate such as pyrex. In this case, the R_{sh} dominates the electrochemical response, being $R_{sh} > R_s$. However, the |Z|-V curves in Figure 4.16c show slight differences in the |Z|-V modulation for the different ionic strengths. Close to the CNP, that is, at V = 0, R_{sh} has its maximum value, thus its contribution to |Z| will be $R_{sh} > R_s$. Differently, at V $\neq$ 0, R_{sh} decreases, thus the contribution of R_s to |Z| is greater at V $\neq$ 0, which explains the slight difference in its modulation with V when increasing the ionic strength of the electrolyte. Despite that, the effect of the ionic strength on the pyrex/graphene electrodes observed in Figure 4.16c is lower than the one observed in graphene electrodes on conductive substrates, as it has been discussed in the previous section (see Figure 4.7).

To analyse the graphene charge modulation, Figure 4.18 presents the graphene G band frequency response to the applied voltage, obtained from the analysis of Raman maps. In Figure 4.18a, we show an exemplary set of the data acquired (V = -0.3 V) of measurements performed at pH 3 and 10. In Figure 4.18b, we depict the ω_G-V curves from the statistical analysis of each Raman map. The charge neutrality point (CNP) is mostly centered around 0.0 V for pH 3, 7 and 10. This further confirms the PEIS results, from which we concluded that the as-transfer pyrex/graphene electrodes can be considered clean (with minimal amount of PMMA residues). The position of the CNP curves presents a very low (below the Raman pixel-to-pixel resolution, 3 cm^{-1}) yet unexpected shift towards positive V from low to high ionic concentration. This low shift is slightly larger at pH 10, but still under the Raman pixel-to-pixel resolution. Further exploration would be useful to confirm that.

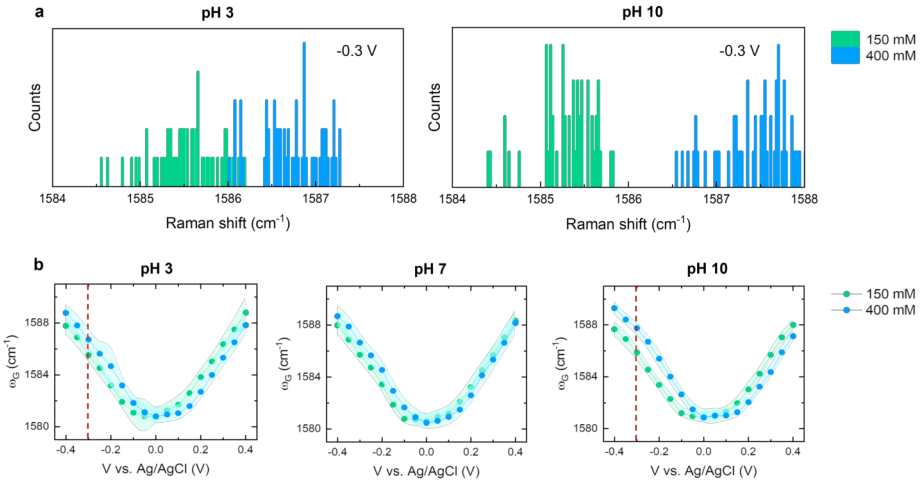


Figure 4.18: Ionic strength and pH effect on measured ω_G by Raman spectroelectrochemistry - (a) Histograms of the ω_G values at each pixel of the Raman maps measured in PBS pH 3 and 10, applying -0.30 V. **(b)** ω_G vs V for pyrex/graphene electrodes in PBS ([KCl] = 150 mM and 400 mM) at pH 3, 7 and 10. Results are obtained from the Raman maps measured at each V.

At this point and considering the discussion above, we can conclude that the electrolyte pH and ionic strength in the studied range do not significantly affect graphene charge modulation in as-transfer pyrex/graphene electrodes.

The evaluation of the effect of residues on graphene, as well as the discussion about ways to quantify and control it is presented in the following section.

4.5 Effect of adsorbed charge on graphene electrodes performance

Until this point, all shown experiments were conducted with electrodes using as-transfer graphene electrodes. This enabled the assessment of the impact of important parameters in graphene technology such as the conductive nature of the substrate and the electrolyte pH and ionic strength. An important parameter to evaluate now is the impact of wafer scale fabrication on device performance.

A methodology for the study of the impact of the wafer scale residues on the electrical performance of graphene has been developed in this section based on the combination of PEIS and Raman spectroscopy. As briefly introduced before, in both dry and wet graphene transfer approaches, a support layer is generally used, normally a polymer; in our case, PMMA (see Section 2.4.1). Once the PMMA/graphene stack is transferred to the target substrate, PMMA is cleaned away with acetone/isopropanol. Despite this cleaning step, it is a great challenge

to obtain a residues-free graphene layer. This implies that a certain amount of residues on the as-transfer samples has to be always taken into account, also confirmed by the discussion in Section 4.4.

PEIS measurements were performed on pyrex/graphene and ITO/graphene after mimicking the clean room wafer-scale fabrication process of electrodes[9]. Figures 4.19a,b shows the Bode plots for each electrode system at pH 7. In Figures 4.19c,d, we plot the capacitance of both systems extracted at 10 Hz[10], from PEIS performed at pH 3, 7 and 10 (Bode plots measured at pH 3 and 10 are depicted in the Annex B, Figure B.6). The dashed black lines in the C-V plots correspond to the capacitance values of the as-transfer samples. As for the as-transfer electrodes (see Figure 4.7), the pyrex/graphene electrode presents |Z| modulation with V, differently from the ITO/graphene. For the case of pyrex/graphene electrodes after fabrication, it is still possible to observe the modulation of C with V (see Figure 4.19d). However, the minimum of the curves is shifted towards negative voltages with respect to the as-transfer curve, and the shift slightly depends on the electrolyte pH. ΔCNP is larger at pH $\geq$ 7. This is attributed to the presence of charged residues, σ_{ads}, in graphene. Noticeably, as already observed in as-transfer samples (Figure 4.16b), the slope of the C curve at pH 3 is slightly lower than at pH 7 and 10. Interestingly, the ITO/graphene electrode system shows higher impedance (lower C values) than the as-transfer system (see Figure 4.7). We hypothesize that the residues and/or residual charge at the graphene surface may significantly influence water intercalation. According to this hypothesis, surface contamination could prevent intercalated water to contact the substrate and the bulk electrolyte.

An important aspect to be discussed when considering the Bode plots in Figure 4.19 is the phase behavior. For pyrex/graphene, a phase change (blue dashed line, not present in the as-transfer electrodes), is observed between 10^2 and 10^4 Hz, which is voltage-dependant, further analysed in Figure 4.20. For ITO/graphene, this phase change appears mostly between 10^2 and $2{\cdot}10^3$ Hz. The voltage dependency of the ITO/graphene case is lower, yet still significant, and inverted to the pyrex/graphene: positive V show less modulation than negative ones. The origin of this is attributed to an additional RC element at the system's equivalent circuit, which may be originated by charged residues remaining at the graphene surface after the fabrication process [217, 218].

[9]The preparation of graphene electrodes mimicking the fabrication process consists on: graphene wet transfer to the target substrate, graphene definition and passivation (see Section 2.4.2. Thus, no track metalization and second metal layer were performed here.

[10]C values were obtained using equation 4.11 with α=1.

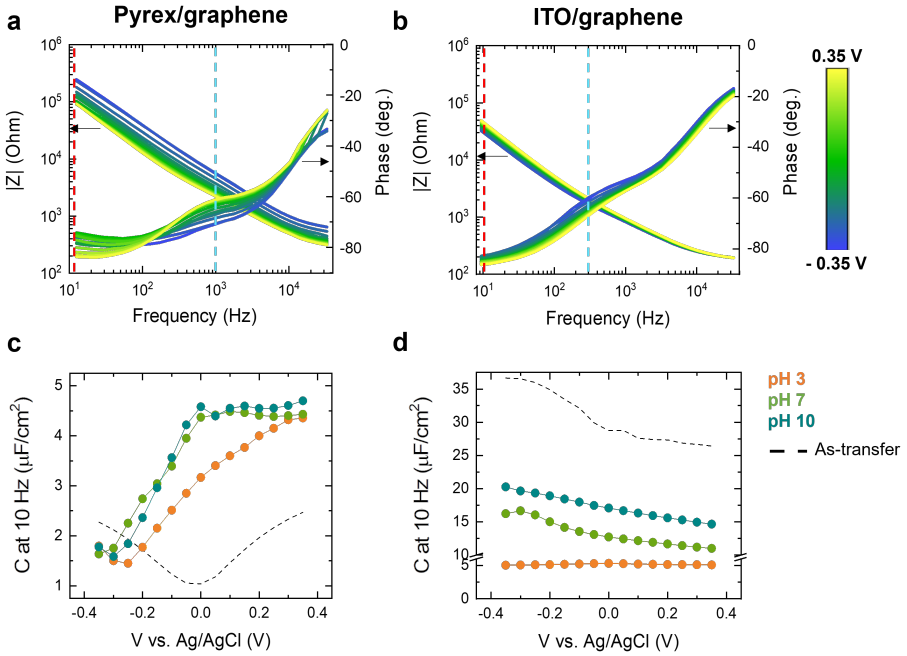


Figure 4.19: PEIS of graphene electrodes after fabrication to assess impact of contamination - **(a)(b)** Bode plots of pyrex/graphene and ITO/graphene electrodes after fabrication. Measurements in PBS, pH 7. **(c)(d)** C vs V extracted at 10 Hz. Dashed lines correspond to the measurements of as-transfer graphene electrodes.

Considering the pyrex/graphene system, Figure 4.20 shows the Bode representation, separating the impedance response in magnitude and phase. A clear phase change is observed, which shifts with pH. The pH-dependent phase change reveals the presence of a frequency range where the electrode has a clearly non-capacitive response, in particular at pH 3. The absence of this phase change in as-transfer graphene electrodes (see Figure 4.5) is an additional evidence of the fact that the pH sensitivity of graphene is originated by the charged residues on its surface.

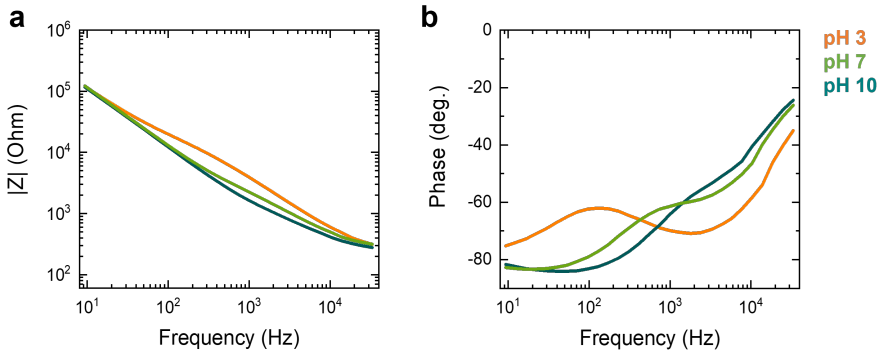


Figure 4.20: PEIS of a pyrex/graphene electrode after fabrication at different pH - (a)(b) |Z| and phase vs frequency of a pyrex/graphene electrode after mimicking the fabrication process at the clean room at pH 3, 7 and 10, at V = 0.3 V.

To test the hypothesis that charged residues, σ_{ads}, at the graphene surface affect electrochemical processes at the graphene-electrolyte interface, we focus the discussion in measurements at pH 7, where the phase change in PEIS is observed at higher frequencies and, thus, the analysis of the phase at low frequencies can be performed. Moreover, differences are noticed when comparing the phase of pyrex/graphene electrodes from the Bode plots of as-transfer and fabricated samples (see Figures 4.5a and 4.19a, for the Bode plots of as-transfer and fabricated samples, respectively). In Figure 4.21, the phase values at 10 Hz of pyrex/graphene electrodes before and after fabrication are plotted vs V. At this low frequency, the phase values that start deviating from 90° indicate charge transfer-related processes. Remarkably, the phase values at 10 Hz of the fabricated electrodes start decreasing (less similar to 90°) at higher V (∼0.35 V) than in the as-transfer electrodes, where the phase decrement is observed at ∼0.15 V. These indicate that surface residues lower the potential barrier at which these processes take place.

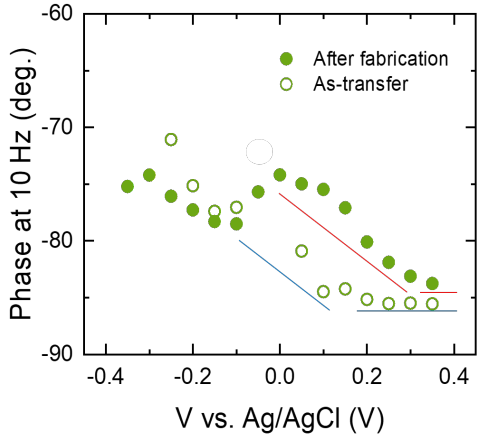


Figure 4.21: Pyrex/graphene phase modulation with voltage at 10 Hz from PEIS measurements - Phase values extracted from PEIS measurements (Bode plot in Figure 4.19a) at 10 Hz, where ORR starts being visible, for measurements in PBS pH 7 on as-transfer and fabricated graphene electrodes. Red and blue lines are a guide to the eye of the tendency of the phase values.

To complement the last PEIS results discussed, in the following we study the effect of surface charge (σ_{ads}) on graphene supported on pyrex and ITO by Raman spectroelectrochemistry. Raman maps on statistically representative areas of each sample were performed in liquid conditions (PBS) varying the electrolyte's pH. Samples were prepared as transfer and after mimicking the clean room fabrication process (see Section 2.4). As explained before, the energy of the G phonon of graphene (ω_G) is related to the Fermi level (E_F) according to equation 2.2. ω_G on clean graphene has a value of 1581.3 cm^{-1} on SiO_2/Si, with no voltage applied. This value depends on the substrate, on the presence of residues and on the applied voltage.

In Figure 4.22, the ω_G in as-transfer and after-fabrication electrodes (a, b, respectively) is shown for different electrolyte pH and ionic strengths. Due to the presence of σ_{ads} and in agreement with the PEIS experiments (Figure 4.19), the pyrex/graphene and ITO/graphene electrodes after fabrication present a CNP shift (ΔCNP) towards more negative voltages. ΔCNP is larger in ITO/graphene electrodes than in pyrex/graphene electrodes, thus indicating higher amount of σ_{ads} on the graphene surface in the case of ITO substrate. Nevertheless, the C_g extracted from these Raman measurements, that, as previously mentioned, can be related with the slope of the ω_G-V curves, is of the same order. As discussed in Section 4.3, similar C_g in the pyrex/graphene and the ITO/graphene electrodes indicates similar charge modulation of graphene in the two systems. Regarding pH response of the electrodes after fabrication, it is more noticeable in ITO/graphene

than in pyrex/graphene. These results indicate that the amount of residues on graphene after the fabrication process depends on the substrate, which is further confirmed in the following.

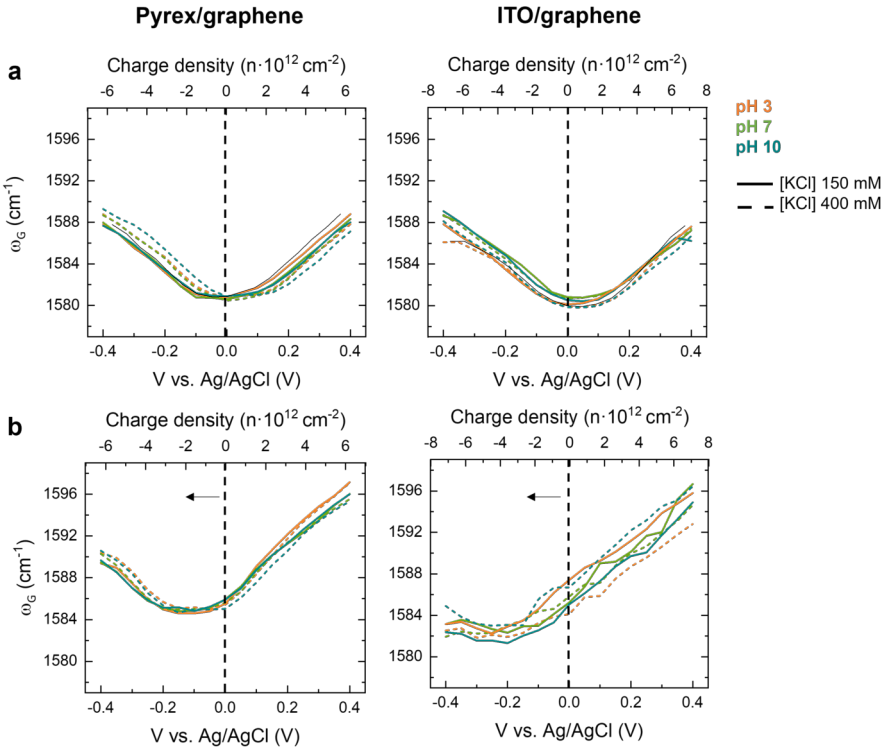


Figure 4.22: Raman spectroscopy of graphene electrodes - (a)(b) ω_G modulation with applied V for pyrex/graphene and ITO/graphene before and after mimicking the wafer-scale fabrication process, respectively. Each curve results from measurements at different pH (3, 7 and 10) and ionic strength ([KCl] = 150 mM and 400 mM).

An XPS study was conducted to assess the contamination introduced by the fabrication process. Figure 4.23a,b depicts the corresponding C 1s and O 1s core levels of the pyrex/graphene and ITO/graphene samples and the bare substrates, pyrex and ITO. Regarding that in the O 1s core level analysis the oxygen contribution is mainly related with the substrates, spectra were energy corrected with respect to the SiO_2, at 533.0 eV [219] for the case of pyrex samples and to the In_2O_3, at 531.0 eV for the case of ITO samples, and fitted as explained in Section F.4.

In pyrex/graphene, the analysis of the C 1s core level of the as-transfer sample shows the presence of four components, assigned to Csp^2 at 284.1 eV, which is the most intense contribution, Csp^3/C-H at 284.8 eV, C=O at 286.0 eV and

O-C=O at 288.4 eV. The Csp^2 contribution is mainly attributed to the presence of graphene and sp^2 coordinated amorphous carbon, in agreement with literature [220]. The rest of the assigned contributions are mainly attributed to the presence of amorphous carbon [221] and PMMA residues from the transfer process (see chemical structure of PMMA in Figure 4.17). The analysis of the C 1s core level of the fabricated pyrex/graphene sample presents four main contributions, assigned to the Csp^2, Csp^3/C-H, C=O and O-C=O. In this case, we attribute the presence of these contributions to PMMA and residues from the cleanroom fabrication process, e. g. the SU8 photoresist, used in the passivation step. Given that the compounds used in the graphene devices fabrication process, which are the source of the residues, are mainly composed by carbon and oxygen, and the exact chemical composition of all of them is not accessible, the XPS analysis here is semi-quantitative. Nevertheless, the increasing C:O intensity ratio, when comparing bare substrate, as-transfer sample and fabricated sample (see Figure 4.23c), is indicative of the increasing amount of carbon species at the surface, which is associated, in a first approximation, with the amount of graphene surface contamination.

In ITO/graphene, the deconvolution of the C 1s core level shows the same four contributions mentioned for the pyrex/graphene sample, mainly associated to amorphous carbon and PMMA residues. In the fabricated sample, similarly to pyrex/graphene, the amount of carbon species on the surface is increased, attested by the increase in the C:O intensity ratio (see Figure 4.23d). Analogously, this is associated to an increased amount of residues on the graphene surface, which is even more noticeable in the ITO/graphene samples than in the pyrex/graphene samples, as previously observed by Raman spectroelectrochemistry (Figure 4.22). Interestingly, the O 1s peak in the ITO/graphene case presents a noticeable change from the bare ITO and as-transfer ITO/graphene to the fabricated ITO/graphene sample. Although the main contribution of this peak is the substrate [222], the increasing contribution mainly assigned to C-OH confirm the increased presence of residues.

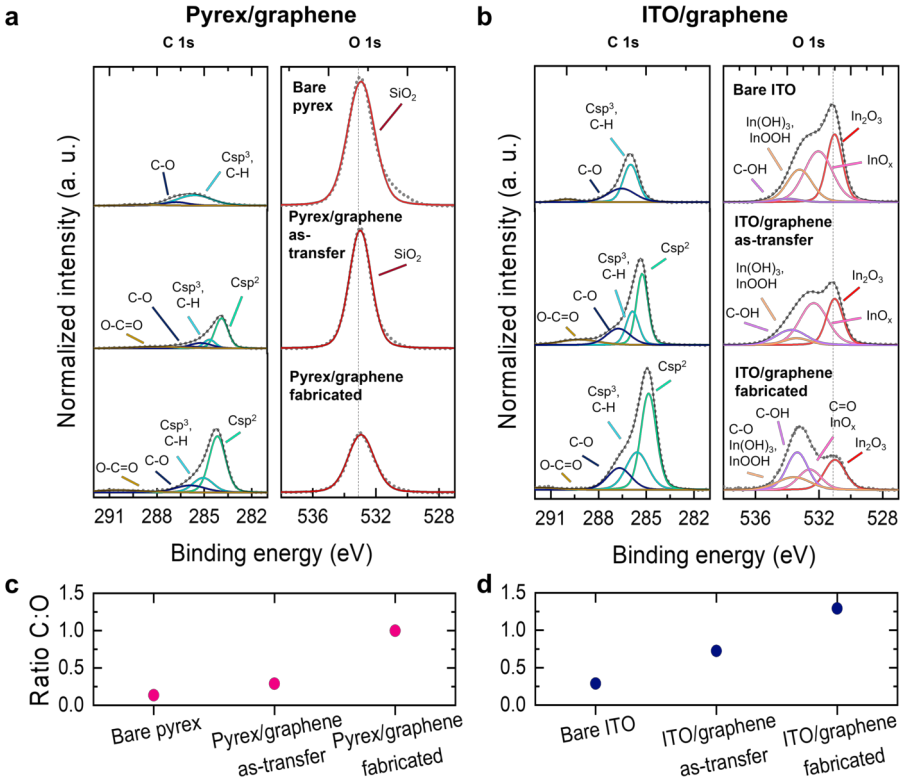


Figure 4.23: XPS analysis of graphene samples on different substrates - **(a)(b)** C 1s and O 1s peak deconvolution for pyrex/graphene and ITO/graphene, respectively. **(c)(d)** C:O ratio calculated in area of bare substrates, as-transfer and fabricated samples.

UPS (He-I, 21.2 eV) was performed to obtain the workfunction (ϕ) of graphene and to evaluate graphene doping induced by the surface residues. The measurements were performed under application of -10 V sample bias to shift the secondary electron background above the work function of the analyser. The procedure of Diaz et al. [223] was followed for work function calculation, knowing:

$$IP = 21.2eV - E_{cut-off} - E_{VB}^{F} \tag{4.23}$$

$$\Phi = IP - E_{VB}^{F} \tag{4.24}$$

where IP is the ionization potential, the $E_{cut-off}$ is the secondary electron cut-off and E_{VB}^{F} is the valence band edge. Table 4.2 summarizes the extracted values from the UPS analysis. IP and Φ values are in good agreement with reported

data for bare ITO, as well as for graphene on pyrex (insulating substrate) [224, 82] and graphene on ITO (n-type semiconductor substrate with a Φ very similar to pristine graphene) [225].

Table 4.2: Band structure extraction from UPS. Energy difference E^F_{VB} between the Fermi level and valence band maximum E_{VB}, secondary electron cut-off $E_{cut-off}$, ionization potential IP and work function Φ, extracted from UPS spectra of the graphene on pyrex and ITO, and of the bare ITO samples.

Sample	E^F_{VB} (eV)	$E_{cut-off}$-E^F_{VB} (eV)	IP (eV)	Φ (eV)
Pyrex/graphene	0	16.7	5.0	4.5
	0	16.1	5.9	5.1
ITO/graphene	0	16.7	4.5	4.5
	0	15.9	5.3	5.3
bare ITO	3	13.8	7.4	4.4

Table 4.3 presents the data related to these measurements (see Figure 4.24). The obtained ϕ values of graphene on the different substrates, pyrex and ITO, which is strongly affected by the type and strength of the substrate-graphene interaction, are in good agreement with literature [226]: being an insulator, pyrex is not expected to alter the graphene's ϕ, which has a reported value of 4.5 ± 0.1 eV [185]. ITO is an n-type semiconductor with a reported ϕ of 4.4 eV [227], which was also confirmed by our experimental measurements. When supported on ITO, the measured graphene's ϕ of 4.5 eV reflects low ITO-graphene interaction. Overall, the ϕ of the samples after fabrication increased (0.6 eV for graphene on pyrex and 0.8 eV for graphene on ITO), illustrating a p-doping due to the residues remaining on the graphene surface. The higher doping observed in the fabricated ITO/graphene surface is in good agreement with the XPS and Raman spectroelectrochemistry results commented above (see Figure 4.22).

Table 4.3: Workfunction values of graphene on different substrates obtained by UPS

Substrate	As-transfer	After fabrication	$\Delta\phi$
Pyrex	4.5	5.1	0.6
ITO	4.5	5.3	0.8

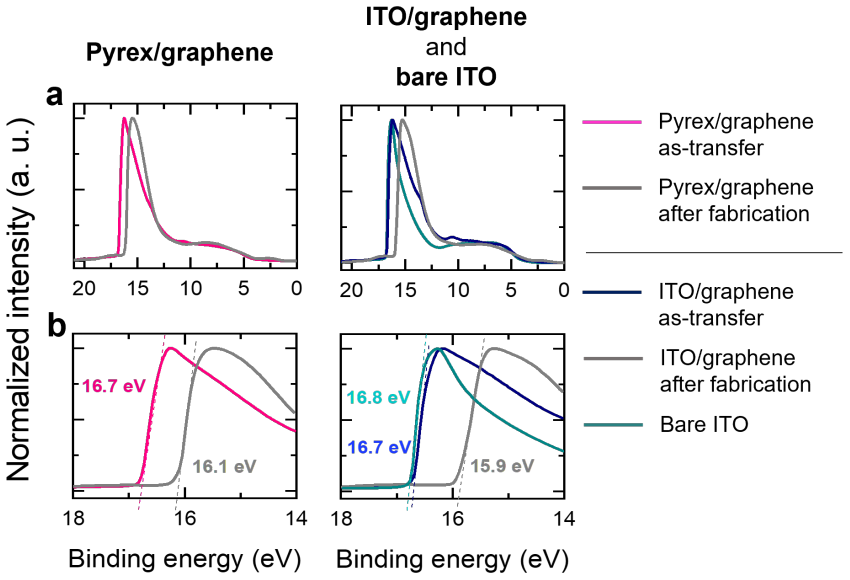


Figure 4.24: UPS analysis of graphene-based surfaces - **(a)** UPS spectra (He-I, 21.2 eV) and **(b)** the secondary electron edge ($E_{cut-off}$). The UPS spectra were corrected with respect to the valence band edges to avoid any charging effects due to the insulating pyrex substrate affecting the absolute position of the $E_{cut-off}$ and valence band edge positions.

Assessment of adsorbed charge on graphene electrodes

With the results discussed until this point, it is clear that fabrication residues impact the electronic properties of graphene electrodes. Considering the difficulty of achieving a completely clean surface after graphene devices fabrication and the challenge of ensuring wafer to wafer reproducibility, we decided to develop a non-destructive method to assess the presence of adsorbed charge, σ_{ads}, on graphene based on Raman spectroscopy. We focused this part of the discussion on the analysis of graphene on pyrex substrates, as pyrex is a non-conductive oxide that allows a clear analysis of the Raman spectra of graphene. Before discussing the experimental results, a brief explanation of the modelling of the graphene/electrolyte interface is provided.

In general terms, the graphene/electrolyte interface system is composed by the substrate, the graphene layer, the residues on graphene and the electrolyte. The charge balance at the graphene/electrolyte interface is described by the equation:

$$\sigma_{subs} + \sigma_{gr} + \sigma_{ads} + \sigma_{diff} = 0 \tag{4.25}$$

where σ_{subs}, σ_{gr}, σ_{ads} and σ_{diff}[11] are the charges attributed to the substrate, the graphene, the surface residues and the electrolyte, respectively. For the case of graphene supported on non-conductive substrates, σ_{subs} is considered a fixed charge. Theoretical modelling of the graphene/electrolyte interface as a function of ion concentration and pH is complex. Here, we use an approximation based on the model by Härtl *et al* [228], which considers the charge balance in equation 4.25 and is graphically represented in terms of potential and charge distribution in Figures 4.25a,b, respectively. When applying $V_{gs} < V_{Dirac}$, there is an electrostatic potential (φ) drop from the graphene surface. σ_{gr} is assumed to have a negative surface charge, according to the model [228, 229] and it drops to the negative surface potential (φ_{diff}), being $\Delta_{\varphi} = \varphi_{gr} - \varphi_{diff}$. The potential drop in the diffuse region is described by the model explained in the introduction of this chapter, and it reaches the potential of the reference electrode (φ_{ref}) in the bulk electrolyte. To fulfill charge neutrality, σ_{gr} and σ_{diff} have to compensate σ_{subs} and σ_{ads}[12]. In general, the charge carrier density in graphene can be expressed as:

$$\sigma_{gr} = C_g \Delta_{\varphi} = C_g(\varphi_{gr} - \varphi_{diff}) \tag{4.26}$$

where C_g is the capacitance of the inner Helmholtz plane (defined as the gate capacitance in equation 2.3, which, as introduced in Chapter 2, is an equivalent form of equation 4.26. Knowing the charge balance expressed by equation 4.25, for a certain σ_{ads}, σ_{gr} will depend on σ_{diff}.

[11] σ_{diff} is directly associated with the ionic concentration of the electrolyte and can be modeled by the so-called Grahame equation, in a first approximation [84].

[12] Considering that σ_{ads} is negative. For a positive σ_{ads}, the diagrams in Figure 4.25 should be modified accordingly.

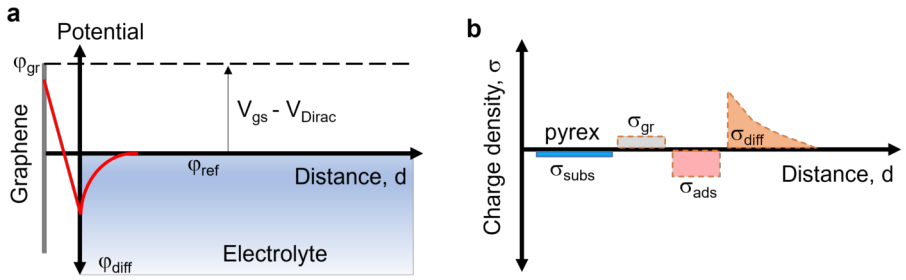


Figure 4.25: Potential and charge schemes of the graphene/electrolyte interface assuming a negative adsorbed charge - (a) Schematic potential profile of the interface when graphene is biased in the hole regime. **(b)** Corresponding charge profile of the interface when $\sigma_{ads} < 0$. The relative size of areas is an approximation and does not correspond to the relative size of charges. In the electron regime, the application of a $V_{gs} > V_{Dirac}$ results in a potential increment from φ_{gr} to the φ_{ref}, described analogously as the potential drop in the holes regime. A more detailed description of that can be found in [229]

As for changes in the electrolyte pH, we consider the approximation described by the equation [230]:

$$\sigma_{ads} \propto \frac{1}{1 + 10^{m(pK_a - pH)}} \tag{4.27}$$

where m is the heterogeneity index of a material, being approximated to 1 for a bare graphene surface [229]. Given that, the important outcome is that σ_{ads} depends on the electrolyte pH and the pKa of the residues on the graphene surface.

According to equation 4.26 and taking into account the relation between the graphene ω_G and the graphene surface potential, explained above, Raman spectroscopy was performed in an electrolyte environment with increasing ionic strength (adjusted by [KCl] in PBS) to calculate the amount of contamination-related charged species at the graphene surface. To this end, we prepared different pyrex/graphene samples: as-transfer electrodes (2 mm diameter), macroelectrodes (2 mm diameter) and wafer-scale electrodes (1 mm diameter). The macroelectrodes were prepared mimicking the cleanroom fabrication protocol, as previously explained; the electrodes were fabricated following the wafer-scale protocol detailed in Section 2.4.

Figures 4.26a,b present the ω_G shift, $\Delta\omega_G$, of graphene on pyrex when increasing the [KCl] of the electrolyte (PBS pH 7) for the different pyrex/graphene samples (as-transfer, macroelectrodes and wafer-scale). As expected, the ω_G and so the $\Delta\varphi_{gr}$ and the charge density remain invariable with ionic strength ([KCl]) variations for the as-transfer graphene. However, for the case of the

macroelectrodes and the wafer-scale electrodes, ω_G varies with [KCl]. Higher shifts ($\sim$8 cm^{-1}) are observed for the wafer-scale electrodes than for the macroelectrodes ($\sim$3.5 cm^{-1}), which following the discussion above, can be related to higher amounts of charged residues at the graphene surface. Specifically, a σ_{ads} of -5.39·10^{12} cm^{-2} and -2.36·10^{12} cm^{-2} are calculated using the model described above and assuming monovalent charges directly at the surface [231], for the wafer-scale electrodes and the macroelectrodes, respectively. The schematics in Figures 4.26c,d illustrate the charge balance in the substrate/graphene/electrolyte interface for this case. For low σ_{ads} (Figure 4.26c), changes in σ_{diff} result in small changes in σ_{gr}. Differently, for high σ_{ads} (Figure 4.26d), the same variation in σ_{diff} results in higher variation in σ_{gr} to maintain charge balance. From this analysis we can correlate the ω_G shift with a certain σ_{ads} value.

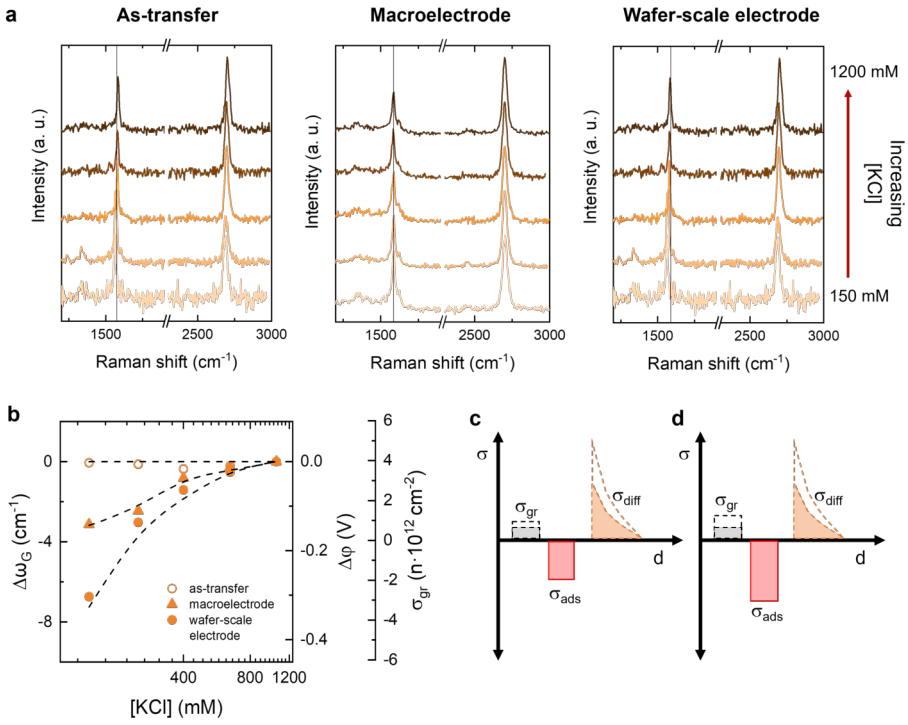


Figure 4.26: Graphene G band frequency vs electrolyte ionic strength - (a) Average Raman spectra from maps of 256 μm^2 for as-transfer, macroelectrode and wafer-scale electrode samples measured in PBS in increasing [KCl]. **(b)** $\Delta\omega_G$ as function of [KCl] in PBS pH 3 with different levels of σ_{ads}, in relation with the three samples studied. $\Delta\omega_G$ is related with $\Delta\varphi$ and σ_{gr} according to equations 4.18 and 2.3, respectively. Black dashed lines are the fitting of the values according to the model explained in the text. **(c)(d)** Scheme of charge distribution in the substrate/graphene/surface charge/electrolyte system and its variation with increasing ionic strength of the electrolyte for different amounts of σ_{ads} (low and high, respectively). σ_{subs} is not represented, as it is considered fixed for pyrex.

In Figure 4.27, the $\Delta\omega_G$ of the wafer-scale graphene electrode is evaluated vs [KCl] at different pH. According to the relation of the ω_G with the graphene Fermi level, the $\Delta\omega_G$ is positive or negative depending on the type of charged residues (positive or negative) at the graphene surface. The measured $\Delta\omega_G$ is shifted in opposite directions from low to high [KCl] for pH 3 and 10. At pH 7, a lower shift ($\sim$2 cm^{-1} with respect to the $\sim$8 cm^{-1} at pH 3 and 10) is measured. According to the model explained above, these shifts correspond to σ_{ads} of -5.39·$10^{-12}$$cm^{-2}$, -1.52·$10^{-12}$$cm^{-2}$ and 5.90·$10^{-12}$$cm^{-2}$ at pH 3, 7 and 10, respectively. These differences confirm that the amount of positive and negative charge on graphene is different, in agreement with the possible different types of residues that may remain after fabrication.

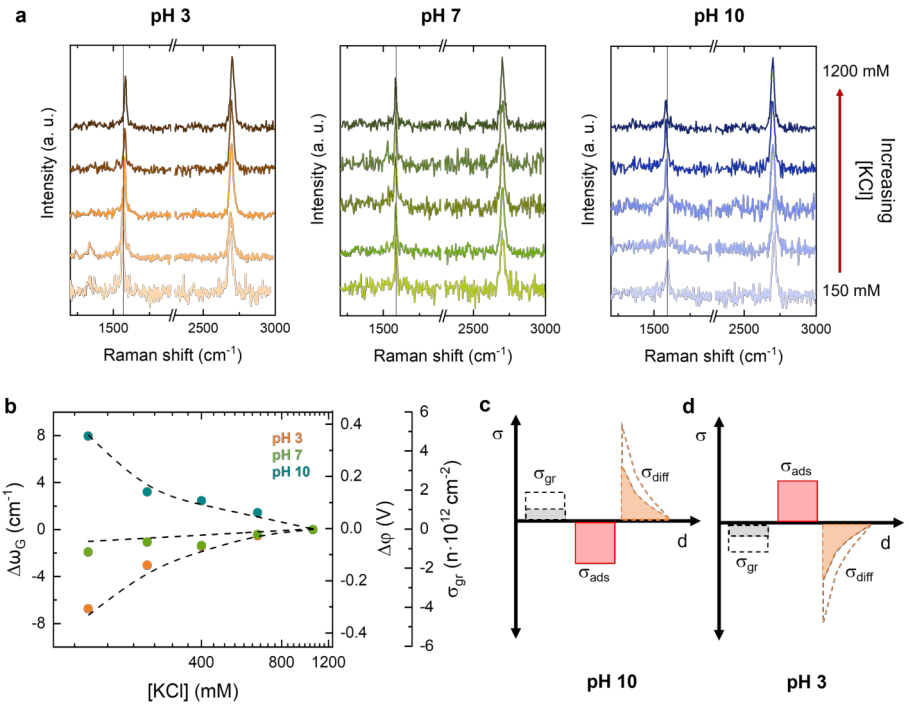


Figure 4.27: Raman spectroscopy of wafer-scale graphene electrodes at different electrolyte pH with increasing [KCl] - (a) Average Raman spectra measured in PBS from maps of 256 μm^2. **(b)** $\Delta\omega_G$ as function of [KCl] at different pH of wafer-scale pyrex/graphene electrodes. $\Delta\omega_G$ is related with $\Delta\varphi$ and σ_{gr} according to equations 4.18 and 2.3, respectively. Black dashed lines are the fitting of the values according to the model explained in the text. **(c)** Scheme of charge distribution in the pyrex/graphene/surface charge/electrolyte system and its variation with the electrolyte pH. σ_{subs} is not represented, as it is considered fixed for pyrex.

Figures 4.27c,d schematically represent the charge balance at the substrate/graphene/electrolyte system depending on the pH. At basic pH, in absence of applied voltage, σ_{gr} is considered positive, as the charged groups at the surface are deprotonated. Differently, at pH 3 (acidic pH), the charged species are protonated, which agrees with a negative σ_{gr}. Increasing σ_{diff} (by adjusting [KCl]) affects σ_{gr}: increasing it to maintain the charge balance established by equation 4.25.

Results depicted in Figures 4.26 and 4.27 correspond to the case of pyrex/graphene, where σ_{subs} is considered invariable with applied voltages. However, when the substrate underneath graphene is conductive, σ_{subs} contribution to the global charge of the system can change. Hence, in conductive substrates/graphene systems, it is not possible to apply the same analysis based on Raman spectroscopy for the study of σ_{ads}. This is visualized in Figures 4.28a,b, where we show the $\Delta\omega_G$ with increasing [KCl] when supported on pyrex and ITO, in as-transfer and fabricated electrodes. It is noted that, while $\Delta\omega_G$ modulation is observed for fabricated pyrex/graphene systems, negligible variations in the $\Delta\omega_G$ with [KCl] are measured for all the ITO/graphene cases. Given that previous XPS and UPS analysis proved the presence of residues on the ITO/graphene fabricated samples, one may expect the analogous $\Delta\omega_G$ modulation than in pyrex/graphene. However, as visualized in the schematics in Figures 4.28c,d, the σ_{subs} of a conductive substrate plays a role in compensating the charge induced to the substrate/graphene/electrolyte system by changes in σ_{diff}.

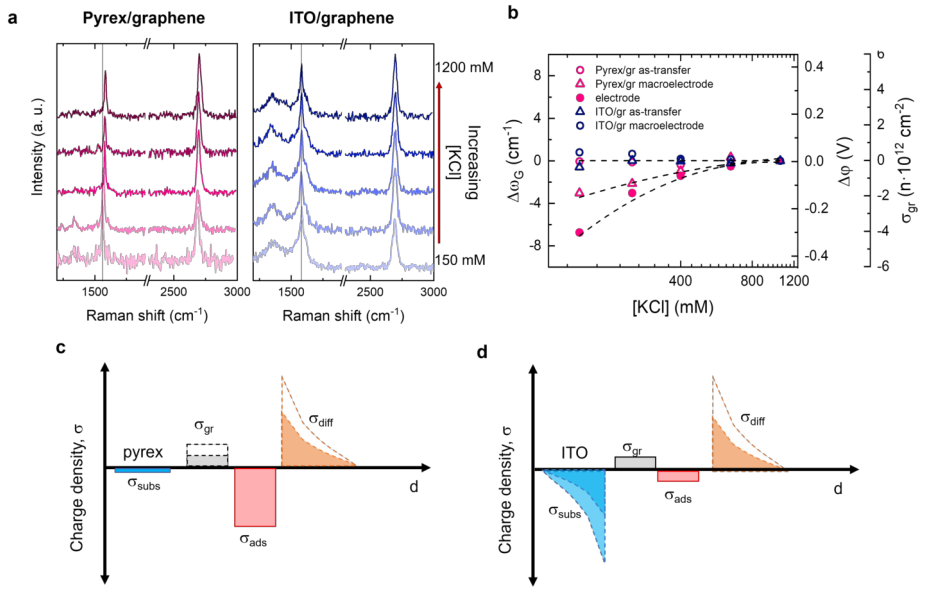


Figure 4.28: Raman spectroscopy of pyrex/graphene and ITO/graphene electrodes with increasing [KCl] - **(a)** Average Raman spectra measured of graphene macroelectrodes in PBS pH 3 from maps of 256 μm^2. **(b)** Graphene $\Delta\omega_G$ as function of [KCl] at a fixed pH (3) on pyrex and ITO substrates. $\Delta\omega_G$ is related with $\Delta\varphi$ and σ_{gr} according to equations 4.18 and 2.3, respectively.Black dashed lines are the fitting of the values according to the model explained in the text. **(c)(d)** Charge distribution scheme of the substrate/graphene/surface charge/electrolyte system and its variation as a function of electrolyte's ionic concentration (σ_{diff}) when graphene is supported on pyrex (non-conductive) and ITO (conductive), respectively.

The above-discussed results provide insight on the quantification of adsorbed charge on graphene. Remarkably, these results shed light to the existing controversy about graphene's pH sensitivity, confirming that graphene sensitivity to pH is originated from the charged residues on its surface rather than from the graphene itself, in agreement with reported studies [212, 230, 232].

4.5.1 Monitoring of wafer-scale fabrication residues on graphene electrodes

The above-presented methodology, based on Raman spectroscopy, for the assessment of σ_{ads} is useful when graphene is on insulating substrates. Thus, we can use it for the evaluation of the degree of residual charge on graphene during the fabrication, facilitating the optimization of the process towards a cleaner fabrication. In principle, all fabrication processes involving the use of resins can result in charged residues on the graphene surface. Huge efforts have been

devoted to the optimization of the graphene transfer towards a cleaner procedure. However, the complete removal of the residues from the fabrication is still highly challenging, so it is the complete removal of the PMMA remaining after graphene transfer. For that reason, it is also crucial to evaluate the fabrication process effect on graphene.

To monitor the amount of residues introduced by each step of the fabrication process, we conducted a systematic characterization using Raman spectroscopy. For that, graphene was transferred on two pyrex wafers, each divided in two parts each. A different fabrication step was performed in each half wafer (see Figure 4.29):

- **1: Graphene transfer:** graphene transfer from the growth substrate to the wafer following the wet transfer method detailed in Section 2.4.1.
- **2: Graphene definition:** protection of the graphene at the electrode's active area (channel) and subsequent etching of the graphene placed out this area with an ICP-RIE step (see Section 2.4).
- **3: 2nd metal evaporation:** evaporation of a Ni/Au layer using electron-beam (see Annex F.1.1) followed by a lift-off.
- **4: Passivation:** SU8 passivation (see Section 2.4).

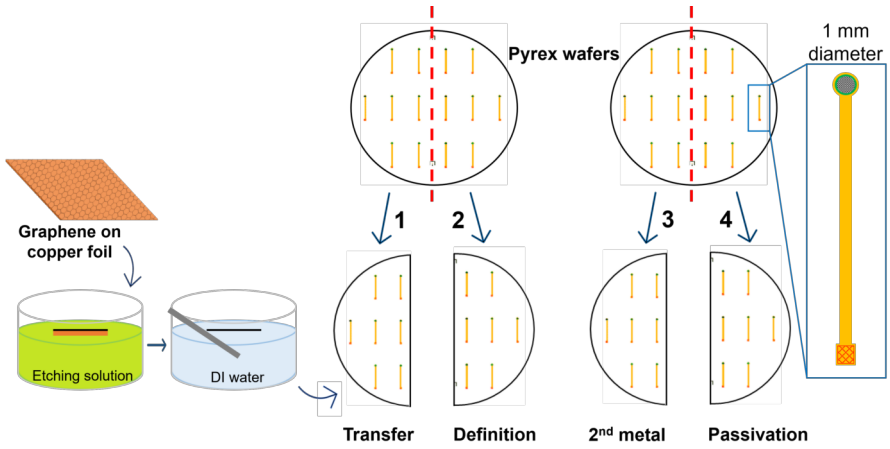


Figure 4.29: Schematics of sample preparation for the assessment of the impact of fabrication residues on graphene's electronic properties - CVD graphene grown on Cu foil is transferred to each half of the pyrex wafers. In 1, only transfer is performed. In 2, process continues until graphene definition. The process in 3 stops after the deposition and lift-off of the 2nd metal layer. In 4 the fabrication is performed completely, as its last step is the passivation.

Raman spectroscopy was performed in PBS varying the ionic concentration, [KCl], of the electrolyte at a fixed pH (10). As previously discussed, ω_G on clean graphene has a value of 1581.3 cm^{-1}, depending on the substrate. With the presence of residues on graphene, this value may vary indicating either holes or electrons doping (negative or positive charge). Figure 4.30a shows the G band frequency of graphene with increasing electrolyte [KCl]. As previously observed, as-transfer graphene presents the lowest ω_G value, which is close to 1581.3 cm^{-1}, indicating a low amount of adsorbed charge. Differently, after the graphene definition step the ω_G reaches 1590.1 cm^{-1} at the lowest [KCl]; the first value is not changed after the second metal deposition. Finally, after passivation, a significant dispersion of ω_G, ranging from 1582.8 cm^{-1} to 1586.0 cm^{-1}, is observed (Figure 4.30b depicts the 3 measured electrodes after passivation, to visualize the differences in these 3 electrodes). This dispersion is indicative of device-to-device doping inhomogeneity: solvents used during passivation could be able to remove previous residues, but not homogeneously in different parts of the wafer. On an electrode after the passivation step, we then performed the Raman spectroscopy measurements in different [KCl] varying the electrolyte pH. Figure 4.30c shows the measured $\Delta\omega_G$ modulation with [KCl] (pH 3-10). A higher $\Delta\omega_G$ modulation is observed at extreme pH (3 and 10), in agreement with the presence of charged species. As previously explained, observation of the up and down shifts of ω_G with increasing [KCl] for varying pH is related with functional groups on the graphene surface that are protonated or deprotonated depending on pH.

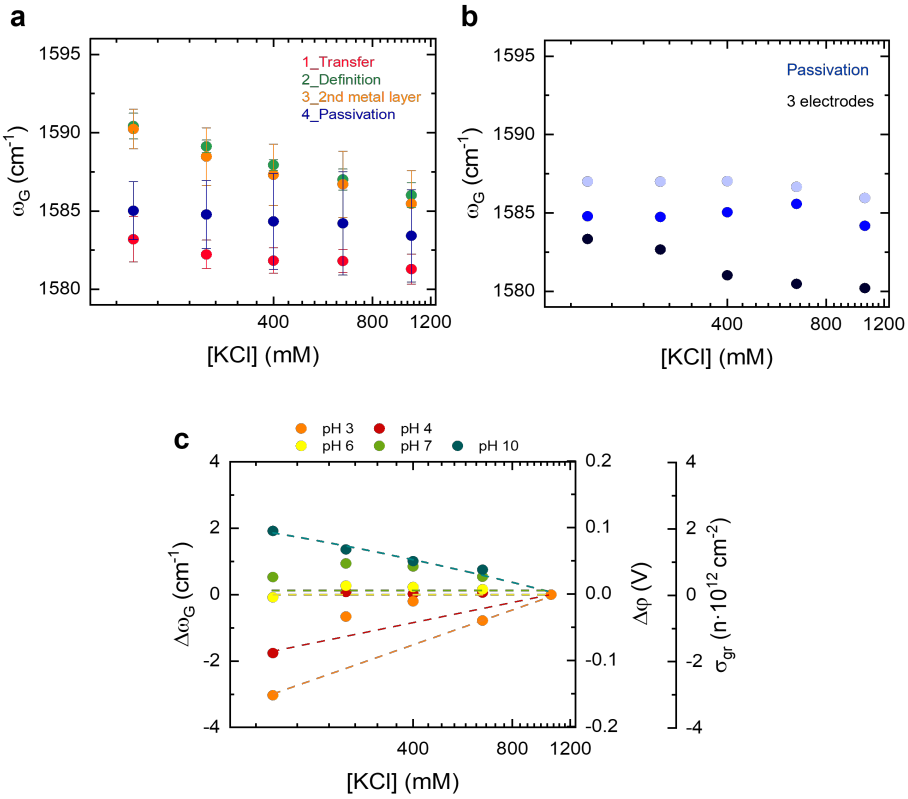


Figure 4.30: Impact of the fabrication on graphene assessed by Raman spectroscopy - **(a)** Graphene ω_G variation with [KCl] in PBS pH 10 from maps of 256 μm^2. n = 3 electrodes. **(b)** Zoom in the ω_G vs [KCl] results of the three electrodes after the passivation step (4th sample in Figure 4.29). **(c)** $\Delta\omega_G$ modulation with pH for finalized graphene electrodes. $\Delta\omega_G$ is related with $\Delta\varphi$ and σ_{gr} according to equations 4.18 and 2.3, respectively. Dashed lines are the fitting of the values according to equation 2.3.

Alternative strategy for the wafer-scale fabrication of graphene devices

To minimize the device-to-device and batch-to-batch inhomogenety resulting from contamination induced by fabrication, many reported efforts have been put to achieve a complete residues-free transfer process [123, 124, 233, 234]; yet, this is far from being successfully accomplished in a reproducible, high-scalable way without leading to graphene degradation [235, 232]. In parallel, researchers have been exploring methods to protect the graphene surface throughout the devices fabrication process. These strategies rely on the use of sacrificial layers, typically metallic, deposited on graphene and removed at the final step of the process; for

instance, titanium (Ti) and yttrium (Y) deposited on graphene at the beginning of the fabrication process have demonstrated to preserve its surface clean [168, 50, 236]. However, these strategies present important drawbacks, for instance, in the case of Ti, it requires the use of hydrofluoric acid, which is incompatible with oxide substrates; in the case of Y, its low availability and high price are certainly relevant issues. More recently, the use of aluminium (Al) as a graphene protection layer has been reported [237, 238]. However, the complete removal of Al was not fully demonstrated, thus potentially introducing undesired metallic doping at the graphene sheet, as well as structural defects [238]. In the following, we propose a not yet reported approach - to the best of our knowledge - to keep the graphene surface clean from fabrication residues, as well as to improve device homogeneity: the use of a sacrificial Cu layer. Cu is already used for graphene growth and etched away as part of the fabrication in the transfer step. Hence, it is attractive to consider the use of Cu to protect graphene in this alternative fabrication approach. However, the adoption of this new fabrication strategy requires a series of considerations, discussed here. The new fabrication procedure, in comparison with the standard protocol, is presented in Figure 4.31.

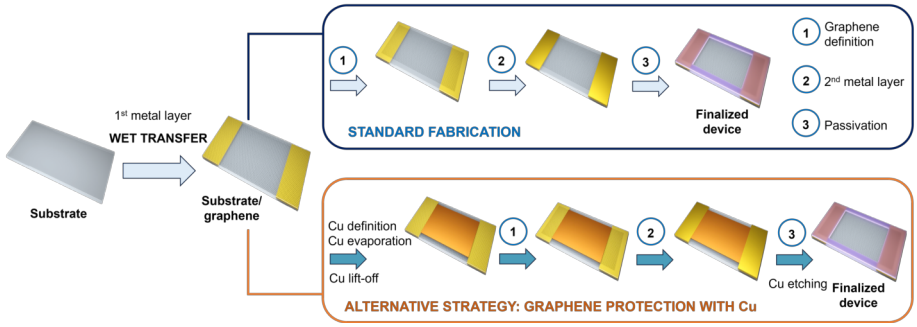


Figure 4.31: Schematics of the fabrication of wafer scale graphene devices - Fabrication steps followed for the preparation of the two wafers conforming this study: for the first wafer, we followed the standard AEMD fabrication protocol (fair blue arrows). For the second wafer (dark blue arrows), we incorporated a Cu sacrificial layer after transferring the graphene to protect its surface throughout the process. The Cu layer was removed using ammonium persulfate at the end of the process.

In the first place, **Cu deposition conditions**, i. e. e-beam evaporation rate and thickness, had to be determined. Based on what is explained in Chapter 3, Cu was deposited at 6-8 Å/s. To ensure a complete protection of the graphene layer, the Cu layer thickness was of 200 nm. As future work, this thickness is planned to be reduced while still ensuring complete protection. Secondly, **Cu etching** was optimized. Cu etching was performed chemically using ammonium persulfate,

$(NH_4)_2S_2O_8$ (0.02 g/ml)[13]. Etching using $FeCl_3$/HCl, which is employed in the transfer process (see Section 2.4.1), was observed to damage graphene in this case. The evaluation of the Cu etching time was carried out by electrochemical analysis (cyclic voltammetry, CV) and XPS, as presented in Figure 4.32, on fabricated graphene macroelectrodes. The CV study show that the peaks corresponding to Cu oxidation (reduction) to Cu^{2+} (Cu) [240] are not present after 7 min immersion in $(NH_4)_2S_2O_8$. Moreover, the XPS analysis of the Cu 1s region confirms the absence of the Cu peak (∼933) eV after etching.

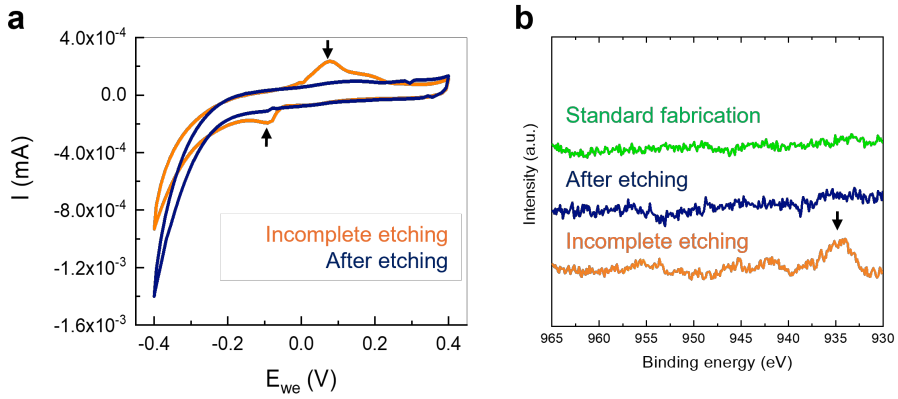


Figure 4.32: Assessment of the effectiveness of the Cu etching with ammonium persulfate - **(a)** Cyclic voltammetry of a graphene electrode (Si/SiO_2 substrate) fabricated with a Cu sacrificial layer before and after Cu etching by immersion in $(NH_4)_2S_2O_8$, 7minutes. Arrows indicate the Cu reduction/oxidation peaks. CV measured in PBS. **(b)** XPS Cu 1s spectra of a graphene electrode before and after Cu etching, and of a graphene electrode fabricated with the standard protocol. The dashed line serves as reference of the metallic Cu 1s peak (∼933 eV).

Finally, regarding the **integration of the Cu protection strategy to the standard fabrication protocol**, two main challenges were identified. The discussion of these challenges, strongly related with the Cu etching, is provided in the Annex B.

To assess the Cu protection effect on the fabrication of graphene devices, we prepared g-SGFETs on two different SiO_2/Si wafers. The first wafer was prepared following the standard fabrication explained in Section 2.4. In the second wafer we evaporated Cu (200 nm) after the graphene transfer and a Cu definition step, and continued following the fabrication protocol (see Figure 4.31). After the passivation step and subsequent SU8 removing, the Cu layer on graphene was wet-etched ($(NH_4)_2S_2O_8$ 0.02 g/ml). Figures 4.33a,b show the Raman ω_{2D} vs ω_G plots, used to account for the strain/doping level of graphene, before and after

[13]Based on previous studies performed in the group [239].

fabrication with the standard and the Cu protection protocols. As previously explained, strain and doping can be differentiated according to the slope along which the scattered data is distributed (see Section 2.5.1). As-transfer graphene (black data) shows a well distributed tendency along a linear function of 2.2 slope, indicating absence of doping and a slight strain gradient, in relation with its coupling with the substrate [241]. After standard fabrication, graphene presents larger dispersion and an increment of the doping level ($5{\cdot}10^{12}$ cm^{-2}) reflected by the data being distributed along a linear function of 0.7 slope. This confirms the observation that the different resins used in the fabrication process leave charged species remaining at the graphene surface in a non-controlled and inhomogenous way. Differently, after fabrication using a Cu protective layer, the ω_{2D} vs ω_G data shows a distribution similar to the one observed for as-transfer graphene. The main effect of the use of Cu is a slight variation in the strain level of graphene ($< 3\%$), that can be attributed to a change in the substrate-graphene coupling, giving the different stiffness of the Cu layer.

To test the devices sensitivity to pH comparing the two fabrication protocols, standard and with the Cu protective layer on graphene, Raman maps were measured in PBS at different pH. In Figures 4.33c,d, the ω_G measured from the graphene transistors is plotted vs pH. The standard fabrication protocol induces significant device-to-device dispersion of the ω_G (Figure 4.33c), as two of the three transistors measured presented pH sensitivity. To investigate the distribution of the σ_{ads} along the device, a map plotting the $\Delta\omega_G$ of the pH measurements performed in 22 transistors is depicted in the Annex B (Figure B.13), and reveals a random distribution of the σ_{ads}, thus confirming device-to-device dispersion. However, after fabrication with Cu protection, the dispersion is reduced (Figure 4.33d), as a more homogeneous response to pH is measured. Particularly, in two of the three transistors, a negligible pH response is detected (Figure 4.33d). These observations confirm that graphene sensitivity to pH can not be attributed to clean graphene, but to the charged species on its surface and that the use of a Cu protection layer preserves graphene surface from charged contaminants along the fabrication process, enhancing device-to-device homogeneity. The electrical characterization of g-SGFETs can be found in the Annex B.

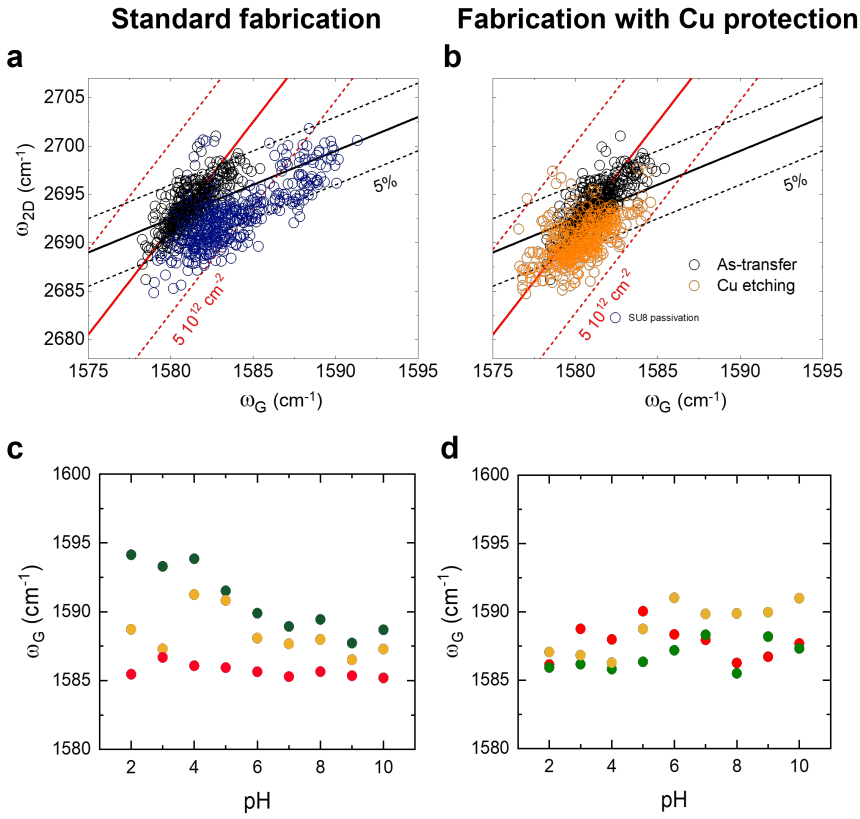


Figure 4.33: Characterization of graphene surfaces on devices fabricated with and without Cu protection - Raman ω_G-ω_G correlation maps of graphene transistors before (black data) and after fabrication using **(a)** the standard protocol and **(b)** a Cu protection layer. Measurements performed in dry conditions. **(c)(d)** Sensitivity to pH assessed by Raman spectroscopy (ω_G vs pH) of graphene surfaces on transistors fabricated without and with Cu protection layer, respectively. n = 3 channels.

5

Graphene functionalization towards a universal biosensing platform based on graphene/pyrene surfaces

The last part of the PhD dissertation is dedicated to study the interface created between graphene and molecules, aiming for applications in the biosensing field. Biosensors are fundamental devices in medicine, being capable to measure biochemical reactions and translate them into signals that can provide information about the concentration of a certain compound - analyte - involved in the reaction. Biosensors are nowadays widely used for diagnosis, disease monitoring and drug discovery among other analytical, biomedical-related applications. Since the beginning of the 20th century, when their basic principle was first reported (M. Cremer, 1906 [242]), biosensors have continuously evolved in alignment with scientific advancements, improving either detection capabilities and information processing. As explained further below, devices based on graphene are currently being explored as promising biosensors.

In this chapter, we highlight the importance of a controlled and reproducible graphene functionalization to develop specific, sensitive and stable biosensors,

with the ultimate aim to integrate them in the next generation of neural implants. In that line, the specific objectives are:

1. To demonstrate the feasibility of a dry graphene functionalization approach with 1-pyrenebutyric acid (PBA).
2. To quantitatively characterise the graphene/PBA platform by combining different experimental techniques.
3. To evaluate the impact of the functionalization on the performance of graphene SGFETs.

5.1 Graphene devices for biosensing applications: g-SFETs

As introduced earlier in this thesis, the use of graphene for biomedical applications has promising perspectives. Among them, graphene-based neural implants have demonstrated to be suitable for brain activity recording [29, 31, 30, 243]. This not only provides deeper understanding on the intriguing mechanisms of the human brain, but also fosters the development of more advanced diagnostic tools. Moreover, graphene-based neural implants have demonstrated their efficacy in stimulating neural structures [244, 245], which contribute to the advancement of new therapeutic treatments of diseases affecting both the central or peripheral nervous systems. The functionality of the next generation of neural implants goes beyond recording and stimulation of brain activity and aims to incorporate drug delivery and *in situ* biosensing of biomolecules functionalities [53, 246, 247].

In general, a biosensor is composed by three parts: a **biological part**, which is the tissue or the biological media from where the parameter of interest is located, a **transducer**, or material that translates the signal from the biological part and the **electronic part**, which is engineered to make the signal comprehensible and measurable by the user.

Prior to the experimental isolation of graphene in 2004 [5], carbon nanotubes (CNTs) were extensively studied as biosensors, and they have continued being studied [248, 249, 250]. However, during the last years, graphene has demonstrated great potential as a transducer in biosensing devices thanks to its outstanding electronic properties, combined with its transparency, flexibility, biocompatibility and high surface to volume ratio [75]. Particularly, this last characteristic is key for the enhancement of a sensor's sensitivity. The first use of graphene as a biosensor is reported in literature in 2008 [251]. In contrast to CNTs, graphene provides easier integration in bulk electronic devices. CNTs are characterized by

being distributed in an anysotropic way at the biosensor active area, as they can interact vertically and horizontally among them, and thus are difficult to control, which is not happening in a bidimensional material like graphene [252]. On top of that, CNTs have been classified as a material with suspected toxicity for human health, thus raising concern about their applications in biomedicine [253, 254, 255]. Graphene-based biosensors are based on electrodes [256] or on field-effect transistors, and they rely on the electrochemical detection approach [257].

5.2 Graphene functionalization strategies

Despite the above-mentioned properties that make graphene suitable for biosensing, graphene is not selective to specific analytes. It is for this reason that functionalization of graphene surface needs to be carried out for it to be used as a biosensor. Once functionalized with biomolecules, graphene's applications perspectives cover a wide range of fields [258, 259, 260, 261]. For instance, in electronics, functionalization of graphene enables the tunability of its band structure, offering band-gap engineering. This may be of high interest to develop microelectronic devices requiring graphene with an electronic band-gap. Moreover, as a result of functionalization, graphene's work function can be tuned [262, 226]. This can be used for the fabrication of n-type or p-type semiconductors. Functionalization of graphene may as well modify not only its electronic, but its mechanical properties, which enable the fabrication of nanodevices with an outstanding combination of these properties for a specific kind of application [263, 264]. In the particular case of biosensing, in which we focus, graphene functionalization with biomolecules is crucial to enable sensing specificity and enhance sensitivity. In the following, the discussion of the state of the art of graphene functionalization will be focused on the biosensors field.

Functionalization of graphene can be achieved covalently or noncovalently [51]. Both approaches constitute a challenging and interesting matter of study, theoretically and experimentally. By covalent functionalization, graphene's extended π-conjugation is altered, which does not happen in noncovalent functionalization [258, 265, 78]. Choosing one or the other approach will depend on the specific requirements of the final application. In this PhD dissertation, noncovalent functionalization is used in order to maintain graphene's electronic properties unaltered.

5.2.1 Noncovalent functionalization of graphene: pyrene derivatives

Noncovalent functionalization of graphene can be based on ionic interactions [266], hydrogen bonding [267], van der Waals forces [268] or $\pi - \pi$ interactions (between the graphene's electronic π system and the one from the molecule of interest), being the two latter the most spread ones. In view of that, graphene can be functionalized with a variety of biomolecules, polymers, drugs, metals and metal oxide-based nanoparticles, quantum dots, magnetic nanostructures, other carbon allotropes (fullerenes, carbon nanotubes), and even graphene analog (MoS_2,WS_2) [52]. Typically, van der Waals forces are developed between graphene and organic molecules or hydrophobic polymers. On the other hand, $\pi - \pi$ interactions are common between graphene and molecules with short to highly extended π system.

The strength of a π-π interaction is lower than a covalent bond [**wetzl_covalent_2023-1**] and it depends on the combined effect of attractive and repulsive forces between graphene and the specific countermolecule. Nevertheless, theoretical studies have proved that these π-interactions have a great effect in tuning the properties of a nanosystem [52]. Particularly, when functionalizing graphene with an organic molecule, the strength of the resulting π-π interaction may be affected by the size of its π system and the functional groups conforming the molecule, which may act as electron donors or acceptors. Pristine graphene demonstrates stronger interaction with small aromatic molecules, due to its extended aromatic system. Pyrene (see Figure 5.1a) is a small molecule composed by four benzene rings, thus constituting a flat aromatic system capable of strongly interaction with the π system of graphene [269]. Pyrene derivatives (see Figure 5.1b for an example, further detailed in the next section), which are organic molecules composed by a pyrene unit and other functional groups, offer interesting possibilities when combined with graphene, as they can tune graphene's electronic properties and can also induce selectivity and specificity towards molecular recognition, which is fundamental for biosensors [270].

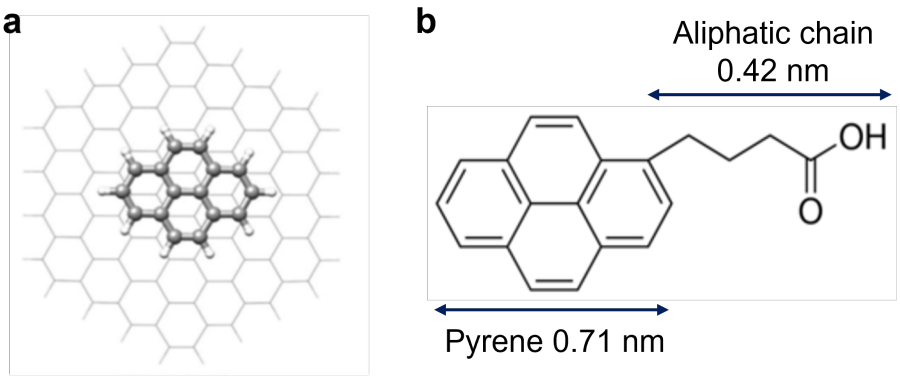


Figure 5.1: Pyrene and 1-pyrenebutyric acid - **(a)** Schematic of a pyrene molecule on graphene. From [269]. **(b)** Chemical structure of a 1-pyrenebutyric acid (PBA) molecule, a pyrene derivative.

5.2.2 Graphene functionalization with 1-pyrenebutyric acid

1-pyrenebutyric acid (PBA) is an organic molecule composed by an aromatic part and an alyphatic chain of 4 carbons ended with a carboxylic acid group (Figure 5.1b). The aromatic system of PBA is pyrene, which allows a π-π interaction with graphene, as previously explained. On the other hand, the alyphatic chain allows the covalent interaction with any other molecule capable to create a bond with the carboxylic group. Hence, PBA on graphene can act as a linker between the bidimensional material with other molecules of interest.

A number of publications have reported the use of PBA-functionalized graphene for sensing applications [271, 272, 273, 274, 56]. However, despite the relevance of the topic, there is still a lack of understanding the graphene/PBA interface. Reported functionalization methods do not present a complete functionalization control, neither a quantification of the amount of the PBA layers on graphene, which is of paramount importance for the development of biosensing devices based on graphene/PBA.

Up to date, most of the reported studies on graphene functionalization with PBA or PBA-derivatives are based on a liquid functionalization strategy, to the best of our knowledge [275]. This basically consists on having the graphene in contact with a solution containing the dissolved PBA molecule and incubate it during a certain time, waiting for graphene and PBA to interact. Afterwards, graphene is removed from the solution and a cleaning step is performed to remove any excess of PBA. Despite being widely used, the liquid-based functionalization presents several drawbacks. First, 1-pyrenebutyric acid's solubility in aqueous solvents is limited. Hence, sometimes organic solvents (e.g. dimethyl sulphoxide,

DMSO) may be needed to enhance its dissolution, which can result in undesired doping, as well as in changes in graphene's morphology. Furthermore, selective functionalization in a specific area of the electronic devices is difficult to achieve by the liquid-based functionalization strategy. Finally, it is very challenging to have reproducibility and high control using the liquid-based functionalization.

To overcome the mentioned disadvantages, we propose an alternative method based on the sublimation of 1-pyrenebutyric acid in high vacuum. By means of the vacuum-based functionalization, we avoid the graphene to be in contact with any type of liquid during the process. Furthermore, by the enabled tunability of the deposition parameters, we allow high control of the deposition of PBA on graphene, which is key for an optimal device design. Finally, the vacuum-based functionalization enables a facile selective functionalization. In the following sections, the results obtained regarding the optimization of the graphene functionalization with PBA with the proposed approach are presented and discussed, the quantification and characterization of the resulting interface is performed and, finally, the evaluation of the performance of the functionalized devices is conducted.

5.3 PBA sublimation for graphene functionalization

First, the viability of PBA sublimation was tested by Differential Scanning Calorimetry (DSC)[1], as presented in Figure 5.2. The DSC measurement consisted on placing a small amount of PBA, a solid powder in ambient conditions, as shown in Figure 5.2c, inside a sample cell and vary the temperature of the cell, first heating and then cooling it at 20°C/min and heating and cooling again at 50°C/min, while monitoring the heat flow. Heat flow changes vs temperature can be then associated with phase transitions of the material under study [276]. In particular, the glass transition temperature (T_g) is a thermodynamical parameter that indicates the temperature at which a molecule changes from a glassy (hard) state to a rubbery (soft) state. Often, the T_g is associated with the melting temperature (T_m) of a small organic molecule. Figure 5.2a,b depicts the results of the Differential Scanning Calorimetry experiment. When performing the first heating ramp, two melting points are visible (marked with arrows in Figure 5.2b). After the second heating ramp, only one melting point appears. The two cooling ramps showed one crystallization point each (Figure 5.2a), meaning PBA crystallizes after each heating-cooling series. In view of that, it is confirmed that,

[1] PerkinElmer 7 DSC. Javier Rodriguez-Viejo's group (ICN2-UAB).

after a first heating ramp up to > 187°C and subsequent cooling, a crystalline pellet of PBA is formed (see Figure 5.2d), which can be used for sublimation multiple times. These results confirmed the usability of the compound for our proposed functionalization approach.

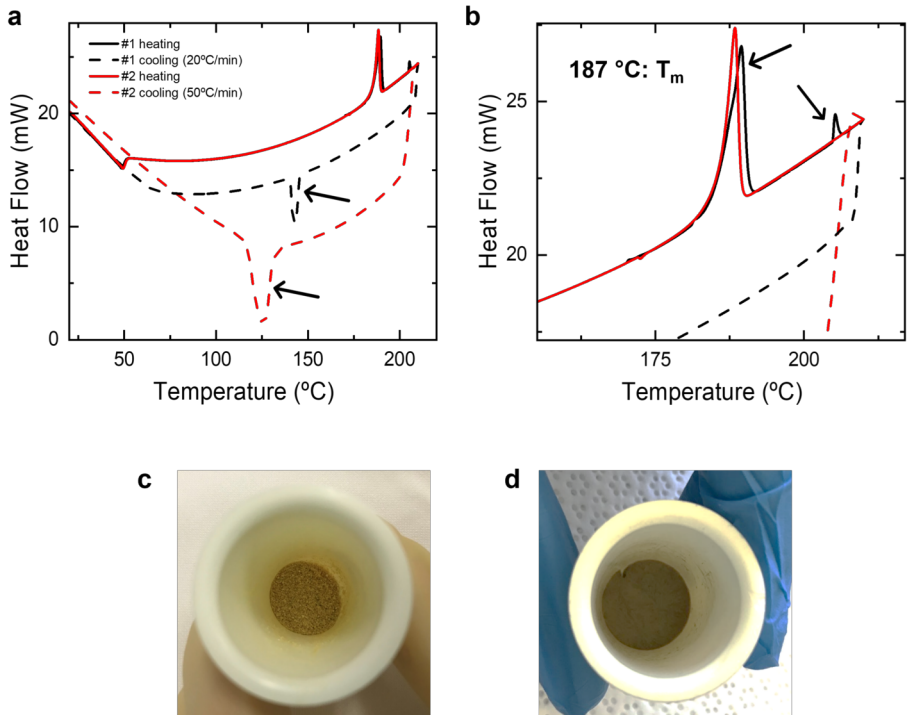


Figure 5.2: Differential Scanning Calorimetry - **(a)** DSC curves of PBA. **(b)** Zoom out of the melting point regime of part (a). **(c)** amount of PBA as-received[2] placed inside a ceramic crucible. **(d)** PBA after heating it at 210°C in a vacuum annealing oven for 10 minutes, under argon atmosphere.

Once proved that the PBA is suitable for in-vacuum sublimation, the viability of the vacuum-based functionalization of graphene with PBA was preliminary tested using XPS. For that, an Organic Molecular Beam Epitaxy (OMBE) evaporator containing PBA was coupled to the XPS equipment (see Annex F.4, Figure F.8) and a pyrex/graphene sample was introduced inside the XPS preparation chamber, maintaining the graphene surface oriented towards the evaporator. When reaching P$\sim 10^{-8}$ mbar and after annealing the pyrex/graphene at 150°C, 10 minutes, the temperature of the crucible with the PBA (T_{PBA}) was gradually increased. When reaching 185°C, slight P increments were detected, attributed to PBA sublimation. At this point, time was controlled and the pyrex/graphene sample was transferred to the analysis chamber to perform XPS

measurements after 10 minutes, 10+20 (30) minutes and 10+20+30 (60) minutes. Finally, the PBA temperature was decreased and the pyrex/graphene sample was annealed at 200°C, 10 minutes, before another XPS measurement. Results are presented in Figures 5.3 and 5.4, with the analysis of the C 1s, O 1s and Si 2p peaks. In this study, the Si 2p signal is attributed to the substrate (pyrex), and therefore the XPS data was energy corrected to the Si^{IV} reference peak at 103.3 eV [277]. At a first view, the C 1s core-level spectra in Figure 5.3a show that the peak intensity increases with increasing time of PBA sublimation, which can be explained by an increasing amount of PBA deposited on graphene. In parallel, the intensity of the oxygen peak (O 1s core-level in Figure 5.3b) decreases with increasing PBA sublimation time, confirming that the major contribution to the intensity of this peak comes from the substrate. Interestingly, a shift is observed at the C 1s (Csp^2 peak) and the O 1s spectra after subsequent PBA depositions. The Si 2p core-level spectra (Figure 5.3c) also confirms that for larger PBA sublimation time, less contribution from the substrate to the XPS spectra. Remarkably, the carbon, oxygen and silicon XPS signals at the initial and final conditions of the experiment, that is, the bare graphene annealed at 150°C, 10 min and the graphene with PBA annealed at 200°C, 10 min, are similar. This confirms that the PBA deposited on graphene after the subsequent sublimations can be removed if the graphene/PBA structure is annealed at a certain temperature (T $\geq$ 200°C). The deconvolution of the XPS spectra in Figure 5.3 is depicted in Figure 5.4.

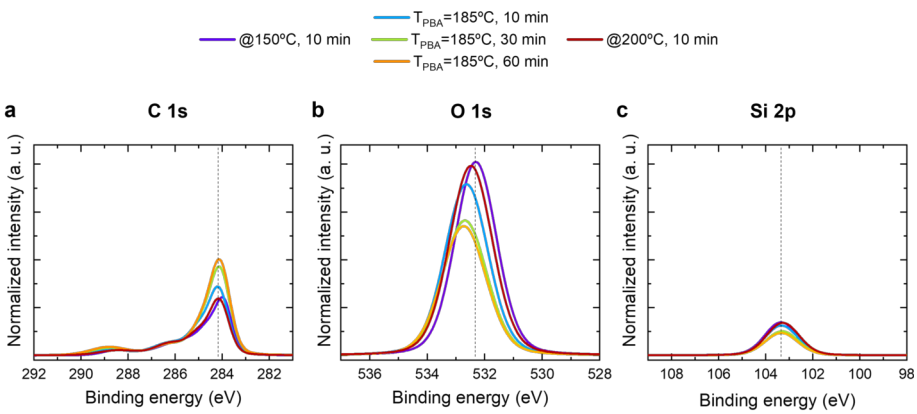


Figure 5.3: XPS monitoring of graphene functionalization with PBA - **(a)(b)(c)** C 1s, O 1s and Si 2p XPS spectra of the different graphene and graphene/PBA surfaces studied, as explained in the text.

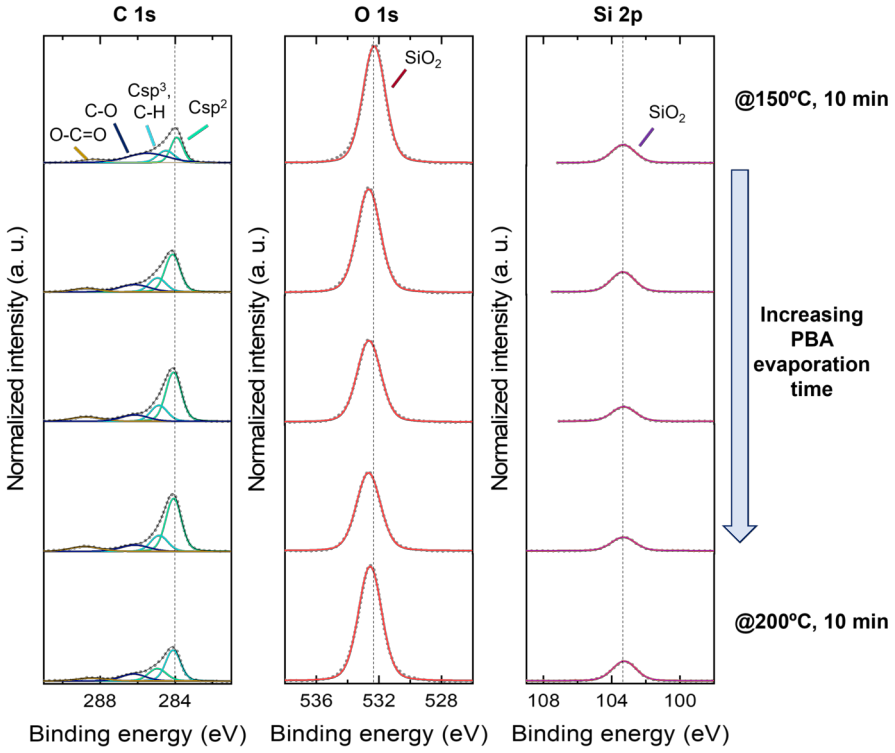


Figure 5.4: XPS monitoring of graphene functionalization with PBA. Peak deconvolution - C 1s, O 1s and Si 2p core-level spectra deconvoluted for the different graphene and graphene/PBA surfaces of the XPS study.

From the above-commented XPS measurements, we confirmed the feasibility of the in-vacuum functionalization of graphene with PBA. However, a more complete understanding of the graphene/PBA surfaces needs further study. For that reason, the design, assembly and setting-up of a dedicated vacuum chamber with all needed coupled components has been part of this PhD thesis, as a fundamental step in this project. The equipment prepared for the in-vacuum functionalization of graphene (Figure 5.5) consists of: (1) a NTEZ evaporator[3] where the crucible containing the PBA is placed; (2) Vacuum pumps to ensure high-vacuum conditions: one mechanical and one turbo pump; (3) Chamber with a sample holder placed between a heater for substrate temperature control and a shutter. The chamber is opened breaking the vacuum with nitrogen flow controlled through a needle valve; (4) a Proportional–Integral–Derivative, PID

[3]Natural Thermal Energy Zone (NTEZ) evaporators are commonly used for the evaporation of organic molecules.

system for crucible and substrate temperature adjustment; (5) Water-based cooling system to prevent overheating of the equipment.

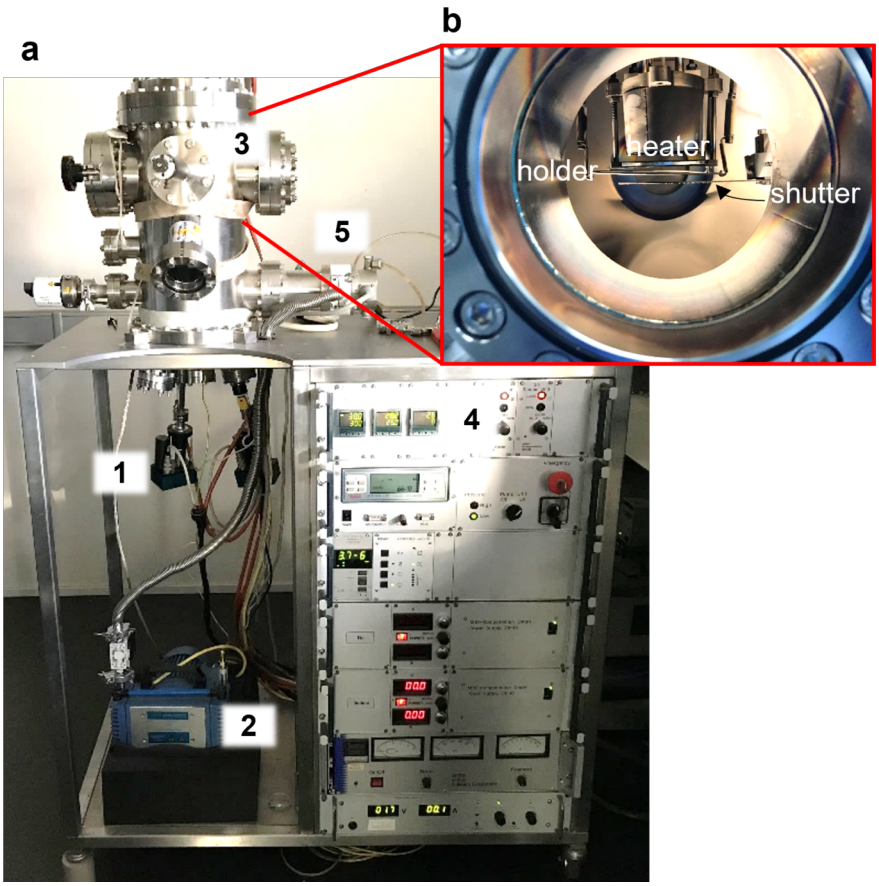


Figure 5.5: Laboratory equipment assembled and used for vacuum-based functionalization of graphene - **(a)** Photograph of the vacuum chamber connected to the NTEZ evaporator, with the principal parts numbered to match its description in the main text. **(b)** Zoom out inside the vacuum chamber, which includes the sample holder, substrate heater and shutter.

Using the information provided by the DSC analysis, the preparation of PBA for graphene functionalization in vacuum is performed as follows. Certain amount of PBA is weighted and placed inside the crucible (filling less than one third of the crucible, as in Figure 5.2c). Then, the crucible containing PBA is placed inside a vacuum annealing oven and it is heated to 120°C for 10 minutes at atmospheric pressure in an Ar-rich atmosphere. Finally, PBA is cooled down to room temperature. Heating and cooling ramps are set to 10°C/min. Once the

1-pyrenebutyric acid is prepared for sublimation (Figure 5.2d), the crucible is placed inside the NTEZ evaporator (see Figure 5.5, component [1]).

The evaporation procedure was performed as follows. First, the graphene substrates are introduced inside the evaporation chamber and activate the pumping system. To reach vacuum values at the range of 10^{-8} mbar, at which the evaporation takes place, the system is left pumping overnight. Then, the substrate temperature (T_{subs}) is set to 350°C and leave at this temperature for 75 minutes. The aim of this step is to remove possible residues remaining at the graphene surface (see Figure 5.6) and ensure the same initial conditions each time we functionalize different samples. It is key to perform this pre-cleaning step inside the vacuum chamber where the deposition of 1-pyrenebutyric molecules takes place, to avoid any recontamination of the surface just before functionalization. After these 75 minutes, the PBA and substrate temperatures at which the process will be performed are set. After stabilization conditions, the shutter is open and the evaporation starts. When sublimation is completed, the shutter is closed and the system is cooled down to room temperature.

As observed in Figure 5.6a, a sample annealing at 350°C for 75 minutes was demonstrated to be effective in removing undesired surface contamination. In agreement with that, the correlated Raman analysis in Figure 5.6b pointed that the annealing treatment decreased the initial p-doping [67] from the as-transfer graphene, mainly due to PMMA residues.

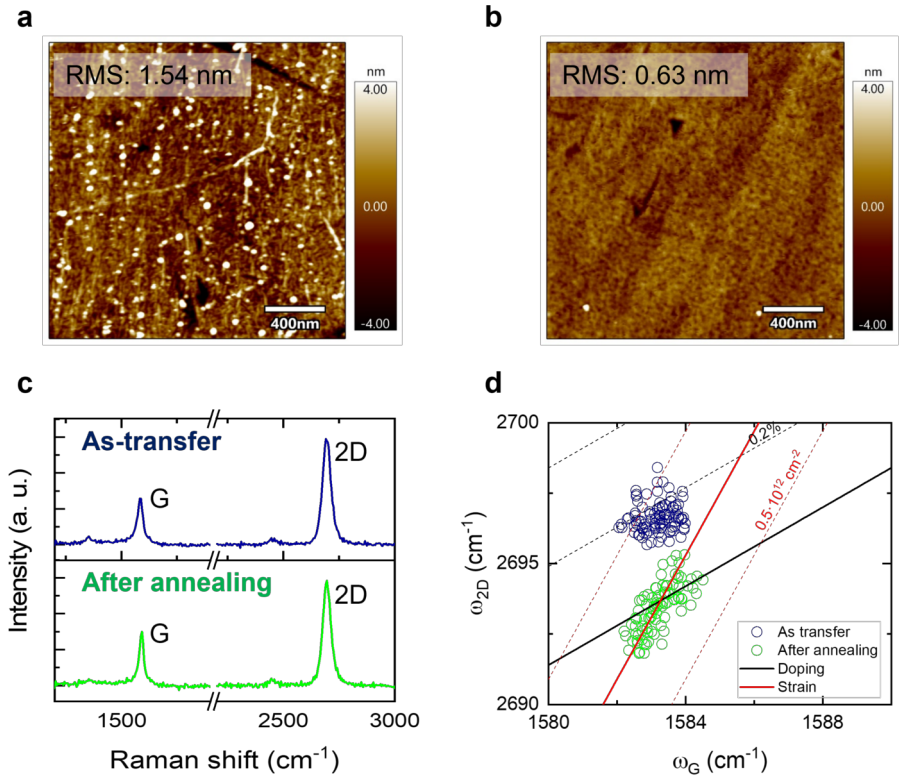


Figure 5.6: Characterization of annealing of as-transfer graphene samples - AFM images before **(a)** and after **(b)** annealing in ultra-high vacuum conditions. **(c)** Raman spectra (average of Raman maps of 100 μm.) and **(d)** Raman ω_{2D}-ω_G correlation maps before and after annealing.

The main techniques used for the characterization of the graphene/PBA surfaces are Raman spectroscopy and AFM. The reason why the study of the in-vacuum functionalization of graphene with PBA is based on those techniques and not on XPS, complementary, is the following. The PBA molecule (Figure 5.1) is composed of carbon, oxygen and hydrogen atoms. Among those, carbon and oxygen are detectable using XPS, as hydrogen does not have core electrons [278]. When deposited on graphene in very small amounts, the detection of PBA is highly difficult if the deposition is not performed inside the XPS vacuum-system, as the incorporation of carbon-based species from the atmosphere when samples are exposed in non-vacuum conditions may take place. The possibility to incorporate a different atom to the PBA molecule, e. g. nitrogen or even fluor to enable an easier detection by XPS was first considered. However, this approach was not carried out, as this kind of chemical modification of the PBA would

substantially vary the functionalization conditions. Nevertheless, it is important to note that XPS and other characterization techniques, that will be further mentioned, are considered fundamental to be used in future works.

The Raman spectra of PBA deposited on graphene, which is compared with a bare graphene spectra in Figure 5.7, presents six peaks at around 1140, 1240, 1400, 1500, 1560 and 1620 cm^{-1}, that have been reported as characteristic pyrene features [279, 280]. Specifically at the vicinity of the graphene G band (Figure 5.7b), the PBA presents 4 peaks. These peaks are The graphene/PBA spectrum shown in Figure 5.7 was obtained from a graphene sample after in-liquid incubation with a PBA 5 mM solution in ethanol, which is the standard method described in literature [56]. However, the strong peaks obtained from this Raman spectra of a graphene/PBA surface correspond to high amounts of PBA deposited on graphene. For lower amounts of PBA on graphene, which is the case of the studies presented in the following sections, the Raman spectroscopy analysis of graphene/PBA is not fundamentally based on the analysis of the characteristic pyrene peaks, as their intensity is very low. For that reason, an advanced characterization methodology is developed, as explained below.

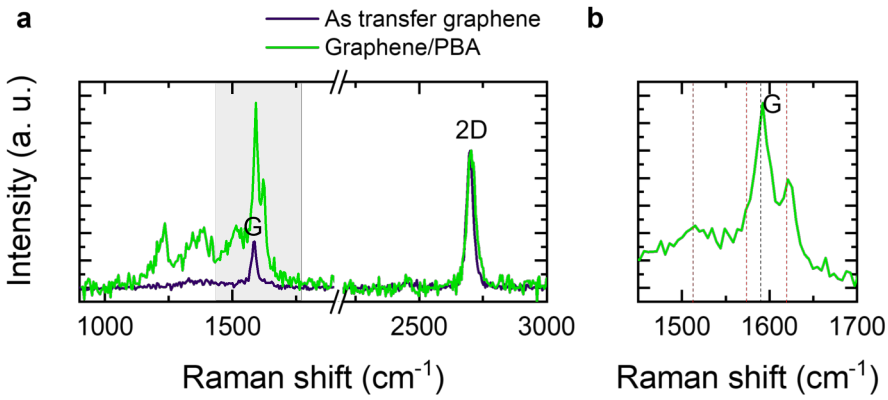


Figure 5.7: Raman spectra of graphene and graphene/PBA - **(a)** Raman spectra of as-transfer graphene and as-transfer graphene after PBA incubation from solution (5 mM). The spectra are acquired in-liquid (PBS). **(b)** Zoom in the shaded area of the graphene/PBA spectrum.

5.4 Optimization of the evaporation parameters

5.4.1 PBA evaporation temperature

Here, results of the study of the optimal temperature at which PBA must be evaporated, T_{PBA}, for the graphene functionalization in vacuum are presented. Considering the DSC results (see Figure 5.2), we performed an evaporation series changing T_{PBA} from 90°C to 130°C, while maintaining time and T_{subs} fixed at 15 minutes and 80°C, respectively. After each evaporation, Raman spectroscopy and AFM analysis were conducted to study the characteristics of the evaporated film.

Figure 5.8a depicts average Raman spectra obtained after each evaporation at the specified T_{PBA} and the corresponding maps showing the G band frequency and the I_{2D}/I_G ratio. As explained previously in this thesis, Raman spectrum of graphene on SiO_2/Si presents a G band at ∼1580 cm^{-1}, a 2D band at ∼2700 cm^{-1} and, for defective graphene, a D band at ∼1350 cm^{-1}. From Figure 5.8a, we observe that the presence of characteristic PBA bands (see Figure 5.7) is very difficult to visualise, not even observed at T < 105°C. However, as T_{PBA} increases, these bands appear more prominently. Fortunately, the presence of PBA can be detected by monitoring changes in the Raman spectra of graphene itself. In Figure 5.8b, we depict ω_G and I_{2D}/I_G as function of the T_{PBA}, and we clearly observe that ω_G increases with increasing T_{PBA}, while I_{2D}/I_G decreases. The ω_G upshift is explained by an increasing of the graphene doping level, induced by the $\pi - \pi$ interaction with the PBA. At the same time, I_G increases with T_{PBA}, as the amount of Csp^2 increases with respect with a bare graphene sample due to the incorporation of the pyrene system. From the presented analysis, we confirmed an increasing amount of PBA on graphene as increasing T_{PBA}. Further analysis is performed in Figure 5.8c, where we present the ω_G-ω_{2D} correlation maps for bare graphene and PBA functionalized graphene: when evaporating at T_{PBA} = 90°C, we observed a slight variation in the strain level, of ∼0.1%, and a very low doping. After evaporation at T_{PBA} = 115°C, slight larger doping and tensile strain with respect to bare graphene sample is measured.

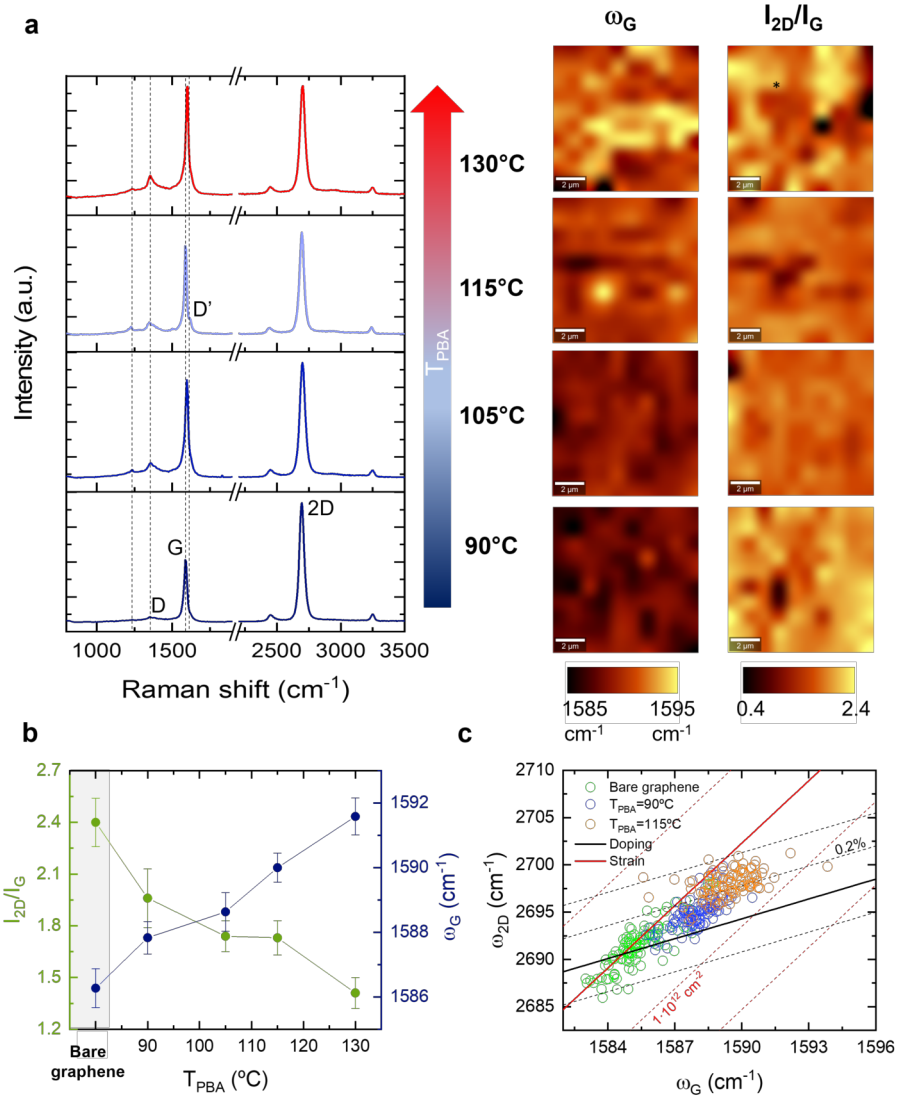


Figure 5.8: Raman characterization of the T_{PBA} series - (a) Average Raman spectra of graphene after functionalization with PBA at different T_{PBA}, as indicated. Results are average from maps of 100 μm^2, shown in the right side of the spectra (scale bar = 2 μm). **(b)** I_{2D}/I_G and ω_G at each T_{PBA} obtained from the corresponding maps. **(c)** ω_G-ω_{2D} correlation maps for graphene and functionalized graphene samples.

Figure 5.9, shows the AFM analysis of the T_{PBA} series. We can observe a direct correlation between T_{PBA} and roughness of the deposited layer, with the roughness RMS increasing with the evaporation temperature. An increase of roughness corresponds to a more irregular surface. A more significant increase

in roughness is measured at T_{PBA} = 130°C. Correlating AFM with the Raman analysis in Figure 5.8, it is confirmed that at T_{PBA} < 105°C, very small amount of PBA molecules is deposited on graphene, whereas at $T_{PBA} \geq$ 115°C, larger amount of molecules is detected.

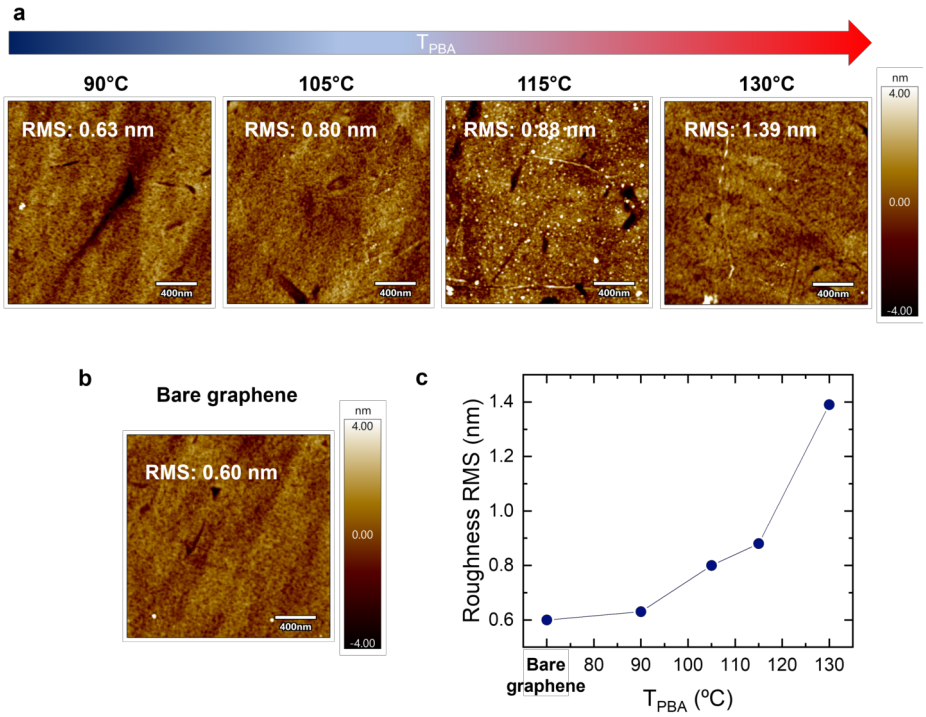


Figure 5.9: AFM characterization of the T_{PBA} series - (a)(b) AFM images of the graphene/PBA samples after evaporation at each T_{PBA} studied, maintaining T_{subs}=80°C and the bare graphene. Scale bar is 400 μm. **(c))** Roughness RMS values for each evaporation temperature.

In view of these results, it can be concluded that the PBA deposition on graphene increases with the evaporation temperature, T_{PBA}. Despite having confirmed the presence of PBA molecules on graphene at T_{PBA} = 90°C and 105°C by monitoring the graphene G band frequency shifts, a higher doping was confirmed at T_{PBA} = 115°C. The higher inhomogeneity measured for the graphene functionalized sample at T_{PBA} = 130°C can indicate an uncontrolled distribution of the PBA layers on graphene at T_{PBA} > 115°C. Therefore, experiments from this point will be conducted using T_{PBA} = 115°C.

5.4.2 Substrate temperature

Another parameter to be optimized for graphene functionalization with 1-pyrenebutyric acid is the temperature at which the graphene substrate is heated during the PBA deposition in the vacuum chamber. For that, we evaporated the PBA at 115°C during 15 minutes at different substrate temperatures (T_{subs}): 40°C, 60°C, 80°C and 100°C. These temperatures were chosen considering the DSC results (Figure 5.2). As for the previous section, we conducted Raman spectroscopy and AFM for analysis.

Raman spectroscopy was performed to confirm the presence of 1-pyrenebutyric acid on graphene in the prepared samples. Results are shown in Figure 5.10 and reveal the presence of PBA in all the cases. For T_{subs} = 40°C and 60°C, the characteristic peaks of the molecule were detected, with a measured ω_G upshift with respect to the bare graphene reference sample. For T_{subs} = 80°C and 100°C, the pyrene-peaks were not as clear, but the ω_G upshift confirms an increase in the doping level (see Figure 5.10b).

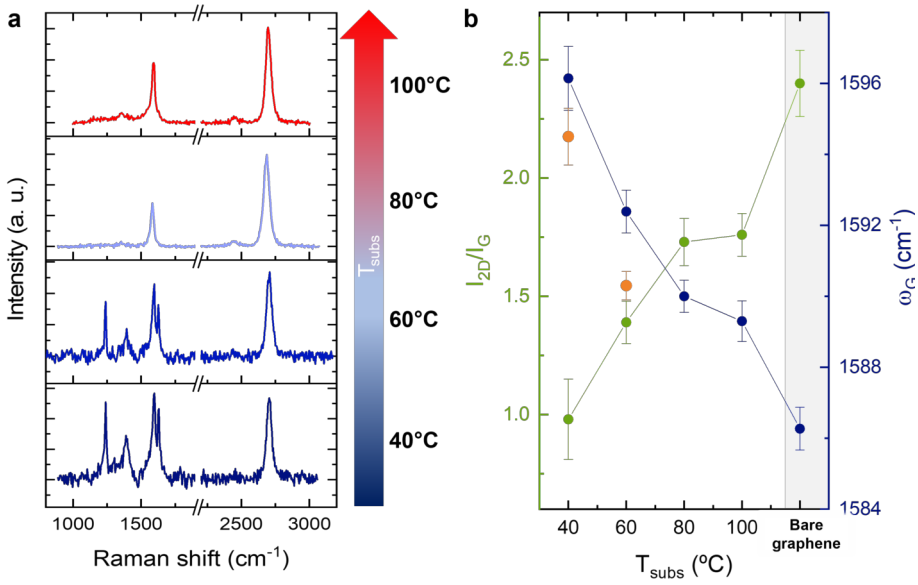


Figure 5.10: Raman characterization of the T_{subs} series - (a) Average Raman spectra of graphene after functionalization with PBA at different T_{subs}, as indicated. Results are average from maps of 100 μm^2. **(b)** I_{2D}/I_G (green) and ω_G (dark blue) versus T_{subs}. The orange points plotted at T_{subs}=40°C and 60°C correspond to the refined Raman analysis described in the text.

In addition, the analysis of I_{2D}/I_G reveals a decreasing of I_{2D}/I_G with lower T_{subs} with respect of the bare graphene reference, indicating a higher amount

of pyrene-like structures at the samples with lower T_{subs}. In this line, the fact that the PBA characteristic Raman peaks were clearly observed only at T_{subs} = 40°C and 60°C confirms a higher amount of PBA deposited on graphene with lower T_{subs}.

Figure 5.11 depicts the AFM images with their roughness RMS values after each evaporation. At the lower T_{subs}, aggregations are observed (signaled with red arrows in the image). These are attributed to PBA clusters deposited non-uniformly on graphene; these low substrate temperatures do not allow the arriving molecules to rearrange on the surface. At $T_{subs} \geq 80$°C, these agglomerations are not observed, indicating a more uniform arrangement of the PBA molecules on graphene, previously confirmed by Raman spectroscopy. Roughness RMS values are extracted in the flat regions of the images, and reveal a decreasing tendency as T_{subs} increases.

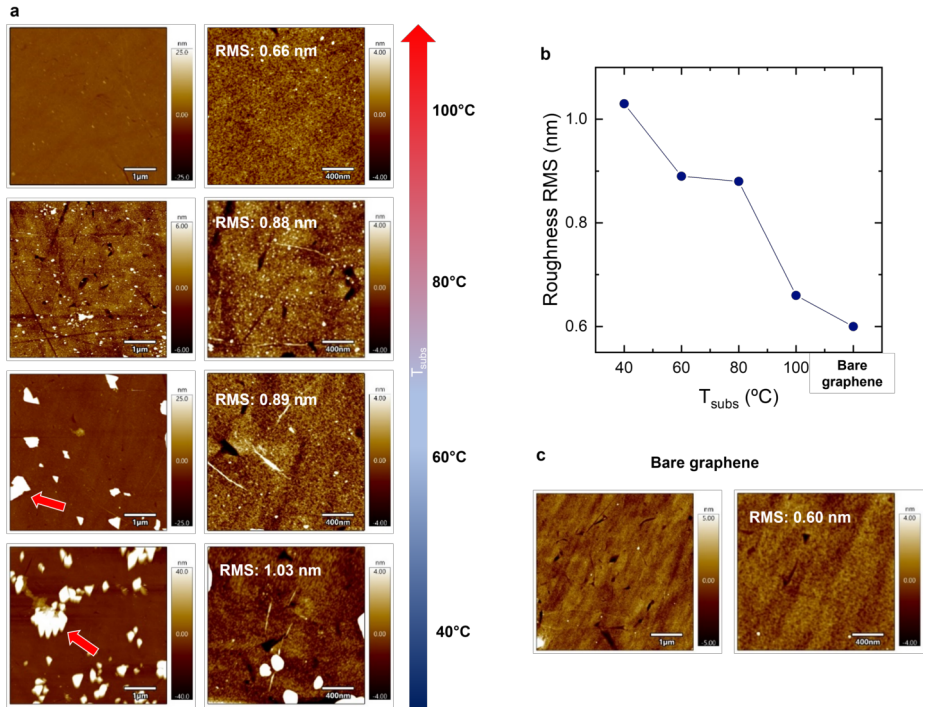


Figure 5.11: AFM characterization of the T_{subs} series - (a)(c) AFM images corresponding to graphene/PBA samples with PBA deposition conducted at T_{subs} 40°C, 60°C, 80°C and 100°C and to bare graphene. Red arrows point to PBA aggregates. AFM scale 1 μm for the 5 μm^2 images and 400 nm for the 2 μm^2 images. **(b)** Roughness RMS versus T_{subs}.

To refine the analysis and investigate the presence of PBA in the areas not corresponding to the clusters of molecules, we analyzed the Raman spectroscopy

maps differentiating the regions with and without PBA aggregates that appeared at T_{subs} = 40°C and 60°C. The result of this analysis, performed eliminating the PBA clusters, is shown in Figures 5.12 and 5.13, and Table 5.1.

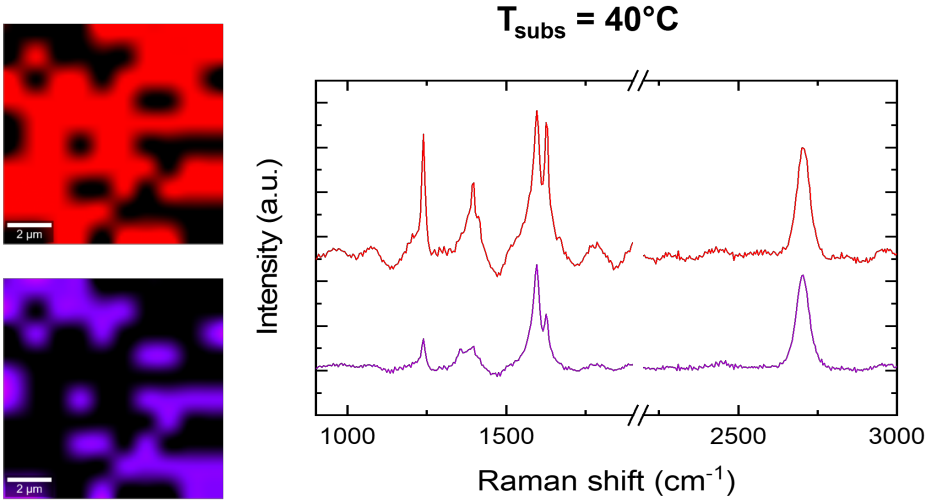


Figure 5.12: T_{subs} 40°C refined Raman spectroscopy characterization - Raman analysis based on clustering the two differentiated graphene/PBA surface regions: in red, the ones showing PBA aggregations and in violet, the flatter regions without PBA aggregations. Scale bar = 2 μm.

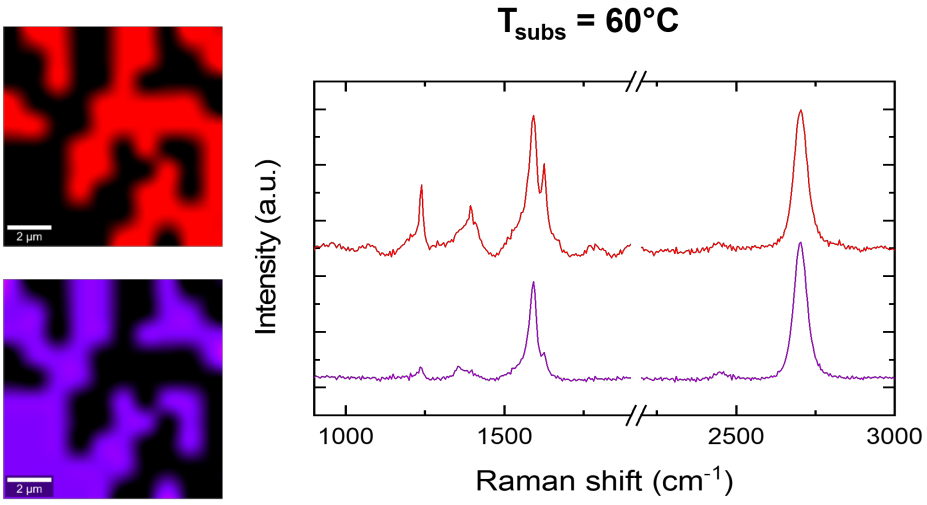


Figure 5.13: T_{subs} 60°C refined Raman spectroscopy characterization - Raman analysis based on clustering the two differentiated graphene/PBA surface regions: in red, the ones showing PBA aggregations and in violet, the flatter regions without PBA aggregations.

Table 5.1: ω_G and I_{2D}/I_G values for the samples corresponding to the T_{subs} study. For T_{subs} = 40°C and 60°C, the two values correspond to the two areas of the samples, with and without PBA aggregates.

T_{subs} (°C)	40	60	80	100
ω_G (cm^{-1})	1594.5 / 1596.4	1590.3 / 1591.3	1590.1	1589.3
I_{2D}/I_G	1.02 / 0.71	1.54 / 1.04	1.73	1.76

While the average spectra of the regions with PBA clusters clearly showed the characteristic pyrene-related Raman features (red spectra in Figures 5.12 and 5.13), the flat regions presented them with less intensity for the case of T_{subs} = 60°C than for the T_{subs} = 40°C (violet spectra), more resembling the average spectra of samples at T_{subs} = 80°C and 100°C. Particularly looking at the flat regions (violet), we observe a ω_G increasing with lowering the T_{subs}, meaning higher amount of PBA molecules deposit on graphene as T_{subs} is lower.

To estimate the number of PBA layers deposited on graphene, we performed AFM, as shown in Figure 5.14, where we compare a bare graphene and a functionalized sample after PBA deposition (T_{PBA} = 115°C and T_{subs} = 80°C, 15 min). The AFM images were acquired at a step area created after peeling-off the material on the substrate.

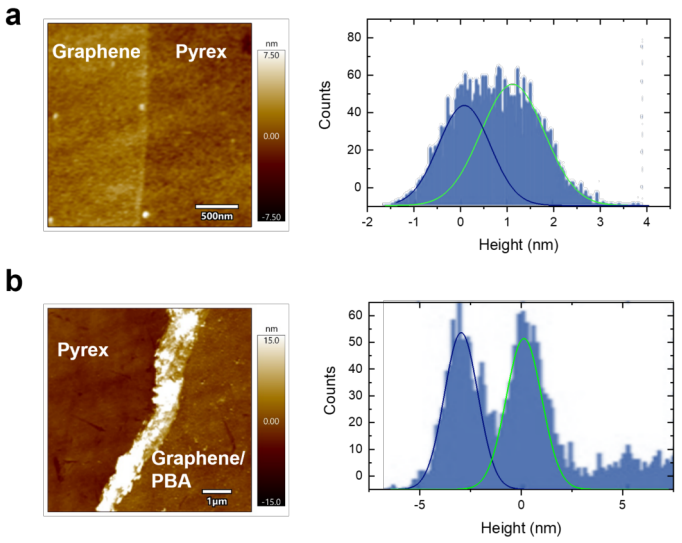


Figure 5.14: AFM step characterization of graphene/PBA - AFM images for **(a)** bare graphene on pyrex and **(b)** graphene/PBA on pyrex with their corresponding histograms of the height distribution.

Table 5.2: Thickness of functionalized graphene. Step analysis of AFM images in Figure 5.14

	Graphene		**1-pyrenbutyric acid (PBA)**	
	Graphene	Pyrex	Graphene/PBA	Pyrex
Height (nm)	1.12	0.06	0.10	-2.80
Step (nm)	**1.06**		**2.90**	

By analysing the step created between the material and the substrate, the calculated thickness of the deposited PBA layer on graphene is of 1.84 nm (see details in Table 5.2). To calculate the amount of PBA layers on graphene, the following considerations can be made: (i) a carbon atom occupies 0.09 nm; (ii) the $\pi-\pi$ stacking distance, or distance between two PBA molecules is estimated as the graphite interlayer spacing, that is 0.335 nm [281]; (iii) the steric hindrance of the PBA aliphatic chain and experimental constraints (AFM resolution and ambient conditions) difficult to quantify but can affect the result only by decreasing the final amount of PBA layers obtained. Based on these considerations, the number of PBA layers is estimated as $n_{PBAlayers} = 1.84/(0.09+0.335) = 4.3$. Thus, by this method, a control of PBA functionalization of graphene can be achieved with a very low amount of PBA layers, in this case ≤ 4.

In summary, in this section we confirmed the feasibility of in-vacuum graphene functionalization with PBA and the control of the resulting graphene/PBA system by the tunability of the deposition parameters. Further studies would be necessary to validate the presence of a uniform, full-covered PBA monolayer on graphene; the establishment of a more complex and refined characterization would involve even more characterization techniques, as briefly introduced at the beginning of this chapter. For instance, quartz crystal microbalance (QCMB) would help in the quantification of the thickness of the PBA deposition. Based on the piezoelectric properties of quartz crystals, QCMB allows the monitoring of mass variations on very thin materials [282]. *In-situ* thickness control of PBA deposition using a quartz crystal-based system was not possible in the home-built equipment used for in-vacuum functionalization of graphene (Figure 5.5). However, future experiments can be designed to complement the thickness quantification of the PBA layers after the deposition is completed and the sample is taken out from the evaporation chamber. Besides QCMB, electrochemical analysis, specifically through cyclic voltammetry for the determination of surface coverage and PEIS, can be useful to complement the graphene/PBA characterization. Finally, synchrotron-based techniques are also to be considered. In that direction, a preliminary test using Grazing-Incidence Wide-Angle X-ray Scattering (GIWAXS)

is shown in the Annex C. Although this work is planned for the future, in this thesis this has not been conducted, as the studies presented cover the initial stage of the proposed in-vacuum functionalization, which requires the construction of the evaporation chamber, the understanding of the evaporation dynamics and the development of an advanced characterization method for very low amount of PBA on graphene.

In the framework of this PhD dissertation, we continued with the analysis of the graphene/PBA surface using $T_{PBA} = 115°C$ and $T_{subs} = 80°C$, 15 minutes as the evaporation parameters, as these ensured the presence of a flat PBA coverage on graphene.

5.5 Graphene/PBA surface characterization

A study based on electrical characterization and Raman spectroelectrochemistry was conducted to complete the study of the graphene/PBA functionalization. For that, the charge neutrality point correlation with the electrolyte pH of graphene functionalized with PBA in an as-transfer graphene sample was investigated. To complete the analysis, the study of a graphene surface functionalized with an analogous pyrene-based molecule but with opposite charge, 1-aminopyrene (AP), was developed (see Annex C for more details about graphene functionalization with AP).

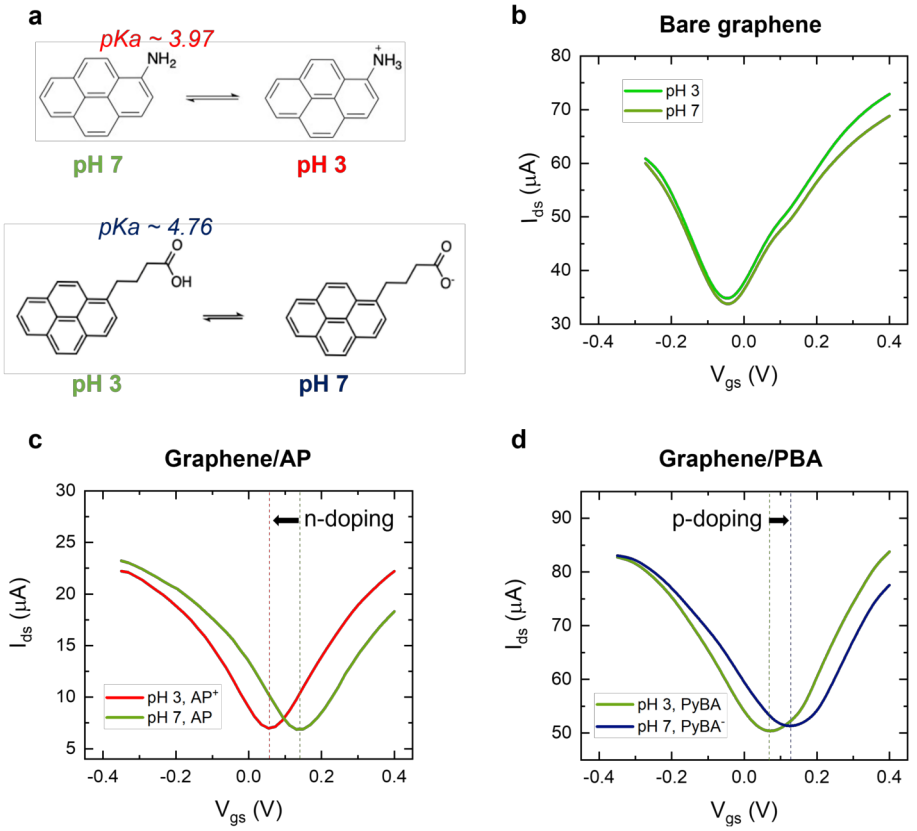


Figure 5.15: (a) Schematics of the acid-base equilibrium for AP and PBA with its corresponding pKa values. I_{DS} - V_g transfer curves of **(b)** bare graphene, **(c)** graphene/AP and **(d)** graphene/PBA acquired in PBS 150 mM in different pH to favour the neutral or protonated/deprotonated form of the functional groups at the graphene surface.

Figure 5.15 shows the I_{DS}-V_{gs} transfer curves measured for each sample in PBS at different pH. For bare graphene (see Figure 5.15b), the CNP is located close to 0.0 V, more precisely at ∼-0.04 V, as expected for an as-transfer graphene sample. When measuring I_{DS}-V_{gs} in bare graphene at different pH, we observe no CNP shift, confirming that the quantity of possible residual PMMA from the transfer process is negligible (see Chapter 4). I_{DS} - V_{gs} transfer curves for graphene/AP and graphene/PBA (Figure 5.15c and d respectively), also present CNP values close to 0.0 V when measuring in PBS at a pH, in which the molecule is in neutral form. When changing the pH of the solution to deprotonate the carboxyl group of PBA, that is, at pH 7, the CNP of the corresponding transfer curve (blue in Figure 5.15c) is shifted 0.06 V towards more positive voltages. In contrast, when protonating the AP amino group at the graphene/AP sample, at pH 3, a CNP shift of 0.08 V is observed towards negative voltages.

These results provide experimental proof of graphene functionalization with the desired molecule. Now, to complete the analysis quantitatively, the specific doping level induced by each functionalization can be calculated using Raman spectroelectrochemistry (see Section 2.5.1). Figure 5.16 depicts the $\Delta\omega_G$ curves acquired as a function of applied voltage (axis below) and charge density (n, axis on top for b and c plots)[4]. Charge density is calculated using $n = C_g(V_g - V_{CNP})/e$, [71] where $C_g = 2.3{\cdot}10^{-6}$ F/cm^2.

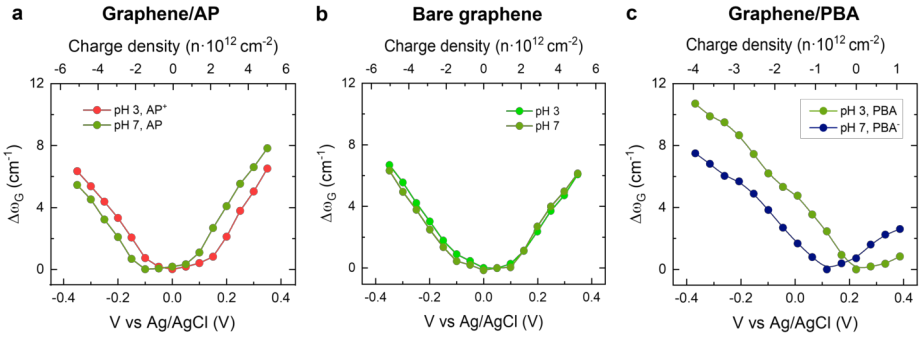


Figure 5.16: Raman spectroelectrochemistry for doping quantification - $\Delta\omega_G$-V curves of **(a)** graphene/AP, **(b)** bare graphene and **(c)** graphene/PBA acquired in PBS 150 mM in different pH to favour the neutral or protonated/deprotonated form of the functional groups at the graphene surface.

In good agreement with the electrical characterization results, bare graphene does not exhibit a variation of the CNP at different pH. For the case of graphene/AP and graphene/PBA, n-doping and p-doping is confirmed, accounting for the CNP shifts measured respectively. Furthermore, functionalization with PBA induces a charge density of $\sim 2.01{\cdot}10^{12}$ cm^{-2} (holes) to the graphene surface in PBS pH 7, where PBA appears in its deprotonated form, and AP functionalization induces a charge density of $\sim 1.24 \cdot 10^{12}$ cm^{-2} (electrons) to the graphene surface in pH 3, where AP is protonated.

5.6 Electrical characterization of graphene/PBA SGFETs

Once the functionalization of graphene with 1-pyrenebutyric acid is demonstrated, the next step is to assess the effect of graphene functionalization on the

[4]CNP shifts measured by Raman spectroelectrochemistry are in the opposite direction to the ones measured by electrical characterization, due to the configuration of the potentiostat (Biologic) and the way the voltage is applied ($V_{gs} \neq$ V vs Ag/AgCl), as explained in Section 2.5.5.

performance of SGFETs. Hence, the main aim is to confirm that graphene/PBA transistors are operational. For that, SGFET arrays were fabricated following the microfabrication process explained in Section 2.4.2, on both pyrex and SiO_2/Si supports. Taking into account that the graphene functionalization studies in this dissertation were performed on pyrex, we wanted to further study it in fabricated devices. Moreover, being SiO_2/Si the standard substrate for the established technology in the AEMD group, it was included in this study. After device fabrication (see Section 2.4.2), graphene functionalization was carried out with PBA at $T_{PBA} = 115°C$, $T_{subs} = 80°C$, 15 min deposition time.

Electrical measurements were performed at the setup described in the Annex F.7, using PBS at different pH. Figure 5.17 presents the electrical characterization of the transistors on pyrex. In Figure 5.17a, I_{ds}-V_{gs} curves analysis reveal a CNP shift (92 mV) towards more positive voltages after PBA deposition, confirming that graphene is effectively functionalized (p-doping induced by the presence of 1-pyrenebutyric acid in a deprotonated form at pH 7). Figure 5.17b shows the CNP values of the measured I_{ds}-V_{gs} curves from pH 2 to pH 10, of bare graphene and graphene/PBA transistors. In general,graphene/PBA transistors present higher CNP values at all pH and higher device-to-device homogeneity. Interestingly, the CNP behaviour with pH follows a similar tendency when comparing the bare graphene and the graphene/PBA transistors. As discussed previously (see Chapter 4, Section 4.5), the sensitivity to pH of graphene-based devices is originated mainly from the charged species at the surface originating from surface contamination. The CNP vs pH tendencies observed in Figure 5.17b indicate that PBA on graphene is not the only charged specie present, as other residues from the fabrication process may also contribute to the pH response. Figure 5.17c depicts the transconductance, g_m, of the curves measured at the different pHs. A slight improve in the graphene/PBA devices is observed, indicating that functionalization with PBA may possibly increase device sensitivity [283]. Finally, Figure 5.17d shows the measured effective gate noise, V_{rms}, of the SGFETs. The origin of the effective gate noise in g-SGFETs has been object of discussion and controversy [86, 284, 285, 286, 287]. Different strategies to reduce it have been suggested, but continue being investigated due to its importance in device performance [288, 289, 290, 291, 292]. The measured V_{rms} is lower in magnitude at all pHs after graphene functionalization. However, the measured V_{rms} of the graphene/PBA SGFETs shown in Figure 5.17d are in the range of what can be obtained considering batch-to-batch inhomogenity (see Annex for more data corresponding to a different fabrication batch of SGFETs). What is important to note, yet, is the higher homogeneity in the V_{rms} values of the graphene/PBA SGFETs. More statistics should be needed to confirm weather

graphene functionalization with PBA could increase device-to-device homogeneity, which would improve the devices performance [293].

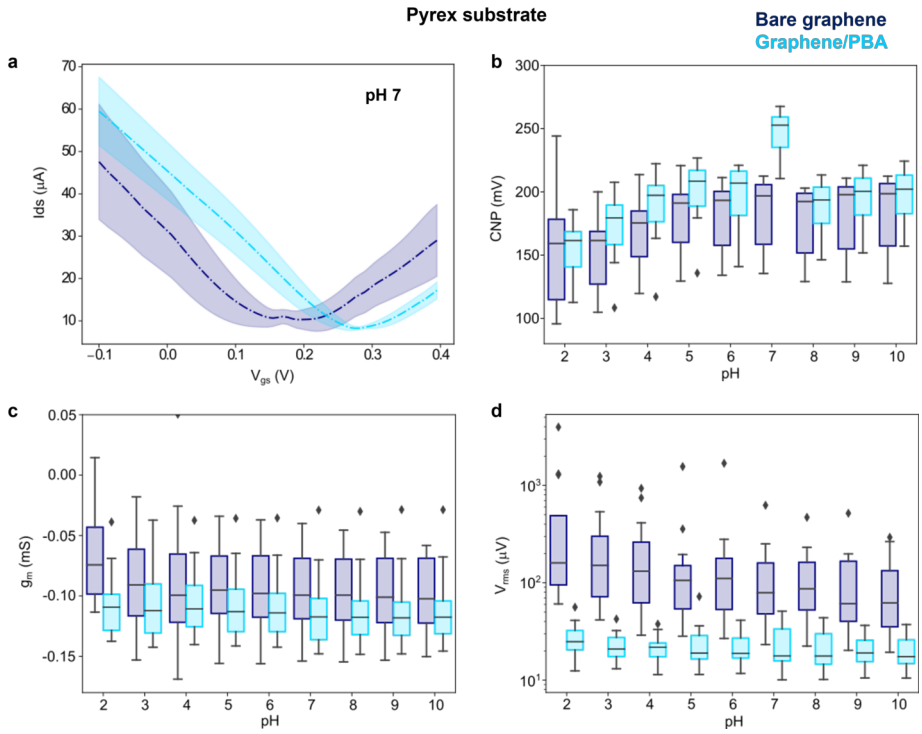


Figure 5.17: Electrical characterization of pyrex/graphene transistors before and after PBA functionalization - **(a)** I_{ds}-V_{gs} curves of graphene and graphene/PBA sGFETs on pyrex. **(b)(c)(d)** CNP, transconductance, g_m and effective gate noise, V_{rms} vs pH, respectively. n = 12 channels.

In Figure 5.18, we depict the electrical characterization of the SGFETs supported on SiO_2/Si. As for the case of the SGFETs on pyrex, a shift of the CNP towards more positive V is measured at pH 7 for the graphene/PBA transistors. In this case, this shift is slightly lower ((14 mV, see Figure 5.18a). A lower CNP shift is attributed to a lower doping level. This is probably related to the different substrate-graphene interaction, depending on graphene being supported on pyrex or on SiO_2/Si, as it has been demonstrated that the substrate underneath graphene can influence the noncovalent functionalization of the material [294, 295]. SiO_2/Si contains different charge trap density that influence graphene carrier distribution [296, 297], differently from the pyrex substrate. We hypothesize that this different charge distribution of the substrate affects the PBA deposition when graphene is on SiO_2/Si, which will be stronger (weaker) in the areas where substrate-graphene electronic coupling is weaker (stronger).

This would possibly signify a less uniform functionalization when compared with pyrex supported graphene. In Figure 5.18b, it is observed that the CNP variation with pH is similar between graphene and graphene/PBA SGFETs, in agreement with what is extracted from Figure 5.17b. As for transconductance, g_m (Figure 5.18c), no significant variations are detected at all pHs, except for a slight improvement after functionalization at pH < 7, meaning that the sensitivity of the graphene and graphene/PBA SGFETs is not different in functionalized devices. Regarding noise characterization, Figure 5.18d shows a slight decrease of the V_{rms} magnitude in graphene/PBA SGFETs, yet in the range of what is considered standard (see Annex C).

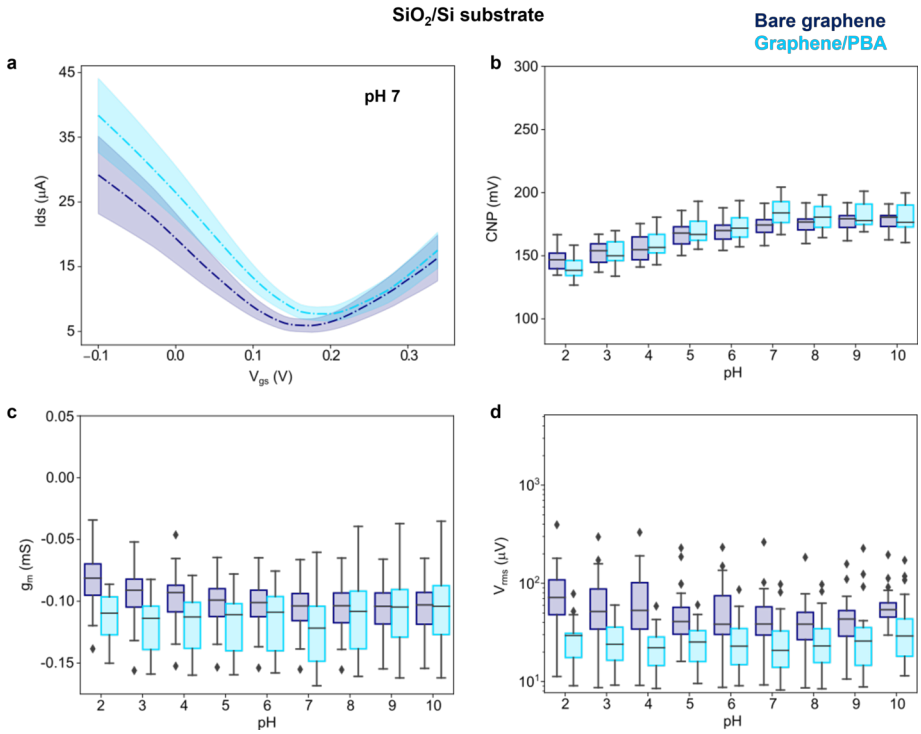


Figure 5.18: Electrical characterization of SiO_2/Si/graphene transistors before and after PBA functionalization - **(a)** I_{ds}-V_{gs} curves of graphene and graphene/PBA sGFETs on SiO_2/Si. **(b)(c)(d)** CNP, transconductance, g_m and effective gate noise, V_{rms} vs pH, respectively. n = 12 channels.

In summary, the results presented in this section reveal that graphene/PBA SGFETs are functional at a pH range of 2-10 and show equivalent performance before and after graphene functionalization. In SGFETs on pyrex, the device-to-device homogeneity is increased in graphene/PBA, in comparison with bare graphene SGFETs; the origin of this improvement in homogeneity is not yet

understood. The sensing capabilities of graphene/PBA SGFETs were tested using thrombin. This proof of concept experiment can be found in the Annex C.3.

6

Conclusions & Outlook

This PhD thesis has contributed with an extensive study of the graphene-related interfacial phenomena, including the material synthesis, surface modification and conforming electronic devices working in liquid and in biomedical applications. In this line, it contributes to the development and understanding of systematic and detailed characterization methodologies to assess graphene interactions with the media surrounding it. Specifically, it responds to main current challenges in graphene technology, which are reproducible high quality, large scale graphene synthesis, improving the wafer-scale fabrication of graphene devices and gaining knowledge and control of graphene functionalization.

In the first chapter of results, we report on the setup and operation of a CVD reactor for the optimization of new Cu-based rigid supports for the large area growth of high-quality graphene. The main experimental part of this chapter is focused on the study of c-sapphire surface reconstruction and the optimization of the Cu thin film deposited on it, with the objective of accomplishing a desired orientation and low roughness for subsequent graphene growth. This study explored the influence of sapphire annealing parameters (H_2, temperature and time) on the resulting Cu surface. We were able to obtain smooth Cu surfaces with large grains and <111> orientation, which were characterized by complementary techniques (SEM, AFM, XRD, EBSD). The main challenge to overcome in this regard was the smoothing of the Cu grain boundaries - grooves -, which were unavoidably present in our surfaces. We identified a technical requirement to avoid them, which involves incorporating substrate heating during Cu deposition;

unfortunately, this was not available in the framework of this thesis, yet is planned to be incorporated in future studies. The consequent problem of having deep grooves at the Cu surfaces is that these introduce non-homogeneity, and thus possible discontinuities at the graphene layer synthesised on them. Despite that, we were able to successfully synthesize high-quality graphene, evidenced by SEM and Raman spectroscopy. From SEM analysis, we assumed that graphene follows the Cu morphology and, thus, the grain sizes are expected to be larger than 50 μm. With this grain size, the event of having grain boundaries inside a transistor channel is unlikely, as the typical channel length for graphene transistors applied to biomedical applications are 50 μm approximately. The transfer process of the synthesised graphene was tested successfully, based on a standard wet approach with slight modifications. A full device fabrication process in cleanroom at wafer scale was accomplished and characterized. In summary, the growth of graphene in the engineered substrates presented opens a path towards the optimization of automatized transfer methods, as well as enabling surface modification before graphene transfer.

In the second chapter, we study the interfacial phenomena of graphene-based electronic devices by considering the whole substrate/graphene/electrolyte system. We present a systematic study involving ad hoc techniques for the physicochemical characterization of graphene surface and complementary in operando morphological characterization. In particular, we analysed as-transfer graphene supported on different substrates, pyrex, ITO and Au, to understand the effect of the substrate nature and the electrolyte pH and ionic strength. Our results highlight the role of water intercalation phenomena, confirmed by KPFM and Raman spectroscopy, confirming a key effect on the electrochemical performance of graphene electrodes. Furthermore, numerical calculations helped us evaluate the impact that the confined water between the substrate and graphene has on the capacitance of graphene electrodes. We also studied the influence of the electrolyte (pH and ionic strength) on the performance of graphene electrodes. Our results shed light to the current controversy in literature about graphene sensitivity to pH, as we demonstrate that clean graphene does not respond to pH variations. On the contrary, charged species remaining as residues from the wafer-scale fabrication process govern this response. This understanding is key to direct efforts towards alternative fabrication strategies that protect the graphene surface from fabrication residues, which are unavoidable in the current technology.

Considering the framework of this dissertation, which is the use of graphene devices in the biomedical field, it was important to analyse the wafer-scale fabrication process impact on the performance of graphene devices. We

demonstrate that adsorbed residues from the fabrication process unavoidably remain at the graphene surface, evidenced by techniques like PEIS and Raman spectroscopy/spectroelectrochemistry. By including XPS and UPS, we confirmed that the type and amount of adsorbed charge on graphene after fabrication depends on the nature of the substrate underneath. With that, we provided a systematic procedure based on in situ Raman spectroscopy to determine the origin of the residues remaining at the graphene surface after wafer-scale fabrication, and to comparatively quantify the amount of adsorbed charge on graphene. Remarkably, we showed that the graphene definition step adds a substantial amount of adsorbed charge that remains homogeneous until the passivation step, which is the final step in the fabrication process. As a result, device-to-device homogeneity is not ensured within a wafer. This indicates that, although the achievement of a clean transfer process is important to preserve the graphene quality, the development of strategies to maintain the graphene surface clean during the fabrication process is of utmost importance and still remains unsolved.

Advancing towards a cleaner and reproducible fabrication strategy of graphene devices is matter of great concern and a major challenge nowadays. In that line, we have proposed the incorporation of a Cu layer acting as a graphene protection strategy throughout the whole cleanroom process. Raman characterization of the Cu-protected graphene revealed that its high quality was preserved, and did not exhibit adsorbed residual charge. Results from this highlight the importance of adjusting current standard fabrication protocols to incorporate the discussed Cu-protection strategy.

In the last part of the results of this thesis, we proposed a novel methodology for a controlled graphene functionalization, a challenge which has limited the use of graphene in biosensing applications. Our functionalization method is based on the physical evaporation of 1-pyrenebutyric acid, a pyrene-based molecule capable to π-π interact with graphene. We studied the deposition parameters, demonstrating a controlled and reproducible graphene functionalization. The developed characterization of graphene/PBA surfaces combines Raman spectroscopy, AFM and electrical measurements. Using that, we were able to quantify less than 4 layers of PBA deposited on graphene. Further studies are suggested (based on GIWAXS, QCMB, and electrochemical techniques) to quantify the functionalization coverage. Moreover, variations between substrates should be taken into account when extending the functionalization methodology to other substrates, such as flexible ones.

In this part, we also performed electronic characterization of graphene/PBA transistors. Our results revealed an equivalent performance of the functionalized

devices to the standard graphene ones; in terms of transconductance and low noise levels. Finally, we assessed the sensing capabilities of the graphene/PBA platform created using thrombin, as a first proof-of-concept. Results revealed that the fabricated graphene/PBA transistors were capable of thrombin detection, opening the door towards depositing PBA on clean graphene surfaces, thus boosting the possibilities of detecting a wide range of analytes. Further work is required to improve sensitivity of graphene/PBA to analytes by achieving cleaner graphene surfaces previous to functionalization. As it has been discussed before, there are not yet effective methods of graphene transfer and surface cleaning after wafer-scale devices fabrication.

All in all, we have demonstrated the importance of a profound understanding on the physicochemistry at the interface between graphene and its surrounding media at all levels, from the material growth to the applications, in order to mature graphene technology and push it forward to its industrialization and clinical translation.

A

Chapter 3 complementary data

A.1 600 nm thickness of copper on c-sapphire

Analogously with the evaporation of 800 nm of Cu on c-sapphire discussed in Chapter 3, we evaporated 600 nm Cu on c-sapphire (e-beam, rate 6-8 Å/s) and performed annealing temperature and time studies. The aim was to explore if reducing the Cu thickness resulted in an ultimate smoother Cu surface for graphene growth. However, no significant improvement with respect to the 800 nm Cu layer was observed, while undesired dewetting was more likely to happen with this thinner surfaces. For that reason, we conducted our experiments in Chapter 3 with a 800 nm Cu layer. SEM and XRD results regarding the conducted annealing processes are depicted in Figures A.1 and A.2.

Increasing the annealing temperature resulted in larger Cu grains, as expected considering the results in Figure 3.10. As for Cu orientation, XRD $2\Theta/\omega$ scans clearly revealed a more preferential Cu<111> when annealing at 1000°C rather than at lower temperatures.

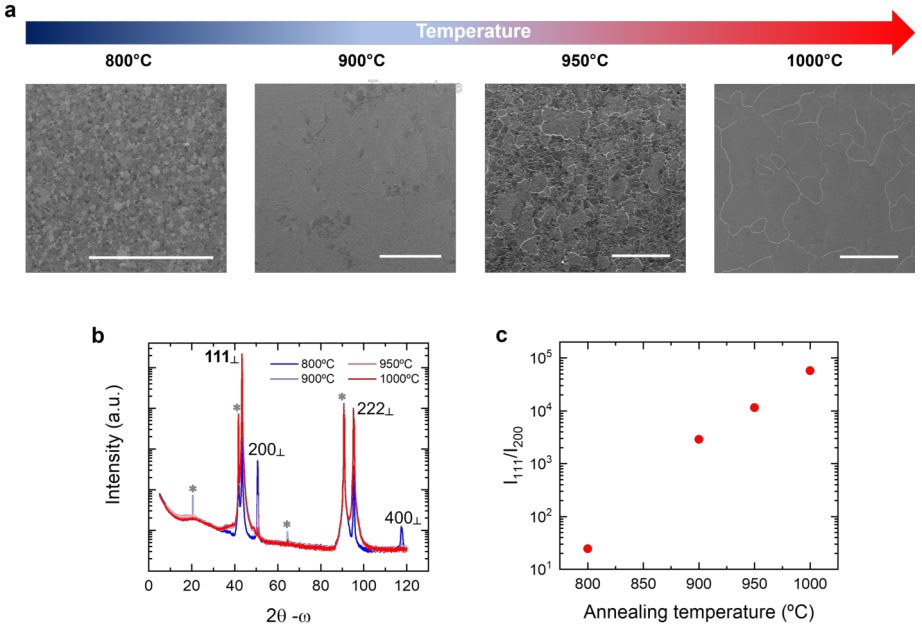


Figure A.1: Temperature series of the annealing of Cu (600nm) on c-sapphire - **(a)** SEM images of each sample of the temperature series. Scale bar in all images: 100 μm. **(b)** $2\Theta/\omega$ spectra of sapphire/Cu samples prepared. **(c)** I_{111}/I_{200} corresponding to spectra in (b).

Annealing time variations affected the Cu surface morphology and orientation as well, with longer times favouring the prevalence of larger grains, which is desired for an optimal graphene growth. Surprisingly, the most Cu<111> oriented surface was measured for the sample annealed during 6 minutes, which was the shortest time tested (see Figure A.2c). Annealing during 20 and 40 minutes did not favour the Cu<111> orientation, while the sample annealed during 60 minutes showed more Cu<111> yet not as preferential as for the 6 minutes one.

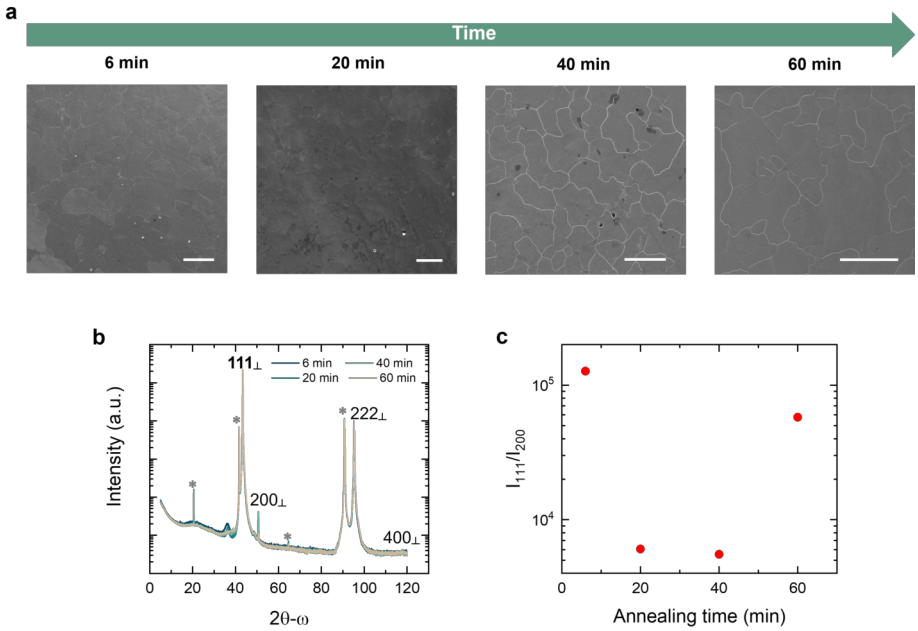


Figure A.2: Time series of the annealing of Cu(600nm) on c-sapphire - **(a)** SEM images of each sample of the time series (T = 1000°C). Scale bar in all images = 100 μm. **(b)** $2\Theta/\omega$ spectra of sapphire/Cu samples prepared. **(c)** I_{111}/I_{200} corresponding to spectra in (b).

A.2 Heating and cooling rates of the copper annealing

To investigate ways to improve the Cu surface quality (lower roughness and smoother boundaries), we performed the 60 minutes annealing at 1000°C of c-sapphire/Cu samples at lower heating and cooling rates with respect to the standard parameters (heating rate = 30°C/min; fast-cooling). Figure A.3a shows the resulting surface after performing the Cu annealing at 17°C/min, which results in the Cu evaporation. In view of that, we tested the 17°C/min heating rate, but reducing the annealing time from 60 to 30 minutes (Figure A.3b). The resulting surface presented irregular grain sizes and contamination, which can be clearly observed at the inset of the image at the right. The identification of the source of this contamination was not possible, yet it may be attributed to the quartz tube impurities or to contamination previously present at the c-sapphire substrate.

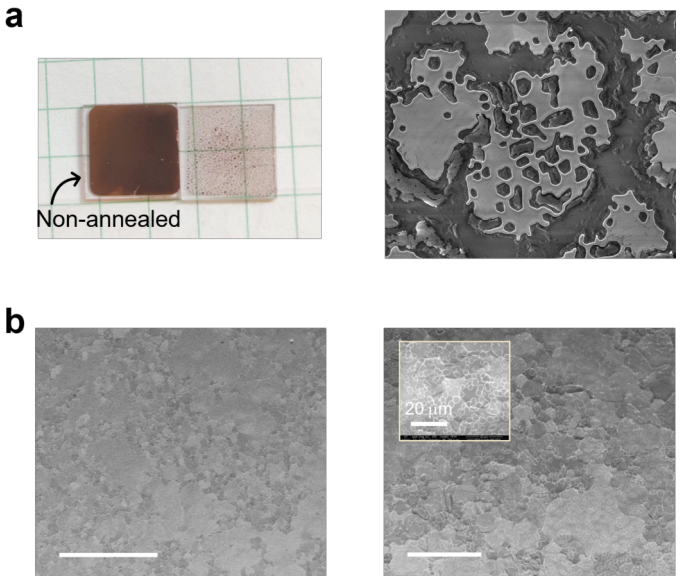


Figure A.3: Variations in the Cu annealing heating rate - (a) (left) Photograph of a sample before and after being annealed at 1000°C during 60 minutes (right) SEM image of the sample after annealing. Scale bar in all images = 100 μm. **(b)** .

In Figure A.4, we show the results corresponding to changes in the Cu annealing cooling rate. In these cases, we observed an increasing of the dewetting phenomenon with respect to the fast-cooling process (white arrows in the SEM images). Furthermore, no smooth, large Cu grains were obtained. Thus, the Cu surface was irregular in terms of smoothness, grain sizes and even impurities were identified (yellow arrow).

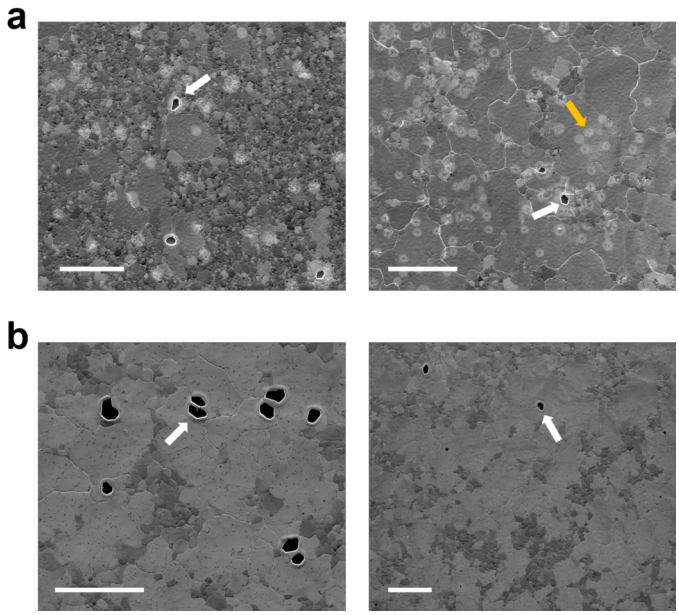


Figure A.4: Variations in the Cu annealing cooling rate - SEM images of annealed c-sapphire/Cu samples (1000°C, 60 minutes) with cooling rates of **(a)** 5°C/min and **(b)** 1°C/min. Scale bar in all samples = 100 μm.

In summary, lowering the heating and cooling rates of the Cu annealing process did not result in an smoother, more homogeneous surface, as it is desired for an optimal graphene growth.

B

Chapter 4 complementary data

B.1 Resources available online

The Python scripts used to analyse and process the data presented can be found in the "PhD Thesis Scripts" repository on my personal Github account:

- In-house Python code for PEIS analysis
- In-house Python code for PEIS fitting

B.2 PEIS fitting parameters

Table B.1: Fitting boundaries for each parameter of the Distributed model equivalent circuit used to determine the CPE from the PEIS data. R_n and R_{ct} (accounting for the processes at the electrode involving charge transfer), are the two contributions of R_{sh}

	Distributed model equivalent circuit				
	CPE	α	R_n	R_{ct}	R_c
Pyrex/graphene	$1{\cdot}10^{-6}<3{\cdot}10^{-6}<1$	$0.85<0.90<1$	$500<5{\cdot}10^{3}<8{\cdot}10^{3}$	$10{\cdot}10^{6}<50{\cdot}10^{6}<100{\cdot}10^{6}$	$335<400<630$
ITO/graphene	$1{\cdot}10^{-6}<3{\cdot}10^{-6}<1$	$0.90<0.95<1$	$1{\cdot}10^{3}<1.1{\cdot}10^{4}<1.5{\cdot}10^{4}$	$1{\cdot}10^{6}<5{\cdot}10^{6}<1{\cdot}10^{8}$	$150<150<154$

Table B.2: Fitting boundaries for each parameter of the Simple model equivalent circuit used to determine the CPE from the PEIS data

	Simple model equivalent circuit			
	CPE	α	R_{sh}	R_s
Bare ITO	$8{\cdot}10^{-8}<50{\cdot}10^{-8}<300{\cdot}10^{-7}$	$0.90<0.95<1$	$0.2{\cdot}10^{5}<0.5{\cdot}10^{5}<10{\cdot}10^{6}$	$145<155<170$
Bare Au	$1{\cdot}10^{-8}<5{\cdot}10^{-8}<200{\cdot}10^{-7}$	$0.85<0.90<0.99$	$0.4{\cdot}10^{6}<1{\cdot}10^{6}<10{\cdot}10^{6}$	$185<200<215$

B.3 Capacitance simulation details and charge density profiles

Analysis of $C_{no-intercalation}$

In the regions of the graphene electrodes without intercalated water ($C_{no-intercalation}$) it is assumed that $C_{no-intercalation} \cong C_{gr}$, where C_{gr} is the capacitance measured from PEIS on the pyrex/graphene electrode. C^{*}_{ITO} can be roughly described by a two-parallel plate element, in correspondence with the beginning of the depletion region of the ITO and its surface, being the distance between them the size of the depletion region. On the other hand, C^{bulk}_{ITO} is spatially defined by the electrolyte (the first plate, ultimately determined by the closest approach of ions to the surface) and the substrate (the second plate, associated to the depletion region in the ITO layer). Considering these descriptions, it can be inferred that $C^{*}_{ITO} > C^{bulk}_{ITO}$. Given that $C_{gr} \ll C^{bulk}_{ITO}$, as extracted from the experimental results, and that $C^{*}_{ITO} \geq C^{bulk}_{ITO}$, it can be concluded that $C_{gr} \ll C^{*}_{ITO}$. Introducing that in equation 4.20, it is achieved that $C_{no-intercalation} \cong C_{gr}$.

General considerations of the numerical simulations

All the numerical simulations described regarding capacitance behaviour with applied V were carried out with an *in-house* code that deals with the self-consistent solution of the Poisson equation, that relates the electrostatic potential, V, and the charge density distribution, ρ, in the structure of study, as defined:

$$\nabla(\varepsilon \nabla V) = \rho \tag{B.1}$$

The charge density in the electrolyte is determined by the ions present in the solution. The relation between the electrostatic potential and the ion distribution is defined by the modified Boltzmann equation:

$$c_i = c_{0,i} \frac{e^{-z_i(V-V_{ref})/\kappa_B T}}{1 - 2\frac{c_{0,i}}{c_{max,i}}(1 - cosh(q|z_i|\frac{V-V_{ref}}{\kappa_B T}))} \tag{B.2}$$

where V_{ref} is the reference potential, $c_{0,i}$ is the bulk concentration of *i-th* ion, z_i is the valence of the *i-th* ion and $c_{max,i}$ its maximum concentration. Thus, it is key to add steric effects in the numerical simulation, which are specifically included through the hard sphere model. In this model, each ion is characterized by an effective ionic radius, R_{eff}, that is related with the maximum concentration allowed ($C_{max} = 1/R_{eff}$). A more detailed description of this model is referenced in [208, 209].

Modelling of C_{ITO}^{bulk}

The bare ITO substrate (see Figure B.1a left) is modelled as a boundary condition, which agrees with its conductive nature. On top of it, an insulating layer models ITO's hydrophobicity. The parameters are set according to the profiles obtained by Molecular Dynamic calculations near hydrophobic and hydrophilic surfaces [298]. The thickness of the layer (1Å) is the approximate size of the plateau region for the hydrophobic profile (Figure B.1a right). The dielectric constant of this region is tuned to fit the experimental data and achieved for $18\varepsilon_0$ (see Figure B.1b).

Modelling of C_{ITO}^{conf}

For the region with confined water at the ITO/graphene electrodes, a structure similar with the bare ITO/bulk electrolyte one is considered. However, in this case, the insulating layer is substituted by a 3.4Å region with a reduced dielectric constant ($13\varepsilon_0$) where only H^+ and OH^- ions are allowed. Steric effects in this region are considered with an effective radius of 1.5 nm (see Figure B.1c). In Figure B.1d, the result modeling of the C_{ITO}^{conf} vs voltage is depicted.

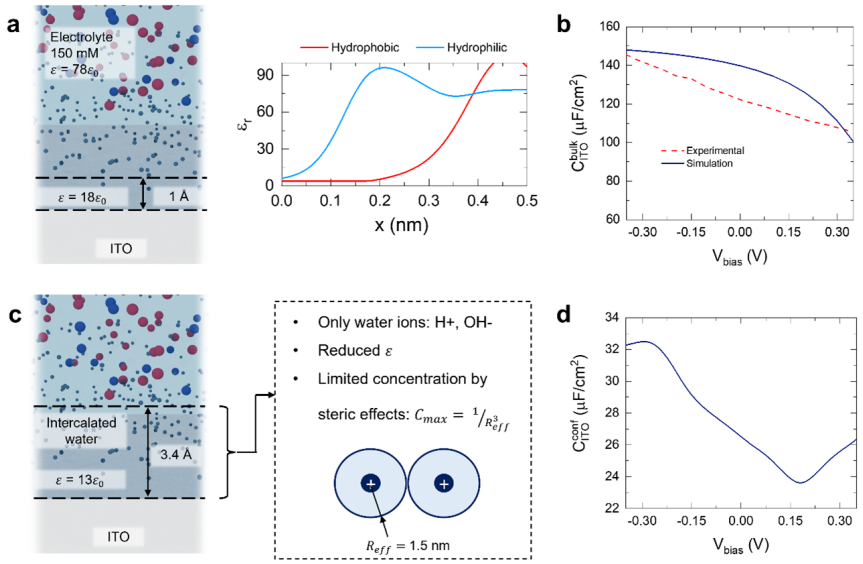


Figure B.1: Numerical simulations of C_{ITO}^{bulk} and C_{ITO}^{conf} - (a) Simulation of the bare ITO-bulk electrolyte system. **(b)** Modelled C_{ITO}^{bulk} compared with the experimental PEIS data. **(c)** Parameters considered for the simulation of the ITO/confined water/bulk electrolyte structure. **(d)** Modelled C_{ITO}^{conf}.

Extended analysis on the impact of ε_w and t_w on the total capacitance

The additional simulations presented here were performed for the ITO/confined water/bulk electrolyte structure to evaluate the effect on the capacitance of varying ε_w and t_w of the confined water region. First, we focus on the ε_w. Figure B.2 shows the charge density profile of the confined water region (N_w) and the bulk electrolyte (N_B), and Figure B.3 depicts the contribution of these regions to the total capacitance.

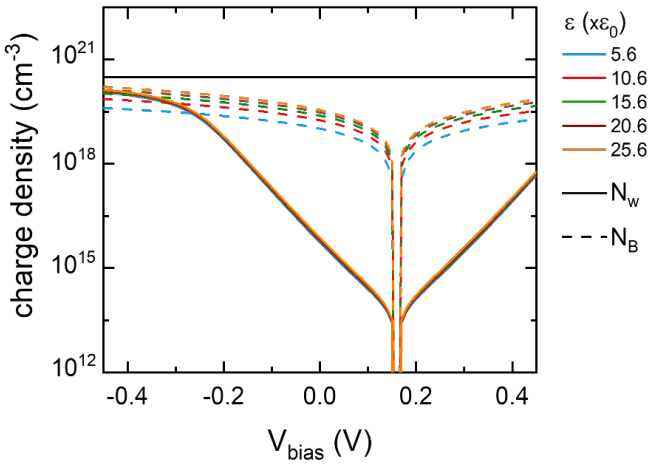


Figure B.2: Effect of ε_w on charge density vs V profiles at the ITO/confined water/bulk electrolyte structure - Charge density profiles of the confined water region N_w and the bulk electrolyte region N_B vs voltage for different ε_w values. The black line indicates the limit defined by the steric effects.

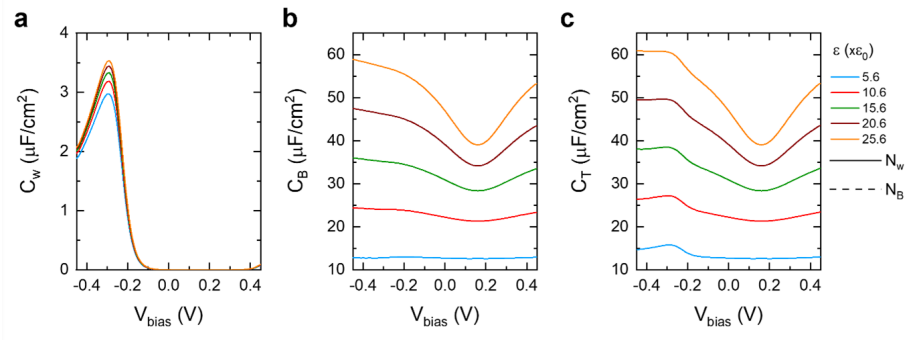


Figure B.3: Contribution of the charge density of the confined water region and the bulk electrolyte to the total capacitance for different ε_w - **(a, b)** Capacitances between the ITO substrate and each of the regions of the structure and **(c)** Modelled C_{ITO}^{bulk} compared with the experimental PEIS data. **(c)** total capacitance of the structure.

The charge density profiles in Figure B.2 indicate that variations in the behaviour with ε_w at the confined water region is insignificant, while in the bulk electrolyte region, the ε_w has a higher effect. In Figure B.3a, a maximum in the capacitance of the C_w agrees with the region at which the charge density (at N_w) starts to saturate. Figure B.3b shows that, at $\varepsilon = 5.6\varepsilon_0$, the capacitance is slightly lower in the voltage range at which the confined water region is charged.

Focusing on t_w variations, analogous simulations are presented in Figures B.4 and B.5.

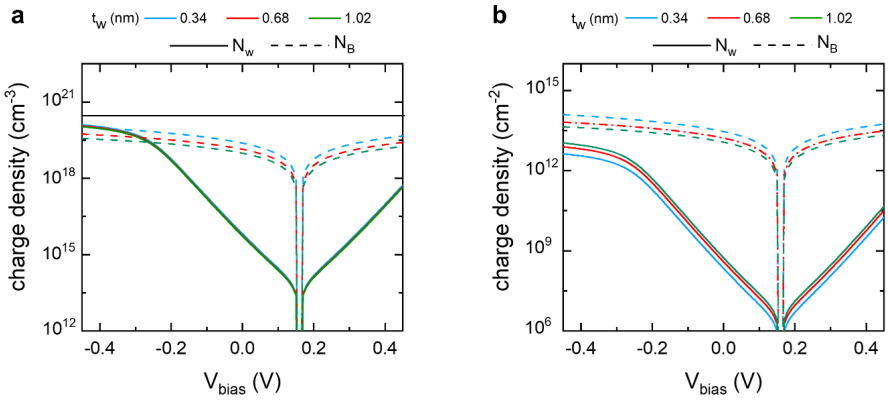


Figure B.4: Effect of t_w on charge density vs V profiles at the ITO/confined water/bulk electrolyte structure - **(a)** Charge density profiles at the confined water region N_w and bulk electrolyte N_B vs voltage for different t_w. The black line indicates the limit defined by steric effects. **(b)** Surface charge density profiles, i. e. the thickness of the regions is considered, as a function of voltage.

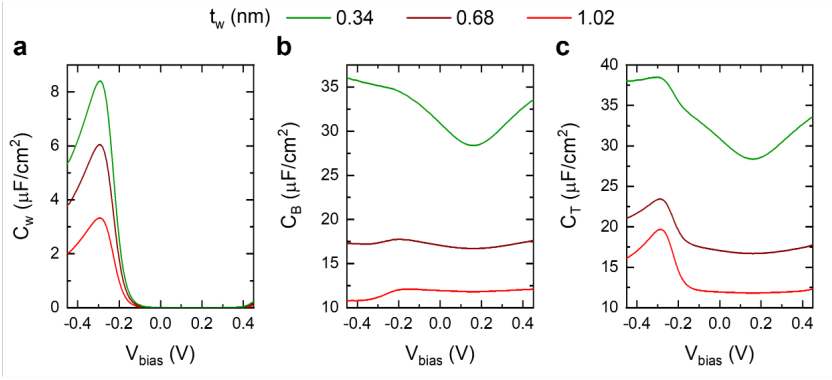


Figure B.5: Contribution of the charge density of the confined water region and the bulk electrolyte to the total capacitance for different t_w - **(a, b)** Capacitances between the ITO substrate and each of the regions of the structure and **(c)** total capacitance of the structure.

As observed, at the vicinity of -0.3 V, the confined water region accumulates enough charge to screen the ITO from the point of the bulk electrolyte. This provokes a large accumulation of charge near the ITO surface, which results in the maximum of C_{ITO} around -0.3 V. At more negative voltage values, the confined water region is not capable to accumulate more charge due to steric effects. Consequently, the capacitance decreases. There, the main charge contribution is attributed to the bulk electrolyte, yet it is less coupled with the ITO due to the presence of the charged confined water region. As the permittivity of

the confined water region increases, the maximum generated by the confined water region is less pronounced, while the capacitance magnitude is increased. This is explained by the better ITO-bulk electrolyte coupling. In this case, the contribution of the bulk electrolyte to the net charge is higher, thus reducing the impact of the charge screening of the confined water region. That is why, for the highest permittivity values, the expected ambipolar capacitance of the electrolyte is observed, but with a decrease at $V_{bias} < 0.3$ V due to the saturation of the confined water region. The profiles charge density profiles of N_w do not reveal variations with t_w (Figure B.4a), yet in the surface density obtained in Figure B.4b it is observed that a thicker region provides a larger surface charge density. This is in agreement with the capacitance profiles depicted in Figure B.5a. In Figure B.4b the lowering of C_B around -0.2 V is evidenced and thus its relation with the confined water region is clearer: the larger the magnitude of C_w, the larger the reduction in the magnitude of C_B.

B.4 PEIS data of pyrex/graphene and ITO/graphene electrodes

The data sets of PEIS measurements on pyrex/graphene and ITO/graphene electrodes at pH 3 and 10 are presented in Figure B.6.

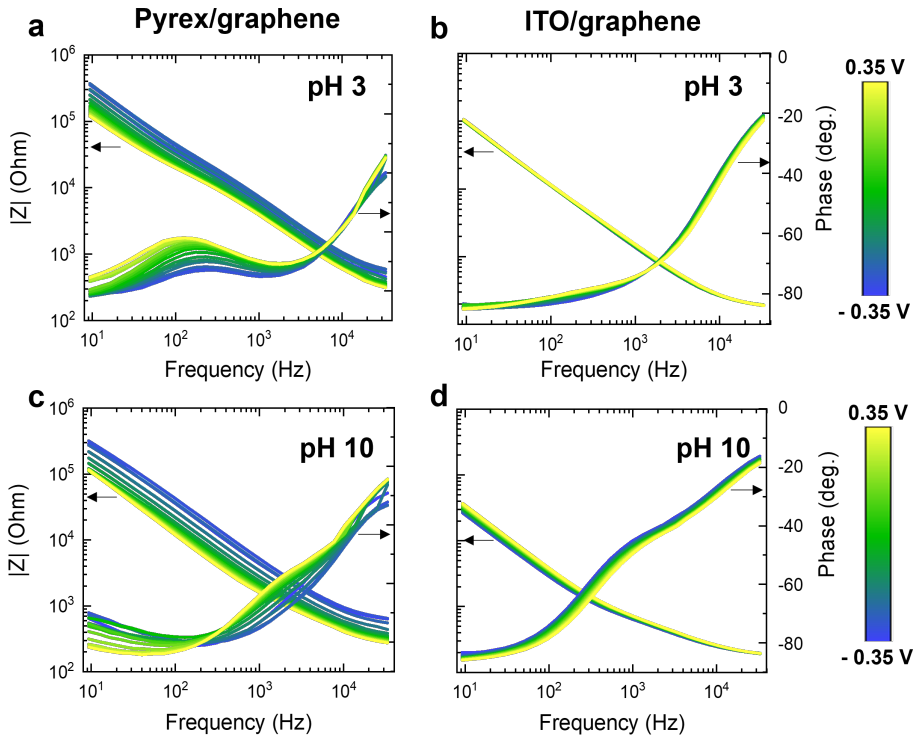


Figure B.6: PEIS of graphene electrodes after fabrication at different pH - (a)(b) Bode plots of pyrex/graphene and ITO/graphene electrodes after fabrication at pH 3. **(c)(d)** Bode plots of pyrex/graphene and ITO/graphene electrodes after fabrication at pH 10.

B.5 Measurements on Au/graphene electrodes

As stated in Chapter 4, Potentiostatic electrochemical impedance, Raman spectroscopy/spectroelectrochemistry, XPS and UPS measurements were also conducted on Au/graphene samples. This section of the Annex depicts the results obtained from them.

Figure B.7 presents the Bode plots and capacitance values at 10 Hz resulting from PEIS measurements on Au/graphene fabricated electrodes[1] in PBS pH 3, 7 and 10.

Figure B.8 shows the ω_G modulation with V obtained from Raman spectroelectrochemistry on Au/graphene electrodes in PBS in different pH and ionic strength. After mimicking the fabrication process, a shift of the CNP towards negative voltages is observed, as an indication of graphene doping.

[1] Mimicking the wafer-scale fabrication process at the cleanroom.

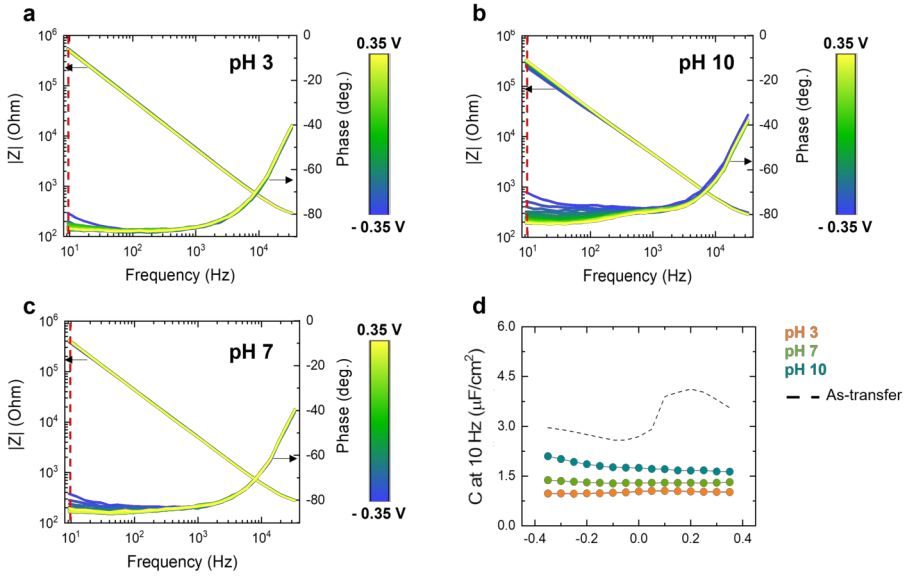


Figure B.7: PEIS of graphene electrodes after fabrication at different pH - (a-c) Bode plots of Au/graphene electrodes after fabrication measured in PBS at pH 3, 10 and 7, respectively. **(d)** Capacitance extracted at 10 Hz.

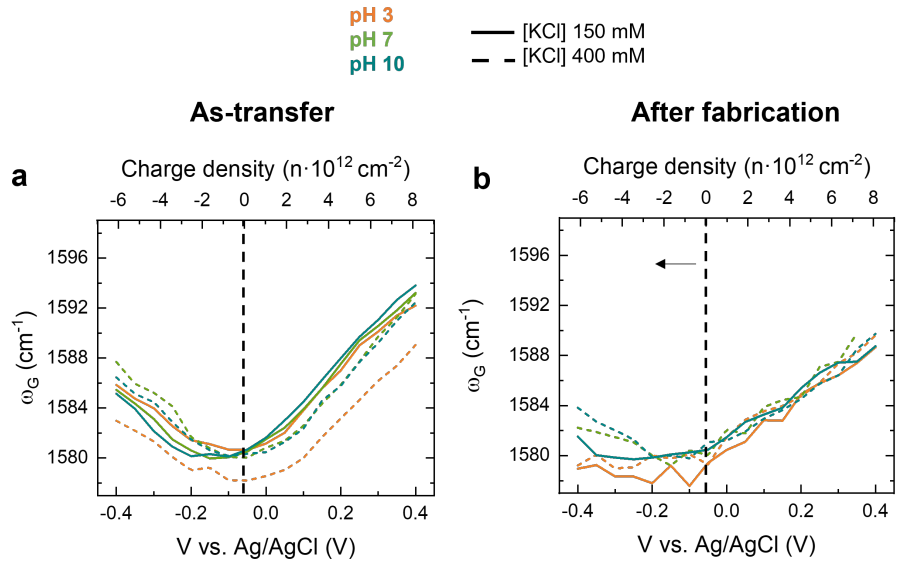


Figure B.8: Raman spectroscopy of Au/graphene electrodes - (a)(b) ω_G modulation with applied V for Au/graphene electrodes before and after mimicking the wafer-scale fabrication process, respectively. Each curve results from measurements in PBS at different pH (3, 7 and 10) and ionic strength ([KCl] = 150 mM and 400 mM.

Figure B.9 shows the C 1s, O 1s and Au 4f core levels of bare Au and Au/graphene samples. Spectra were energy corrected with respect to the Au_0 (Au $4f_{7/2}$) peak at 84.0 eV [299] and the fitting was performed as explained in Section F.4. The presence of carbon and oxygen in the bare Au sample is very low, as the Au^0 peak is significantly more intense. The analysis of the C 1s core level of the as-transfer sample shows the presence of two main components, Csp^2 and Csp^3/C-H. As previously explained (see Chapter 4), these contributions are mainly attributed to the presence of graphene and sp^2 coordinated amorphous carbon [220]. In the Au/graphene fabricated sample, a contribution assigned to the presence of C-O appears, in addition to the two contributions at the as-transfer sample. This is associated with the presence of residues from the fabrication process. Regarding the analysis of the O 1s core level, the bare Au does not show a significant amount of oxygen, which is expected. In as-transfer and fabricated Au/graphene, a peak associated to the presence of C-O (∼533 eV [300]) is measured.

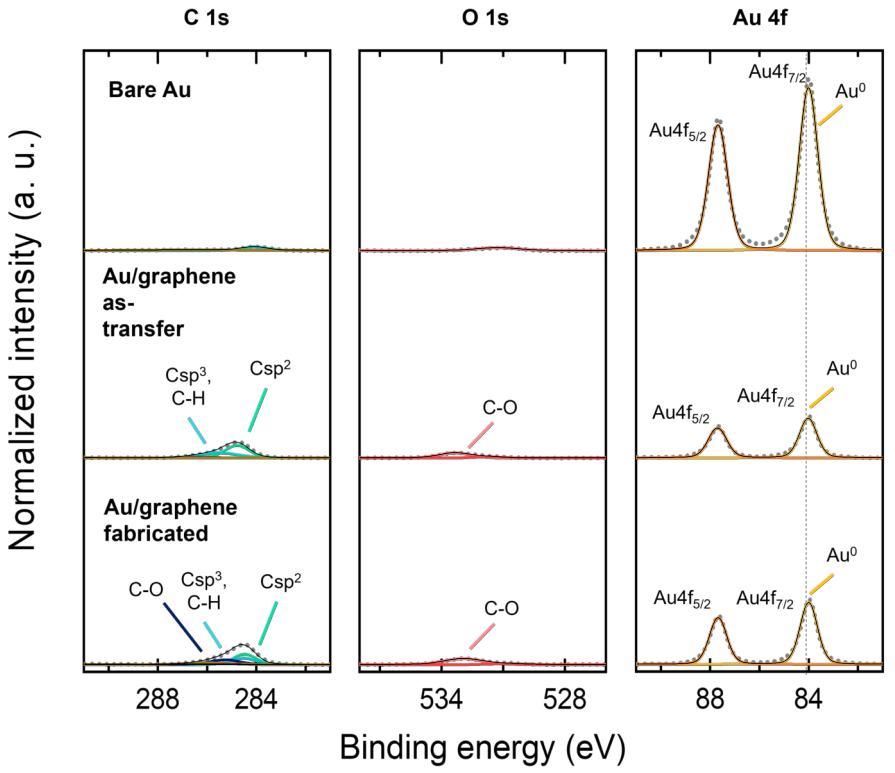


Figure B.9: XPS analysis of Au/graphene electrodes - C 1s, O 1s and Au 4f peak deconvolution for bare Au and Au/graphene samples as-transfer and after fabrication.

The UPS analysis of the Au/graphene and bare Au is summarized in Table B.3 and Figure B.10. This analysis was conducted as detailed in Chapter 4, Section 4.5.

Table B.3: Band structure extraction from UPS on Au/graphene. Energy difference E^F_{VB} between the Fermi level and valence band maximum E_{VB}, secondary electron cut-off $E_{cut-off}$, ionization potential IP and work function Φ, extracted from UPS spectra of the graphene on Au, and of the bare Au samples.

Sample	E^F_{VB} (eV)	$E_{cut-off}$-E^F_{VB} (eV)	IP (eV)	Φ (eV)
Au/graphene	0	16.6	4.6	4.6
	0	16.0	5.2	5.2
bare Au	0	16.8	4.4	4.4

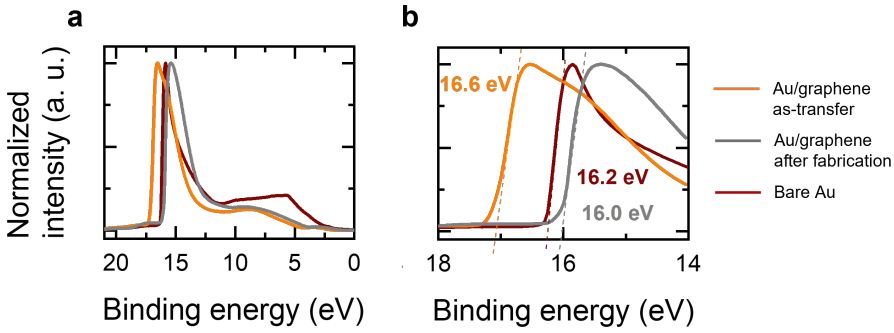


Figure B.10: UPS analysis of Au/graphene electrodes - **(a)** UPS spectra (He-I, 21.2 eV) and **(b)** the secondary electron edge ($E_{cut-off}$) of bare Au and Au/graphene samples as-transfer and after fabrication.

Figure B.11 depicts the Raman spectroscopy analysis of Au/graphene electrodes in PBS with increasing [KCl]. As discussed in Chapter 4, when graphene is on a conductive substrate, the substrate contributes as a variable charge to maintaining the system's charge balance (see equation 4.25), represented for this particular case in Figure B.11. This explains the lack of ω_G modulation with increasing the electrolyte's ionic strength (see Figures B.11a,b).

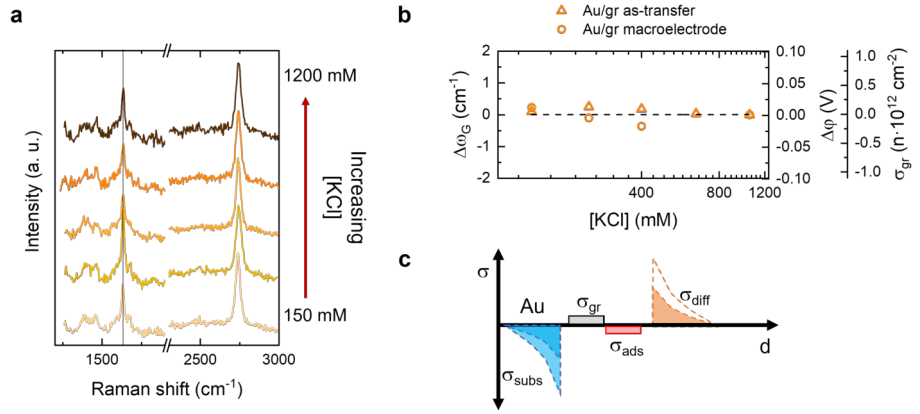


Figure B.11: Raman spectroscopy of Au/graphene electrodes after fabrication in PBS with increasing [KCl] - **(a)** Raman spectra from the average of Raman maps (256 μm^2), PBS pH 3. **(b)** $\Delta\omega_G$ as function of [KCl] at different pH of wafer-scale pyrex/graphene electrodes. $\Delta\omega_G$ is related with $\Delta\varphi$ and σ_{gr} according to equations 4.18 and 2.3, respectively. Black dashed lines correspond to the fitting of the values according to equation 2.3, explained in Chapter 4. **(c)** Scheme of charge distribution in the Au/graphene/surface charge/electrolyte system and its variation with the electrolyte ionic strength.

B.6 Challenges on the integration of the Cu protection strategy to the standard fabrication of wafer-scale graphene electronic devices

Ideally, Cu would have to be deposited on graphene right after graphene transfer, to avoid the surface to get in contact with any photolithography resin. However, this requires a Cu wet etching for defining the area of the Cu protection window, instead of a Cu lift-off (with a previous Cu definition step). When this was intended, the Cu layer was laterally overetched (see Figure B.12a). While this issue remains under study, we decided to move forward by depositing the Cu on graphene after a Cu definition step and assess the compatibility of this strategy with preserving graphene's structure and properties. The second challenge identified is related with the difficulty to uniformly remove photolithography resins, that may be overcured and thus compromise obtaining a high yield of working devices. A representative image of an unsuccessfully etched transistor channel after fabrication with Cu is showed in Figure B.12b. Optically, two different areas are distinguished, one corresponding to graphene (as in the blue square) and the other corresponding to graphene covered by a remaining resin

layer (as in the red square). Analogously to the first challenge described in Chapter 4, this remains under study.

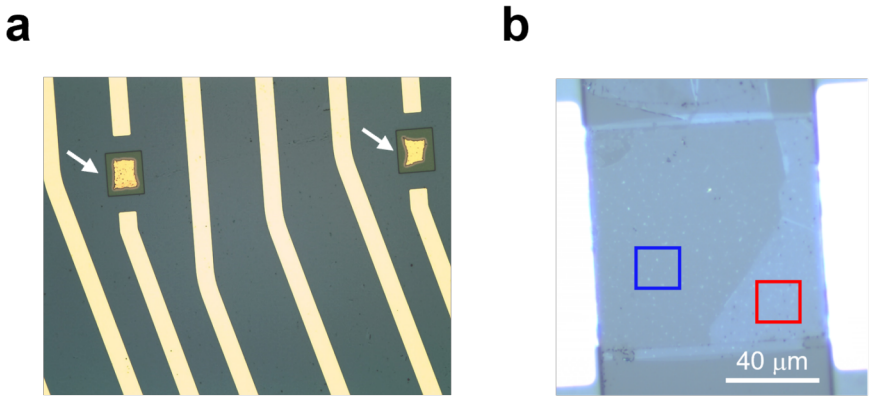


Figure B.12: Issues in the integration of the graphene protection with Cu to the standard fabrication protocol - **(a)** Cu layer on graphene during the fabrication laterally overetched after a wet-etching step $(NH_4)_2S_2O_8$ 0.02 g/ml). **(b)** Graphene of a transistor channel after fabrication with a Cu sacrificial layer defined previously to Cu evaporation. The graphene channel (areas as in the blue square) is partially covered by an undetermined resin layer (areas as in the red square).

Figure B.13a shows an optical image of a 48-gSGFET array on SiO_2/Si fabricated following the standard procedure (see 2.4). In Figure B.13b, a map depicting the $\Delta\omega_G$ values measured according to each transistor is shown. As stated in Chapter 4, this spatial map was represented with the aim to visualize the σ_{ads} distribution along the array, which is inhomogenous. While the fabrication protocol with Cu remains under study, electrical characterization of gSGFETs on SiO_2/Si and on pyrex, without and with Cu protection, was conducted as a preliminary experiment. Given the acquired knowledge about the influence of the substrate on pH dependency, and knowing that the water intercalation phenomena may enable the substrate to be in contact with the bulk electrolyte, it is important to use substrates without surface functional groups that may be charged. That justifies the use of pyrex in our case, alternatively to the standard SiO_2/Si. Figures B.13c,d, show the I_{ds}-V_{gs} transfer curves acquired. Comparing the I_{ds}-V_{gs} curves, the Cu-protected ones show higher homogeneity in both SiO_2/Si and pyrex substrates, in agreement with the Raman spectroscopy measurements (see Chapter 4). The fact that the CNP of the transistors fabricated with Cu appears at higher voltages than the CNP of the transistors fabricated using the standard protocol may be due to an incomplete removal of the Cu

or of the photolithography resins. As explained before, this is currently being addressed. Nevertheless, from these results, it is confirmed that the alternative fabrication strategy with Cu protection is promising and, thus, needs more study.

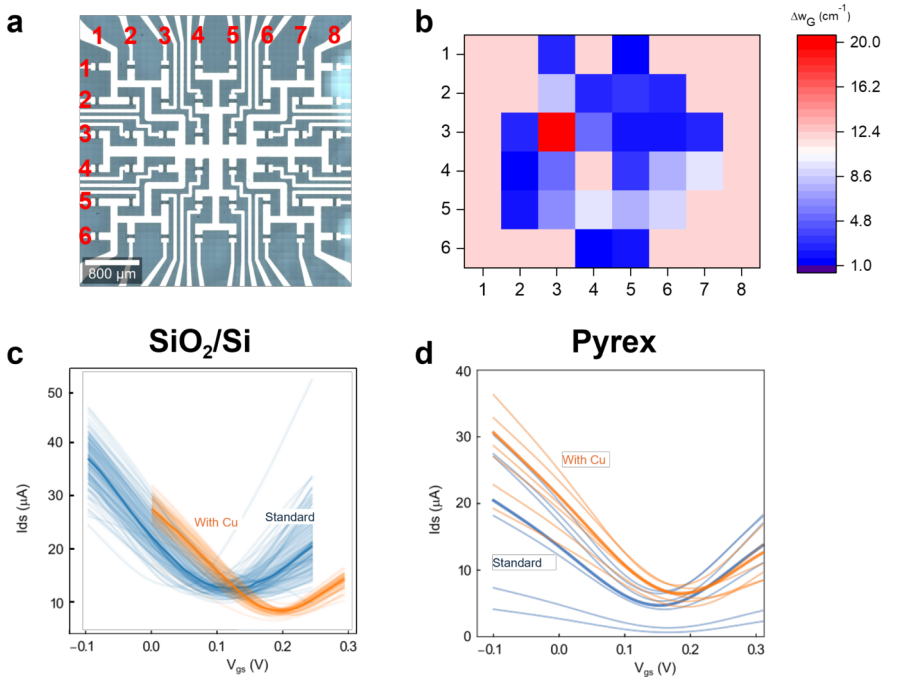


Figure B.13: Electrical characterization of gSGFETs fabricated by standard fabrication and using a protective Cu layer - **(a)** Optical image of the 48-gSGFETs array on SiO_2/Si fabricated following the standard protocol detailed in Section 2.4. **(b)** Map showing the $\Delta\omega_G$ of each transistor measured of the 48-gSGFETs array on SiO_2/Si. **(c)(d)** Electrical characterization of the gSGFETs on SiO_2/Si an pyrex, respectively, fabricated with and without a Cu protective layer on graphene. Measurements are performed in PBS, pH 7.

C

Chapter 5 complementary data

C.1 Aminopyrene deposition on graphene

A DSC of aminopyrene (AP) was performed[1] to test the suitability of the molecule to be sublimated for dry graphene functionalization in vacuum. As depicted in Figure C.1, AP presents one melting point at 118°C. Crystallization of AP after each heating-cooling process carried out was confirmed by the crystallization point maintained after the third cooling ramp, appearing at 84°C.

[1]Laboratory of the Thermal properties of nanoscale materials group, UAB-ICN2

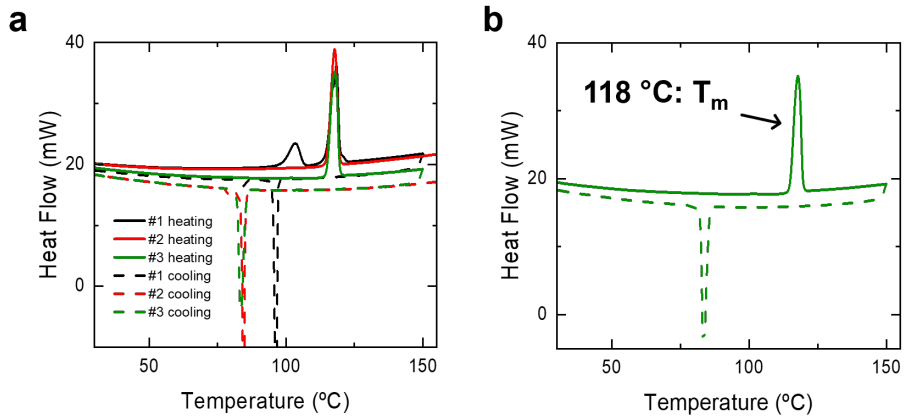


Figure C.1: Differential Scanning Calorimmetry (DSC) analysis of AP - **(a)** All the curves measured **(b)** Final heating-cooling ramps showing one melting point at 118°C and a crystallization point at 84°C.

In view of the DSC analysis, we prepared the AP to be used for graphene functionalization by weighting a small amount of it inside the ceramic crucible and annealing it at 140 °C in an Ar atmosphere (∼ atmospheric pressure). Once it was cooled down to room temperature, it was placed inside the vacuum chamber 5.5 for evaporation.

The in-vacuum graphene functionalization with AP was carried out with the following parameters: $T_{AP} = 50°C$, $T_{subs} = 40°C$, 5 minutes and the resulting surface was analysed by Raman spectroscopy and AFM, as shown in Figure C.2. The characteristic pyrene features in the Raman spectra (red arrows in Figure C.2a) confirmed the presence of this molecule on graphene, and AFM did not reveal the presence of big aggregations. Differently from when functionalizing with PBA, where the aim was to advance towards the obtention of a controlled layer of molecules on graphene, in this case, the objective was to ensure AP deposition with any need of quantification control. Therefore, no further characterization was performed.

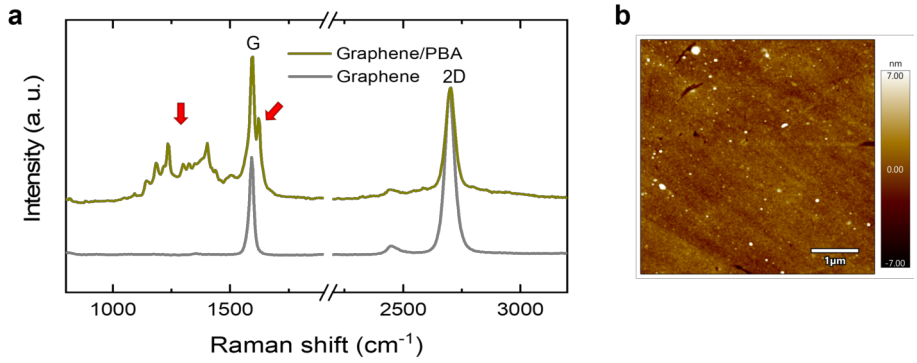


Figure C.2: Characterization of graphene/AP - **(a)** Average Raman spectra of graphene before and after AP functionalization. **(b)** AFM image of the graphene/AP surface.

C.2 Standard effective gate noise values of gSGFETs

The electrical characterization of graphene and graphene/PBA SGFETS in Chapter 5 shows that effective gate noise values, V_{rms} in the standard range of the technology fabricated at the AEMD group. Figure depicts data corresponding to different 48-gSGFETs array devices (see Figure 2.21).

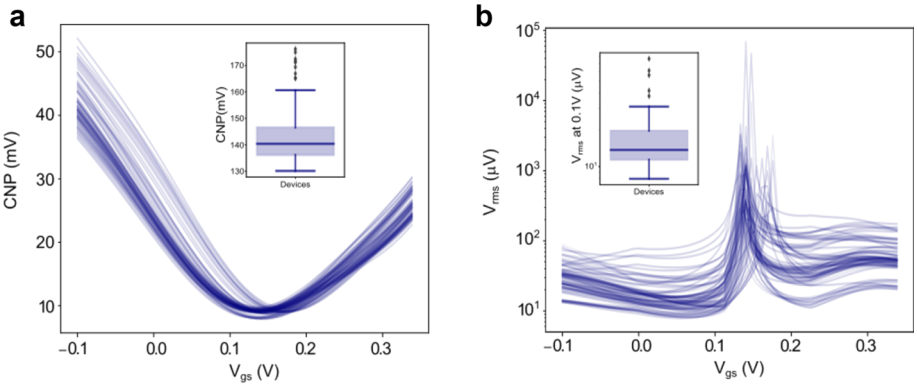


Figure C.3: Electrical characterization of graphene gSFETs (standard) - **(a)(b)** CNP and effective gate noise, V_{rms} of gSFETs on SiO_2/Si. Measurements performed in PBS pH 7. n = 287.

C.3 Aptamer incorporation to graphene/PBA surfaces and thrombin detection

The aim of this study is to demonstrate the utility of the graphene/PBA surface as a biosensing platform performing *in-vitro* thrombin detection, serving as a fundamental starting point towards using this interface for the detection of a broader spectrum of analytes, including neurotransmitters.

As for the previous section, the fabrication and functionalization of the graphene/PBA SGFETs was conducted according to section 2.4 on a pyrex support. The aptamer (TBA) attachment to the graphene/PBA surface was performed by the formation of a peptide bond between the carboxyl group of the PBA and the amine group of the TBA, based on [56]. The detailed mechanism of this chemical process is represented in Figure C.4, and was performed in a chamber where the graphene/PBA SGFETs were placed to enable the required liquid conditions: first, the carboxyl group of the PBA was activated adding 100 mM of N-ethyl-N'-(3-(dimethylamino)propyl)carbodiimide (EDC) and 20 mM of N-hydroxysuccinimide (NHS) prepared in PBS pH 7. Through the intermediate (B) the NHS ester was formed (C) and we proceeded with the addition of the TBA aptamer. This was left overnight and enabled the peptide bonds formation between the PBA and the TBA (D). As a final step, the remaining terminal carboxyl that were not bound to any aptamer unit were blocked with by adding a 100 mM ethanolamine solution in PBS. This was performed to prevent unspecific binding with possible free carboxyl groups. At the end of the process, the resulting system was the one represented in E.

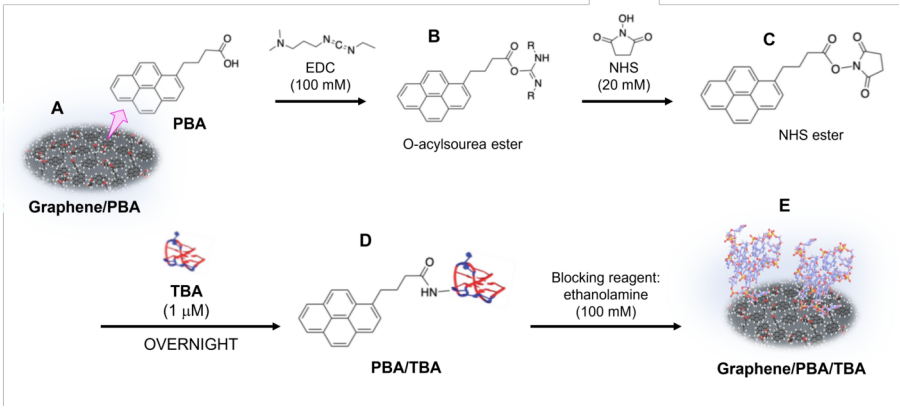


Figure C.4: Aptamer binding to graphene/PBA - EDC/NHS coupling mechanism for the attachment of the TBA aptamer to the graphene/PBA surface and subsequent free -COOH groups blocking. All the solutions were prepared in PBS 10 mM (Sigma Aldrich), pH 7.4. After the formation of D and E, the g-SGFETs surface was rinsed vigorously with PBS.

The evaluation of the sensing capabilities of the prepared g-SGFETs was carried out by exposing them to different thrombin concentrations, ranging from 0.208 nM to 208 nM. To compare this with the reported results from an in-liquid functionalization approach [56], we used SiO_2/Si as substrate for the devices. After confirming the graphene functionalization with PBA and subsequent aptamer attachment (Figure C.5a), we monitored the CNP variations after incubation with the different thrombin solutions (Figure C.5b). We observed that the measured CNP shifted towards more negative voltages after each incubation, ending with a total ΔCNP of 14 mV. The negative shift responds to n-doping induced by thrombin, which is positively charged at pH 7 [301, 302]. The stabilization of the CNP after incubation at [208 nM] suggested a saturation point at this concentration [56]. A final incubation in PBS after the last thrombin concentration resulted in a negligible ΔCNP. This confirmed the strong binding between the TBA and the thrombin, which is reported to be Kd ∼100 nm [303].

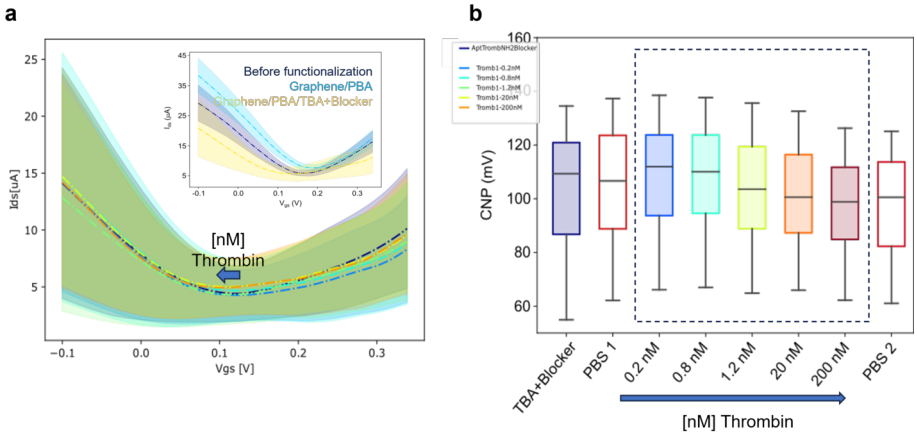


Figure C.5: Thrombin detection - **(a)** I_{ds}-V_{gs} curves of the g-SGFETs: before and after PBA functionalization and after TBA+Blocker addition. **(b)** CNP from the curves in **(a)**. **(c)** I_{ds}-V_{gs} curves of the g-SGFETs: after TBA+Blocker addition (dark blue) and after incubation in different thrombin concentrations, as indicated by the legend. **(d)** CNP extracted from the I_{ds}-V_{gs} curves in **(c)**. n=14 channels.

C.4 Grazing Incidence Small-angle X-ray scattering on graphene/PBA surfaces

Grazing Incidence Small-angle X-ray scattering (GIWAXS) is a non-destructive technique that uses synchrotron radiation sources to analyze the structure (size, geometry, alignment and distribution) of thin layers on flat substrates at the nanoscale (3-50 nm). Because it uses a reflection geometry, it achieves surface and near surface sensitive scattering, and its use has been increased lately due to a the raising demand and the incorporation of dedicated beamlines at more synchrotrons around the world. Hence, it is becoming a standard tool to probe thin films and nanostructured surfaces, in combination with other techniques such as AFM and transmission electron microscopy (TEM) [304].

GIWAXS measurements were carried out at the ALBA synchrotron facilities (Cerdanyola del Vallès, Barcelona) in order to advance in the quantification of 1-pyrenebutyric layers deposited on graphene with the dry approach presented in Chapter 5. Specifically, we used beamline BL11 NCD-SWEET GIWAXS endstation (energy 12.4 keV) with a Rayonix LX255HS detector. Figure C.6 shows the 2D GIWAXS patterns obtained for a graphene/PBA sample (functionalization conditions: T_{PBA}=115°C, T_{subs}=80°C, 15 minutes). Apart from a contribution attributed to the substrate (pyrex, SiO_2), no characteristic signal from the PBA layer was measured. This can be due to different hypothetical situations: first, that the PBA layer is too thin to be detected, or it is not showing enough electronic contrast. Second, that the order level of the molecules is low or absent, therefore no peaks from it are shown. In Chapter 5, we calculated < 4 PBA layers on graphene with the cited functionalization conditions, which would explain the absence of signal from the molecules in Figure C.6. For future analysis, we propose the characterization of thicker PBA layers to evaluate the signals they present, and subsequently decrease the layer thickness to ensure the minimum visible thickness by GIWAXS.

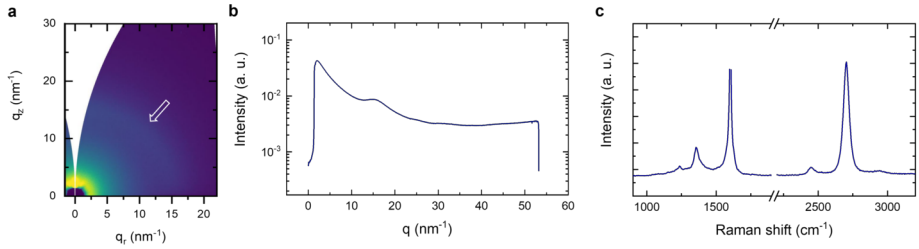


Figure C.6: 2D GIWAXS of graphene/PBA - **(a)** 2D GIWAXS patterns of a graphene/PBA sample on a pyrex support. The arrow indicates the signal attributed to SiO_2. **(b)** Corresponding azimuthal integrations of 2D GIWAXS patterns.

D

Water intercalation in graphene devices

Confined water underneath graphene is present from the transfer process of graphene to the substrate [201, 200, 176]. Furthermore, considering situations in which graphene devices are immersed in an aqueous electrolyte, for instance during the fabrication of the devices or their use for applications in biosensing, water intercalation exists [202]. Therefore, even carrying out a water-free transfer process, water intercalates while the device is being used. Since this phenomena is unavoided, it is of paramount importance that we assess its impact on graphene-based devices performance. Earlier in this thesis (see Chapter 4), we refer to a study regarding this topic developed on graphene electrodes. Here, we discuss water intercalation effects on g-SGFETs.

There are a number of experimental ways to observe intercalated water between graphene and the substrate [174, 201, 305, 306, 176, 307]. However, a specific quantification of this water is difficult. In view of that, we carried out a preliminary study with the clear objective to see the water intercalation effect on the device functionality.

Raman spectroscopy of graphene provides information about substrate-graphene coupling by analyzing shifts in frequency of the 2D band (ω_{2D}), as stated in Chapter 4. With the aim of monitoring water intercalation dynamics, we performed time scan Raman spectra in PBS. While graphene is immersed in an aqueous media, a red-shift of the ω_{2D} is observed progressively over time until 1.5

hours, when it stabilizes (Figure D.1a). A shift of around 3.5 cm^{-1} is measured and consistent for all the measured as transfer pyrex/graphene samples, as shown in Figure D.1b. A ω_{2D} red-shift is indicative of graphene decoupling from the substrate, previously attributed to water intercalation [203, 204]. Adhesion force maps were also acquired for water intercalation observation. In Figure D.1c, images correspond to maps acquired before and after the sample was immersed in PBS for 2 hours, demonstrating the different behaviour depending on the situation. After immersion, the tip-sample adhesion force registered decreased in homogeneity along the scanned surface, indicative of a non-uniform intercalated water distribution between graphene and the substrate underneath, which is represented in the histogram at Figure D.1d.

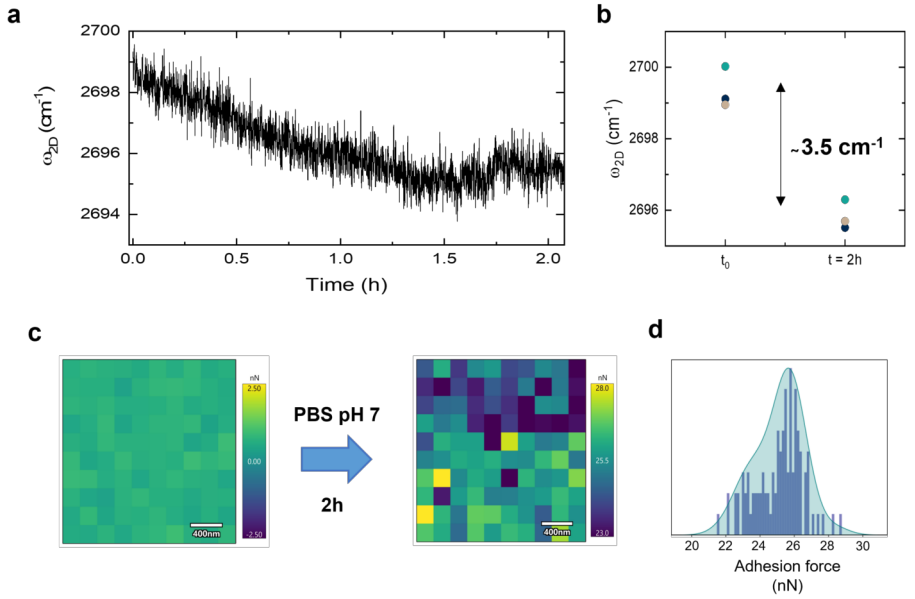


Figure D.1: Water intercalation in as-transfer graphene on pyrex - (a) Graphene ω_{2D} evolution with time in PBS. **(b)** Statistical data corresponding to 3 different as transfer pyrex/graphene samples. **(c)** AFM adhesion force map before (left) and after (right) 2h in PBS and **(d)** the histogram adhesion force analysis after immersion.

Moving forward, we evaluated the presence of water intercalation on fabricated devices. To that aim, we designed a platform of g-SGFETs on a Si/SiO_2 support, containing different transistors, specifically including different size and width/length (W/L) ratios (see Figure D.2b) and different passivation designs (see Figure D.2c). In the AEMD group standard technology, passivation of the graphene transistors is performed covering the two contact edges of the channel.

This raised the question of the water being intercalated through the channel edges or not. Therefore, we included a passivation covering the four edges of the channel for this to be clarified.

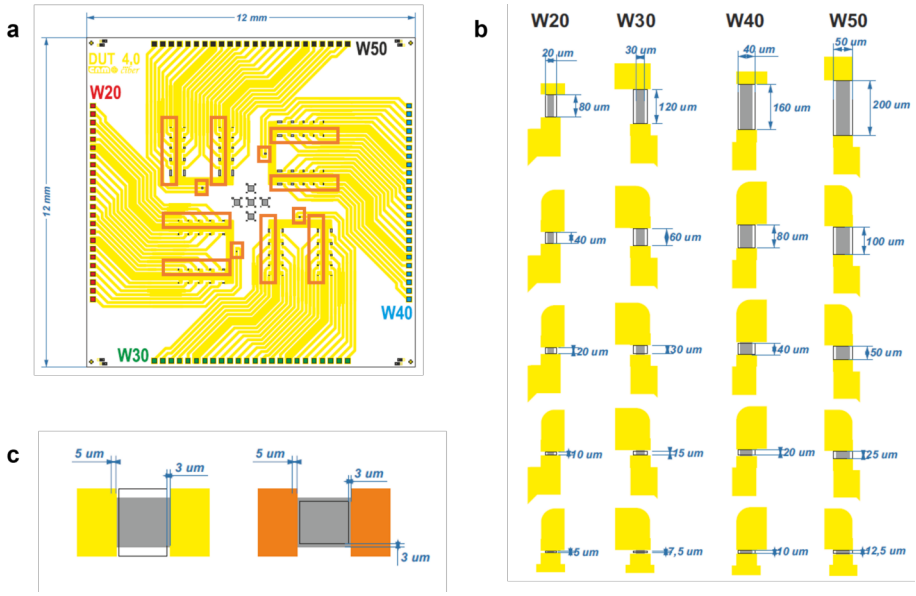


Figure D.2: Device under test (DUT) - **(a)** Mask of the DUT designed for water intercalation studies. **(b)** Size and width/length (W/L) ratios. **(c)** Passivation designs.

Figure D.3a depicts the Raman average spectra of a graphene transistor before and after immersion in PBS (pH 7) for 2 hours, as shown in Chapter 4. Figures D.3b,c show the histogram of the graphene 2D band position for a 50×50 μm and a 200×50 μm transistor respectively. A ω_{2D} red-shift of $\sim$ 7.0 cm^{-1} is extracted for the smaller transistor, while a red-shift of $\sim$ 3.5 cm^{-1} is observed for the larger one after the 2h immersion in PBS, in agreement with results on as transfer graphene (Figure D.1b). Interestingly, no differences were found regarding the passivation design, supporting the hypothesis of water intercalation happening through graphene grain boundaries.

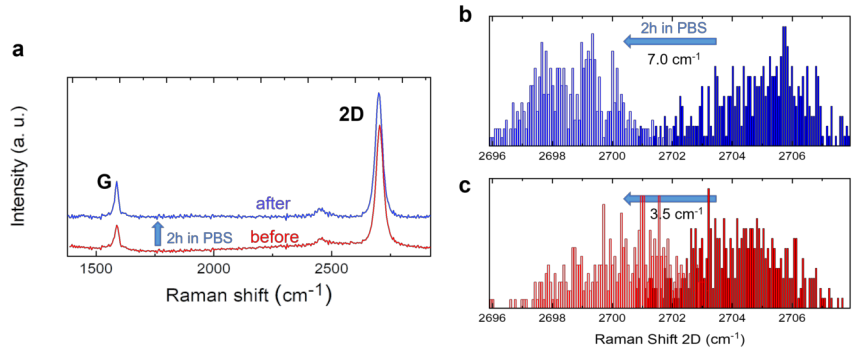


Figure D.3: Water intercalation in graphene devices observed by Raman spectroscopy - (a) Average Raman spectra of graphene as part of a transistor channel in a DUT before and after 2h immersion in PBS. **(b)(c)** Histogram analysis of the ω_{2D} for graphene transistors of 50×50 μm and 200×50 μm, respectively.

Adhesion force AFM mapping was not possible for the fabricated samples as residual charge on graphene surface impossibilited correct performance. Instead, the KPFM images in Figure 4.11d (see Chapter 4) and the corresponding histogram analysis demonstrate that, starting from a fabricated device, immersion in an aqueous electrolyte (PBS) favours non-homogeneous water intercalation between graphene and the substrate underneath, as water "islands" are clearly formed.

The g-SGFETs electrical characterization is shown in Figure D.4. A decrement of the devices noise level (V_{rms}) is measured, after being in PBS for 2 hours, which represents an improving on the devices performance. Differently, regarding transconductance (g_m), it decreased after PBS immersion, which involves a negative effect in device performance, as it means a decrement in sensitivity []. Finally, an important fact to be remarked is the absence of two differentiated kind of behaviors that could be related to the two different types of passivation in the device design. This allowed us to discard the hypothesis of water intercalation occurring significantly through the transistors channel edges, and to confirm that water mainly intercalates through graphene boundaries, in agreement with literature [308]. Taking that into account, efforts towards finding effective strategies to prevent water intercalation through graphene grain boundaries should be considered. A proposed approach would be the addition of a very thin layer of a dielectric, e.g. alumina (Al_2O_3) by selective atomic layer deposition on the graphene grain boundaries, as it has been demonstrated using metals [309].

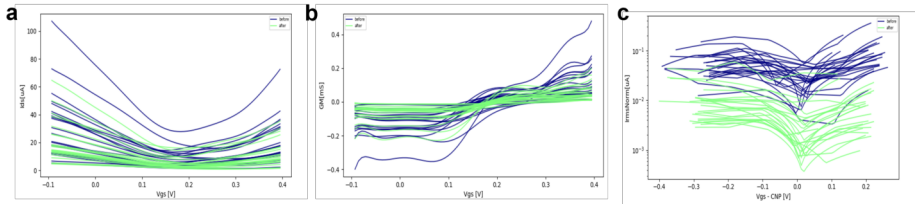


Figure D.4: Electrical characterization of gSGFETs before and after immersion in PBS - (a)(b)(c) I_{ds}-V_{gs} transfer curves, transconductance g_m and V_{rms} from the DUTs characterization.

In summary, this study highlights the role of water intercalation in device performance and remarks the difficulty to control the amount of confined water in graphene devices from the earliest stages of preparation (graphene transfer) to the latest. In one hand, graphene transfer has been intended to be optimized in literature to avoid the presence of water underneath graphene by incorporating annealing processes or improve dry approaches. Nevertheless, a complete, direct substrate-graphene interaction is still challenging to be accomplished at this stage. On the other hand, the wafer-scale fabrication process at the clean room involves cleaning steps in-liquid, which despite being time-controlled, may also induce non-homogeneities from sample to sample. Finally, if the final application given for the fabricated graphene devices is developed in a liquid environment, which is the case of neural implants or biosensing devices in the biomedical field, water intercalation phenomena is of paramount importance to be controlled.

E

In-liquid Dual-Harmonic KPFM for the study of electronic properties of graphene materials and devices

In the line of gaining knowledge about the graphene-related interfaces in an electronic device operating in liquid, we investigated DH-KPFM as a complementary technique to the work discussed in this thesis. The training and development of the experiments presented in this DH-KPFM study were performed in the framework of an international research stay at the Functional Atomic Force Microscopy Group (F-AFM), Center for Nanophase Materials Sciences (CNMS) of the Oak Ridge National Laboratory (Tennessee, USA).

DH-KPFM is a derivative of KPFM that, contrary to this one, works without applying a DC bias (V_{DC}) between the tip and the sample. Thus, DH-KPFM is known as an "open-loop" KPFM approach [310]. When a conductive tip approaches a conducting sample, the electrostatic force induced has three contributions. The first one, F_{DC}, appears due to the static DC bending. Then, the second and third contributions come from the cantilever oscillating at two harmonic frequencies: F_{ω} and $F_{2\omega}$. These harmonic responses are described by:

$$F_\omega = \frac{dC}{dz}[V_{DC} - V_{CPD}]V_{AC}sin(\omega t) \tag{E.1}$$

$$F_{2\omega} = -\frac{1}{4}\frac{dC}{dz}V_{AC}^2 cos(2\omega t) \tag{E.2}$$

By combining E.1 and E.2, we can obtain the contact potential difference (V_{CPD}) between the tip and the sample, which can be further related with work function values (see equation E.4 further above):

$$V_{CPD} = \frac{A_\omega cos(\varphi_\omega)}{A_{2\omega}}\frac{V_{AC}}{4X_{gain}} \tag{E.3}$$

where A_ω and $A_{2\omega}$ are the electrostatic force first and second harmonic amplitude responses respectively, X_{gain} the coefficient resulting of dividing the gains of the cantilever at ω and 2ω and φ_ω is the phase of the ω response [311]. In DH-KPFM studies, the images corresponding to acquired mixed response of the first harmonic ($A_\omega cos(\varphi_\omega)$), the $A_{2\omega}$ and the resulting V_{CPD} are generally shown. The first harmonic mixed response contains information of both the magnitude and sign of the sample's surface charge with respect to the tip. The second harmonic amplitude responds to changes in the probe-sample capacitor geometry. Hence, contrast in $A_{2\omega}$ images is related to changes in the capacitance gradient (C'_z) [311, 312]. V_{CPD} can be related to the sample's work function (Φ_{sample}) by [311, 313]:

$$V_{CPD} = \frac{\Delta\Phi}{e} = \frac{\Phi_{tip} - \Phi_{sample}}{e} \tag{E.4}$$

where e is the elementary charge.

In 2014, Collins *et al* demonstrated contact potential difference (CPD) imaging of as grown graphene on a copper foil in a liquid media for the first time [311]. This opened a door to the direct observation of graphene electronic behaviour in electrolytes, which is of high interest considering its applications in biomedicine.

We prepared graphene samples on pyrex and ITO substrates to scan them by DH-KPFM[1] and test the imaging capabilities in increasing ionic concentrations of PBS. Additionally, we aimed to assess how the substrate nature influenced the measurement of graphene work function in water. We scanned for image acquisition at an area of the sample which included four different regions, as indicated in Figure E.1: the bare substrate, bare Au, graphene on substrate and graphene on Au. The bare Au region served as a reference. We used Multi75E-G AFM probes[2] (Cr/Pt), with a resonant frequency of 75 kHz.

[1] Asylum Research MFP-3D.
[2] Budget Sensors

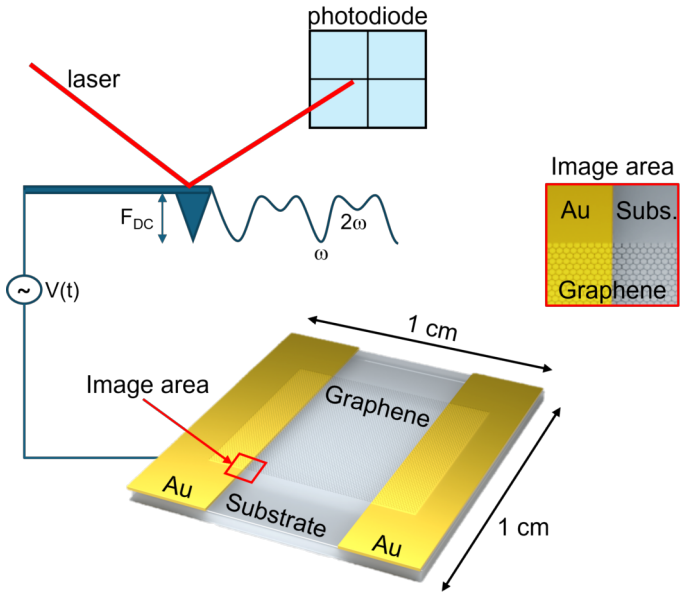


Figure E.1: DH-KPFM setup - Schematic representation of the DH-KPFM experimental setup used for the measurements in this study and the image area where the scans were performed.

First, we performed the measurements in ambient (dry) conditions. Then, we scanned in MQ-water and continued with subsequent measurements in the different PBS solutions, starting with an ionic concentration of 1 μM. Results are depicted in figures E.2 and E.3 for graphene on pyrex and ITO substrates, respectively. As observed, measurements were possible until [PBS] = 1 mM, where the electric double layer charge relaxation and Debye times are not low enough to ensure operability due to mobile charged ions inducing charge screening, among other related phenomena [311, 312].

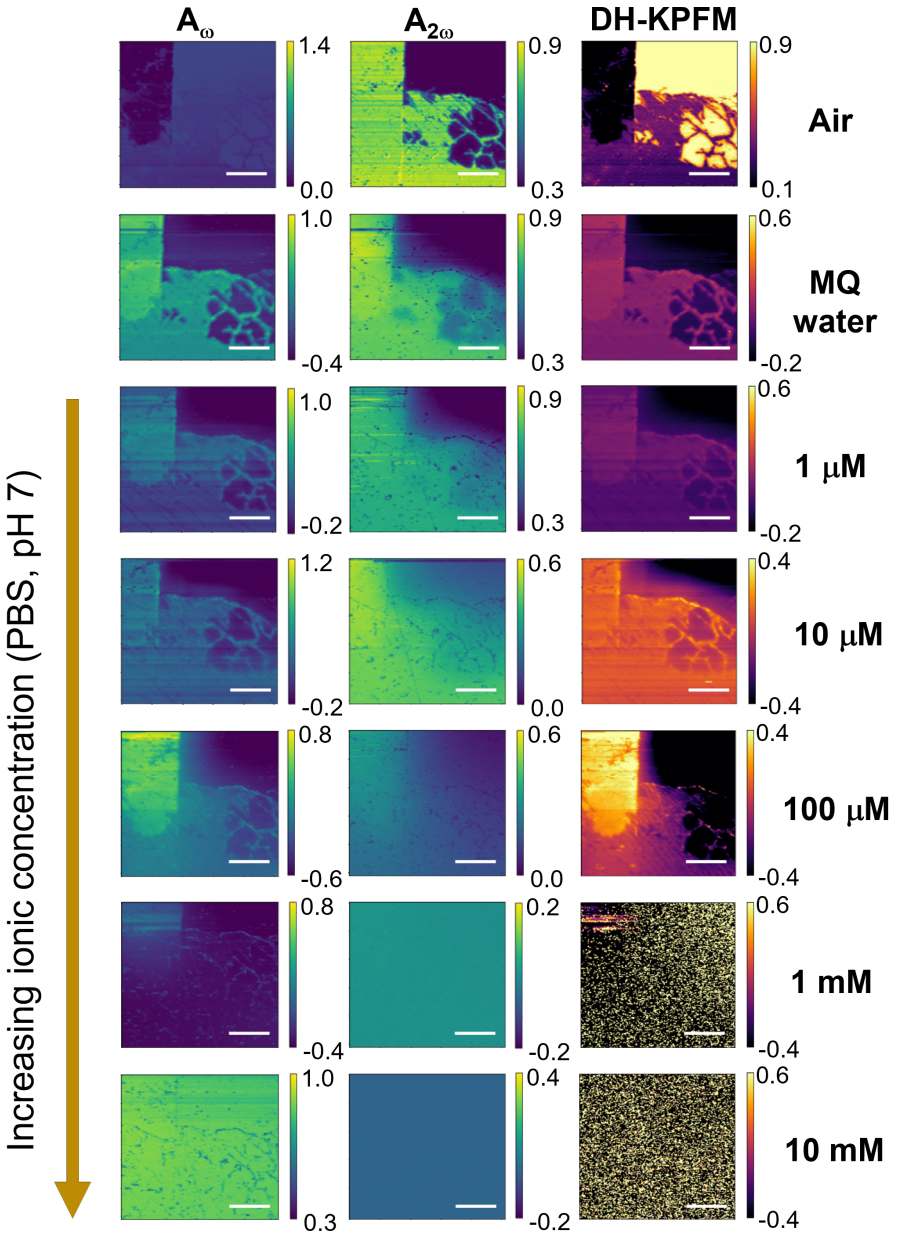


Figure E.2: In-liquid DH-KPFM on pyrex/graphene - First and second harmonic responses ($A_\omega\cos(\varphi_\omega)$ and $A_{2\omega}$ respectively), and the resulting V_{CPD} of a pyrex/graphene sample in dry and in liquid conditions. Scale bar in all images is 20 μm.

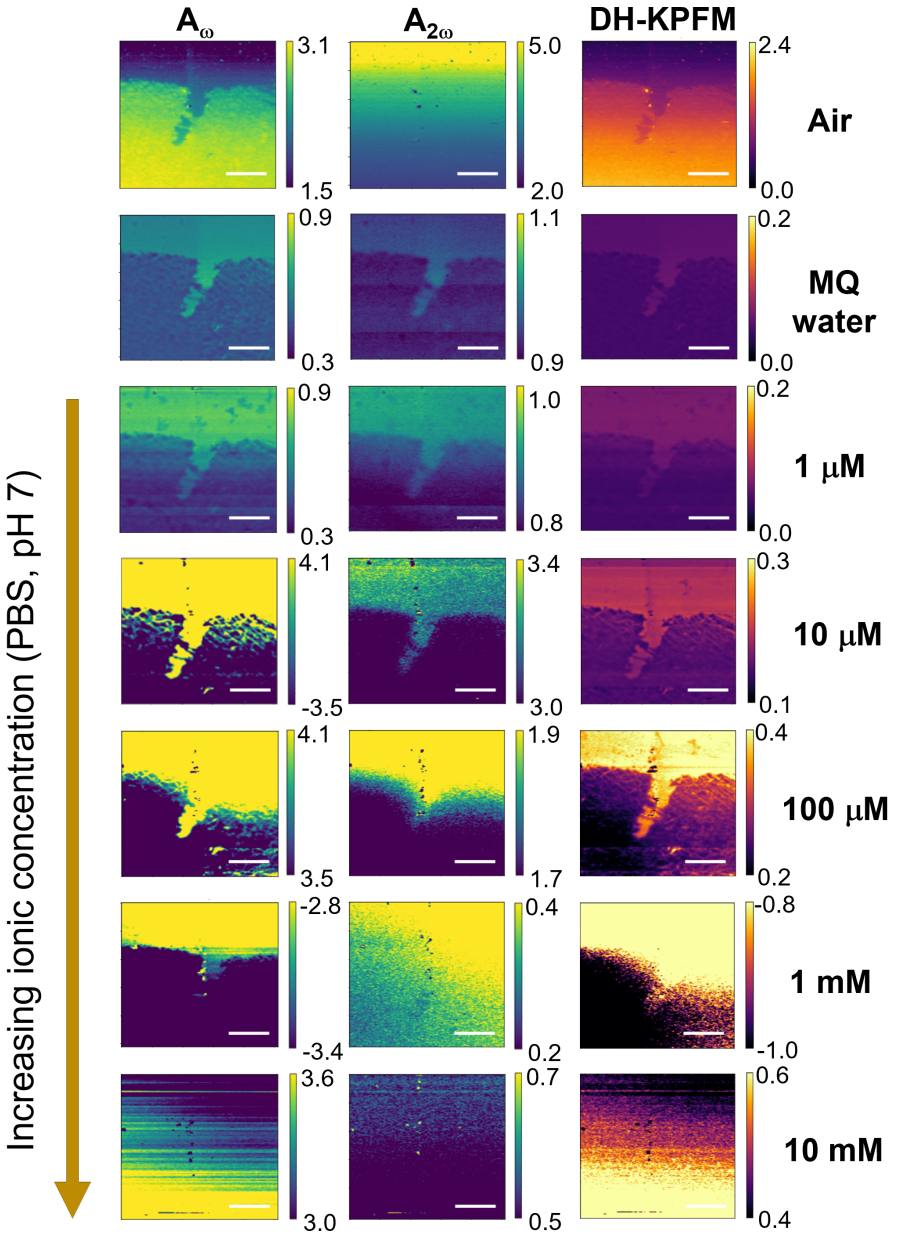


Figure E.3: In-liquid DH-KPFM on ITO/graphene - First and second harmonic responses ($A_\omega cos(\varphi_\omega)$ and $A_{2\omega}$ respectively), and the resulting V_{CPD} of an ITO/graphene sample in dry and in liquid conditions. Scale bar in all images is 20 μm.

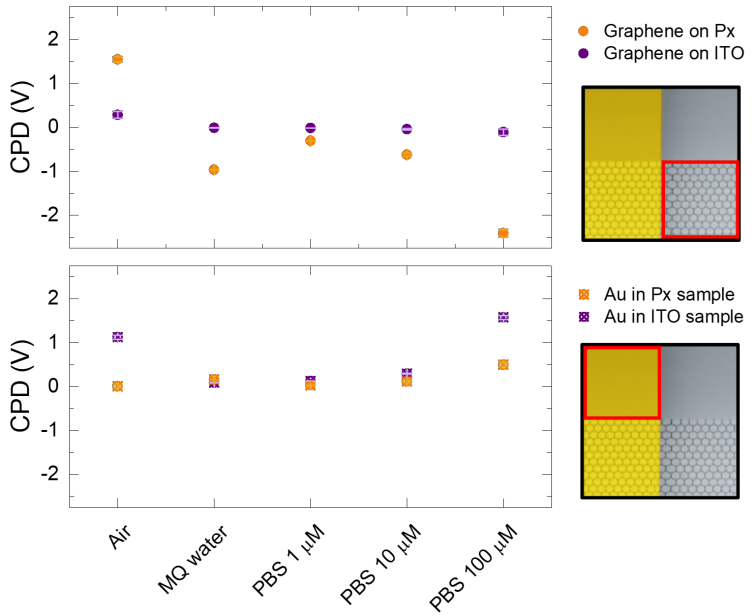


Figure E.4: CPD values from DH-KPFM - CPD values of (top) tip-graphene on pyrex and ITO substrates and (bottom) tip-Au, under different imaging conditions: dry (air), MQ water and PBS in increasing concentrations. CPD values of tip-graphene were calculated with respect to the tip-Au CPD values.

As plotted in Figure E.4, the CPD of tip-graphene in air was measured to be 1.548±0.065 V and 0.286±0.079 V when supported on pyrex and ITO respectively. This is consistent with the conductive nature of the two substrates: as ITO is conductive, its work function is more similar to the one of the tip, thus the measured CPD of ITO/graphene is less than for pyrex/graphene, being pyrex a non-conductive support. In MQ-water, the tip-graphene CPD values were -0.961±0.005 V and -0.008±0.004 V respectively. Remarkably, the sign of the surface charge was shifted to the opposite with respect to the one measured in air in both cases, as a consequence of a change in the first harmonic response. Regarding the magnitude of the tip-graphene CPD, we observed a decrement in both systems: $|\Delta_{CPD,air-MQ}| \sim 1.56$ and 1.24 V for graphene on pyrex and ITO respectively. According to equation E.4, a decrement in V_{CPD} is related with an increasing of the Φ_{sample}, in our case, the graphene's work function. Knowing that an increasing of the graphene's work function indicates more p-doping level [314, 315], and that water on graphene induces p-doping [316, 317], our results revealed that the water ability to induce p-doping is higher when graphene is on pyrex than on ITO. The substrate influence on the graphene doping by its interaction

with water has been previously studied [318]. However, the techniques used so far (KPFM in controlled humidity levels) didn't allow direct measurements in liquid. Thus, the presented DH-KPFM measurements here not only represent the first measurements of as-transfer CVD graphene on substrates of different nature, but pave the path towards in-situ and in-operando monitoring of graphene devices electronic behavior in water.

E.1 DH-KPFM of an in-operando gSGFET

One of the most important parameters to optimize for improving gSGFETs fabrication is the devices contact resistance (R_c) [319]. A high R_c in graphene transistors detriments its performance and is caused, among other parameters, by the work function differences between graphene and the contacting metals [320, 321, 322, 323]. Thus, knowing the values of the contact resistance of a standard fabricated device will facilitate the optimization of the fabrication procedure. The contact resistance of graphene transistors can be evaluated by what is known as the transfer length method (TLM), which consists on measuring the total resistance of devices with different channel lengths, normally in a back gate configuration, applying different back-gate voltages (Vg) [324, 325]. KPFM, as a technique that allows the mapping of the graphene surface potential, has been also used to obtain R_c values of graphene devices [322] in dry conditions. To the best of our knowledge, this parameter has never been measured using in-liquid DH-KPFM. However, direct visualization of the surface potential distribution while measuring the R_c of gSGFETs in liquid is of high interest considering the biological applications of the devices.

To perform in-liquid DH-KPFM of gSGFETs, we designed devices supported on pyrex, as represented in Figure E.5, taking into account the following requirements:

- Channel length: it must be in the range of the devices used in the standard technology, while enabling a stable DH-KPFM measurement. Thus, the designed devices were of 20 μm.
- A surface of the Au contacts must be left exposed (non-passivated). This responds to the need of measuring the potential at the drain and the source for subsequent R_c measurement.

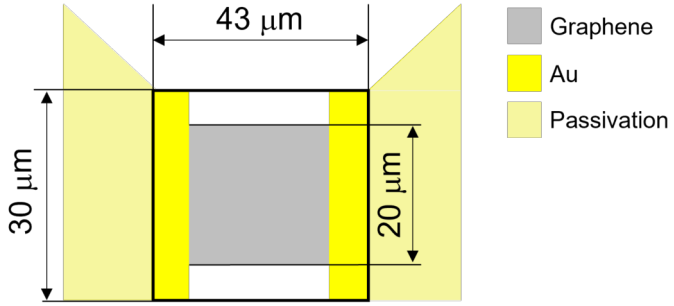


Figure E.5: Transistor design for in-liquid DH-KPFM measurements - Schematics of graphene transistors designed for in-liquid DH-KPFM measurements. Its fabrication was carried out following the lithography-based protocol described in section 2.4.2.

As a first experiment, we performed DH-KPFM in dry conditions. Image acquisition was carried out while applying different V_{DS}, as presented in Figure E.6, using an electrical force modulation (EFM) AFM probe[3] (Pt/Ir), with a resonant frequency of 75 kHz. From the images in Figure E.6a-c, we confirmed that a successful DH-KPFM measurement was achieved, as the voltage change could be monitored accordingly. The analysis of the voltage drop through the graphene channel in Figure E.6d demonstrated good correlation with analogous KPFM experiments reported [322]. Then, we placed a droplet of Milli-Q water on the device to perform in-liquid DH-KPFM. Figure E.7a-c show the harmonic responses and the CPD along the analysed graphene transistor while applying different V_{DS}. Interestingly, the CPD distribution presented the behavior plotted in FigureE.7d, which was different from the expected voltage drop through the graphene channel measured in dry conditions. To provide an explanation of this, more devices should be analyzed - unfortunately not possible within the duration of this dissertation -. This would enable us to assess weather this measurement was affected by any experimental perturbation, like a possible short-circuit enabled by water in contact with the cantilever of the AFM tip.

[3]NanoWorld

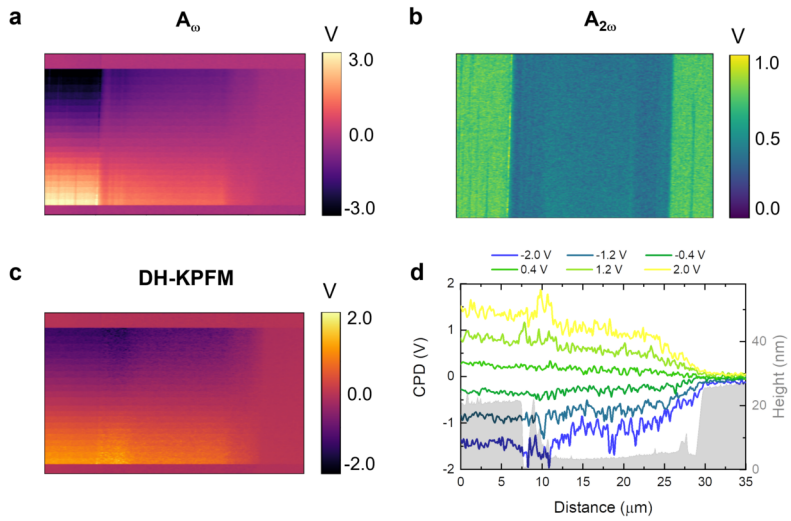


Figure E.6: DH-KPFM of an *in-operando* graphene transistor - (a, b, c) First and second harmonic responses and the resulting V_{CPD}, respectively, of a graphene transistor fabricated on a pyrex support while applying different V_{DS}, from 2.0 V to -2.0 V in steps of 0.2 V. The width of all images is 35 μm; χ_{gain}=1.05; V_{AC}=1.5 V; DH=20 nm. **(d)** CPD analysis of the device, showing some of the voltage profiles measured.

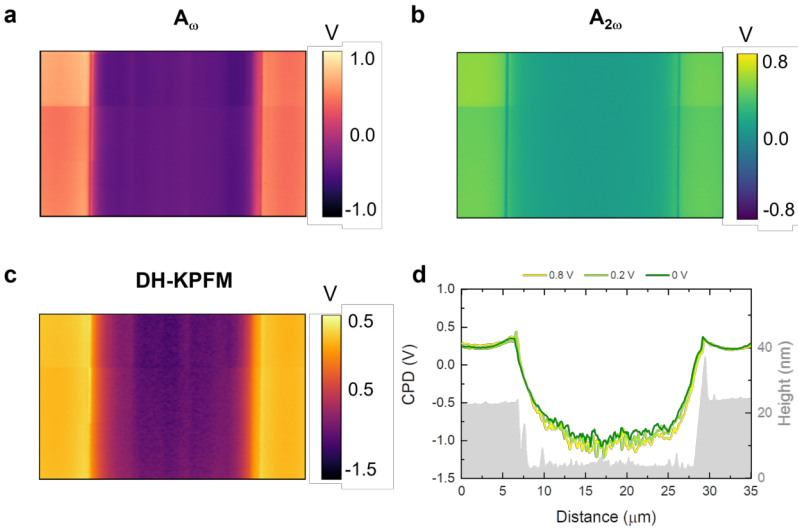


Figure E.7: in-liquid DH-KPFM of an *in-operando* graphene transistor - (a)(b)(c) First and second harmonic responses and the resulting V_{CPD}, respectively, of a graphene transistor fabricated on a pyrex support while applying different V_{DS} (0.0, 0.2 and 0.8V) in MQ water. The width of all images is 35 μm; χ_{gain}=1.05; V_{AC}=1.4 V; DH=20 nm. **(d)** CPD analysis of the device, showing the voltage profiles measured.

F

Experimental techniques: fundamentals and equipment

F.1 Metal deposition

Metal deposition was part of two global processes in this thesis:

1. **Copper deposition:** in Chapter 3, for the preparation of rigid substrates for CVD graphene growth. 800 nm of 99.99% purity Cu[1] were deposited on SiO_2/Si and c-plane sapphire substrates. In Chapter 4, for the deposition of a Cu protection layer during graphene devices fabrication, as a proposed approach to prevent the accumulation of fabrication residues on graphene surface.

2. **Metallic contacts of graphene devices:** for the first and second metal layer as steps of the wafer scale fabrication process, detailed in Section 2.4.2.

Both kind of depositions were performed by electron-beam evaporation, described below.

[1] Kurt J. Lesker

F.1.1 Electron-beam evaporation

Metal evaporation by e-beam is carried out under high vacuum conditions. After introducing the substrate inside the vacuum chamber, the process starts with the heating of a tungsten filament at a temperature that enables the emission of an electron beam. Thanks to the presence of electric and magnetic fields, this beam heats a crucible containing the source material - the metal aimed to be evaporated -. The high vacuum conditions allow the metallic particles to travel from the crucible to the substrate in a direct path, with minimal collisions with residual gas molecules.

The device where all the electron-beam (e-beam) evaporations of this thesis have been performed is an AJA International Inc. ATC-8E Orion e-beam, placed inside the ICN2 clean room and shown in Figure F.1. A load-lock chamber connected to the main chamber through a load-lock valve allows the loading of the samples without breaking the ultra high vacuum ($1{\cdot}10^{-8}$ mbar) needed for the evaporation, which can be maintained at the main chamber. The e-beam gun and the source metals are located inside the main chamber. Samples are placed in holders facing down, as the deposition is performed vertically, from the source metals inside inert crucibles at the bottom of the chamber. Possible contamination from the crucibles containing the source metals is further prevented thanks to a water cooling system, which ensures that the material right in contact with the crucible remains in a solid form, and to the fact that the evaporation occurs at a highly localized point. Moreover, the chamber contains a shutter located, in the closed position, between the sample and the metal source. This shutter can be maintained closed at the very first moments of evaporation, when degassing of the crucible and the metal may occur and thus possibly contaminate the sample. Then, the shutter can be opened and the evaporation on the sample starts. A calibrated quartz crystal allows the *in-situ* control of the deposition rate and thickness.

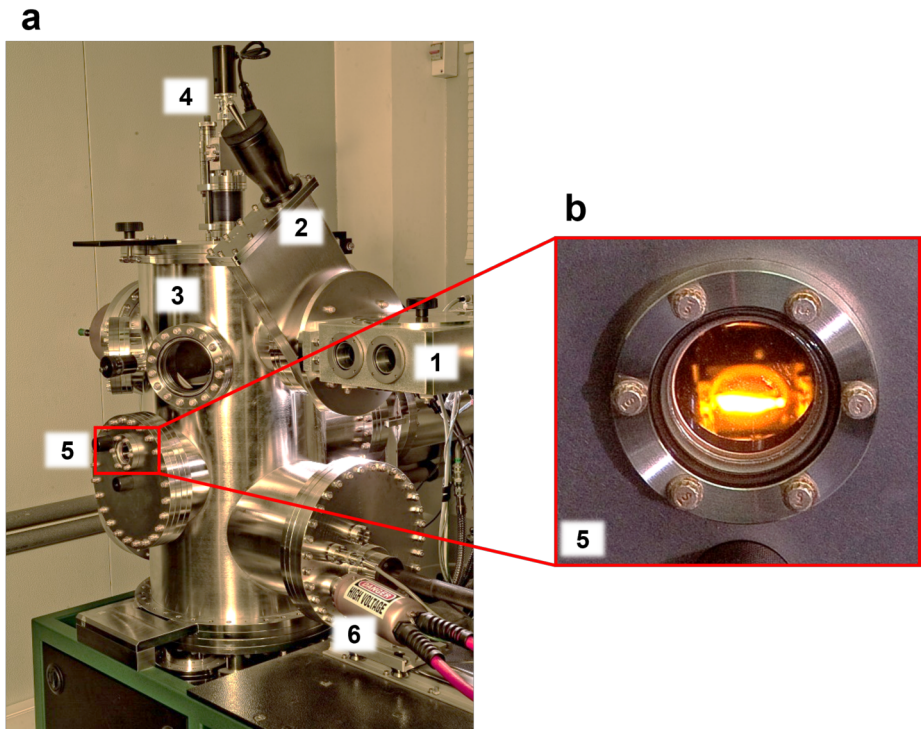


Figure F.1: (a) Photograph of the AJA International Inc. ATC-8E Orion e-beam used for metal deposition, where [1] is the load-lock chamber, [2] is the load-lock valve, [3] is the main chamber, where the sample is placed facing down for evaporation [4] is the sample manipulator that is used to align the sample at the specific position for evaporation, [5] is where the crucible containing the metal to be evaporated is placed, and [6] is the power supply to the electron gun. **(b)** Heated crucible containing the metal to be evaporated.

F.2 Raman spectroscopy

Raman spectroscopy is a non-destructive vibrational technique that is broadly used for the structural characterization of a wide range of surfaces and compounds. This technique is named after the Indian physicist Chandrasekhara Venkata Raman, who first explained the inelastic scattering of light phenomena and won the Nobel prize in 1930 for its discovery. Since then, Raman spectroscopy has been developed as light sources - lasers - and detection systems have evolved. Nowadays, it is widely used in diverse scientific areas and has been paramount in the development of the nanoscience and nanotechnology field.

Raman spectroscopy is based on the interaction of an electromagnetic radiation with the chemical bonds of a sample. As a result of this interaction, the electrons forming the chemical bond oscillate and emit radiation in all directions. The

emitted photon to a higher virtual energy state resulting from the interaction can return to the initial energy state in an elastic energy interaction, also known as Rayleigh interaction. However, if the emitted photon returns to a different vibrational state than the initial one, the interaction is defined as inelastic, also known as Raman Stokes. Finally, if the emitted phonon goes from an excited state to another one energetically lower, the interaction is defined by anti-Stokes. The mentioned interactions are represented in a simplified manner in Figure F.2, together with the mathematical expressions describing the energy of the dispersed photon in each case.

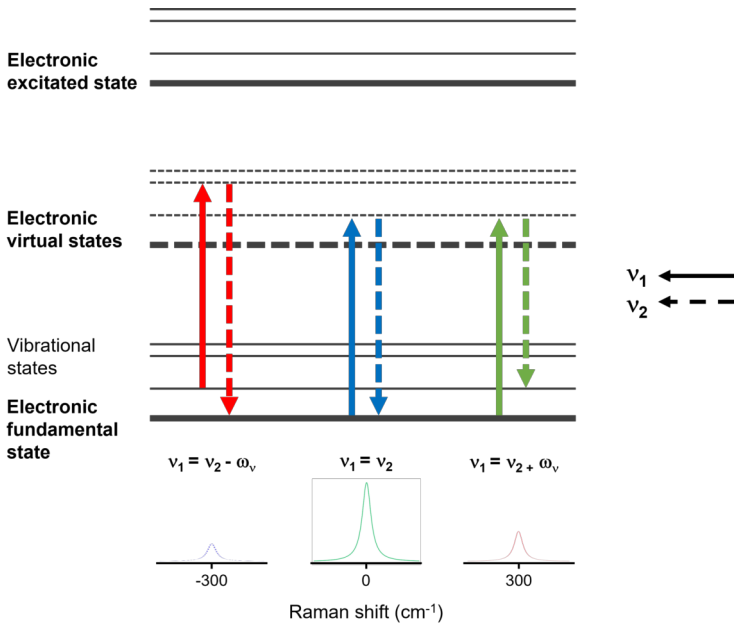


Figure F.2: Basic principle of Raman spectroscopy - Representation of the different electronic states of a system with the given dispersions: anti-Stokes (red), Rayleigh (blue) and Stokes (green). The curves underneath represent the intensity relations of the Raman signals from the three dispersions. In this representation, we follow the criteria that assigns positive Raman frequencies to the Stokes type of dispersion and negative Raman frequencies to the anti-Stokes ones. However, the anti-Stokes dispersion is higher in energy, according to $E = \hbar c\nu$, where $\hbar$ is the Planck constant and c is the speed of light.

Raman maps were acquired with a 488 nm laser (2 mW) and analysed with the WITec PROJECT 5.0 software, using the algorithm options, as follows: **(1)** Crop the spectrum in the x axis from ∼900 cm^{-1} to ∼3000 cm^{-1}, which forms the zone of interest (for graphene), **(2)** Cosmic-rays removal, this option filters the signal to remove undesired artifacts, **(3)** Background subtraction using a

polynomial function to flatten the spectra, **(4)** Fitting of the Raman bands throughout the mapped area with a Lorentzian fitting function.

The Raman spectroscopy equipment used in this thesis is a WITec confocal Raman spectroscope, shown in Figure F.3. It has an excitation laser source (wavelengths of 488 nm and 633 nm available), a light collection system based on lens with a monochromator, and a charge-coupled device (CCD) detector.

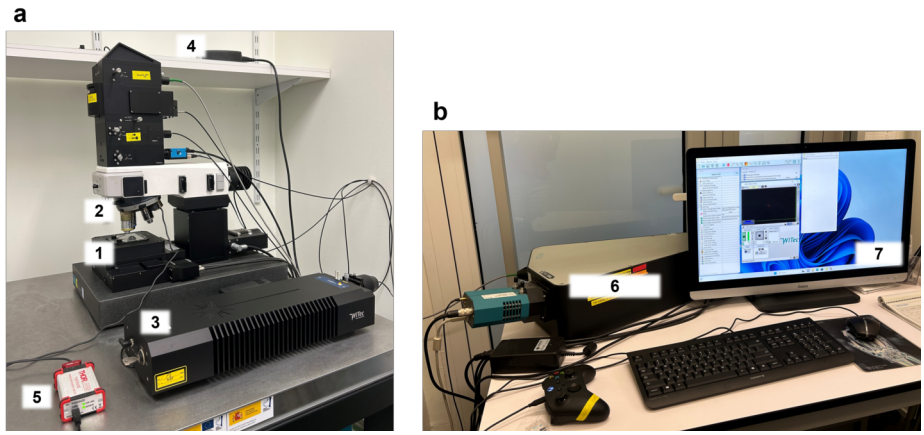


Figure F.3: Raman spectroscopy equipment - **(a)** Photograph of the WITec Raman spectroscope used in this thesis, where [1] is the sample stage, [2] is the stage with the microscope objectives, [3] and [4] are the 488 nm and 633 nm laser sources, respectively, and [5] is the laser power meter (Thorlabs). **(b)** Photograph of the CCD detector [6] and the monitor [7] of the computer coupled to the Raman spectrometer.

F.3 AFM and KPFM

The Atomic Force Microscopy (AFM) basic principle was first introduced in 1986 by Binnig, Quate and Gerber [326]. It is based on the interaction between an AFM tip mounted on a cantilever when being approached to a sample surface and scanning it. AFM can be operated in diverse modes depending on the application (contact, non-contact and intermediate), which makes it a very versatile tool for surface analysis. For the studies presented in this thesis, we mainly used the intermediate (widely known as tapping) mode.

When the tip and the sample are placed sufficiently close, the cantilever is deflected obeying Hook's law, as a result of a repulsive force created, oscillating at its resonant frequency in tapping mode. The cantilever deflection responds to changes of the sample surface, and its scanning is controlled by a piezoelectric ceramic scanner that covers the xyz directions. The tracking of the deflection changes is performed by a laser beam, which is aligned at the top of the tip

position at the cantilever. The laser beam is reflected to a position sensitive photodetector and the tapping AFM topography three dimensional image is displayed as a pseudocolor plot. AFM resolution is given by the coefficient between the cantilever resonant frequency and the frequency change at full width half maximum (FWHM).

The Kelvin Probe Force Microscopy (KPFM) is a variation of AFM that allows the measurement of a sample's surface potential. Hence, it can be used to obtain work function values. In KPFM, a conductive tip is placed close to a conductive sample surface. This results in the generation of an electrical force. When the tip and the sample are electrically connected, their Fermi levels align and there exist a potential difference between the Fermi level of the element with lowest work function and the vacuum level. Then, a V_{DC} is applied compensating the tip-sample work function difference. This voltage value is what is showed at the resulting KPFM image, named the contact potential difference. Figure F.4 depicts a schematic representation of the KPFM working principle.

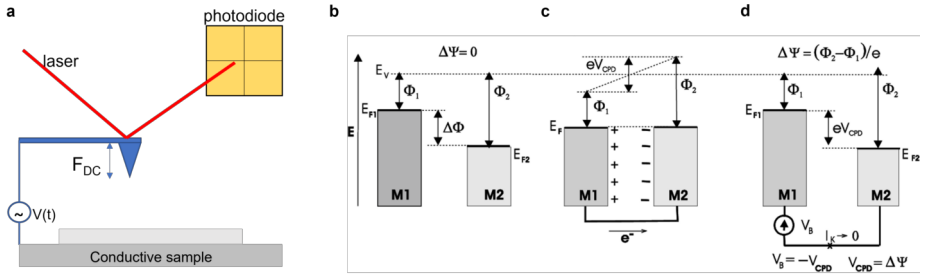


Figure F.4: Representation of the KPFM working principle - (a) Scheme of the main parts of the KPFM measurement, which is conducted in an AFM equipment. Schematic energy diagrams of the E_F of the conductive tip (M1) and a sample (M2) during a KPFM measurement: **(b)** first, the tip and the sample are not in electrical contact. **(c)** When they are electrically connected, their E_F align. **(d)** The application of a V_{DC} compensates the difference between the tip's and sample's work function.

The AFM/KPFM equipment used in this thesis (Figure F.5) is a commercially available MFP-3D Origin, from Oxford Instruments Asylum Research.

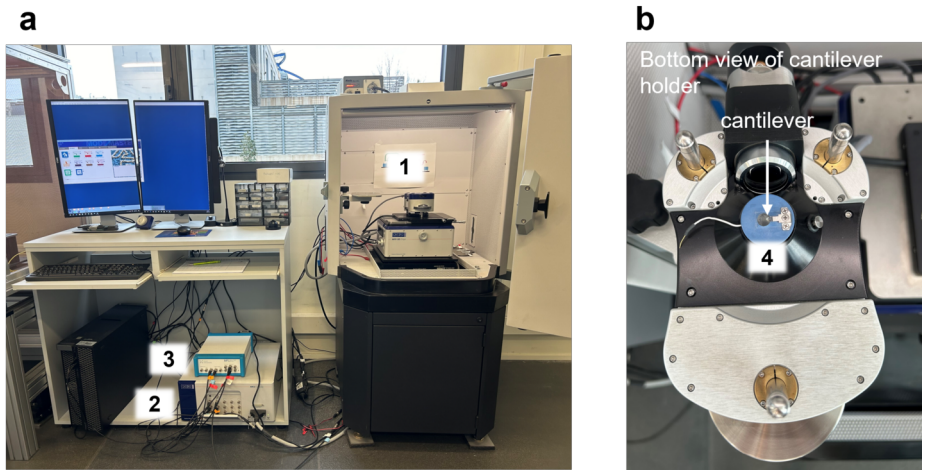


Figure F.5: AFM setup - (a)(b) Photographs of the AFM equipment used at the AEMD laboratory, where [1] is the AFM inside an acoustic enclosure with vibrational isolation, [2] is the controller, which houses power supplies and the electronics needed to control the scan motion and data acquisition from the microscope, [3] is the lock-in amplifier needed for DH-KPFM measurements and [4] is the bottom part of the AFM head, which contains controls to move the laser spot and the cantilever along the sample's surface.

F.4 X-ray and ultraviolet photoelectron spectroscopy

X-ray photoelectron spectroscopy (XPS) has been developed since the 1950s, when the first application of photoemission as analysis method was presented , years after the first time it was performed (H. Hertz and W. Hallwachs, 1887) and of the theoretical description of the photoelectric effect (Einstein, 1905 [327]). XPS is nowadays extensively used for the analysis of the elemental composition of surfaces. Ultraviolet photoelectron spectroscopy (UPS) is based on the same principle as XPS, but it uses lower excitation energies. UPS is a powerful technique for the measurement of valence band structures and the electronic properties of materials [328].

We used XPS for the chemical analysis of sapphire and graphene surfaces and UPS for the measurement of graphene work function when being supported on different substrates.

When a material is irradiated with photons, electrons are ejected thanks to the energy transmitted to them (photoelectric effect). In XPS, samples are irradiated with soft X-rays ($\sim$6 keV) and the kinetic energy of the emitted electrons is analyzed. At energies below the workfunction of the material, photons are not

capable to eject electrons from the surface. At energies above, irradiating photons are able to eject the highest energy electrons located at the Fermi level. Electrons at the core level need an additional energy to be ejected, i. e. the binding energy (BE). Hence, the kinetic energy (KE) that will be measured for a photoelectron with an initial BE can be described as:

$$KE = h\upsilon - BE - \Phi_{sample} - (\Phi_{spectrometer} - \Phi_{sample}) = h\upsilon - BE - \Phi_{spectrometer} \tag{F.1}$$

where the spectrometer workfunction ($\Phi_{spectrometer}$) is a constant value and the BE is a material property, independent from the X-ray source used. In an XPS spectrum, the photoelectron peaks that appear correspond to a specific element and the orbital from which electrons were ejected (e. g. "C 1s" accounts for electrons emitted from the 1s orbital of a carbon atom). Figure F.6 schematically represents the theoretical principle of XPS.

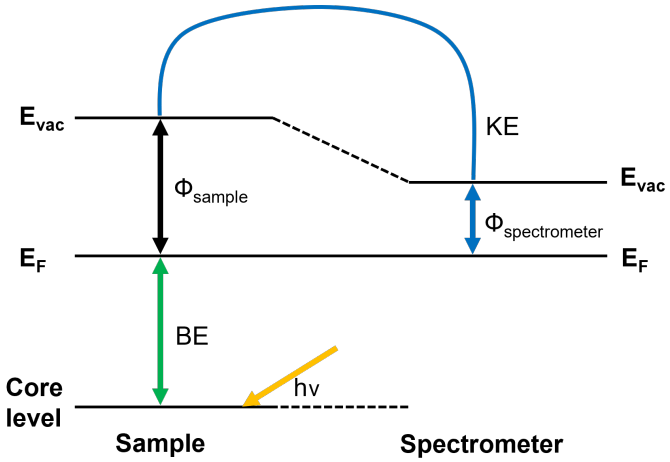


Figure F.6: Band diagram to illustrate the XPS basic principle - hυ corresponds to the energy of the photon absorbed by an electron at the core level of an atom in the sample. This electron is ejected at a kinetic energy (KE), which is the sum of the binding energy (BE) and the workfunction of the sample (Φ_{sample}). Adapted from [329].

Only the electrons at the surface of the sample are able to be emitted when irradiated, as electrons situated deeper will be affected by inelastic scattering, resulting in an energy loss. For that reason, XPS is a powerful surface technique, and its surface sensitivity depends on the energy of the X-ray source [329].

UPS is based on the same physical principle as XPS. However, in this case, the excitation of the sample core levels is performed with ultraviolet photons.

Consequently, the measured spectra in UPS can be used to relate the peaks with molecular orbitals.

The XPS and UPS measurements showed in this dissertation were performed using a SPECS PHOIBOS 150 hemispherical energy analyser located at the ICN2 (see Figure F.7), with 3 UHV chambers (load lock, preparation and analysis). The X-ray source (WR50) is equipped with aluminum and silver targets and a FOCUS 500 X-ray monochromator; and the analyser is an hemispherical Phoibos 150. The photon energy used for the XPS experiments was 14886.6 eV. The samples to be analysed were prepared and introduced inside the analysis chamber, which operates at a pressure of $<10^{-9}$ mbar. The XPS and UPS data analysis was performed using the CasaXPS v2.3.17 software. XPS peak fitting of the analysed core level spectra involved: (1) reference peak adjustment to the 284.8 eV peak of the Csp^2-associated contribution. (2) setting of a linear background. (3) Use of reference samples to set constraints for peak positions, FWHM and peak shapes.

To perform the measurements explained in Chapter 5, Section 5.3, corresponding to in-vacuum graphene functionalization with PBA monitored by XPS, an OMBE evaporator was coupled to the XPS equipment, as shown in Figure F.8. The graphene sample is placed inside the XPS preparation chamber, where it needs to be tilted for the graphene to face the crucible in the evaporator, where the PBA molecules are located. The temperature of the crucible inside the evaporator is monitored by a termocouple in direct contact with it, and it is controlled using an external power supply[2]. After each evaporation, the graphene sample is transferred to the XPS analysis chamber, always being maintained under vacuum conditions, as the preparation and analysis chambers are connected. Then, the measurement is performed using the conditions explained above.

[2]Keithley

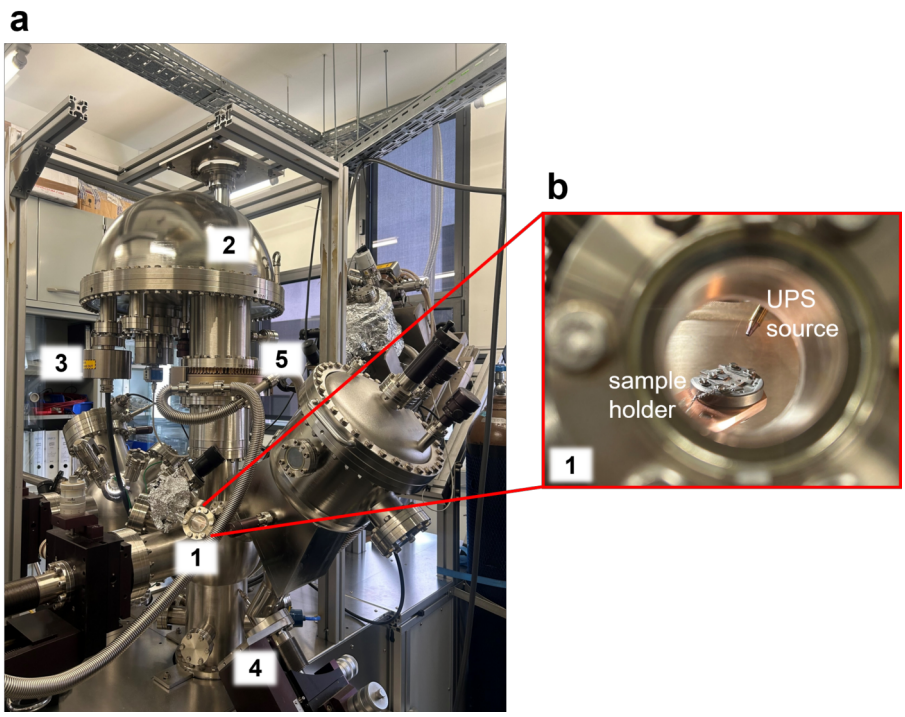


Figure F.7: XPS-UPS equipment - **(a)** Photograph of the equipment used to perform XPS and UPS measurements, where [1] is the analysis chamber, [2] is the accelerator, [3] is the detector and [4] and [5] are the XPS and UPS sources, respectively. **(b)** Analysis chamber showing the sample holder and the UPS source. The XPS source does not appear in the image as it is located more at the left.

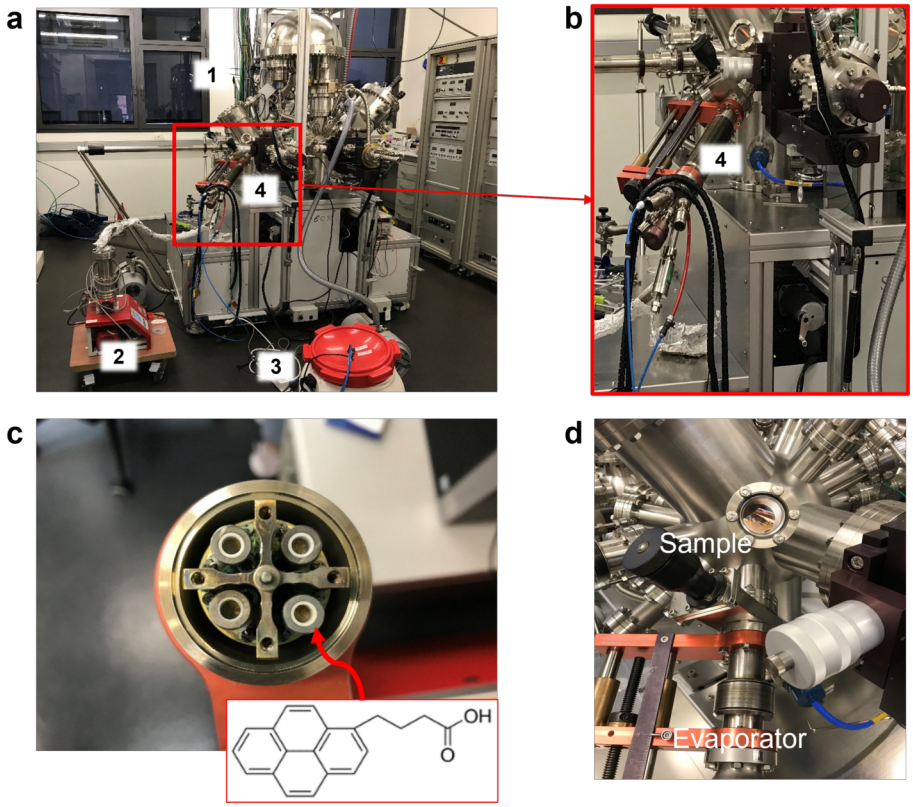


Figure F.8: XPS system with a coupled OMBE evaporator - **(a)** Photograph of the equipment used to perform XPS measurements after PBA evaporation on graphene samples, where [1] is the whole XPS equipment described in Figure F.7, [2] is the vacuum pump connected to the OMBE evaporator, [3] is the water cooling source and [4] is the OMBE evaporator. **(b)** Zoom in the OMBE evaporator coupled to the XPS preparation chamber. **(c)** Inside of the OMBE evaporator, with 4 crucibles, one of them filled with an amount of PBA. **(d)** Photograph showing the OMBE evaporator coupled to the XPS preparation chamber.

F.5 SEM and EBSD

The fundamentals of SEM were first described by M. Knoll in 1935 and the first time it was used to scan a solid surface was in 1942 by Zworykin *et al* [330]. Electron backscatter diffraction (EBSD) is a SEM based technique that allows crystallographic analysis of a sample's surface microstructure, thus providing information about the orientation of single grains and phases [331]. Both SEM and EBSD are non-destructive techniques. Nowadays, the use of SEM and EBSD is highly extended in 2D materials and thin film research [332].

In SEM, a conductive sample is introduced in a vacuum chamber where an electron beam is focused on its surface and scans it in a rectangular raster pattern. When an electron beam interacts with the sample, different signals are generated depending on the depth of surface interaction. Among them, SEM mainly uses secondary electrons (SE), which are of low energy (< 50 eV), reflected or back-scattered electrons (BSE), which are of higher energy. The signal is collected by a detector, amplified and converted into an electrical voltage. The scan lines collected result in a picture point (pixel) array, and therefore an image can be formed.

To measure the Cu grain sizes from the images obtained by SEM of the studies showed in Chapter 3, we used the ImageJ open-source software [333]. From an original SEM image, the analysis was conducted following these steps from the automatized algorithm: **(1)** Set scale from original image, **(2)** Crop to remove image caption, **(3)** Make binary, **(4)** Analyse Particles from the "Analyse" menu, **(5)** the program provides a list of measurements including the are for each grain. In some cases where the thresholding option resulted more complicated due to low contrast in the images, the measurement was performed with the manual option of the software, masking grain by grain. This manual option, although being more time-consuming, ensured precision in those cases. Grain size results with the average deviation are presented using the Origin data processor.

In EBSD, vacuum and sample requirements for optimal analysis, are analogous to SEM. The main difference is that the sample is mounted in a platform which is tilted at a certain angle facing a phosphor screen detector. This detector collects the diffraction from back-scattered electrons that impact on atomic planes at angles satisfying the Bragg equation:

$$n\lambda = 2d\sin(\theta) \tag{F.2}$$

where n is an integer, λ is the electron wavelength, d is the spacing of the diffracting plane and θ is the electrons angle of incidence). The diffraction of BSE at the detector creates what is known as a Kikuchi pattern, which can be visualized at a computer thanks to a CCD camera. Then, the lines conforming the Kikuchi pattern are indexed by assigning Miller indices[3] to them and according to the material that is being analysed. Finally, an image showing the crystallographic orientation of the sample is generated in a form that each pixel corresponds to a unique line/band.

[3]Miller indices are a notation system composed by three integers, <hkl>, used for the description of a family of lattice planes in crystallography.

The SEM measurements in this thesis were performed in a Quanta 650 FEG with an Everhart-Thornley secondary electron signal detection (see Figure F.9. Previously to be introduced inside the vacuum chamber for analysis, samples were nitrogen-blowed. The working distance (between the sample and the beam exit) set was 10 mm. In general we used 20 kV acceleration voltage for image acquisition, except for the sapphire/copper samples, where we used 0.2 kV. The EBSD measurements were performed in a Zeiss Merlin FEG-SEM with an EBSD detector located at the *Servei de Microscòpia* at the Biosciences Faculty of the *Universitat Autònoma de Barcelona* (UAB) with the Channel 5 software from Oxforn Instruments. Samples were also nitrogen-blowed previously to be introduced inside the chamber. The working distance was set at 12 mm with an acceleration voltage of 20 kV and the sample was tilted 70° from the horizontal.

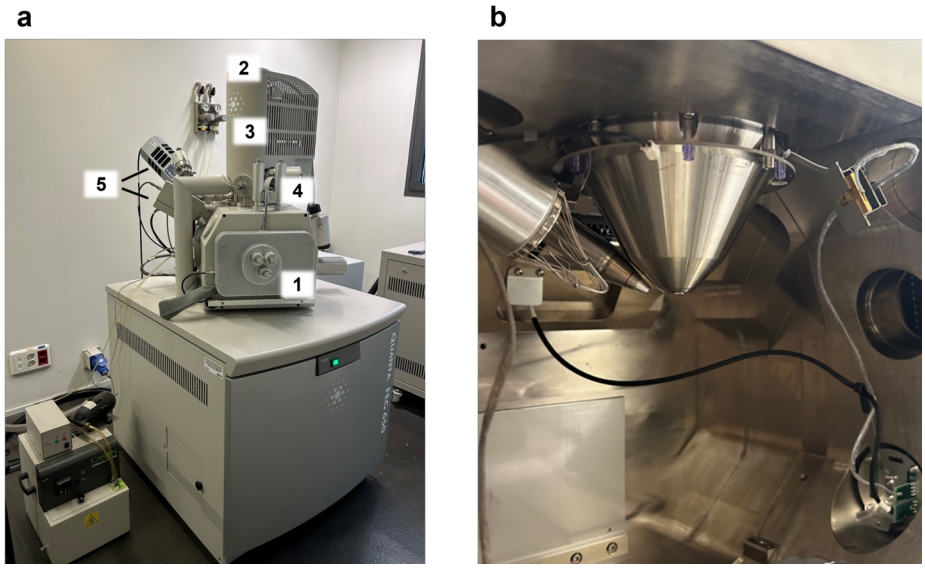


Figure F.9: SEM Quanta 650 FEG at ICN2 - **(a)** Photograph of the equipment used for the SEM measurements at ICN2, where [1] is the sample chamber, [2] is the electron gun, [3] and [4] are the condenser and objective lens, respectively, and [5] marks the secondary electron and backscattered electron detectors. **(b)** Photograph of the inside of the sample chamber, with the secondary electron detector (left) and the backscattered electron detector (right).

F.6 X-ray diffraction

In XRD, a sample is irradiated with X-rays and those interact with the electrons of the atoms forming it. As a result, the X-rays are scattered in an array of waves in different directions. These waves can cancel each other (destructive

interference), or enable the diffraction (constructive) if the Bragg's law is satisfied (F.2). Each family of planes present in the sample produces a diffraction intensity peak at a specific diffraction angle, which enables the identification of a present crystallographic orientation at the resulting intensity peak spectrum obtained after the measurement. There, the position of each peak is determined by the distance between diffracting planes of atoms. We used XRD to characterize the crystallographic structure of the prepared copper surfaces on rigid substrates in Chapter 3, as a complement to the EBSD data. In particular, we performed standard $2\theta - \omega$ measurements and Pole figures analysis, as explained in Section 2.5.4.

XRD was performed using a Malvern PANalytical X'pert Pro MRD (Materials Research Diffractometer) located at the ICN2 facilities. Figure F.10 shows a photograph of this equipment. The diffractometer consists of an X-Ray tube, a horizontal $2\theta - \omega$ goniometer allowing sample rotation for the definition of the incident (ω) and reflection (θ) angles, and a diffraction intensity detector (PIXcel). The equipment uses a monochromatic X-ray source radiation which is a Cu K anode at a wavelength of $\lambda = 1.54187$ Å. Data analysis was performed using the X'pert PAN Analytical data viewer software and the Origin data processor.

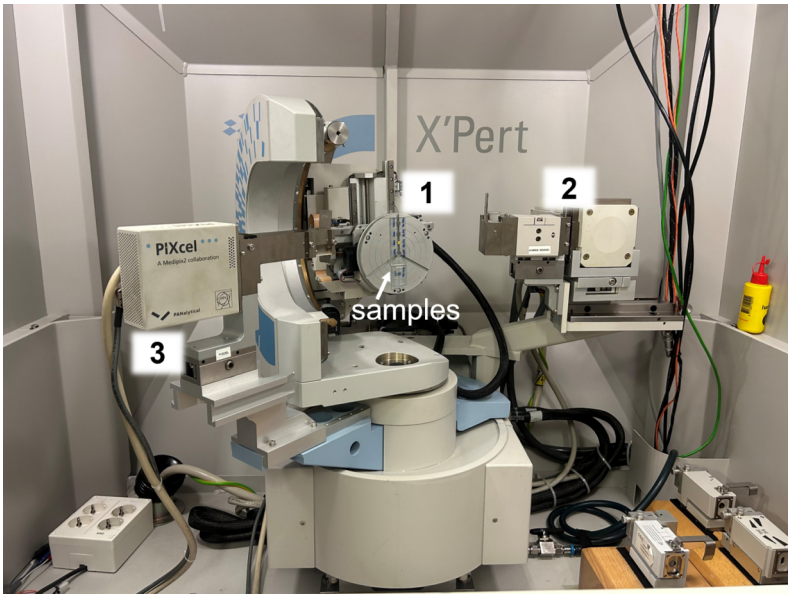


Figure F.10: XRD equipment - Photograph of the equipment used for the XRD measurements, where [1] is the rotatory platform (goniometer) where the samples are placed [2] X-ray tube and [3] is the PIXcel detector.

F.7 Electrical characterization of gSGFETs

The characterization of g-SGFETs was performed in the setup shown in Figure F.11. The sample is placed in a PDMS platform and the drain and source channels of 24 transistors are connected to a Printed Circuit Board (PCB). This is is connected to a Data Acquisition card (DAQ card), which digitalises and transmits the measured signal to a computer. A direct current source polarises the operational amplifiers from the PCB. The gate electrode is connected to the socket and placed in the electrolyte container (PBS) of the PDMS platform, where the sample is. An *in-house* Python script is used to control the measurements, which applies the specified V_{gs} (generally between 0 and 400 mV with 20 mV steps) and V_{ds} (50 mV), while measuring I_{ds}.

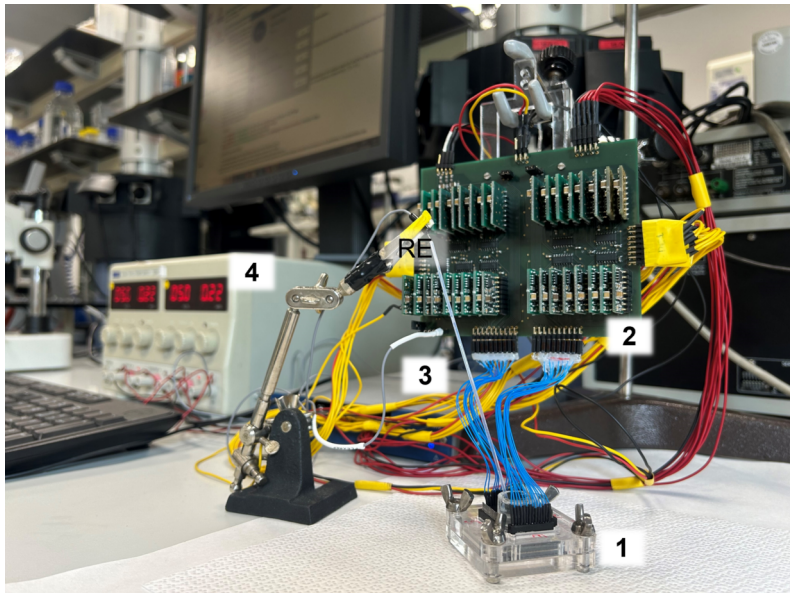


Figure F.11: gSGFETs characterization setup - Photograph of the setup used for the electrical characterization of fabricated gSGFETs, where [1] is the PDMS platform, [2] is the PCB, with drain and source connections, [3] is the gate electrode (Ag/AgCl) needed for the measurements and [4] is the DC source.

Publications

The work presented in this PhD dissertation has resulted in the following publications.

Peer-reviewed journal contribution:

- **Delgà-Fernández, M.**; Toral-López, A.; Guimerà-Brunet, A.; Pérez-Marín, A. P.; González-Marín, E.; Godoy, A.; Garrido, J. A.; del Corro, E., Interfacial phenomena governing performance of graphene electrodes in aqueous electrolyte. *Under review.*

Conference contributions:

- **Delgà-Fernández, M.**; de la Cruz, J. M.; Garrido, J. A.; del Corro, E., Raman spectroscopy as a tool for studying the graphene-electrolyte interaction. **Poster presentation**, Graphene Brazil International Conference, 2019, 9-10 September 2019, Rio de Janeiro, Brazil.

- **Delgà-Fernández, M.**; de la Cruz, J. M.; Garrido, J. A.; del Corro, E., Raman spectroscopy as a tool for studying the graphene-electrolyte interaction. **Poster presentation**, JPhD Conference - 4th scientific meeting of BNC-b students, 7 June 2019, Bellaterra, Spain.

- **Delgà-Fernández, M.**; de la Cruz, J. M.; Garrido, J. A.; del Corro, E., Understanding the electronic interaction at the graphene-electrolyte interface. **Poster presentation**, International Winterschool on Electronic Properties of Novel Materials, 7-14 March 2020, Kirchberg in Tirol, Austria.

- **Delgà-Fernández, M.**; de la Cruz, J. M.; Garrido, J. A.; del Corro, E., Understanding electronic interactions at the graphene-electrolyte interface. **Poster presentation**, Graphene conference, 19-23 October 2020, Online event.

- **Delgà-Fernández, M.**; del Corro, E.; Collins, L.; Checa, M.; Illa, X.; Pérez-Marín, A. P.; Garrido, J. A., Ionic concentration and substrate dependent

surface potential of single layer graphene by in-liquid Dual-Harmonic KPFM. **Oral presentation**, Graphene conference, 15-17 June 2022, Paris, France.

- **Delgà-Fernández, M.**; Caicedo Roque, J.; Prats-Alfonso, E.; Brosel, S.; Illa, X.; Guimerà-Brunet, A.; Garrido, J. A.; del Corro, E., Towards a universal biosensing platform based on graphene/pyrene surfaces for neurotransmitters. **Poster presentation**, PuzzleX, 15-17 November 2022, Barcelona, Spain.

- **Delgà-Fernández, M.**; del Corro, E.; Caicedo Roque, J.; Garrido, J. A., Towards a universal biosensing platform based on graphene/pyrene surfaces for neurotransmitters. **Oral presentation**, NanoBio&Med, 22-24 November 2022, Barcelona, Spain.

- **Delgà-Fernández, M.**; del Corro, E.; Collins, L.; Checa, M.; Illa, X.; Pérez-Marín, A. P.; Garrido, J. A., In-liquid Dual-Harmonic KPFM for the study of electronic properties of single layer graphene. **Oral presentation**, MRS Meeting, 27 November - 02 December 2022, Boston (Massachusetts), EUA.

- **Delgà-Fernández, M.**; Toral-López, A.; González-Marín, E.; Godoy, A.; Guimerà-Brunet, A.; Garrido, J. A.; del Corro, E., Understanding the substrate-graphene-electrolyte interaction. **Poster presentation**, Graphene Flagship: Symposium on Graphene & 2D Materials in Health & Environment, Medicine & Sensing, 26-28 April 2023, Rome, Italy.

- **Delgà-Fernández, M.**; Toral-López, A.; González-Marín, E.; Godoy, A.; Guimerà-Brunet, A.; Garrido, J. A.; del Corro, E., Understanding the electronic interaction at the substrate-graphene-electrolyte interface. **Poster presentation**, Graphene Flagship: Graphene Week, 4-8 September 2023, Gothenburg, Sweden.

- **Delgà-Fernández, M.**; Galceran, A.; Caicedo Roque, J.; Illa, X.; Garrido, J. A.; del Corro, E., Towards a universal biosensing platform based on graphene/pyrene surfaces for neurotransmitters. **Poster presentation**, MRS Meeting, 22-26 April, 2024, Seattle (Washington), EUA.

References

[1] I.M. Ross. "The invention of the transistor". en. In: *Proceedings of the IEEE* 86.1 (Jan. 1998), pp. 7–28. ISSN: 00189219. DOI: 10.1109/5.658752. URL: http://ieeexplore.ieee.org/document/658752/ (visited on 02/20/2024).

[2] Richard R. Nelson. "The Link Between Science and Invention: The Case of the Transistor". en. In: *The Rate and Direction of Inventive Activity*. Princeton University Press, Dec. 1962, pp. 549–584. ISBN: 978-1-4008-7976-2. DOI: 10.1515/9781400879762-022. URL: https://www.degruyter.com/document/doi/10.1515/9781400879762-022/html (visited on 02/20/2024).

[3] Suman Datta, Wriddhi Chakraborty, and Marko Radosavljevic. "Toward attojoule switching energy in logic transistors". en. In: *Science* 378.6621 (Nov. 2022), pp. 733–740. ISSN: 0036-8075, 1095-9203. DOI: 10.1126/science.ade7656. URL: https://www.science.org/doi/10.1126/science.ade7656 (visited on 02/19/2024).

[4] Aaron D. Franklin. "Nanomaterials in transistors: From high-performance to thin-film applications". en. In: *Science* 349.6249 (Aug. 2015), aab2750. ISSN: 0036-8075, 1095-9203. DOI: 10.1126/science.aab2750. URL: https://www.science.org/doi/10.1126/science.aab2750 (visited on 02/20/2024).

[5] K. S. Novoselov et al. "Electric Field Effect in Atomically Thin Carbon Films". en. In: *Science* 306.5696 (Oct. 2004), pp. 666–669. ISSN: 0036-8075, 1095-9203. DOI: 10.1126/science.1102896. URL: https://www.science.org/doi/10.1126/science.1102896 (visited on 09/01/2023).

[6] Pablo Ares and Kostya S. Novoselov. "Recent advances in graphene and other 2D materials". en. In: *Nano Materials Science* 4.1 (Mar. 2022), pp. 3–9. ISSN: 25899651. DOI: 10.1016/j.nanoms.2021.05.

002. URL: https://linkinghub.elsevier.com/retrieve/pii/S2589965121000209 (visited on 02/20/2024).

[7] Katarzyna M Szostak. "Neural Interfaces for Intracortical Recording: Requirements, Fabrication Methods, and Characteristics". en. In: *Frontiers in Neuroscience* 11 (2017).

[8] David Williams F. "On the mechanisms of biocompatibility". en. In: *Biomaterials* 29 (2008), pp. 2941–2953. DOI: doi:10.1016/j.biomaterials.2008.04.023.

[9] John P. Seymour and Daryl R. Kipke. "Neural probe design for reduced tissue encapsulation in CNS". en. In: *Biomaterials* 28.25 (Sept. 2007), pp. 3594–3607. ISSN: 01429612. DOI: 10.1016/j.biomaterials.2007.03.024. URL: https://linkinghub.elsevier.com/retrieve/pii/S014296120700258X (visited on 05/28/2024).

[10] Lohitash Karumbaiah. "Relationship between intracortical electrode design and chronic recording function". en. In: (2013).

[11] Susan Schmidt, Kenneth Horch, and Richard Normann. "Biocompatibility of silicon-based electrode arrays implanted in feline cortical tissue". en. In: *Journal of Biomedical Materials Research* 27.11 (Nov. 1993), pp. 1393–1399. ISSN: 0021-9304, 1097-4636. DOI: 10.1002/jbm.820271106. URL: https://onlinelibrary.wiley.com/doi/10.1002/jbm.820271106 (visited on 05/28/2024).

[12] Roy Biran, David C Martin, and Patrick A Tresco. "Neuronal cell loss accompanies the brain tissue response to chronically implanted silicon microelectrode arrays". en. In: *Experimental Neurology* (2005).

[13] Jessica K Nguyen. "Mechanically-compliant intracortical implants reduce the neuroinflammatory response". en. In: *J. Neural Eng.* (2014).

[14] Zhuolin Xiang, Jingquan Liu, and Chengkuo Lee. "A flexible three-dimensional electrode mesh: An enabling technology for wireless brain–computer interface prostheses". en. In: *Microsystems & Nanoengineering* 2.1 (May 2016), p. 16012. ISSN: 2055-7434. DOI: 10.1038/micronano.2016.12. URL: https://www.nature.com/articles/micronano201612 (visited on 05/28/2024).

[15] Jonathan Viventi et al. "Flexible, foldable, actively multiplexed, high-density electrode array for mapping brain activity in vivo". en. In: *Nature Neuroscience* 14.12 (Dec. 2011), pp. 1599–1605. ISSN: 1097-6256, 1546-1726. DOI: 10.1038/nn.2973. URL: https://www.nature.com/articles/nn.2973 (visited on 05/28/2024).

[16] Stefano Toffanin et al. “N-type perylene-based organic semiconductors for functional neural interfacing”. en. In: *Journal of Materials Chemistry B* 1.31 (2013), p. 3850. ISSN: 2050-750X, 2050-7518. DOI: 10.1039/c3tb20555j. URL: https://xlink.rsc.org/?DOI=c3tb20555j (visited on 05/28/2024).

[17] Swarup Biswas et al. “Recent advancements in implantable neural links based on organic synaptic transistors”. en. In: *Exploration* 4.2 (Apr. 2024), p. 20220150. ISSN: 2766-8509, 2766-2098. DOI: 10.1002/EXP.20220150. URL: https://onlinelibrary.wiley.com/doi/10.1002/EXP.20220150 (visited on 05/28/2024).

[18] Yi Qiang et al. “Transparent arrays of bilayer-nanomesh microelectrodes for simultaneous electrophysiology and two-photon imaging in the brain”. en. In: *Science Advances* 4.9 (Sept. 2018), eaat0626. ISSN: 2375-2548. DOI: 10.1126/sciadv.aat0626. URL: https://www.science.org/doi/10.1126/sciadv.aat0626 (visited on 08/28/2023).

[19] Weiyang Yang, Yan Gong, and Wen Li. “A Review: Electrode and Packaging Materials for Neurophysiology Recording Implants”. en. In: *Frontiers in Bioengineering and Biotechnology* 8 (Jan. 2021), p. 622923. ISSN: 2296-4185. DOI: 10.3389/fbioe.2020.622923. URL: https://www.frontiersin.org/articles/10.3389/fbioe.2020.622923/full (visited on 06/09/2024).

[20] Lee Changgu et al. “Measurement of the Elastic Properties and Intrinsic Strength of Monolayer Graphene”. en. In: *Science* 321.5887 (July 2008), pp. 385–388. ISSN: 0036-8075, 1095-9203. DOI: 10.1126/science.1156211. URL: https://www.science.org/doi/10.1126/science.1156211 (visited on 02/20/2024).

[21] R. R. Nair et al. “Fine Structure Constant Defines Visual Transparency of Graphene”. en. In: *Science* 320.5881 (June 2008), pp. 1308–1308. ISSN: 0036-8075, 1095-9203. DOI: 10.1126/science.1156965. URL: https://www.science.org/doi/10.1126/science.1156965 (visited on 02/20/2024).

[22] Duygu Kuzum et al. “Transparent and flexible low noise graphene electrodes for simultaneous electrophysiology and neuroimaging”. en. In: *Nature Communications* 5.1 (Oct. 2014), p. 5259. ISSN: 2041-1723. DOI: 10.1038/ncomms6259. URL: https://www.nature.com/articles/ncomms6259 (visited on 08/17/2023).

[23] Yichen Lu et al. “Ultralow Impedance Graphene Microelectrodes with High Optical Transparency for Simultaneous Deep Two-Photon Imaging in Transgenic Mice”. en. In: *Advanced Functional Materials* 28.31 (Aug. 2018), p. 1800002. ISSN: 1616-301X, 1616-3028. DOI: 10.1002/adfm.201800002. URL: https://onlinelibrary.wiley.com/doi/10.1002/adfm.201800002 (visited on 02/27/2024).

[24] Josef Jampilek and Katarina Kralova. “Advances in Drug Delivery Nanosystems Using Graphene-Based Materials and Carbon Nanotubes”. en. In: *Materials* 14.5 (Feb. 2021), p. 1059. ISSN: 1996-1944. DOI: 10.3390/ma14051059. URL: https://www.mdpi.com/1996-1944/14/5/1059 (visited on 02/27/2024).

[25] Martin Thunemann et al. “Deep 2-photon imaging and artifact-free optogenetics through transparent graphene microelectrode arrays”. en. In: *Nature Communications* 9.1 (May 2018), p. 2035. ISSN: 2041-1723. DOI: 10.1038/s41467-018-04457-5. URL: https://www.nature.com/articles/s41467-018-04457-5 (visited on 02/27/2024).

[26] Diep Nguyen et al. “Novel Graphene Electrode for Retinal Implants: An in vivo Biocompatibility Study”. en. In: *Frontiers in Neuroscience* 15 (Mar. 2021), p. 615256. ISSN: 1662-453X. DOI: 10.3389/fnins.2021.615256. URL: https://www.frontiersin.org/articles/10.3389/fnins.2021.615256/full (visited on 02/27/2024).

[27] Siva Kumar Krishnan et al. “Graphene-Based Field-Effect Transistors in Biosensing and Neural Interfacing Applications: Recent Advances and Prospects”. en. In: *Analytical Chemistry* 95.5 (Feb. 2023), pp. 2590–2622. ISSN: 0003-2700, 1520-6882. DOI: 10.1021/acs.analchem.2c03399. URL: https://pubs.acs.org/doi/10.1021/acs.analchem.2c03399 (visited on 09/01/2023).

[28] Dong-Wook Park et al. “Electrical Neural Stimulation and Simultaneous *in Vivo* Monitoring with Transparent Graphene Electrode Arrays Implanted in GCaMP6f Mice”. en. In: *ACS Nano* 12.1 (Jan. 2018), pp. 148–157. ISSN: 1936-0851, 1936-086X. DOI: 10.1021/acsnano.7b04321. URL: https://pubs.acs.org/doi/10.1021/acsnano.7b04321 (visited on 02/27/2024).

[29] Benno M Blaschke et al. “Mapping brain activity with flexible graphene micro-transistors”. en. In: *2D Materials* 4.2 (Feb. 2017), p. 025040. ISSN: 2053-1583. DOI: 10.1088/2053-1583/aa5eff. URL: https://iopscience.iop.org/article/10.1088/2053-1583/aa5eff (visited on 02/15/2024).

[30] Eduard Masvidal-Codina et al. “High-resolution mapping of infraslow cortical brain activity enabled by graphene microtransistors”. en. In: *Nature Materials* 18.3 (Mar. 2019), pp. 280–288. ISSN: 1476-1122, 1476-4660. DOI: 10.1038/s41563-018-0249-4. URL: https://www.nature.com/articles/s41563-018-0249-4 (visited on 07/11/2023).

[31] Andrea Bonaccini Calia et al. “Full-bandwidth electrophysiology of seizures and epileptiform activity enabled by flexible graphene microtransistor depth neural probes”. en. In: *Nature Nanotechnology* 17.3 (Mar. 2022), pp. 301–309. ISSN: 1748-3387, 1748-3395. DOI: 10.1038/s41565-021-01041-9. URL: https://www.nature.com/articles/s41565-021-01041-9 (visited on 02/15/2024).

[32] R. Garcia-Cortadella et al. “Graphene active sensor arrays for long-term and wireless mapping of wide frequency band epicortical brain activity”. en. In: *Nature Communications* 12.1 (Jan. 2021), p. 211. ISSN: 2041-1723. DOI: 10.1038/s41467-020-20546-w. URL: https://www.nature.com/articles/s41467-020-20546-w (visited on 08/25/2023).

[33] X. Hong et al. “High-Mobility Few-Layer Graphene Field Effect Transistors Fabricated on Epitaxial Ferroelectric Gate Oxides”. en. In: *Physical Review Letters* 102.13 (Apr. 2009). arXiv:0810.4466 [cond-mat], p. 136808. ISSN: 0031-9007, 1079-7114. DOI: 10.1103/PhysRevLett.102.136808. URL: http://arxiv.org/abs/0810.4466 (visited on 05/30/2024).

[34] Sukang Bae et al. “Roll-to-roll production of 30-inch graphene films for transparent electrodes”. en. In: *Nature Nanotechnology* 5.8 (Aug. 2010), pp. 574–578. ISSN: 1748-3387, 1748-3395. DOI: 10.1038/nnano.2010.132. URL: https://www.nature.com/articles/nnano.2010.132 (visited on 05/29/2024).

[35] N. Reckinger and B. Hackens. “Identifying and abating copper foil impurities to optimize graphene growth”. en. In: *Applied Surface Science* 641 (Dec. 2023), p. 158555. ISSN: 01694332. DOI: 10.1016/j.apsusc.2023.158555. URL: https://linkinghub.elsevier.com/retrieve/pii/S0169433223022353 (visited on 05/29/2024).

[36] Soo Min Kim et al. “The effect of copper pre-cleaning on graphene synthesis”. en. In: (2013).

[37] Peter Bøggild. “Research on scalable graphene faces a reproducibility gap”. en. In: *nature communications* (2023).

[38] Xiaowei Du et al. “Electrochemistry Investigation on the Graphene/Electrolyte Interface”. en. In: *Electroanalysis* 27.12 (Dec. 2015), pp. 2760–2765. ISSN: 10400397. DOI: 10.1002/elan.201500302. URL: https://onlinelibrary.wiley.com/doi/10.1002/elan.201500302 (visited on 06/26/2023).

[39] Ghulam Abbas et al. “Electrostatic Gating of Monolayer Graphene by Concentrated Aqueous Electrolytes”. en. In: *The Journal of Physical Chemistry Letters* 14.18 (May 2023), pp. 4281–4288. ISSN: 1948-7185, 1948-7185. DOI: 10.1021/acs.jpclett.3c00814. URL: https://pubs.acs.org/doi/10.1021/acs.jpclett.3c00814 (visited on 08/27/2023).

[40] Shanshan Yang et al. “Nature of the Electrical Double Layer on Suspended Graphene Electrodes”. en. In: *Journal of the American Chemical Society* 144.29 (July 2022), pp. 13327–13333. ISSN: 0002-7863, 1520-5126. DOI: 10.1021/jacs.2c03344. URL: https://pubs.acs.org/doi/10.1021/jacs.2c03344 (visited on 09/20/2023).

[41] Martin Pykal et al. “Ion Interactions across Graphene in Electrolyte Aqueous Solutions”. en. In: *The Journal of Physical Chemistry C* 123.15 (Apr. 2019), pp. 9799–9806. ISSN: 1932-7447, 1932-7455. DOI: 10.1021/acs.jpcc.8b12055. URL: https://pubs.acs.org/doi/10.1021/acs.jpcc.8b12055 (visited on 09/20/2023).

[42] Daniel J. Cole, Priscilla K. Ang, and Kian Ping Loh. “Ion Adsorption at the Graphene/Electrolyte Interface”. en. In: *The Journal of Physical Chemistry Letters* 2.14 (July 2011), pp. 1799–1803. ISSN: 1948-7185, 1948-7185. DOI: 10.1021/jz200765z. URL: https://pubs.acs.org/doi/10.1021/jz200765z (visited on 09/20/2023).

[43] Muhammad Taqi-uddeen Safian, Khalid Umar, and Mohamad Nasir Mohamad Ibrahim. “Synthesis and scalability of graphene and its derivatives: A journey towards sustainable and commercial material”. en. In: *Journal of Cleaner Production* 318 (Oct. 2021), p. 128603. ISSN: 09596526. DOI: 10.1016/j.jclepro.2021.128603. URL: https://linkinghub.elsevier.com/retrieve/pii/S0959652621028080 (visited on 05/29/2024).

[44] Gabriela Borin Barin et al. “Optimized graphene transfer: Influence of polymethylmethacrylate (PMMA) layer concentration and baking time on graphene final performance”. en. In: *Carbon* 84 (Apr. 2015), pp. 82–90. ISSN: 00086223. DOI: 10.1016/j.carbon.2014.11.040. URL: https://linkinghub.elsevier.com/retrieve/pii/S0008622314011269 (visited on 02/12/2024).

[45] Jingyi Qu et al. “Evaporable Glass-State Molecule-Assisted Transfer of Clean and Intact Graphene onto Arbitrary Substrates”. en. In: *ACS Applied Materials & Interfaces* 11.18 (May 2019), pp. 16272–16279. ISSN: 1944-8244, 1944-8252. DOI: 10.1021/acsami.8b21946. URL: https://pubs.acs.org/doi/10.1021/acsami.8b21946 (visited on 06/09/2024).

[46] Yamujin Jang et al. “Performance Improvement of Residue-Free Graphene Field-Effect Transistor Using Au-Assisted Transfer Method”. en. In: *Sensors* 21.21 (Oct. 2021), p. 7262. ISSN: 1424-8220. DOI: 10.3390/s21217262. URL: https://www.mdpi.com/1424-8220/21/21/7262 (visited on 01/10/2024).

[47] M. Bahri et al. “Toward clean and crackless polymer-assisted transfer of CVD-grown graphene and its recent advances in GFET-based biosensors”. en. In: *Materials Today Chemistry* 22 (Dec. 2021), p. 100578. ISSN: 24685194. DOI: 10.1016/j.mtchem.2021.100578. URL: https://linkinghub.elsevier.com/retrieve/pii/S2468519421001580 (visited on 06/09/2024).

[48] Zhaoning Hu et al. “Rapid and Scalable Transfer of Large-Area Graphene Wafers”. en. In: *Advanced Materials* 35.29 (July 2023), p. 2300621. ISSN: 0935-9648, 1521-4095. DOI: 10.1002/adma.202300621. URL: https://onlinelibrary.wiley.com/doi/10.1002/adma.202300621 (visited on 06/09/2024).

[49] Patrícia D. Cabral et al. “Clean-Room Lithographical Processes for the Fabrication of Graphene Biosensors”. en. In: *Materials* 13.24 (Dec. 2020), p. 5728. ISSN: 1996-1944. DOI: 10.3390/ma13245728. URL: https://www.mdpi.com/1996-1944/13/24/5728 (visited on 06/09/2024).

[50] Panagiotis C. Theofanopoulos et al. “High-yield fabrication method for high-frequency graphene devices using titanium sacrificial layers”. en. In: *Journal of Vacuum Science & Technology B, Nanotechnology and Microelectronics: Materials, Processing, Measurement, and Phenomena* 37.4 (July 2019), p. 041801. ISSN: 2166-2746, 2166-2754. DOI: 10.1116/1.5098324. URL: https://pubs.aip.org/jvb/article/37/4/041801/591346/High-yield-fabrication-method-for-high-frequency (visited on 02/06/2024).

[51] Vasilios Georgakilas et al. “Functionalization of Graphene: Covalent and Non-Covalent Approaches, Derivatives and Applications”. en. In: *Chemical Reviews* 112.11 (Nov. 2012), pp. 6156–6214. ISSN: 0009-2665, 1520-6890. DOI: 10.1021/cr3000412. URL: https://pubs.acs.org/doi/10.1021/cr3000412 (visited on 06/26/2023).

[52] Vasilios Georgakilas et al. “Noncovalent Functionalization of Graphene and Graphene Oxide for Energy Materials, Biosensing, Catalytic, and Biomedical Applications”. en. In: *Chemical Reviews* 116.9 (May 2016), pp. 5464–5519. ISSN: 0009-2665, 1520-6890. DOI: 10.1021/acs.chemrev.5b00620. URL: https://pubs.acs.org/doi/10.1021/acs.chemrev.5b00620 (visited on 06/26/2023).

[53] Kostas Kostarelos et al. “Graphene in the Design and Engineering of Next-Generation Neural Interfaces”. en. In: *Advanced Materials* 29.42 (Nov. 2017), p. 1700909. ISSN: 0935-9648, 1521-4095. DOI: 10.1002/adma.201700909. URL: https://onlinelibrary.wiley.com/doi/10.1002/adma.201700909 (visited on 09/18/2023).

[54] A. H. Castro Neto et al. “The electronic properties of graphene”. en. In: *Reviews of Modern Physics* 81.1 (Jan. 2009), pp. 109–162. ISSN: 0034-6861, 1539-0756. DOI: 10.1103/RevModPhys.81.109. URL: https://link.aps.org/doi/10.1103/RevModPhys.81.109 (visited on 02/08/2024).

[55] D. C. Elias et al. “Dirac cones reshaped by interaction effects in suspended graphene”. en. In: *Nature Physics* 7.9 (Sept. 2011), pp. 701–704. ISSN: 1745-2473, 1745-2481. DOI: 10.1038/nphys2049. URL: https://www.nature.com/articles/nphys2049 (visited on 02/28/2024).

[56] Sergi Brosel-Oliu et al. “Single-Step Functionalization Strategy of Graphene Microtransistor Array with Chemically Modified Aptamers for Biosensing Applications”. en. In: *Small* (Dec. 2023), p. 2308857. ISSN: 1613-6810, 1613-6829. DOI: 10.1002/smll.202308857. URL: https://onlinelibrary.wiley.com/doi/10.1002/smll.202308857 (visited on 12/28/2023).

[57] Bin Zhang et al. “Low-Temperature Chemical Vapor Deposition Growth of Graphene from Toluene on Electropolished Copper Foils”. en. In: *ACS Nano* 6.3 (Mar. 2012), pp. 2471–2476. ISSN: 1936-0851, 1936-086X. DOI: 10.1021/nn204827h. URL: https://pubs.acs.org/doi/10.1021/nn204827h (visited on 01/30/2024).

[58] Ji Won Suk et al. “Transfer of CVD-Grown Monolayer Graphene onto Arbitrary Substrates”. en. In: *ACS Nano* 5.9 (Sept. 2011), pp. 6916–6924. ISSN: 1936-0851, 1936-086X. DOI: 10.1021/nn201207c. URL: https://pubs.acs.org/doi/10.1021/nn201207c (visited on 01/30/2024).

[59] Sang Yoon Yang et al. “Metal-Etching-Free Direct Delamination and Transfer of Single-Layer Graphene with a High Degree of Freedom”. en. In: *Small* 11.2 (Jan. 2015), pp. 175–181. ISSN: 16136810. DOI: 10.1002/

smll.201401196. URL: https://onlinelibrary.wiley.com/doi/10.1002/smll.201401196 (visited on 02/25/2024).

[60] Bozhong Zhuang et al. "Ways to eliminate PMMA residues on graphene —— superclean graphene". en. In: *Carbon* 173 (Mar. 2021), pp. 609–636. ISSN: 00086223. DOI: 10.1016/j.carbon.2020.11.047. URL: https://linkinghub.elsevier.com/retrieve/pii/S000862232031126X (visited on 07/03/2023).

[61] V. Zólyomi, J. Koltai, and J. Kürti. "Resonance Raman spectroscopy of graphite and graphene". en. In: *physica status solidi (b)* 248.11 (Nov. 2011), pp. 2435–2444. ISSN: 0370-1972, 1521-3951. DOI: 10.1002/pssb.201100295. URL: https://onlinelibrary.wiley.com/doi/10.1002/pssb.201100295 (visited on 03/25/2024).

[62] A. C. Ferrari et al. "Raman Spectrum of Graphene and Graphene Layers". en. In: *Physical Review Letters* 97.18 (Oct. 2006), p. 187401. ISSN: 0031-9007, 1079-7114. DOI: 10.1103/PhysRevLett.97.187401. URL: https://link.aps.org/doi/10.1103/PhysRevLett.97.187401 (visited on 09/01/2023).

[63] Ado Jorio et al. *Raman spectroscopy in graphene related systems*. en. Weinheim: Wiley-VCH, 2011. ISBN: 978-3-527-40811-5.

[64] Kai Yan et al. "Formation of Bilayer Bernal Graphene: Layer-by-Layer Epitaxy via Chemical Vapor Deposition". en. In: *Nano Letters* (2011).

[65] Andrea C Ferrari. "Raman spectroscopy as a versatile tool for studying the properties of graphene". en. In: *NATURE NANOTECHNOLOGY* 8 (2013).

[66] Andrea Cabrero-Vilatela et al. "Towards a general growth model for graphene CVD on transition metal catalysts". en. In: *Nanoscale* 8.4 (2016), pp. 2149–2158. ISSN: 2040-3364, 2040-3372. DOI: 10.1039/C5NR06873H. URL: http://xlink.rsc.org/?DOI=C5NR06873H (visited on 03/29/2024).

[67] Ji Eun Lee et al. "Optical separation of mechanical strain from charge doping in graphene". en. In: *Nature Communications* 3.1 (Aug. 2012), p. 1024. ISSN: 2041-1723. DOI: 10.1038/ncomms2022. URL: https://www.nature.com/articles/ncomms2022 (visited on 06/26/2023).

[68] Zhen Hua Ni et al. "Uniaxial Strain on Graphene: Raman Spectroscopy Study and Band-Gap Opening". en. In: *ACS Nano* 2.11 (Nov. 2008), pp. 2301–2305. ISSN: 1936-0851, 1936-086X. DOI: 10.1021/nn800459e. URL: https://pubs.acs.org/doi/10.1021/nn800459e (visited on 03/29/2024).

[69] Mingyuan Huang et al. “Probing Strain-Induced Electronic Structure Change in Graphene by Raman Spectroscopy”. en. In: *Nano Letters* 10.10 (Oct. 2010), pp. 4074–4079. ISSN: 1530-6984, 1530-6992. DOI: 10.1021/nl102123c. URL: https://pubs.acs.org/doi/10.1021/nl102123c (visited on 03/29/2024).

[70] Fei Ding et al. “Stretchable Graphene: A Close Look at Fundamental Parameters through Biaxial Straining”. en. In: *Nano Letters* 10.9 (Sept. 2010), pp. 3453–3458. ISSN: 1530-6984, 1530-6992. DOI: 10.1021/nl101533x. URL: https://pubs.acs.org/doi/10.1021/nl101533x (visited on 03/29/2024).

[71] Jun Yan et al. “Electric Field Effect Tuning of Electron-Phonon Coupling in Graphene”. en. In: *Physical Review Letters* 98.16 (Apr. 2007). arXiv:cond-mat/0612634, p. 166802. ISSN: 0031-9007, 1079-7114. DOI: 10.1103/PhysRevLett.98.166802. URL: http://arxiv.org/abs/cond-mat/0612634 (visited on 06/29/2023).

[72] Tomasz Tański et al. “Introductory Chapter: Why Atomic Force Microscopy (AFM) is One of the Leading Methods of Surface Morphology Research of all Engineering Material Groups”. en. In: *Atomic-force Microscopy and Its Applications*. Ed. by Tomasz Tański, Marcin Staszuk, and Bogusław Ziębowicz. IntechOpen, Jan. 2019. ISBN: 978-1-78985-169-4 978-1-78985-170-0. DOI: 10.5772/intechopen.80446. URL: https://www.intechopen.com/books/atomic-force-microscopy-and-its-applications/introductory-chapter-why-atomic-force-microscopy-afm-is-one-of-the-leading-methods-of-surface-morpho (visited on 03/29/2024).

[73] S. V. Borisov and N. V. Podberezskaya. “X-ray diffraction analysis: A brief history and achievements of the first century”. en. In: *Journal of Structural Chemistry* 53.S1 (Dec. 2012), pp. 1–3. ISSN: 0022-4766, 1573-8779. DOI: 10.1134/S0022476612070013. URL: http://link.springer.com/10.1134/S0022476612070013 (visited on 01/31/2024).

[74] Peter Fromherz et al. “A Neuron-Silicon Junction: A Retzius Cell of the Leech on an Insulated-Gate Field-Effect Transistor”. en. In: *Science* 252.5010 (May 1991), pp. 1290–1293. ISSN: 0036-8075, 1095-9203. DOI: 10.1126/science.1925540. URL: https://www.science.org/doi/10.1126/science.1925540 (visited on 03/25/2024).

[75] Markus Dankerl et al. “Graphene Solution-Gated Field-Effect Transistor Array for Sensing Applications”. en. In: *Advanced Functional Materials* 20.18 (Sept. 2010), pp. 3117–3124. ISSN: 1616-301X, 1616-3028. DOI: 10.

1002/adfm.201000724. URL: https://onlinelibrary.wiley.com/doi/10.1002/adfm.201000724 (visited on 05/20/2024).

[76] Kelli R Williams et al. "Progress of graphene devices for electrochemical biosensing in electrically excitable cells". en. In: *Progress in Biomedical Engineering* 3.2 (Apr. 2021), p. 022003. ISSN: 2516-1091. DOI: 10.1088/2516-1091/abe55b. URL: https://iopscience.iop.org/article/10.1088/2516-1091/abe55b (visited on 02/07/2024).

[77] Fabrizio Torricelli et al. "Electrolyte-gated transistors for enhanced performance bioelectronics". en. In: *Nature Reviews Methods Primers* 1.1 (Oct. 2021), p. 66. ISSN: 2662-8449. DOI: 10.1038/s43586-021-00065-8. URL: https://www.nature.com/articles/s43586-021-00065-8 (visited on 02/07/2024).

[78] Cecilia Wetzl et al. "The Covalent Functionalization of Surface-Supported Graphene: An Update". en. In: *Angewandte Chemie International Edition* 62.6 (Feb. 2023), e202212857. ISSN: 1433-7851, 1521-3773. DOI: 10.1002/anie.202212857. URL: https://onlinelibrary.wiley.com/doi/10.1002/anie.202212857 (visited on 02/18/2024).

[79] Sihan Chen and Rashid Bashir. "Advances in field-effect biosensors towards point-of-use". en. In: *Nanotechnology* 34.49 (Dec. 2023), p. 492002. ISSN: 0957-4484, 1361-6528. DOI: 10.1088/1361-6528/acf3f0. URL: https://iopscience.iop.org/article/10.1088/1361-6528/acf3f0 (visited on 02/07/2024).

[80] Ramon Garcia-Cortadella et al. "Distortion-Free Sensing of Neural Activity Using Graphene Transistors". en. In: *Small* 16.16 (Apr. 2020), p. 1906640. ISSN: 1613-6810, 1613-6829. DOI: 10.1002/smll.201906640. URL: https://onlinelibrary.wiley.com/doi/10.1002/smll.201906640 (visited on 02/23/2024).

[81] Howard Reiss and Adam Heller. "The absolute potential of the standard hydrogen electrode: a new estimate". en. In: *The Journal of Physical Chemistry* 89.20 (Sept. 1985), pp. 4207–4213. ISSN: 0022-3654, 1541-5740. DOI: 10.1021/j100266a013. URL: https://pubs.acs.org/doi/abs/10.1021/j100266a013 (visited on 02/12/2024).

[82] G. Giovannetti et al. "Doping Graphene with Metal Contacts". en. In: *Physical Review Letters* 101.2 (July 2008), p. 026803. ISSN: 0031-9007, 1079-7114. DOI: 10.1103/PhysRevLett.101.026803. URL: https://link.aps.org/doi/10.1103/PhysRevLett.101.026803 (visited on 10/31/2023).

[83] Young-Jun Yu et al. “Tuning the Graphene Work Function by Electric Field Effect”. en. In: *Nano Letters* 9.10 (Oct. 2009), pp. 3430–3434. ISSN: 1530-6984, 1530-6992. DOI: 10.1021/nl901572a. URL: https://pubs.acs.org/doi/10.1021/nl901572a (visited on 02/12/2024).

[84] Lucas H. Hess, Max Seifert, and Jose A. Garrido. “Graphene Transistors for Bioelectronics”. en. In: *Proceedings of the IEEE* 101.7 (July 2013), pp. 1780–1792. ISSN: 0018-9219, 1558-2256. DOI: 10.1109/JPROC.2013.2261031. URL: http://ieeexplore.ieee.org/document/6518189/ (visited on 02/12/2024).

[85] Aldert Van der Ziel. *Noise in solid state devices and circuits*. New York : Wiley, 1986. ISBN: 0-471-83234-0.

[86] Iddo Heller et al. “Charge Noise in Graphene Transistors”. en. In: *Nano Letters* 10.5 (May 2010), pp. 1563–1567. ISSN: 1530-6984, 1530-6992. DOI: 10.1021/nl903665g. URL: https://pubs.acs.org/doi/10.1021/nl903665g (visited on 02/12/2024).

[87] F. Bonaccorso et al. “Graphene photonics and optoelectronics”. en. In: *Nature Photonics* 4.9 (Sept. 2010), pp. 611–622. ISSN: 1749-4885, 1749-4893. DOI: 10.1038/nphoton.2010.186. URL: https://www.nature.com/articles/nphoton.2010.186 (visited on 02/08/2024).

[88] Adrián Gutiérrez-Cruz et al. “A review of top-down and bottom-up synthesis methods for the production of graphene, graphene oxide and reduced graphene oxide”. en. In: *Journal of Materials Science* 57.31 (Aug. 2022), pp. 14543–14578. ISSN: 0022-2461, 1573-4803. DOI: 10.1007/s10853-022-07514-z. URL: https://link.springer.com/10.1007/s10853-022-07514-z (visited on 09/18/2023).

[89] A.J. Van Bommel, J.E. Crombeen, and A. Van Tooren. “LEED and Auger electron observations of the SiC(0001) surface”. en. In: *Surface Science* 48.2 (Mar. 1975), pp. 463–472. ISSN: 00396028. DOI: 10.1016/0039-6028(75)90419-7. URL: https://linkinghub.elsevier.com/retrieve/pii/0039602875904197 (visited on 09/15/2023).

[90] J Hass, W A De Heer, and E H Conrad. “The growth and morphology of epitaxial multilayer graphene”. en. In: *Journal of Physics: Condensed Matter* 20.32 (Aug. 2008), p. 323202. ISSN: 0953-8984, 1361-648X. DOI: 10.1088/0953-8984/20/32/323202. URL: https://iopscience.iop.org/article/10.1088/0953-8984/20/32/323202 (visited on 09/15/2023).

[91] Michael L. Bolen et al. “Graphene formation mechanisms on 4 H -SiC (0001)”. en. In: *Physical Review B* 80.11 (Sept. 2009), p. 115433. ISSN: 1098-0121, 1550-235X. DOI: 10.1103/PhysRevB.80.115433. URL: https://link.aps.org/doi/10.1103/PhysRevB.80.115433 (visited on 02/24/2024).

[92] Wataru Norimatsu and Michiko Kusunoki. “Epitaxial graphene on SiC{0001}: advances and perspectives”. en. In: *Physical Chemistry Chemical Physics* 16.8 (2014), p. 3501. ISSN: 1463-9076, 1463-9084. DOI: 10.1039/c3cp54523g. URL: http://xlink.rsc.org/?DOI=c3cp54523g (visited on 09/15/2023).

[93] Chenxing Wang, Hitoshi Nakahara, and Yahachi Saito. “*In situ* SEM/STM observations and growth control of monolayer graphene on SiC (0001) wide terraces”. en. In: *Surface and Interface Analysis* 48.11 (Nov. 2016), pp. 1221–1225. ISSN: 0142-2421, 1096-9918. DOI: 10.1002/sia.6098. URL: https://analyticalsciencejournals.onlinelibrary.wiley.com/doi/10.1002/sia.6098 (visited on 02/24/2024).

[94] Konstantin V. Emtsev et al. “Towards wafer-size graphene layers by atmospheric pressure graphitization of silicon carbide”. en. In: *Nature Materials* 8.3 (Mar. 2009), pp. 203–207. ISSN: 1476-1122, 1476-4660. DOI: 10.1038/nmat2382. URL: https://www.nature.com/articles/nmat2382 (visited on 02/08/2024).

[95] C Virojanadara et al. “Large homogeneous mono-/bi-layer graphene on 6H–SiC(0 0 0 1) and buffer layer elimination”. en. In: *Journal of Physics D: Applied Physics* 43.37 (Sept. 2010), p. 374010. ISSN: 0022-3727, 1361-6463. DOI: 10.1088/0022-3727/43/37/374010. URL: https://iopscience.iop.org/article/10.1088/0022-3727/43/37/374010 (visited on 02/08/2024).

[96] M. Sprinkle et al. “Epitaxial graphene: the material for graphene electronics”. en. In: *physica status solidi (RRL) – Rapid Research Letters* 3.6 (Sept. 2009). ISSN: 1862-6254, 1862-6270. DOI: 10.1002/pssr.200903180. URL: https://onlinelibrary.wiley.com/doi/10.1002/pssr.200903180 (visited on 02/08/2024).

[97] Ye-Chuang Han et al. “Epitaxial Growth of Graphene on SiC by Thermal Shock Annealing Within Seconds”. en. In: *Advanced Functional Materials* 34.4 (Jan. 2024), p. 2307298. ISSN: 1616-301X, 1616-3028. DOI: 10.1002/adfm.202307298. URL: https://onlinelibrary.wiley.com/doi/10.1002/adfm.202307298 (visited on 02/08/2024).

[98] Baojun Sun et al. “Synthesis of Wafer-Scale Graphene with Chemical Vapor Deposition for Electronic Device Applications”. en. In: *Advanced Materials Technologies* 6.7 (July 2021), p. 2000744. ISSN: 2365-709X, 2365-709X. DOI: 10.1002/admt.202000744. URL: https://onlinelibrary.wiley.com/doi/10.1002/admt.202000744 (visited on 02/08/2024).

[99] Fengning Liu et al. “Achievements and Challenges of Graphene Chemical Vapor Deposition Growth”. en. In: *Advanced Functional Materials* 32.42 (Oct. 2022), p. 2203191. ISSN: 1616-301X, 1616-3028. DOI: 10.1002/adfm.202203191. URL: https://onlinelibrary.wiley.com/doi/10.1002/adfm.202203191 (visited on 02/08/2024).

[100] Prakash R. Somani, Savita P. Somani, and Masayoshi Umeno. “Planer nano-graphenes from camphor by CVD”. en. In: *Chemical Physics Letters* 430.1-3 (Oct. 2006), pp. 56–59. ISSN: 00092614. DOI: 10.1016/j.cplett.2006.06.081. URL: https://linkinghub.elsevier.com/retrieve/pii/S0009261406009018 (visited on 02/08/2024).

[101] Johann Coraux et al. “Structural Coherency of Graphene on Ir(111)”. en. In: *Nano Letters* 8.2 (Feb. 2008), pp. 565–570. ISSN: 1530-6984, 1530-6992. DOI: 10.1021/nl0728874. URL: https://pubs.acs.org/doi/10.1021/nl0728874 (visited on 02/08/2024).

[102] Xuesong Li et al. “Large-Area Synthesis of High-Quality and Uniform Graphene Films on Copper Foils”. en. In: *Science* 324.5932 (June 2009), pp. 1312–1314. ISSN: 0036-8075, 1095-9203. DOI: 10.1126/science.1171245. URL: https://www.science.org/doi/10.1126/science.1171245 (visited on 08/27/2023).

[103] Robert S. Weatherup et al. “In Situ Graphene Growth Dynamics on Polycrystalline Catalyst Foils”. en. In: *Nano Letters* 16.10 (Oct. 2016), pp. 6196–6206. ISSN: 1530-6984, 1530-6992. DOI: 10.1021/acs.nanolett.6b02459. URL: https://pubs.acs.org/doi/10.1021/acs.nanolett.6b02459 (visited on 02/08/2024).

[104] Jae-Hyun Lee et al. “Wafer-Scale Growth of Single-Crystal Monolayer Graphene on Reusable Hydrogen-Terminated Germanium”. en. In: *Science* 344.6181 (Apr. 2014), pp. 286–289. ISSN: 0036-8075, 1095-9203. DOI: 10.1126/science.1252268. URL: https://www.science.org/doi/10.1126/science.1252268 (visited on 02/08/2024).

[105] Xiaohong An et al. “Large-Area Synthesis of Graphene on Palladium and Their Raman Spectroscopy”. en. In: *The Journal of Physical Chemistry C* 116.31 (Aug. 2012), pp. 16412–16420. ISSN: 1932-7447, 1932-7455. DOI:

10.1021/jp301196u. URL: https://pubs.acs.org/doi/10.1021/jp301196u (visited on 02/08/2024).

[106] Ming Huang et al. "Highly Oriented Monolayer Graphene Grown on a Cu/Ni(111) Alloy Foil". en. In: *ACS Nano* 12.6 (June 2018), pp. 6117–6127. ISSN: 1936-0851, 1936-086X. DOI: 10.1021/acsnano.8b02444. URL: https://pubs.acs.org/doi/10.1021/acsnano.8b02444 (visited on 02/08/2024).

[107] Yong Zhang et al. "Chemical vapor deposition grown graphene on Cu-Pt alloys". en. In: *Materials Letters* 193 (Apr. 2017), pp. 255–258. ISSN: 0167577X. DOI: 10.1016/j.matlet.2017.01.089. URL: https://linkinghub.elsevier.com/retrieve/pii/S0167577X17301052 (visited on 02/08/2024).

[108] Xiangping Chen, Lili Zhang, and Shanshan Chen. "Large area CVD growth of graphene". en. In: *Synthetic Metals* 210 (Dec. 2015), pp. 95–108. ISSN: 03796779. DOI: 10.1016/j.synthmet.2015.07.005. URL: https://linkinghub.elsevier.com/retrieve/pii/S0379677915300138 (visited on 07/03/2023).

[109] Yongdong Xu and Xiu-Tian Yan. "Chemical Vapour Deposition Systems Design". In: *Chemical Vapour Deposition. Engineering Materials and Processes*. Springer, London, 2010. ISBN: 978-1-84882-893-3. URL: https://doi.org/10.1007/978-1-84882-894-0_3.

[110] G.A. López and E.J. Mittemeijer. "The solubility of C in solid Cu". en. In: *Scripta Materialia* 51.1 (July 2004), pp. 1–5. ISSN: 13596462. DOI: 10.1016/j.scriptamat.2004.03.028. URL: https://linkinghub.elsevier.com/retrieve/pii/S1359646204001769 (visited on 03/25/2024).

[111] Cecilia Mattevi, Hokwon Kim, and Manish Chhowalla. "A review of chemical vapour deposition of graphene on copper". en. In: *J. Mater. Chem.* 21.10 (2011), pp. 3324–3334. ISSN: 0959-9428, 1364-5501. DOI: 10.1039/C0JM02126A. URL: http://xlink.rsc.org/?DOI=C0JM02126A (visited on 03/25/2024).

[112] Hui Gao et al. "Synthesis of Large-Area and Monolayer of Graphene: Role of Transition Metal Support and Growth Time by CVD Method". en. In: *Advanced Materials Research* 306-307 (Aug. 2011), pp. 331–335. ISSN: 1662-8985. DOI: 10.4028/www.scientific.net/AMR.306-307.331. URL: https://www.scientific.net/AMR.306-307.331 (visited on 02/24/2024).

[113] Zhancheng Li et al. “Low-Temperature Growth of Graphene by Chemical Vapor Deposition Using Solid and Liquid Carbon Sources”. en. In: *ACS Nano* 5.4 (Apr. 2011), pp. 3385–3390. ISSN: 1936-0851, 1936-086X. DOI: 10.1021/nn200854p. URL: https://pubs.acs.org/doi/10.1021/nn200854p (visited on 02/24/2024).

[114] Niclas S. Mueller et al. “Growing graphene on polycrystalline copper foils by ultra-high vacuum chemical vapor deposition”. en. In: *Carbon* 78 (Nov. 2014), pp. 347–355. ISSN: 00086223. DOI: 10.1016/j.carbon.2014.07.011. URL: https://linkinghub.elsevier.com/retrieve/pii/S0008622314006344 (visited on 02/24/2024).

[115] Pierre Trinsoutrot et al. “High quality graphene synthesized by atmospheric pressure CVD on copper foil”. en. In: *Surface and Coatings Technology* 230 (Sept. 2013), pp. 87–92. ISSN: 02578972. DOI: 10.1016/j.surfcoat.2013.06.050. URL: https://linkinghub.elsevier.com/retrieve/pii/S0257897213005653 (visited on 02/24/2024).

[116] Lorenzo Pedrazzetti et al. “Graphene Growth on Electroformed Copper Substrates by Atmospheric Pressure CVD”. en. In: *Materials* 15.4 (Feb. 2022), p. 1572. ISSN: 1996-1944. DOI: 10.3390/ma15041572. URL: https://www.mdpi.com/1996-1944/15/4/1572 (visited on 02/24/2024).

[117] Xuesong Li et al. “Large-Area Graphene Single Crystals Grown by Low-Pressure Chemical Vapor Deposition of Methane on Copper”. en. In: *Journal of the American Chemical Society* 133.9 (Mar. 2011), pp. 2816–2819. ISSN: 0002-7863, 1520-5126. DOI: 10.1021/ja109793s. URL: https://pubs.acs.org/doi/10.1021/ja109793s (visited on 02/24/2024).

[118] Sreekar Bhaviripudi et al. “Role of Kinetic Factors in Chemical Vapor Deposition Synthesis of Uniform Large Area Graphene Using Copper Catalyst”. en. In: *Nano Letters* 10.10 (Oct. 2010), pp. 4128–4133. ISSN: 1530-6984, 1530-6992. DOI: 10.1021/nl102355e. URL: https://pubs.acs.org/doi/10.1021/nl102355e (visited on 02/24/2024).

[119] Stefanos Chaitoglou and Enric Bertran. “Effect of temperature on graphene grown by chemical vapor deposition”. en. In: *Journal of Materials Science* 52.13 (July 2017), pp. 8348–8356. ISSN: 0022-2461, 1573-4803. DOI: 10.1007/s10853-017-1054-1. URL: http://link.springer.com/10.1007/s10853-017-1054-1 (visited on 03/29/2024).

[120] HoKwon Kim et al. “Activation Energy Paths for Graphene Nucleation and Growth on Cu”. en. In: *ACS Nano* 6.4 (Apr. 2012), pp. 3614–3623. ISSN: 1936-0851, 1936-086X. DOI: 10.1021/nn3008965. URL: https://pubs.acs.org/doi/10.1021/nn3008965 (visited on 05/13/2024).

[121] Nan Liu et al. “The origin of wrinkles on transferred graphene”. en. In: *Nano Research* 4.10 (Oct. 2011), pp. 996–1004. ISSN: 1998-0124, 1998-0000. DOI: 10.1007/s12274-011-0156-3. URL: http://link.springer.com/10.1007/s12274-011-0156-3 (visited on 01/19/2024).

[122] Gang Hee Han et al. “Influence of Copper Morphology in Forming Nucleation Seeds for Graphene Growth”. en. In: *Nano Letters* 11.10 (Oct. 2011), pp. 4144–4148. ISSN: 1530-6984, 1530-6992. DOI: 10.1021/nl201980p. URL: https://pubs.acs.org/doi/10.1021/nl201980p (visited on 02/09/2024).

[123] Sang Jin Kim et al. “Ultraclean Patterned Transfer of Single-Layer Graphene by Recyclable Pressure Sensitive Adhesive Films”. en. In: *Nano Letters* 15.5 (May 2015), pp. 3236–3240. ISSN: 1530-6984, 1530-6992. DOI: 10.1021/acs.nanolett.5b00440. URL: https://pubs.acs.org/doi/10.1021/acs.nanolett.5b00440 (visited on 01/19/2024).

[124] Wei Sun Leong et al. “Paraffin-enabled graphene transfer”. en. In: *Nature Communications* 10.1 (Feb. 2019), p. 867. ISSN: 2041-1723. DOI: 10.1038/s41467-019-08813-x. URL: https://www.nature.com/articles/s41467-019-08813-x (visited on 01/19/2024).

[125] Benjamin Huet et al. “Fundamental limitations in transferred CVD graphene caused by Cu catalyst surface morphology”. en. In: *Carbon* 163 (Aug. 2020), pp. 95–104. ISSN: 00086223. DOI: 10.1016/j.carbon.2020.02.074. URL: https://linkinghub.elsevier.com/retrieve/pii/S0008622320302220 (visited on 01/19/2024).

[126] Mark P. Levendorf et al. “Transfer-Free Batch Fabrication of Single Layer Graphene Transistors”. en. In: *Nano Letters* 9.12 (Dec. 2009), pp. 4479–4483. ISSN: 1530-6984, 1530-6992. DOI: 10.1021/nl902790r. URL: https://pubs.acs.org/doi/10.1021/nl902790r (visited on 02/09/2024).

[127] Youngbin Lee et al. “Wafer-Scale Synthesis and Transfer of Graphene Films”. en. In: *Nano Letters* 10.2 (Feb. 2010), pp. 490–493. ISSN: 1530-6984, 1530-6992. DOI: 10.1021/nl903272n. URL: https://pubs.acs.org/doi/10.1021/nl903272n (visited on 02/09/2024).

[128] Yun-Hi Lee and Jong-Hee Lee. “Scalable growth of free-standing graphene wafers with copper(Cu) catalyst on SiO2/Si substrate: Thermal conductivity of the wafers”. en. In: *Applied Physics Letters* 96.8 (Feb. 2010), p. 083101. ISSN: 0003-6951, 1077-3118. DOI: 10.1063/1.3324698. URL: https://pubs.aip.org/apl/article/96/8/083101/237858/

Scalable-growth-of-free-standing-graphene-wafers (visited on 02/09/2024).

[129] Li Tao et al. "Uniform Wafer-Scale Chemical Vapor Deposition of Graphene on Evaporated Cu (111) Film with Quality Comparable to Exfoliated Monolayer". en. In: *The Journal of Physical Chemistry C* 116.45 (Nov. 2012), pp. 24068–24074. ISSN: 1932-7447, 1932-7455. DOI: 10.1021/jp3068848. URL: https://pubs.acs.org/doi/10.1021/jp3068848 (visited on 01/25/2024).

[130] Li Tao et al. "Synthesis of High Quality Monolayer Graphene at Reduced Temperature on Hydrogen-Enriched Evaporated Copper (111) Films". en. In: *ACS Nano* 6.3 (Mar. 2012), pp. 2319–2325. ISSN: 1936-0851, 1936-086X. DOI: 10.1021/nn205068n. URL: https://pubs.acs.org/doi/10.1021/nn205068n (visited on 01/25/2024).

[131] Gao Yang et al. "Structure of graphene and its disorders: a review". en. In: *Science and Technology of Advanced Materials* 19.1 (Dec. 2018), pp. 613–648. ISSN: 1468-6996, 1878-5514. DOI: 10.1080/14686996.2018.1494493. URL: https://www.tandfonline.com/doi/full/10.1080/14686996.2018.1494493 (visited on 02/09/2024).

[132] Benjamin Huet and Jean-Pierre Raskin. "Role of Cu foil in-situ annealing in controlling the size and thickness of CVD graphene domains". en. In: *Carbon* 129 (Apr. 2018), pp. 270–280. ISSN: 00086223. DOI: 10.1016/j.carbon.2017.12.043. URL: https://linkinghub.elsevier.com/retrieve/pii/S0008622317312769 (visited on 02/25/2024).

[133] Jincan Zhang et al. "Controlled Growth of Single-Crystal Graphene Films". en. In: *Advanced Materials* 32.1 (Jan. 2020), p. 1903266. ISSN: 0935-9648, 1521-4095. DOI: 10.1002/adma.201903266. URL: https://onlinelibrary.wiley.com/doi/10.1002/adma.201903266 (visited on 02/09/2024).

[134] Robert M. Jacobberger and Michael S. Arnold. "Graphene Growth Dynamics on Epitaxial Copper Thin Films". en. In: *Chemistry of Materials* 25.6 (Mar. 2013), pp. 871–877. ISSN: 0897-4756, 1520-5002. DOI: 10.1021/cm303445s. URL: https://pubs.acs.org/doi/10.1021/cm303445s (visited on 04/05/2024).

[135] Ken Verguts et al. "Epitaxial Al $_2$ O $_3$ (0001)/Cu(111) Template Development for CVD Graphene Growth". en. In: *The Journal of Physical Chemistry C* 120.1 (Jan. 2016), pp. 297–304. ISSN: 1932-7447, 1932-7455. DOI: 10.1021/acs.jpcc.5b09461. URL: https://pubs.acs.org/doi/10.1021/acs.jpcc.5b09461 (visited on 01/07/2024).

[136] Bing Deng et al. “Growth of Ultraflat Graphene with Greatly Enhanced Mechanical Properties”. en. In: *Nano Letters* 20.9 (Sept. 2020), pp. 6798–6806. ISSN: 1530-6984, 1530-6992. DOI: 10.1021/acs.nanolett.0c02785. URL: https://pubs.acs.org/doi/10.1021/acs.nanolett.0c02785 (visited on 08/27/2023).

[137] M. Yoshimoto et al. “Atomic-scale formation of ultrasmooth surfaces on sapphire substrates for high-quality thin-film fabrication”. en. In: *Applied Physics Letters* 67.18 (Oct. 1995), pp. 2615–2617. ISSN: 0003-6951, 1077-3118. DOI: 10.1063/1.114313. URL: https://pubs.aip.org/apl/article/67/18/2615/521919/Atomic-scale-formation-of-ultrasmooth-surfaces-on (visited on 02/02/2024).

[138] J R Heffelfinger, M W Bench, and C B Carter. “Steps and the structure of the (0001) a-alumina surface”. en. In: *Surface Science* (1997).

[139] E. Thune et al. “Nanostructured sapphire vicinal surfaces as templates for the growth of self-organized oxide nanostructures”. en. In: *Applied Surface Science* 256.3 (Nov. 2009), pp. 924–928. ISSN: 01694332. DOI: 10.1016/j.apsusc.2009.08.089. URL: https://linkinghub.elsevier.com/retrieve/pii/S0169433209012331 (visited on 02/02/2024).

[140] R. Verre et al. “Equilibrium faceting formation in vicinal Al2O3 (0001) surface caused by annealing”. en. In: *Surface Science* 606.23-24 (Dec. 2012), pp. 1815–1820. ISSN: 00396028. DOI: 10.1016/j.susc.2012.07.024. URL: https://linkinghub.elsevier.com/retrieve/pii/S0039602812002634 (visited on 02/02/2024).

[141] F. Cuccureddu et al. “Surface morphology of c-plane sapphire (-alumina) produced by high temperature anneal”. en. In: *Surface Science* 604.15-16 (Aug. 2010), pp. 1294–1299. ISSN: 00396028. DOI: 10.1016/j.susc.2010.04.017. URL: https://linkinghub.elsevier.com/retrieve/pii/S0039602810001780 (visited on 02/02/2024).

[142] Christian Martin Schäfer. “Synthesis and device integration of two-dimensional MOCVD MoS2 Ąlms”. en. PhD thesis. Universitat Autònoma de Barcelona, 2023.

[143] Linlin Cao et al. “Study on the Influence of Sapphire Crystal Orientation on Its Chemical Mechanical Polishing”. en. In: *Applied Sciences* 10.22 (Nov. 2020), p. 8065. ISSN: 2076-3417. DOI: 10.3390/app10228065. URL: https://www.mdpi.com/2076-3417/10/22/8065 (visited on 02/02/2024).

[144] Rongrong Wang. “Atomic Step Formation on Sapphire Surface in Ultra-precision Manufacturing”. en. In: *Scientific Reports* ().

[145] Yuki Hayashi et al. “Heteroepitaxy between wurtzite and corundum materials”. en. In: *Journal of Applied Physics* 113.18 (May 2013), p. 183523. ISSN: 0021-8979, 1089-7550. DOI: 10.1063/1.4804328. URL: https://pubs.aip.org/jap/article/113/18/183523/1014309/Heteroepitaxy-between-wurtzite-and-corundum (visited on 05/23/2024).

[146] Aki Tosaka et al. “Influence of step morphology on the structural phase transition of the -Al2O3(0001) surface”. en. In: *Applied Physics Letters* 104.22 (June 2014), p. 221601. ISSN: 0003-6951, 1077-3118. DOI: 10.1063/1.4881334. URL: https://pubs.aip.org/apl/article/104/22/221601/26607/Influence-of-step-morphology-on-the-structural (visited on 02/25/2024).

[147] Tao Ma et al. “Smooth epitaxial copper film on sapphire surface suitable for high quality graphene growth”. en. In: *Thin Solid Films* 646 (Jan. 2018), pp. 12–16. ISSN: 00406090. DOI: 10.1016/j.tsf.2017.11.009. URL: https://linkinghub.elsevier.com/retrieve/pii/S0040609017308453 (visited on 01/07/2024).

[148] Carl V. Thompson. “Solid-State Dewetting of Thin Films”. en. In: *Annual Review of Materials Research* 42.1 (Aug. 2012), pp. 399–434. ISSN: 1531-7331, 1545-4118. DOI: 10.1146/annurev-matsci-070511-155048. URL: https://www.annualreviews.org/doi/10.1146/annurev-matsci-070511-155048 (visited on 01/31/2024).

[149] Hiroki Ago et al. “Epitaxial Growth and Electronic Properties of Large Hexagonal Graphene Domains on Cu(111) Thin Film”. en. In: *Applied Physics Express* 6.7 (July 2013), p. 075101. ISSN: 1882-0778, 1882-0786. DOI: 10.7567/APEX.6.075101. URL: https://iopscience.iop.org/article/10.7567/APEX.6.075101 (visited on 01/20/2024).

[150] Yan Jin et al. “Roles of H $_2$ in annealing and growth times of graphene CVD synthesis over copper foil”. en. In: *J. Mater. Chem. A* 2.38 (Aug. 2014), pp. 16208–16216. ISSN: 2050-7488, 2050-7496. DOI: 10.1039/C4TA02557A. URL: http://xlink.rsc.org/?DOI=C4TA02557A (visited on 02/25/2024).

[151] Ahmed Ibrahim et al. “Effects of annealing on copper substrate surface morphology and graphene growth by chemical vapor deposition”. en. In: *Carbon* 94 (Nov. 2015), pp. 369–377. ISSN: 00086223. DOI: 10.1016/j.carbon.2015.06.067. URL: https://linkinghub.elsevier.com/retrieve/pii/S0008622315300154 (visited on 02/25/2024).

[152] Hong Wang et al. “Controllable Synthesis of Submillimeter Single-Crystal Monolayer Graphene Domains on Copper Foils by Suppressing Nucleation”. en. In: *Journal of the American Chemical Society* 134.8 (Feb. 2012), pp. 3627–3630. ISSN: 0002-7863, 1520-5126. DOI: 10.1021/ja2105976. URL: https://pubs.acs.org/doi/10.1021/ja2105976 (visited on 02/25/2024).

[153] Lin Gan and Zhengtang Luo. “Turning off Hydrogen To Realize Seeded Growth of Subcentimeter Single-Crystal Graphene Grains on Copper”. en. In: *ACS Nano* 7.10 (Oct. 2013), pp. 9480–9488. ISSN: 1936-0851, 1936-086X. DOI: 10.1021/nn404393b. URL: https://pubs.acs.org/doi/10.1021/nn404393b (visited on 02/25/2024).

[154] Da Hee Jung et al. “Effects of Hydrogen Partial Pressure in the Annealing Process on Graphene Growth”. en. In: *The Journal of Physical Chemistry C* 118.7 (Feb. 2014), pp. 3574–3580. ISSN: 1932-7447, 1932-7455. DOI: 10.1021/jp410961m. URL: https://pubs.acs.org/doi/10.1021/jp410961m (visited on 02/25/2024).

[155] Jian Liu et al. “Effects of H2 annealing on polycrystalline copper substrates for graphene growth during low pressure chemical vapor deposition”. en. In: *Materials Letters* 153 (Aug. 2015), pp. 132–135. ISSN: 0167577X. DOI: 10.1016/j.matlet.2015.03.150. URL: https://linkinghub.elsevier.com/retrieve/pii/S0167577X15005467 (visited on 02/25/2024).

[156] RSC. URL: https://www.rsc.org/periodic-table/element/29/copper.

[157] Sanghoon Park et al. “Effect of grain boundaries on electrical properties of polycrystalline graphene”. en. In: *Carbon* 112 (Feb. 2017), pp. 142–148. ISSN: 00086223. DOI: 10.1016/j.carbon.2016.11.010. URL: https://linkinghub.elsevier.com/retrieve/pii/S0008622316309800 (visited on 01/31/2024).

[158] Qinghong Yuan et al. “Formation of Graphene Grain Boundaries on Cu(100) Surface and a Route Towards Their Elimination in Chemical Vapor Deposition Growth”. en. In: *Scientific Reports* 4.1 (Oct. 2014), p. 6541. ISSN: 2045-2322. DOI: 10.1038/srep06541. URL: https://www.nature.com/articles/srep06541 (visited on 01/31/2024).

[159] Baoshan Hu et al. “Epitaxial growth of large-area single-layer graphene over Cu(1 1 1)/sapphire by atmospheric pressure CVD”. en. In: *Carbon* 50.1 (Jan. 2012), pp. 57–65. ISSN: 00086223. DOI: 10.1016/j.carbon.2011.08.002. URL: https://linkinghub.elsevier.com/retrieve/pii/S0008622311006282 (visited on 01/20/2024).

[160] E. Knoll and H. Bialas. "Growth modes of epitaxial copper films on c-sapphire". en. In: *Thin Solid Films* 250.1-2 (Oct. 1994), pp. 42–46. ISSN: 00406090. DOI: 10.1016/0040-6090(94)90162-7. URL: https://linkinghub.elsevier.com/retrieve/pii/0040609094901627 (visited on 04/05/2024).

[161] Yui Ogawa et al. "Domain Structure and Boundary in Single-Layer Graphene Grown on Cu(111) and Cu(100) Films". en. In: *The Journal of Physical Chemistry Letters* 3.2 (Jan. 2012), pp. 219–226. ISSN: 1948-7185, 1948-7185. DOI: 10.1021/jz2015555. URL: https://pubs.acs.org/doi/10.1021/jz2015555 (visited on 04/05/2024).

[162] Kongara M. Reddy et al. "High quality, transferrable graphene grown on single crystal Cu(111) thin films on basal-plane sapphire". en. In: *Applied Physics Letters* 98.11 (Mar. 2011), p. 113117. ISSN: 0003-6951, 1077-3118. DOI: 10.1063/1.3569143. URL: https://pubs.aip.org/apl/article/98/11/113117/323483/High-quality-transferrable-graphene-grown-on (visited on 04/05/2024).

[163] Kyung Pyo Hong et al. "Real-Time Optical Visualization of Graphene Defects and Grain Boundaries by the Thermal Oxidation of a Graphene-Coated Copper Foil". en. In: *ACS Applied Nano Materials* 1.6 (June 2018), pp. 2515–2520. ISSN: 2574-0970, 2574-0970. DOI: 10.1021/acsanm.8b00646. URL: https://pubs.acs.org/doi/10.1021/acsanm.8b00646 (visited on 01/26/2024).

[164] Dinh Loc Duong et al. "Probing graphene grain boundaries with optical microscopy". en. In: *Nature* 490.7419 (Oct. 2012), pp. 235–239. ISSN: 0028-0836, 1476-4687. DOI: 10.1038/nature11562. URL: https://www.nature.com/articles/nature11562 (visited on 01/26/2024).

[165] Yuqing Song et al. "Graphene Transfer: Paving the Road for Applications of Chemical Vapor Deposition Graphene". en. In: *Small* 17.48 (Dec. 2021), p. 2007600. ISSN: 1613-6810, 1613-6829. DOI: 10.1002/smll.202007600. URL: https://onlinelibrary.wiley.com/doi/10.1002/smll.202007600 (visited on 02/08/2024).

[166] Liubov A. Belyaeva et al. "Liquids relax and unify strain in graphene". en. In: *Nature Communications* 11.1 (Feb. 2020), p. 898. ISSN: 2041-1723. DOI: 10.1038/s41467-020-14637-x. URL: https://www.nature.com/articles/s41467-020-14637-x (visited on 01/19/2024).

[167] C Bautista-Flores, R Y Sato-Berrú, and D Mendoza. "Raman spectroscopy of CVD graphene during transfer process from copper to SiO $_2$ /Si substrates". en. In: *Materials Research Express* 6.1 (Oct. 2018), p. 015601. ISSN: 2053-1591. DOI: 10.1088/2053-1591/aae32f. URL: https://iopscience.iop.org/article/10.1088/2053-1591/aae32f.

[168] C. A. Joiner et al. "Cleaning graphene with a titanium sacrificial layer". en. In: *Applied Physics Letters* 104.22 (June 2014), p. 223109. ISSN: 0003-6951, 1077-3118. DOI: 10.1063/1.4881886. URL: https://pubs.aip.org/apl/article/104/22/223109/26714/Cleaning-graphene-with-a-titanium-sacrificial (visited on 06/26/2023).

[169] Ji Won Suk et al. "Enhancement of the Electrical Properties of Graphene Grown by Chemical Vapor Deposition via Controlling the Effects of Polymer Residue". en. In: *Nano Letters* 13.4 (Apr. 2013), pp. 1462–1467. ISSN: 1530-6984, 1530-6992. DOI: 10.1021/nl304420b. URL: https://pubs.acs.org/doi/10.1021/nl304420b (visited on 06/26/2023).

[170] Ahreum Choi et al. "Residue-free photolithographic patterning of graphene". en. In: *Chemical Engineering Journal* 429 (Feb. 2022), p. 132504. ISSN: 13858947. DOI: 10.1016/j.cej.2021.132504. URL: https://linkinghub.elsevier.com/retrieve/pii/S1385894721040821 (visited on 01/10/2024).

[171] Yunpeng Yan et al. "Recovering the Intrinsic Electrical Property of a Graphene Field-Effect Transistor by Interface Cleaning Technology". en. In: *ACS Applied Electronic Materials* 5.6 (June 2023), pp. 3113–3119. ISSN: 2637-6113, 2637-6113. DOI: 10.1021/acsaelm.3c00187. URL: https://pubs.acs.org/doi/10.1021/acsaelm.3c00187 (visited on 01/10/2024).

[172] Sun Sang Kwon et al. "Electrical Double Layer of Supported Atomically Thin Materials". en. In: *Nano Letters* 19.7 (July 2019), pp. 4588–4593. ISSN: 1530-6984, 1530-6992. DOI: 10.1021/acs.nanolett.9b01563. URL: https://pubs.acs.org/doi/10.1021/acs.nanolett.9b01563 (visited on 06/26/2023).

[173] Huachao Yang et al. "Substrate Effects in Graphene-Based Electric Double-Layer Capacitors: The Pivotal Interplays between Ions and Solvents". en. In: *ChemElectroChem* 4.11 (Nov. 2017), pp. 2966–2974. ISSN: 21960216. DOI: 10.1002/celc.201700733. URL: https://onlinelibrary.wiley.com/doi/10.1002/celc.201700733 (visited on 10/02/2023).

[174] Jihye Shim et al. “Water-Gated Charge Doping of Graphene Induced by Mica Substrates”. en. In: *Nano Letters* 12.2 (Feb. 2012), pp. 648–654. ISSN: 1530-6984, 1530-6992. DOI: 10.1021/nl2034317. URL: https://pubs.acs.org/doi/10.1021/nl2034317 (visited on 01/10/2024).

[175] Yanlei Wang and Zhiping Xu. “Water Intercalation for Seamless, Electrically Insulating, and Thermally Transparent Interfaces”. en. In: *ACS Applied Materials & Interfaces* 8.3 (Jan. 2016), pp. 1970–1976. ISSN: 1944-8244, 1944-8252. DOI: 10.1021/acsami.5b10173. URL: https://pubs.acs.org/doi/10.1021/acsami.5b10173 (visited on 06/26/2023).

[176] Michele Magnozzi et al. “Fast detection of water nanopockets underneath wet-transferred graphene”. en. In: *Carbon* 118 (July 2017), pp. 208–214. ISSN: 00086223. DOI: 10.1016/j.carbon.2017.03.022. URL: https://linkinghub.elsevier.com/retrieve/pii/S0008622317302634 (visited on 06/26/2023).

[177] F. O. Koenig. “The Thermodynamics of the Electrocapillary Curve. II. The Variation of the Electrocapillary Curve with Composition.” en. In: *The Journal of Physical Chemistry* 38.3 (Mar. 1934), pp. 339–363. ISSN: 0092-7325, 1541-5740. DOI: 10.1021/j150354a007. URL: https://pubs.acs.org/doi/abs/10.1021/j150354a007 (visited on 01/11/2024).

[178] H. Helmholtz. “Ueber einige Gesetze der Vertheilung elektrischer Ströme in körperlichen Leitern mit Anwendung auf die thierisch-elektrischen Versuche”. de. In: *Annalen der Physik* 165.6 (Jan. 1853), pp. 211–233. ISSN: 0003-3804, 1521-3889. DOI: 10.1002/andp.18531650603. URL: https://onlinelibrary.wiley.com/doi/10.1002/andp.18531650603 (visited on 01/11/2024).

[179] Joshua D. Elliott et al. “The electrochemical double layer at the graphene/aqueous electrolyte interface: what we can learn from simulations, experiments, and theory”. en. In: *Journal of Materials Chemistry C* 10.41 (2022), pp. 15225–15262. ISSN: 2050-7526, 2050-7534. DOI: 10.1039/D2TC01631A. URL: http://xlink.rsc.org/?DOI=D2TC01631A (visited on 09/29/2023).

[180] Allen J. Bard and Larry R. Faulkner. *Electrochemical methods: fundamentals and applications*. en. 2. edition. New York Weinheim: Wiley, 2001. ISBN: 978-0-471-04372-0.

[181] D. L. John, L. C. Castro, and D. L. Pulfrey. “Quantum capacitance in nanoscale device modeling”. en. In: *Journal of Applied Physics* 96.9 (Nov. 2004), pp. 5180–5184. ISSN: 0021-8979, 1089-7550. DOI: 10.1063/1.

1803614. URL: https://pubs.aip.org/jap/article/96/9/5180/954226/Quantum-capacitance-in-nanoscale-device-modeling (visited on 04/08/2024).

[182] Jilin Xia et al. "Measurement of the quantum capacitance of graphene". en. In: *Nature Nanotechnology* 4.8 (Aug. 2009), pp. 505–509. ISSN: 1748-3387, 1748-3395. DOI: 10.1038/nnano.2009.177. URL: https://www.nature.com/articles/nnano.2009.177 (visited on 10/02/2023).

[183] Meryl D. Stoller et al. "Interfacial capacitance of single layer graphene". en. In: *Energy & Environmental Science* 4.11 (2011), p. 4685. ISSN: 1754-5692, 1754-5706. DOI: 10.1039/c1ee02322e. URL: http://xlink.rsc.org/?DOI=c1ee02322e (visited on 04/08/2024).

[184] Hengxing Ji et al. "Capacitance of carbon-based electrical double-layer capacitors". en. In: *Nature Communications* 5.1 (Feb. 2014), p. 3317. ISSN: 2041-1723. DOI: 10.1038/ncomms4317. URL: https://www.nature.com/articles/ncomms4317 (visited on 01/14/2024).

[185] Clement Hébert et al. "Flexible Graphene Solution-Gated Field-Effect Transistors: Efficient Transducers for Micro-Electrocorticography". en. In: *Advanced Functional Materials* 28.12 (Mar. 2018), p. 1703976. ISSN: 1616-301X, 1616-3028. DOI: 10.1002/adfm.201703976. URL: https://onlinelibrary.wiley.com/doi/10.1002/adfm.201703976 (visited on 04/02/2024).

[186] Samantha Michelle Gateman et al. "On the use of a constant phase element (CPE) in electrochemistry". en. In: *Current Opinion in Electrochemistry* 36 (Dec. 2022), p. 101133. ISSN: 24519103. DOI: 10.1016/j.coelec.2022.101133. URL: https://linkinghub.elsevier.com/retrieve/pii/S2451910322001983 (visited on 11/07/2023).

[187] Mark E. Orazem and Bernard Tribollet. *Electrochemical impedance spectroscopy*. en. The Electrochemical Society series. Hoboken (New Jersey): Wiley, 2008. ISBN: 978-0-470-04140-6.

[188] Sverre Holm, Thomas Holm, and Ørjan Grøttem Martinsen. "Simple circuit equivalents for the constant phase element". en. In: *PLOS ONE* 16.3 (Mar. 2021). Ed. by Muhammad Zubair, e0248786. ISSN: 1932-6203. DOI: 10.1371/journal.pone.0248786. URL: https://dx.plos.org/10.1371/journal.pone.0248786 (visited on 04/02/2024).

[189] Simon Drieschner et al. "Frequency response of electrolyte-gated graphene electrodes and transistors". en. In: *Journal of Physics D: Applied Physics* 50.9 (Mar. 2017), p. 095304. ISSN: 0022-3727, 1361-6463. DOI: 10.1088/

1361-6463/aa5443. URL: https://iopscience.iop.org/article/10.1088/1361-6463/aa5443 (visited on 06/27/2023).

[190] Francisco Pasadas et al. "Exploiting Ambipolarity in Graphene Field-Effect Transistors for Novel Designs on High-Frequency Analog Electronics". en. In: *Small* (Aug. 2023), p. 2303595. ISSN: 1613-6810, 1613-6829. DOI: 10.1002/smll.202303595. URL: https://onlinelibrary.wiley.com/doi/10.1002/smll.202303595 (visited on 11/19/2023).

[191] Charles Mackin, Elaine McVay, and Tomás Palacios. "Frequency Response of Graphene Electrolyte-Gated Field-Effect Transistors". en. In: *Sensors* 18.2 (Feb. 2018), p. 494. ISSN: 1424-8220. DOI: 10.3390/s18020494. URL: https://www.mdpi.com/1424-8220/18/2/494 (visited on 10/16/2023).

[192] M.V. Cheremisin. "Quantum capacitance of the monolayer graphene". en. In: *Physica E: Low-dimensional Systems and Nanostructures* 69 (May 2015), pp. 153–158. ISSN: 13869477. DOI: 10.1016/j.physe.2015.01.018. URL: https://linkinghub.elsevier.com/retrieve/pii/S1386947715000193 (visited on 01/14/2024).

[193] Maximilian Schalenbach et al. "Physicochemical Mechanisms of the Double-Layer Capacitance Dispersion and Dynamics: An Impedance Analysis". en. In: *The Journal of Physical Chemistry C* 125.10 (Mar. 2021), pp. 5870–5879. ISSN: 1932-7447, 1932-7455. DOI: 10.1021/acs.jpcc.0c11335. URL: https://pubs.acs.org/doi/10.1021/acs.jpcc.0c11335 (visited on 01/14/2024).

[194] Maximilian Schalenbach et al. "Double layer capacitances analysed with impedance spectroscopy and cyclic voltammetry: validity and limits of the constant phase element parameterization". en. In: *Physical Chemistry Chemical Physics* 23.37 (2021), pp. 21097–21105. ISSN: 1463-9076, 1463-9084. DOI: 10.1039/D1CP03381F. URL: http://xlink.rsc.org/?DOI=D1CP03381F (visited on 08/29/2023).

[195] Ali Hassanzadeh, Mohammad Hossein Habibi, and Asghar Zeini-Isfahani. "STUDY OF ELECTRONIC STRUCTURE OF TIN-DOPED In2O3 (ITO) FILM DEPOSITED ON GLASS". en. In: *Acta Chim. Slov.* (2004).

[196] Guillaume Froehlicher and Stéphane Berciaud. "Raman spectroscopy of electrochemically gated graphene transistors: Geometrical capacitance, electron-phonon, electron-electron, and electron-defect scattering". en. In: *Physical Review B* 91.20 (May 2015), p. 205413. ISSN: 1098-0121, 1550-235X. DOI: 10.1103/PhysRevB.91.205413. URL: https://link.aps.org/doi/10.1103/PhysRevB.91.205413 (visited on 02/25/2024).

[197] Simone Pisana et al. “Breakdown of the adiabatic Born–Oppenheimer approximation in graphene”. en. In: *Nature Materials* 6.3 (Mar. 2007), pp. 198–201. ISSN: 1476-1122, 1476-4660. DOI: 10.1038/nmat1846. URL: https://www.nature.com/articles/nmat1846 (visited on 04/05/2024).

[198] P. T. Araujo et al. “Phonon Self-Energy Corrections to Nonzero Wave-Vector Phonon Modes in Single-Layer Graphene”. en. In: *Physical Review Letters* 109.4 (July 2012), p. 046801. ISSN: 0031-9007, 1079-7114. DOI: 10.1103/PhysRevLett.109.046801. URL: https://link.aps.org/doi/10.1103/PhysRevLett.109.046801 (visited on 04/05/2024).

[199] Michele Lazzeri and Francesco Mauri. “Nonadiabatic Kohn Anomaly in a Doped Graphene Monolayer”. en. In: *Physical Review Letters* 97.26 (Dec. 2006), p. 266407. ISSN: 0031-9007, 1079-7114. DOI: 10.1103/PhysRevLett.97.266407. URL: https://link.aps.org/doi/10.1103/PhysRevLett.97.266407 (visited on 10/24/2023).

[200] Ken Verguts et al. “Controlling Water Intercalation Is Key to a Direct Graphene Transfer”. en. In: *ACS Applied Materials & Interfaces* 9.42 (Oct. 2017), pp. 37484–37492. ISSN: 1944-8244, 1944-8252. DOI: 10.1021/acsami.7b12573. URL: https://pubs.acs.org/doi/10.1021/acsami.7b12573 (visited on 06/26/2023).

[201] Kevin T. He et al. “Scanning Tunneling Microscopy Study and Nanomanipulation of Graphene-Coated Water on Mica”. en. In: *Nano Letters* 12.6 (June 2012), pp. 2665–2672. ISSN: 1530-6984, 1530-6992. DOI: 10.1021/nl202613t. URL: https://pubs.acs.org/doi/10.1021/nl202613t (visited on 01/10/2024).

[202] Yanlei Wang et al. “Intercalated water layers promote thermal dissipation at bio–nano interfaces”. en. In: *Nature Communications* 7.1 (Sept. 2016), p. 12854. ISSN: 2041-1723. DOI: 10.1038/ncomms12854. URL: https://www.nature.com/articles/ncomms12854 (visited on 10/27/2023).

[203] Ang-Yu Lu et al. “Decoupling of CVD graphene by controlled oxidation of recrystallized Cu”. en. In: *RSC Advances* 2.7 (2012), p. 3008. ISSN: 2046-2069. DOI: 10.1039/c2ra01281b. URL: http://xlink.rsc.org/?DOI=c2ra01281b (visited on 10/02/2023).

[204] Sukhyun Hong et al. “Formation of graphene nanostructures using laser induced vaporization of entrapped water”. en. In: *Carbon* 183 (Oct. 2021), pp. 84–92. ISSN: 00086223. DOI: 10.1016/j.carbon.2021.06.071. URL: https://linkinghub.elsevier.com/retrieve/pii/S0008622321006588 (visited on 10/02/2023).

[205] Yue Hong et al. “Interfacial icelike water local doping graphene”. en. In: *Nanoscale* (2019). ISSN: 2040-3364, 2040-3372. DOI: DOI : 10 . 1039 / C9NR05832J. URL: https : / / pubs . rsc . org / en / content / articlelanding/2019/nr/c9nr05832j/unauth#!divAbstract (visited on 01/10/2024).

[206] Jean-François Olivieri, James T. Hynes, and Damien Laage. “Confined Water’s Dielectric Constant Reduction Is Due to the Surrounding Low Dielectric Media and Not to Interfacial Molecular Ordering”. en. In: *The Journal of Physical Chemistry Letters* 12.17 (May 2021), pp. 4319–4326. ISSN: 1948-7185, 1948-7185. DOI: 10.1021/acs.jpclett.1c00447. URL: https://pubs.acs.org/doi/10.1021/acs.jpclett.1c00447 (visited on 01/25/2024).

[207] L. Fumagalli et al. “Anomalously low dielectric constant of confined water”. en. In: *Science* 360.6395 (June 2018), pp. 1339–1342. ISSN: 0036-8075, 1095-9203. DOI: 10.1126/science.aat4191. URL: https://www.science.org/doi/10.1126/science.aat4191 (visited on 03/16/2024).

[208] A. Toral-Lopez et al. “Assessment of three electrolyte–molecule electrostatic interaction models for 2D material based BioFETs”. en. In: *Nanoscale Advances* 1.3 (2019), pp. 1077–1085. ISSN: 2516-0230. DOI: 10.1039/C8NA00109J. URL: http://xlink.rsc.org/?DOI=C8NA00109J (visited on 03/18/2024).

[209] A. Toral-Lopez et al. “Graphene BioFET sensors for SARS-CoV-2 detection: a multiscale simulation approach”. en. In: *Nanoscale Advances* 4.14 (2022), pp. 3065–3072. ISSN: 2516-0230. DOI: 10.1039/D2NA00357K. URL: http://xlink.rsc.org/?DOI=D2NA00357K (visited on 03/18/2024).

[210] Shayan Angizi et al. “Graphene versus concentrated aqueous electrolytes: the role of the electrochemical double layer in determining the screening length of an electrolyte”. en. In: *npj 2D Materials and Applications* 7.1 (Sept. 2023), p. 67. ISSN: 2397-7132. DOI: 10.1038/s41699-023-00431-y. URL: https : / / www . nature . com / articles / s41699 - 023 - 00431 - y (visited on 01/14/2024).

[211] Benjamin Mailly-Giacchetti et al. “pH sensing properties of graphene solution-gated field-effect transistors”. en. In: *Journal of Applied Physics* 114.8 (Aug. 2013), p. 084505. ISSN: 0021-8979, 1089-7550. DOI: 10.1063/1.4819219. URL: https : / / pubs . aip . org / jap / article / 114 / 8 / 084505 / 368134 / pH - sensing - properties - of - graphene - solution - gated (visited on 04/12/2024).

[212] Wangyang Fu et al. “Graphene Transistors Are Insensitive to pH Changes in Solution”. en. In: *Nano Letters* 11.9 (Sept. 2011), pp. 3597–3600. ISSN: 1530-6984, 1530-6992. DOI: 10.1021/nl201332c. URL: https://pubs.acs.org/doi/10.1021/nl201332c (visited on 04/12/2024).

[213] Michel Wehrhold et al. “pH Sensitivity of Interfacial Electron Transfer at a Supported Graphene Monolayer”. In: *Nanoscale* 11.31 (2019), pp. 14742–14756. ISSN: 2040-3364. DOI: DOI:10.1039/c9nr05049c.

[214] Yao Yao et al. “An Electrochemical in Situ Infrared Spectroscopic Study of Graphene/Electrolyte Interface under Attenuated Total Reflection Configuration”. en. In: *The Journal of Physical Chemistry C* 119.39 (Oct. 2015), pp. 22452–22459. ISSN: 1932-7447, 1932-7455. DOI: 10.1021/acs.jpcc.5b06325. URL: https://pubs.acs.org/doi/10.1021/acs.jpcc.5b06325 (visited on 01/27/2024).

[215] Gerald Wiegand et al. “Electrical Properties of Supported Lipid Bilayer Membranes”. en. In: *The Journal of Physical Chemistry B* 106.16 (Apr. 2002), pp. 4245–4254. ISSN: 1520-6106, 1520-5207. DOI: 10.1021/jp014337e. URL: https://pubs.acs.org/doi/10.1021/jp014337e (visited on 05/16/2024).

[216] Ana Fernández et al. “PMMA stability under hydrothermal conditions”. en. In: *The Journal of Supercritical Fluids* 198 (July 2023), p. 105938. ISSN: 08968446. DOI: 10.1016/j.supflu.2023.105938. URL: https://linkinghub.elsevier.com/retrieve/pii/S089684462300102X (visited on 04/15/2024).

[217] Alexandros Ch. Lazanas and Mamas I. Prodromidis. “Electrochemical Impedance SpectroscopyA Tutorial”. en. In: *ACS Measurement Science Au* 3.3 (June 2023), pp. 162–193. ISSN: 2694-250X, 2694-250X. DOI: 10.1021/acsmeasuresciau.2c00070. URL: https://pubs.acs.org/doi/10.1021/acsmeasuresciau.2c00070 (visited on 11/19/2023).

[218] Benno M Blaschke. “Graphene transistors for bioelectronic applications”. PhD thesis. Fakultät für Physik: Technische Universität München, 2017.

[219] Jhonn Cañón and Andrew V. Teplyakov. “XPS characterization of cobalt impregnated SiO $_2$ and -Al $_2$ O $_3$”. en. In: *Surface and Interface Analysis* 53.5 (May 2021), pp. 475–481. ISSN: 0142-2421, 1096-9918. DOI: 10.1002/sia.6935. URL: https://analyticalsciencejournals.onlinelibrary.wiley.com/doi/10.1002/sia.6935 (visited on 04/15/2024).

[220] D. Ferrah et al. “XPS investigations of graphene surface cleaning using H $_2$ - and Cl $_2$ -based inductively coupled plasma”. en. In: *Surface and Interface Analysis* 48.7 (July 2016), pp. 451–455. ISSN: 0142-2421, 1096-9918. DOI: 10.1002/sia.6010. URL: https://analyticalsciencejournals.onlinelibrary.wiley.com/doi/10.1002/sia.6010 (visited on 10/22/2023).

[221] Lauren H. Grey, Heng-Yong Nie, and Mark C. Biesinger. “Defining the nature of adventitious carbon and improving its merit as a charge correction reference for XPS”. en. In: *Applied Surface Science* 653 (Apr. 2024), p. 159319. ISSN: 01694332. DOI: 10.1016/j.apsusc.2024.159319. URL: https://linkinghub.elsevier.com/retrieve/pii/S0169433224000333 (visited on 04/15/2024).

[222] Carrie Donley et al. “Characterization of IndiumTin Oxide Interfaces Using X-ray Photoelectron Spectroscopy and Redox Processes of a Chemisorbed Probe Molecule: Effect of Surface Pretreatment Conditions”. en. In: *Langmuir* 18.2 (Jan. 2002), pp. 450–457. ISSN: 0743-7463, 1520-5827. DOI: 10.1021/la011101t. URL: https://pubs.acs.org/doi/10.1021/la011101t (visited on 10/22/2023).

[223] Horacio Coy Diaz, Rafik Addou, and Matthias Batzill. “Interface properties of CVD grown graphene transferred onto MoS $_2$ (0001)”. en. In: *Nanoscale* 6.2 (2014), pp. 1071–1078. ISSN: 2040-3364, 2040-3372. DOI: 10.1039/C3NR03692H. URL: http://xlink.rsc.org/?DOI=C3NR03692H (visited on 02/07/2024).

[224] Rusen Yan et al. “Determination of graphene work function and graphene-insulator-semiconductor band alignment by internal photoemission spectroscopy”. en. In: *Applied Physics Letters* 101.2 (July 2012), p. 022105. ISSN: 0003-6951, 1077-3118. DOI: 10.1063/1.4734955. URL: https://pubs.aip.org/apl/article/101/2/022105/128222/Determination-of-graphene-work-function-and (visited on 04/01/2024).

[225] Xinming Li and Hongwei Zhu. “The graphene–semiconductor Schottky junction”. en. In: (2016).

[226] Samira Naghdi, Gonzalo Sanchez-Arriaga, and Kyong Yop Rhee. “Tuning the work function of graphene toward application as anode and cathode”. en. In: *Journal of Alloys and Compounds* 805 (Oct. 2019), pp. 1117–1134. ISSN: 09258388. DOI: 10.1016/j.jallcom.2019.07.187. URL: https://linkinghub.elsevier.com/retrieve/pii/S0925838819326994 (visited on 11/02/2023).

[227] Y. Park et al. “Work function of indium tin oxide transparent conductor measured by photoelectron spectroscopy”. en. In: *Applied Physics Letters* 68.19 (May 1996), pp. 2699–2701. ISSN: 0003-6951, 1077-3118. DOI: 10.1063/1.116313. URL: https://pubs.aip.org/apl/article/68/19/2699/65869/Work-function-of-indium-tin-oxide-transparent (visited on 05/08/2024).

[228] Andreas Härtl. “Novel concepts for biosensors using diamond-based field effect transistors”. PhD thesis. Fakultät für Physik: Technische Universität München, 2008. URL: https://mediatum.ub.tum.de/667395.

[229] Benno Martin Blaschke. “Graphene solution-gated field-effect transistors”. Diplomarbeit. Technische Universität München, 2012.

[230] Iddo Heller et al. “Influence of Electrolyte Composition on Liquid-Gated Carbon Nanotube and Graphene Transistors”. en. In: *Journal of the American Chemical Society* 132.48 (Dec. 2010), pp. 17149–17156. ISSN: 0002-7863, 1520-5126. DOI: 10.1021/ja104850n. URL: https://pubs.acs.org/doi/10.1021/ja104850n (visited on 05/08/2024).

[231] Lucas H. Hess et al. “Graphene Transistors with Multifunctional Polymer Brushes for Biosensing Applications”. en. In: *ACS Applied Materials & Interfaces* 6.12 (June 2014), pp. 9705–9710. ISSN: 1944-8244, 1944-8252. DOI: 10.1021/am502112x. URL: https://pubs.acs.org/doi/10.1021/am502112x (visited on 05/19/2024).

[232] Yung-Chang Lin et al. “Graphene Annealing: How Clean Can It Be?” en. In: *Nano Letters* 12.1 (Jan. 2012), pp. 414–419. ISSN: 1530-6984, 1530-6992. DOI: 10.1021/nl203733r. URL: https://pubs.acs.org/doi/10.1021/nl203733r (visited on 05/08/2024).

[233] Seung-Il Kim et al. “Performance enhancement of amorphous WO3 assisted graphene-based electronic devices: Aspect of surface engineering”. en. In: *Applied Surface Science* 556 (Aug. 2021), p. 149763. ISSN: 01694332. DOI: 10.1016/j.apsusc.2021.149763. URL: https://linkinghub.elsevier.com/retrieve/pii/S0169433221008394 (visited on 02/12/2024).

[234] Maki Nakatani et al. “Ready-to-transfer two-dimensional materials using tunable adhesive force tapes”. en. In: *Nature Electronics* (Feb. 2024). ISSN: 2520-1131. DOI: 10.1038/s41928-024-01121-3. URL: https://www.nature.com/articles/s41928-024-01121-3 (visited on 02/12/2024).

[235] Hossein Sojoudi et al. "Impact of post-growth thermal annealing and environmental exposure on the unintentional doping of CVD graphene films". en. In: *Journal of Vacuum Science & Technology B, Nanotechnology and Microelectronics: Materials, Processing, Measurement, and Phenomena* 30.4 (July 2012), p. 041213. ISSN: 2166-2746, 2166-2754. DOI: 10.1116/1.4731472. URL: https://pubs.aip.org/jvb/article/30/4/041213/467640/Impact-of-post-growth-thermal-annealing-and (visited on 02/12/2024).

[236] Ning C. Wang et al. "Reducing graphene device variability with yttrium sacrificial layers". en. In: *Applied Physics Letters* 110.22 (May 2017), p. 223106. ISSN: 0003-6951, 1077-3118. DOI: 10.1063/1.4984090. URL: https://pubs.aip.org/apl/article/110/22/223106/33940/Reducing-graphene-device-variability-with-yttrium (visited on 02/06/2024).

[237] Zhangfu Chen et al. "Enhanced photolithography with Al film insertion for large-scale patterning of CVD graphene". en. In: *Optical Materials Express* 8.8 (Aug. 2018), p. 2403. ISSN: 2159-3930. DOI: 10.1364/OME.8.002403. URL: https://opg.optica.org/abstract.cfm?URI=ome-8-8-2403 (visited on 05/19/2024).

[238] Junqiang Wang et al. "Improving consistency and performance of graphene-based devices via Al sacrificial layer". en. In: *Colloid and Interface Science Communications* 56 (Sept. 2023), p. 100743. ISSN: 22150382. DOI: 10.1016/j.colcom.2023.100743. URL: https://linkinghub.elsevier.com/retrieve/pii/S221503822300050X (visited on 02/12/2024).

[239] Ramon Garcia-Cortadella. "High-Bandwidth Graphene Neural Interfaces". PhD thesis. Universitat Autònoma de Barcelona, 2021.

[240] Arvind Jaikumar et al. "Electrochemical Deposition of Copper on Graphene with High Heat Transfer Coefficient". en. In: *ECS Transactions* 66.30 (July 2015), pp. 55–64. ISSN: 1938-5862, 1938-6737. DOI: 10.1149/06630.0055ecst. URL: https://iopscience.iop.org/article/10.1149/06630.0055ecst (visited on 04/25/2024).

[241] Quan Wang et al. "Effects of silicon dioxide surface roughness on Raman characteristics and mechanical properties of graphene". en. In: *RSC Adv.* 4.98 (2014), pp. 55087–55093. ISSN: 2046-2069. DOI: 10.1039/C4RA08369E. URL: https://xlink.rsc.org/?DOI=C4RA08369E (visited on 05/19/2024).

[242] Max Cremer. "Über die Ursache der elektromotorischen Eigenschaften der Gewebe, zugleich ein Beitrag zur Lehre von den polyphasischen Elektrolytketten". In: *Zeitschrift fur Biologie* 47 (1906), pp. 562–608.

[243] A Camassa et al. "Chronic full-band recordings with graphene micro-transistors as neural interfaces for discrimination of brain states". In: *Nanoscale Horiz.* (2024). DOI: doi:10.1039/d3nh00440f. URL: https://pubmed.ncbi.nlm.nih.gov/38329118/.

[244] Siyuan Zhao et al. "Full activation pattern mapping by simultaneous deep brain stimulation and fMRI with graphene fiber electrodes". en. In: *Nature Communications* 11.1 (Apr. 2020), p. 1788. ISSN: 2041-1723. DOI: 10.1038/s41467-020-15570-9. URL: https://www.nature.com/articles/s41467-020-15570-9 (visited on 02/15/2024).

[245] Jeongsik Lim et al. "Hybrid graphene electrode for the diagnosis and treatment of epilepsy in free-moving animal models". en. In: *NPG Asia Materials* 15.1 (Feb. 2023), p. 7. ISSN: 1884-4057. DOI: 10.1038/s41427-023-00464-1. URL: https://www.nature.com/articles/s41427-023-00464-1 (visited on 02/15/2024).

[246] Md Eshrat E. Alahi et al. "Recent Advancements in Graphene-Based Implantable Electrodes for Neural Recording/Stimulation". en. In: *Sensors* 23.24 (Dec. 2023), p. 9911. ISSN: 1424-8220. DOI: 10.3390/s23249911. URL: https://www.mdpi.com/1424-8220/23/24/9911 (visited on 05/23/2024).

[247] Mohammad Karbalaei Akbari et al. "Functional Two-Dimensional Materials for Bioelectronic Neural Interfacing". en. In: *Journal of Functional Biomaterials* 14.1 (Jan. 2023), p. 35. ISSN: 2079-4983. DOI: 10.3390/jfb14010035. URL: https://www.mdpi.com/2079-4983/14/1/35 (visited on 05/23/2024).

[248] Kannan Balasubramanian and Marko Burghard. "Biosensors based on carbon nanotubes". en. In: *Analytical and Bioanalytical Chemistry* 385.3 (June 2006), pp. 452–468. ISSN: 1618-2642, 1618-2650. DOI: 10.1007/s00216-006-0314-8. URL: http://link.springer.com/10.1007/s00216-006-0314-8 (visited on 02/15/2024).

[249] Madalina M. Barsan et al. "Carbon nanotube modified carbon cloth electrodes: Characterisation and application as biosensors". en. In: *Electrochimica Acta* 85 (Dec. 2012), pp. 203–209. ISSN: 00134686. DOI: 10.1016/j.electacta.2012.08.048. URL: https://linkinghub.elsevier.com/retrieve/pii/S0013468612013382 (visited on 05/14/2024).

[250] Seyyed Mostafa Monavari et al. “Carbon nanotubes and nanobelts as potential materials for biosensor”. en. In: *Scientific Reports* 13.1 (Feb. 2023), p. 3118. ISSN: 2045-2322. DOI: 10.1038/s41598-023-29862-9. URL: https://www.nature.com/articles/s41598-023-29862-9 (visited on 02/15/2024).

[251] Nihar Mohanty and Vikas Berry. “Graphene-Based Single-Bacterium Resolution Biodevice and DNA Transistor: Interfacing Graphene Derivatives with Nanoscale and Microscale Biocomponents”. en. In: *Nano Letters* 8.12 (Dec. 2008), pp. 4469–4476. ISSN: 1530-6984, 1530-6992. DOI: 10.1021/nl802412n. URL: https://pubs.acs.org/doi/10.1021/nl802412n (visited on 11/29/2023).

[252] Wenrong Yang et al. “Carbon Nanomaterials in Biosensors: Should You Use Nanotubes or Graphene?” en. In: *Angewandte Chemie International Edition* 49.12 (Mar. 2010), pp. 2114–2138. ISSN: 1433-7851, 1521-3773. DOI: 10.1002/anie.200903463. URL: https://onlinelibrary.wiley.com/doi/10.1002/anie.200903463 (visited on 11/29/2023).

[253] Shoji Fukushima et al. “Carcinogenicity of multi-walled carbon nanotubes: challenging issue on hazard assessment”. en. In: *Journal of Occupational Health* 60.1 (Jan. 2018), pp. 10–30. ISSN: 1341-9145, 1348-9585. DOI: 10.1539/joh.17-0102-RA. URL: https://academic.oup.com/joh/article/60/1/10-30/7250967 (visited on 02/17/2024).

[254] Agnes B. Kane, Robert H. Hurt, and Huajian Gao. “The asbestos-carbon nanotube analogy: An update”. en. In: *Toxicology and Applied Pharmacology* 361 (Dec. 2018), pp. 68–80. ISSN: 0041008X. DOI: 10.1016/j.taap.2018.06.027. URL: https://linkinghub.elsevier.com/retrieve/pii/S0041008X18302941 (visited on 02/17/2024).

[255] Arul Prakash Francis and Thiyagarajan Devasena. “Toxicity of carbon nanotubes: A review”. en. In: *Toxicology and Industrial Health* 34.3 (Mar. 2018), pp. 200–210. ISSN: 0748-2337, 1477-0393. DOI: 10.1177/0748233717747472. URL: http://journals.sagepub.com/doi/10.1177/0748233717747472 (visited on 02/17/2024).

[256] Christoph Fenzl et al. “Laser-Scribed Graphene Electrodes for Aptamer-Based Biosensing”. en. In: *ACS Sensors* 2.5 (May 2017), pp. 616–620. ISSN: 2379-3694, 2379-3694. DOI: 10.1021/acssensors.7b00066. URL: https://pubs.acs.org/doi/10.1021/acssensors.7b00066 (visited on 05/14/2024).

[257] Li Zhang et al. “Electrochemical biosensors represent promising detection tools in medical field”. en. In: *Advanced Sensor and Energy Materials* 2.4 (Dec. 2023), p. 100081. ISSN: 2773045X. DOI: 10.1016/j.asems.2023.100081. URL: https://linkinghub.elsevier.com/retrieve/pii/S2773045X23000365 (visited on 02/15/2024).

[258] Kunal S. Mali et al. “Nanostructuring graphene for controlled and reproducible functionalization”. en. In: *Nanoscale* 7.5 (2015), pp. 1566–1585. ISSN: 2040-3364, 2040-3372. DOI: 10.1039/C4NR06470D. URL: http://xlink.rsc.org/?DOI=C4NR06470D (visited on 02/18/2024).

[259] Jana Brndiarova et al. “Functionalized graphene transistor for ultrasensitive detection of carbon quantum dots”. en. In: *Journal of Applied Physics* 126.21 (Dec. 2019), p. 214303. ISSN: 0021-8979, 1089-7550. DOI: 10.1063/1.5120757. URL: https://pubs.aip.org/jap/article/126/21/214303/156516/Functionalized-graphene-transistor-for (visited on 05/19/2024).

[260] Gonzalo E. Fenoy et al. “Acetylcholine biosensor based on the electrochemical functionalization of graphene field-effect transistors”. en. In: *Biosensors and Bioelectronics* 148 (Jan. 2020), p. 111796. ISSN: 09565663. DOI: 10.1016/j.bios.2019.111796. URL: https://linkinghub.elsevier.com/retrieve/pii/S0956566319308759 (visited on 05/19/2024).

[261] Zhiling Guo et al. “Surface Functionalization of Graphene-Based Materials: Biological Behavior, Toxicology, and Safe-By-Design Aspects”. en. In: *Advanced Biology* 5.9 (Sept. 2021), p. 2100637. ISSN: 2701-0198, 2701-0198. DOI: 10.1002/adbi.202100637. URL: https://onlinelibrary.wiley.com/doi/10.1002/adbi.202100637 (visited on 02/18/2024).

[262] Rajni Garg, Naba Dutta, and Namita Choudhury. “Work Function Engineering of Graphene”. en. In: *Nanomaterials* 4.2 (Apr. 2014), pp. 267–300. ISSN: 2079-4991. DOI: 10.3390/nano4020267. URL: http://www.mdpi.com/2079-4991/4/2/267 (visited on 02/15/2024).

[263] Ming Fang et al. “Covalent polymer functionalization of graphene nanosheets and mechanical properties of composites”. en. In: *Journal of Materials Chemistry* 19.38 (2009), p. 7098. ISSN: 0959-9428, 1364-5501. DOI: 10.1039/b908220d. URL: https://xlink.rsc.org/?DOI=b908220d (visited on 05/23/2024).

[264] Yu Wang et al. “Effect of non-covalent functionalisation on thermal and mechanical properties of graphene-polymer nanocomposites”. en. In: *Carbon* 102 (June 2016), pp. 311–318. ISSN: 00086223. DOI: 10.1016/

j.carbon.2016.02.069. URL: https://linkinghub.elsevier.com/retrieve/pii/S0008622316301622 (visited on 05/23/2024).

[265] Natalia Alzate-Carvajal and Adina Luican-Mayer. "Functionalized Graphene Surfaces for Selective Gas Sensing". en. In: *ACS Omega* 5.34 (Sept. 2020), pp. 21320–21329. ISSN: 2470-1343, 2470-1343. DOI: 10.1021/acsomega.0c02861. URL: https://pubs.acs.org/doi/10.1021/acsomega.0c02861 (visited on 02/18/2024).

[266] Yanyu Liang et al. "Dispersion of Graphene Sheets in Organic Solvent Supported by Ionic Interactions". en. In: *Advanced Materials* 21.17 (May 2009), pp. 1679–1683. ISSN: 0935-9648, 1521-4095. DOI: 10.1002/adma.200803160. URL: https://onlinelibrary.wiley.com/doi/10.1002/adma.200803160 (visited on 05/14/2024).

[267] Xiaodong Wang et al. "Non-covalently functionalized graphene strengthened poly(vinyl alcohol)". en. In: *Materials & Design* 139 (Feb. 2018), pp. 372–379. ISSN: 02641275. DOI: 10.1016/j.matdes.2017.11.023. URL: https://linkinghub.elsevier.com/retrieve/pii/S0264127517310547 (visited on 05/14/2024).

[268] Mirosław Woszczyna et al. "All-Carbon Vertical van der Waals Heterostructures: Non-destructive Functionalization of Graphene for Electronic Applications". en. In: *Advanced Materials* 26.28 (July 2014), pp. 4831–4837. ISSN: 0935-9648, 1521-4095. DOI: 10.1002/adma.201400948. URL: https://onlinelibrary.wiley.com/doi/10.1002/adma.201400948 (visited on 05/14/2024).

[269] Thanawit Kuamit et al. "Effects of shape, size, and pyrene doping on electronic properties of graphene nanoflakes". en. In: *Journal of Molecular Modeling* 23.12 (Dec. 2017), p. 355. ISSN: 1610-2940, 0948-5023. DOI: 10.1007/s00894-017-3521-7. URL: http://link.springer.com/10.1007/s00894-017-3521-7 (visited on 01/03/2024).

[270] Michael Holzinger, Serge Cosnier, and Paulo Henrique M. Buzzetti. "The versatility of pyrene and its derivatives on sp2 carbon nanomaterials for bioelectrochemical applications". en. In: *Synthetic Metals* 292 (Jan. 2023), p. 117219. ISSN: 03796779. DOI: 10.1016/j.synthmet.2022.117219. URL: https://linkinghub.elsevier.com/retrieve/pii/S0379677922002132 (visited on 01/03/2024).

[271] Xuan Zhang et al. "Application of graphene–pyrenebutyric acid nanocomposite as probe oligonucleotide immobilization platform in a DNA biosensor". en. In: *Materials Science and Engineering: C* 33.7 (Oct.

2013), pp. 3851–3857. ISSN: 09284931. DOI: 10.1016/j.msec.2013.05.022. URL: https://linkinghub.elsevier.com/retrieve/pii/S092849311300310X (visited on 05/23/2024).

[272] Chao-yi Zhu et al. "Predicting the Level of Background Current Noise in Graphene Biosensor through a Non-Covalent Functionalization Process". en. In: *Crystals* 13.2 (Feb. 2023), p. 359. ISSN: 2073-4352. DOI: 10.3390/cryst13020359. URL: https://www.mdpi.com/2073-4352/13/2/359 (visited on 05/23/2024).

[273] Deana Kwong Hong Tsang et al. "Chemically Functionalised Graphene FET Biosensor for the Label-free Sensing of Exosomes". en. In: *Scientific Reports* 9.1 (Sept. 2019), p. 13946. ISSN: 2045-2322. DOI: 10.1038/s41598-019-50412-9. URL: https://www.nature.com/articles/s41598-019-50412-9 (visited on 05/23/2024).

[274] Sabrine Toumi et al. "Conductivity monitoring of PBASE functionalized CVD graphene electrode for biosensor applications". en. In: *Journal of Applied Electrochemistry* (Jan. 2024). ISSN: 0021-891X, 1572-8838. DOI: 10.1007/s10800-023-02060-1. URL: https://link.springer.com/10.1007/s10800-023-02060-1 (visited on 05/23/2024).

[275] Misbah Shahzadi et al. "Highly Efficient, Non-Covalent Functionalization of CVD-Graphene via Novel Pyrene-Based Supporter Construct". en. In: *Chemosensors* 11.2 (Jan. 2023), p. 83. ISSN: 2227-9040. DOI: 10.3390/chemosensors11020083. URL: https://www.mdpi.com/2227-9040/11/2/83 (visited on 02/18/2024).

[276] Pooria Gill, Tahereh Tohidi Moghadam, and Bijan Ranjbar. "Differential Scanning Calorimetry Techniques: Applications in Biology and Nanoscience". en. In: 21.4 (2010).

[277] Th. Gross et al. "An XPS analysis of different SiO_2 modifications employing a C 1s as well as an Au $4f_{7/2}$ static charge reference". en. In: *Surface and Interface Analysis* 18.1 (Jan. 1992), pp. 59–64. ISSN: 0142-2421, 1096-9918. DOI: 10.1002/sia.740180110. URL: https://analyticalsciencejournals.onlinelibrary.wiley.com/doi/10.1002/sia.740180110 (visited on 05/14/2024).

[278] Nenad Stojilovic. "Why Can't We See Hydrogen in X-ray Photoelectron Spectroscopy?" en. In: *Journal of Chemical Education* 89.10 (Sept. 2012), pp. 1331–1332. ISSN: 0021-9584, 1938-1328. DOI: 10.1021/ed300057j. URL: https://pubs.acs.org/doi/10.1021/ed300057j (visited on 05/16/2024).

[279] Hideaki Shinohara, Yoshihiro Yamakita, and Koichi Ohno. "Raman spectra of polycyclic aromatic hydrocarbons. Comparison of calculated Raman intensity distributions with observed spectra for naphthalene, anthracene, pyrene, and perylene". en. In: *Journal of Molecular Structure* 442.1-3 (Feb. 1998), pp. 221–234. ISSN: 00222860. DOI: 10.1016/S0022-2860(97)00335-9. URL: https://linkinghub.elsevier.com/retrieve/pii/S0022286097003359 (visited on 05/16/2024).

[280] Lisseth Gavilan et al. "Raman Spectroscopic Study of Pyrene in Cosmic Dust Analogues: Evolution from the Gas to the Solid Phase". en. In: *ACS Earth and Space Chemistry* 6.9 (Sept. 2022), pp. 2215–2225. ISSN: 2472-3452, 2472-3452. DOI: 10.1021/acsearthspacechem.2c00136. URL: https://pubs.acs.org/doi/10.1021/acsearthspacechem.2c00136 (visited on 05/23/2024).

[281] Malkolm Hinnemo et al. "On Monolayer Formation of Pyrenebutyric Acid on Graphene". en. In: *Langmuir* 33.15 (Apr. 2017), pp. 3588–3593. ISSN: 0743-7463, 1520-5827. DOI: 10.1021/acs.langmuir.6b04237. URL: https://pubs.acs.org/doi/10.1021/acs.langmuir.6b04237 (visited on 06/26/2023).

[282] Piramon Hampitak et al. "Protein interactions and conformations on graphene-based materials mapped using a quartz-crystal microbalance with dissipation monitoring (QCM-D)". en. In: *Carbon* 165 (Sept. 2020), pp. 317–327. ISSN: 00086223. DOI: 10.1016/j.carbon.2020.04.093. URL: https://linkinghub.elsevier.com/retrieve/pii/S0008622320304243 (visited on 05/16/2024).

[283] Dmitry Kireev et al. "Graphene transistors for interfacing with cells: towards a deeper understanding of liquid gating and sensitivity". en. In: *Scientific Reports* 7.1 (July 2017), p. 6658. ISSN: 2045-2322. DOI: 10.1038/s41598-017-06906-5. URL: https://www.nature.com/articles/s41598-017-06906-5 (visited on 02/18/2024).

[284] S Rumyantsev et al. "Electrical and noise characteristics of graphene field-effect transistors: ambient effects, noise sources and physical mechanisms". en. In: *Journal of Physics: Condensed Matter* 22.39 (Oct. 2010), p. 395302. ISSN: 0953-8984, 1361-648X. DOI: 10.1088/0953-8984/22/39/395302. URL: https://iopscience.iop.org/article/10.1088/0953-8984/22/39/395302 (visited on 02/18/2024).

[285] Alexander A. Balandin. "Low-frequency 1/f noise in graphene devices". en. In: *Nature Nanotechnology* 8.8 (Aug. 2013), pp. 549–555. ISSN: 1748-3387,

1748-3395. DOI: 10.1038/nnano.2013.144. URL: https://www.nature.com/articles/nnano.2013.144 (visited on 02/18/2024).

[286] Paritosh Karnatak et al. "Current crowding mediated large contact noise in graphene field-effect transistors". en. In: *Nature Communications* 7.1 (Dec. 2016), p. 13703. ISSN: 2041-1723. DOI: 10.1038/ncomms13703. URL: https://www.nature.com/articles/ncomms13703 (visited on 02/18/2024).

[287] Christian M. Schaefer et al. "Carbon Incorporation in MOCVD of MoS_2 Thin Films Grown from an Organosulfide Precursor". en. In: *Chemistry of Materials* 33.12 (June 2021), pp. 4474–4487. ISSN: 0897-4756, 1520-5002. DOI: 10.1021/acs.chemmater.1c00646. URL: https://pubs.acs.org/doi/10.1021/acs.chemmater.1c00646 (visited on 08/15/2023).

[288] Eiichiro Watanabe et al. "Low contact resistance metals for graphene based devices". en. In: *Diamond and Related Materials* 24 (Apr. 2012), pp. 171–174. ISSN: 09259635. DOI: 10.1016/j.diamond.2012.01.019. URL: https://linkinghub.elsevier.com/retrieve/pii/S0925963512000295 (visited on 02/18/2024).

[289] Wei Li et al. "Ultraviolet/ozone treatment to reduce metal-graphene contact resistance". en. In: *Applied Physics Letters* 102.18 (May 2013), p. 183110. ISSN: 0003-6951, 1077-3118. DOI: 10.1063/1.4804643. URL: https://pubs.aip.org/apl/article/102/18/183110/126648/Ultraviolet-ozone-treatment-to-reduce-metal (visited on 02/18/2024).

[290] Wei Sun Leong, Chang Tai Nai, and John T. L. Thong. "What Does Annealing Do to Metal–Graphene Contacts?" en. In: *Nano Letters* 14.7 (July 2014), pp. 3840–3847. ISSN: 1530-6984, 1530-6992. DOI: 10.1021/nl500999r. URL: https://pubs.acs.org/doi/10.1021/nl500999r (visited on 02/18/2024).

[291] Xiangyu Yan et al. "Edge-Contact Formed by Oxygen Plasma and Rapid Thermal Annealing to Improve Metal-Graphene Contact Resistance". en. In: *ECS Journal of Solid State Science and Technology* 7.2 (2018), pp. M11–M15. ISSN: 2162-8769, 2162-8777. DOI: 10.1149/2.0251802jss. URL: https://iopscience.iop.org/article/10.1149/2.0251802jss (visited on 02/18/2024).

[292] Masahiro Kamada et al. "Suppression of 1/f noise in graphene due to anisotropic mobility fluctuations induced by impurity motion". en. In: *Communications Physics* 6.1 (Aug. 2023), p. 207. ISSN: 2399-3650. DOI: 10.1038/s42005-023-01321-x. URL: https://www.nature.com/articles/s42005-023-01321-x (visited on 02/18/2024).

[293] Gokuraju Thriveni and Kaustab Ghosh. “Advancement and Challenges of Biosensing Using Field Effect Transistors”. en. In: *Biosensors* 12.8 (Aug. 2022), p. 647. ISSN: 2079-6374. DOI: 10.3390/bios12080647. URL: https://www.mdpi.com/2079-6374/12/8/647 (visited on 05/19/2024).

[294] Päivi Järvinen et al. “Molecular Self-Assembly on Graphene on SiO $_2$ and h-BN Substrates”. en. In: *Nano Letters* 13.7 (July 2013), pp. 3199–3204. ISSN: 1530-6984, 1530-6992. DOI: 10.1021/nl401265f. URL: https://pubs.acs.org/doi/10.1021/nl401265f (visited on 02/18/2024).

[295] J. M. MacLeod and F. Rosei. “Molecular Self-Assembly on Graphene”. en. In: *Small* 10.6 (Mar. 2014), pp. 1038–1049. ISSN: 1613-6810, 1613-6829. DOI: 10.1002/smll.201301982. URL: https://onlinelibrary.wiley.com/doi/10.1002/smll.201301982 (visited on 02/18/2024).

[296] D. R. Young. “Charge Trapping in SiO2”. In: *The Physics and Chemistry of SiO2 and the Si-SiO2 Interface*. Helms, C.R., Deal, B.E. (eds). Springer, Boston, MA, 1988, pp. 487–498. ISBN: 978-1-4899-0776-9. URL: https://link.springer.com/chapter/10.1007/978-1-4899-0774-5_54.

[297] Sebastian Wittmann et al. “Dielectric Surface Charge Engineering for Electrostatic Doping of Graphene”. en. In: *ACS Applied Electronic Materials* 2.5 (May 2020), pp. 1235–1242. ISSN: 2637-6113, 2637-6113. DOI: 10.1021/acsaelm.0c00051. URL: https://pubs.acs.org/doi/10.1021/acsaelm.0c00051 (visited on 02/18/2024).

[298] Nadine Schwierz, Dominik Horinek, and Roland R. Netz. “Reversed Anionic Hofmeister Series: The Interplay of Surface Charge and Surface Polarity”. en. In: *Langmuir* 26.10 (May 2010), pp. 7370–7379. ISSN: 0743-7463, 1520-5827. DOI: 10.1021/la904397v. URL: https://pubs.acs.org/doi/10.1021/la904397v (visited on 03/18/2024).

[299] Alexander Yu. Klyushin et al. “A near ambient pressure XPS study of Au oxidation”. en. In: *Physical Chemistry Chemical Physics* 16.17 (2014), p. 7881. ISSN: 1463-9076, 1463-9084. DOI: 10.1039/c4cp00308j. URL: https://xlink.rsc.org/?DOI=c4cp00308j (visited on 06/08/2024).

[300] P.R. Norton. “An investigation of the adsorption of oxygen and oxygen containing species on platinum by photoelectron spectroscopy”. en. In: *Surface Science* 47.1 (Jan. 1975), pp. 98–114. ISSN: 00396028. DOI: 10.1016/0039-6028(75)90276-9. URL: https://linkinghub.elsevier.com/retrieve/pii/0039602875902769 (visited on 06/08/2024).

[301] C C Heuck et al. “The role of surface charge on the accelerating action of heparin on the antithrombin III-inhibited activity of alpha-thrombin.” en. In: *Journal of Biological Chemistry* 260.8 (Apr. 1985), pp. 4598–4603. ISSN: 00219258. DOI: 10.1016/S0021-9258(18)89113-X. URL: https://linkinghub.elsevier.com/retrieve/pii/S002192581889113X (visited on 02/18/2024).

[302] Kristine S. Alexander, Michael G. Fried, and David H. Farrell. “Role of Electrostatic Interactions in Binding of Thrombin to the Fibrinogen Chain”. en. In: *Biochemistry* 51.16 (Apr. 2012), pp. 3445–3450. ISSN: 0006-2960, 1520-4995. DOI: 10.1021/bi2016519. URL: https://pubs.acs.org/doi/10.1021/bi2016519 (visited on 02/18/2024).

[303] Bin Deng et al. “Aptamer binding assays for proteins: The thrombin example—A review”. en. In: *Analytica Chimica Acta* 837 (July 2014), pp. 1–15. ISSN: 00032670. DOI: 10.1016/j.aca.2014.04.055. URL: https://linkinghub.elsevier.com/retrieve/pii/S0003267014005091 (visited on 02/18/2024).

[304] P. Müller-Buschbaum. “A Basic Introduction to Grazing Incidence Small-Angle X-Ray Scattering”. en. In: *Applications of Synchrotron Light to Scattering and Diffraction in Materials and Life Sciences*. Ed. by Marian Gomez et al. Vol. 776. Series Title: Lecture Notes in Physics. Berlin, Heidelberg: Springer Berlin Heidelberg, 2009, pp. 61–89. ISBN: 978-3-540-95967-0 978-3-540-95968-7. DOI: 10.1007/978-3-540-95968-7_3. URL: https://link.springer.com/10.1007/978-3-540-95968-7_3 (visited on 03/09/2024).

[305] O. Ochedowski, B. Kleine Bussmann, and M. Schleberger. “Graphene on Mica - Intercalated Water Trapped for Life”. en. In: *Scientific Reports* 4.1 (Aug. 2014), p. 6003. ISSN: 2045-2322. DOI: 10.1038/srep06003. URL: https://www.nature.com/articles/srep06003 (visited on 08/25/2023).

[306] Jin Heui Hwang et al. “Local conductance mapping of water-intercalated graphene on mica”. en. In: *Applied Physics Letters* 109.24 (Dec. 2016), p. 241602. ISSN: 0003-6951, 1077-3118. DOI: 10.1063/1.4972233. URL: https://pubs.aip.org/apl/article/109/24/241602/32066/Local-conductance-mapping-of-water-intercalated (visited on 06/26/2023).

[307] Haojie Lang et al. “Role of Interfacial Water in the Tribological Behavior of Graphene in an Electric Field”. en. In: *Nano Letters* 22.15 (Aug. 2022), pp. 6055–6061. ISSN: 1530-6984, 1530-6992. DOI: 10.1021/acs.nanolett.

2c00361. URL: https://pubs.acs.org/doi/10.1021/acs.nanolett.2c00361 (visited on 07/05/2023).

[308] Xiaofeng Feng, Sabine Maier, and Miquel Salmeron. "Water Splits Epitaxial Graphene and Intercalates". en. In: *Journal of the American Chemical Society* 134.12 (Mar. 2012), pp. 5662–5668. ISSN: 0002-7863, 1520-5126. DOI: 10.1021/ja3003809. URL: https://pubs.acs.org/doi/10.1021/ja3003809 (visited on 05/27/2024).

[309] Kwanpyo Kim et al. "Selective metal deposition at graphene line defects by atomic layer deposition". en. In: *Nature Communications* 5.1 (Sept. 2014), p. 4781. ISSN: 2041-1723. DOI: 10.1038/ncomms5781. URL: https://www.nature.com/articles/ncomms5781 (visited on 02/18/2024).

[310] Sascha Sadewasser and Thilo Glatzel, eds. *Kelvin Probe Force Microscopy: From Single Charge Detection to Device Characterization*. en. Vol. 65. Springer Series in Surface Sciences. Cham: Springer International Publishing, 2018. ISBN: 978-3-319-75686-8 978-3-319-75687-5. DOI: 10.1007/978-3-319-75687-5. URL: https://link.springer.com/10.1007/978-3-319-75687-5 (visited on 02/26/2024).

[311] Liam Collins et al. "Dual harmonic Kelvin probe force microscopy at the graphene–liquid interface". en. In: *Applied Physics Letters* 104.13 (Mar. 2014), p. 133103. ISSN: 0003-6951, 1077-3118. DOI: 10.1063/1.4870074. URL: https://pubs.aip.org/apl/article/104/13/133103/23977/Dual-harmonic-Kelvin-probe-force-microscopy-at-the (visited on 08/01/2023).

[312] Liam Collins et al. "Probing charge screening dynamics and electrochemical processes at the solid–liquid interface with electrochemical force microscopy". en. In: *Nature Communications* 5.1 (May 2014), p. 3871. ISSN: 2041-1723. DOI: 10.1038/ncomms4871. URL: https://www.nature.com/articles/ncomms4871 (visited on 08/01/2023).

[313] Wilhelm Melitz et al. "Kelvin probe force microscopy and its application". en. In: *Surface Science Reports* 66.1 (Jan. 2011), pp. 1–27. ISSN: 01675729. DOI: 10.1016/j.surfrep.2010.10.001. URL: https://linkinghub.elsevier.com/retrieve/pii/S0167572910000841 (visited on 01/23/2024).

[314] Ali Ashraf et al. "Doping-Induced Tunable Wettability and Adhesion of Graphene". en. In: *Nano Letters* 16.7 (July 2016), pp. 4708–4712. ISSN: 1530-6984, 1530-6992. DOI: 10.1021/acs.nanolett.6b02228. URL: https://pubs.acs.org/doi/10.1021/acs.nanolett.6b02228 (visited on 03/10/2024).

[315] Chen Klein, Doron Cohen-Elias, and Gabby Sarusi. "Controlling graphene work function by doping in a MOCVD reactor". en. In: *Heliyon* 4.12 (Dec. 2018), e01030. ISSN: 24058440. DOI: 10.1016/j.heliyon.2018.e01030. URL: https://linkinghub.elsevier.com/retrieve/pii/S2405844018349284 (visited on 03/10/2024).

[316] M Temmen et al. "Hydration layers trapped between graphene and a hydrophilic substrate". en. In: *New Journal of Physics* 16.5 (May 2014), p. 053039. ISSN: 1367-2630. DOI: 10.1088/1367-2630/16/5/053039. URL: https://iopscience.iop.org/article/10.1088/1367-2630/16/5/053039 (visited on 03/10/2024).

[317] Tjeerd R. J. Bollmann et al. "Hole-doping of mechanically exfoliated graphene by confined hydration layers". en. In: *Nano Research* 8.9 (Sept. 2015), pp. 3020–3026. ISSN: 1998-0124, 1998-0000. DOI: 10.1007/s12274-015-0807-x. URL: http://link.springer.com/10.1007/s12274-015-0807-x (visited on 03/10/2024).

[318] C Melios et al. "Water on graphene: review of recent progress". en. In: *2D Materials* 5.2 (Jan. 2018), p. 022001. ISSN: 2053-1583. DOI: 10.1088/2053-1583/aa9ea9. URL: https://iopscience.iop.org/article/10.1088/2053-1583/aa9ea9 (visited on 03/10/2024).

[319] Aaron D. Franklin et al. "Double Contacts for Improved Performance of Graphene Transistors". en. In: *IEEE Electron Device Letters* 33.1 (Jan. 2012), pp. 17–19. ISSN: 0741-3106, 1558-0563. DOI: 10.1109/LED.2011.2173154. URL: http://ieeexplore.ieee.org/document/6081897/ (visited on 08/14/2023).

[320] Seung Min Song et al. "Determination of Work Function of Graphene under a Metal Electrode and Its Role in Contact Resistance". en. In: *Nano Letters* 12.8 (Aug. 2012), pp. 3887–3892. ISSN: 1530-6984, 1530-6992. DOI: 10.1021/nl300266p. URL: https://pubs.acs.org/doi/10.1021/nl300266p (visited on 10/31/2023).

[321] Adrien Allain et al. "Electrical contacts to two-dimensional semiconductors". en. In: *Nature Materials* 14.12 (Dec. 2015), pp. 1195–1205. ISSN: 1476-1122, 1476-4660. DOI: 10.1038/nmat4452. URL: https://www.nature.com/articles/nmat4452 (visited on 03/11/2024).

[322] Carlos Alvarado Chavarin et al. "On the origin of contact resistances in graphene devices fabricated by optical lithography". en. In: *Applied Physics A* 122.2 (Feb. 2016), p. 58. ISSN: 0947-8396, 1432-0630. DOI: 10.1007/s00339-015-9582-5. URL: http://link.springer.com/10.1007/s00339-015-9582-5 (visited on 03/11/2024).

[323] Filippo Giubileo and Antonio Di Bartolomeo. "The role of contact resistance in graphene field-effect devices". en. In: *Progress in Surface Science* 92.3 (Aug. 2017), pp. 143–175. ISSN: 00796816. DOI: 10.1016/j.progsurf.2017.05.002. URL: https://linkinghub.elsevier.com/retrieve/pii/S0079681617300126 (visited on 03/11/2024).

[324] Johanna Anteroinen et al. "Extraction of Graphene-Titanium Contact Resistances using Transfer Length Measurement and a Curve-Fit Method". en. In: 6.8 (2012).

[325] Amit Gahoi et al. "Contact resistance study of various metal electrodes with CVD graphene". en. In: *Solid-State Electronics* 125 (Nov. 2016), pp. 234–239. ISSN: 00381101. DOI: 10.1016/j.sse.2016.07.008. URL: https://linkinghub.elsevier.com/retrieve/pii/S0038110116300880 (visited on 03/12/2024).

[326] G. Binnig, C. F. Quate, and Ch. Gerber. "Atomic Force Microscope". en. In: *Physical Review Letters* 56.9 (Mar. 1986), pp. 930–933. ISSN: 0031-9007. DOI: 10.1103/PhysRevLett.56.930. URL: https://link.aps.org/doi/10.1103/PhysRevLett.56.930 (visited on 01/23/2024).

[327] A. Einstein. "Über einen die Erzeugung und Verwandlung des Lichtes betreffenden heuristischen Gesichtspunkt". de. In: *Annalen der Physik* 322.6 (Jan. 1905), pp. 132–148. ISSN: 0003-3804, 1521-3889. DOI: 10.1002/andp.19053220607. URL: https://onlinelibrary.wiley.com/doi/10.1002/andp.19053220607 (visited on 02/13/2024).

[328] Noboru Suzuki. "Chapter 13 - X-Ray Photoelectron Spectroscopy and its Application to Carbon". In: *Carbon Alloys*. Ed. by Ei-ichi YASUDA et al. Oxford: Elsevier Science, 2003, pp. 211–222. ISBN: 978-0-08-044163-4. DOI: https://doi.org/10.1016/B978-008044163-4/50013-9. URL: https://www.sciencedirect.com/science/article/pii/B9780080441634500139.

[329] Fred A. Stevie and Carrie L. Donley. "Introduction to x-ray photoelectron spectroscopy". en. In: *Journal of Vacuum Science & Technology A: Vacuum, Surfaces, and Films* 38.6 (Dec. 2020), p. 063204. ISSN: 0734-2101, 1520-8559. DOI: 10.1116/6.0000412. URL: https://pubs.aip.org/jva/article/38/6/063204/1024200/Introduction-to-x-ray-photoelectron-spectroscopy (visited on 02/14/2024).

[330] A. Bogner et al. "A history of scanning electron microscopy developments: Towards "wet-STEM" imaging". en. In: *Micron* 38.4 (June 2007), pp. 390–401. ISSN: 09684328. DOI: 10.1016/j.micron.2006.06.008. URL: https:

//linkinghub.elsevier.com/retrieve/pii/S0968432806001016 (visited on 01/31/2024).

[331] Adam J. Schwartz et al., eds. *Electron Backscatter Diffraction in Materials Science*. en. Boston, MA: Springer US, 2009. ISBN: 978-0-387-88135-5 978-0-387-88136-2. DOI: 10.1007/978-0-387-88136-2. URL: https://link.springer.com/10.1007/978-0-387-88136-2 (visited on 01/31/2024).

[332] Kalsoom Akhtar et al. "Scanning Electron Microscopy: Principle and Applications in Nanomaterials Characterization". en. In: *Handbook of Materials Characterization*. Ed. by Surender Kumar Sharma. Cham: Springer International Publishing, 2018, pp. 113–145. ISBN: 978-3-319-92954-5 978-3-319-92955-2. DOI: 10.1007/978-3-319-92955-2_4. URL: http://link.springer.com/10.1007/978-3-319-92955-2_4 (visited on 01/31/2024).

[333] Caroline A Schneider, Wayne S Rasband, and Kevin W Eliceiri. "NIH Image to ImageJ: 25 years of image analysis". en. In: *Nature Methods* 9.7 (July 2012), pp. 671–675. ISSN: 1548-7091, 1548-7105. DOI: 10.1038/nmeth.2089. URL: https://www.nature.com/articles/nmeth.2089 (visited on 04/05/2024).